Buckling Behavior of Spirally Welded Steel Tubes

Nicolas Blaine Pueppke

for the degree of:

Master of Science in Civil Engineering

Date of Submission: 11 August, 2014
Date of Defense: 20 August, 2014

Committee:

Ir. A.M. Gresnigt	Delft University of Technology Steel, Hybrid, and Composite Structures Section
Prof. ir. F.S.K. Bijlaard	Delft University of Technology Steel, Hybrid, and Composite Structures Section
Dr. ir. M.A.N. Hendriks	Delft University of Technology Structural Mechanics Section
Ir. S.H.J. van Es	Delft University of Technology Steel, Hybrid, and Composite Structures Section

Structural Mechanics Section, Department of Structural Engineering
Faculty of Civil Engineering and Geosciences
Delft University of Technology, Delft, The Netherlands

Author: Nicolas Pueppke
Student Number: 4224450
email: n.pueppke@student.tudelft.nl

Abstract

This report deals with the buckling behavior of spirally welded steel tubes. First, an existing analytical solution and the results of an extended experimental investigation are investigated. The imperfections measured during testing are investigated and classified, and methods are proposed to incorporate them into finite element models. Buckling analyses are carried out using finite element software, the resulting eigenmodes are characterized, and the response of tubes to various combinations of buckling modes is investigated.

Next, the tubes themselves are modeled, incorporating these imperfections, full material models, and residual stresses. The results are compared to the results of the experimental program. Statistical analyses are also performed to investigate the accuracy of the models.

Finally, parameter studies are carried out in order to investigate the effect that various parameters have on the response of the tubes, both in terms of critical curvature and maximum moment. The parameters are characterized based on their significance, and recommendations are made for future research.

Preface

This thesis report is submitted in partial fulfillment of the requirements of the degree of Master of Science in Civil Engineering at Delft University of Technology in Delft, The Netherlands. The subject of this report concerns the buckling behavior of welded steel tubes. It was undertaken in order to complement and extend an experimental test program related to spirally and longitudinally welded steel tubes which was recently carried out in Delft. In particular, the purpose of this study was to create finite element models of the tubes which were physically tested in order to use them for parameter studies and to make them available for future parameter studies.

In this section, I would like to thank the people who have supported me throughout my studies. I would especially like to thank my friends and family for always being there for me, regardless of what mistakes I may have committed or achievements I may have accomplished. I would also like to thank my committee for their support, especially Mr. S.H.J. van Es of Delft University of Technology for always being willing to answer my questions and for his constructive and detailed comments about my work. I would also like to acknowledge Mr. van Es for providing the experimental data which I used to compare to my models, as well as the schematic of the test setup and all photographs which I used. Finally, I would like to give special thanks to Mr. Daniel Vasilikis of the University of Thessaly for providing the residual stress distribution and some of the material data which I used, as well as his willingness to answer any questions I had related to the creation of finite element models.

I hope that this report will help to focus future research efforts into the behavior of welded steel tubes and inspire the reader to continue their own work in creative and relevant ways.

Nicolas Pueppke

Table of Contents

List of Figures

List of Tables

List of Symbols

a	-	horizontal half-ovalization of tube	*mm*
b	-	vertical half-ovalization of tube, length of curvature bracket	*mm*
d.f.	-	degrees of freedom of a statistical sample	
D	-	outside diameter of tube	*mm*
ΔD	-	total horizontal ovalization of tube	*mm*
E	-	modulus of elasticity	*Mpa*
f_{resid}	-	residual stress	*MPa*
f_y	-	nominal yield stress	*MPa*
$f_{y,ref}$	-	reference yield stress	*MPa*
f_t	-	ultimate tensile stress	*Mpa*
F	-	observed value of F-statistic	
F_{crit}	-	critical value of F-statistic for 95% confidence	
I	-	moment of inertia	mm^4
k	-	curvature	*/mm*
k_{buck}	-	curvature at onset of buckling	*/mm*
k_{crit}	-	curvature corresponding to maximum moment	*/mm*
k_y	-	curvature at first yield	*/mm*
δk	-	change in curvature	*/mm*
L	-	length of tube	*mm*
L_{hinge}	-	length of plastic hinge	*mm*
M	-	section moment	*kNm*
M_{buck}	-	moment at onset of buckling	*kNm*
M_e	-	elastic moment	*kNm*
M_{ep}	-	section moment in analytical model where elastoplastic material properties have been used	*kNm*
M_m	-	maximum moment based on current curvature in analytical model	*kNm*
M_{max}	-	maximum moment in moment-curvature relation	*kNm*
M_p	-	plastic moment	*kNm*
m_p	-	plate plastic moment	*kNm/m*
m_y	-	plate moment	*kNm/m*
n	-	sample size	

n_p	-	plate plastic normal force	*kNm/m*
n_y	-	plate normal force	*kNm/m*
p	-	p-value (proability that regression coefficient = 0)	
r	-	radius of tube	*mm*
R^2	-	coefficient of determination	
s	-	arc length	*mm*
SE	-	standard error	
SS	-	sum of squares	
t	-	thickness of tube	*mm*
t_{crit}	-	critical value of t-distribution for 95% confidence	
$t_{observed}$	-	observed t-value of regression coefficient	
2w	-	imperfection height	*mm*
y	-	vertical deflection of curvature bracket	*mm*
α	-	rotation of end support	*rad*
ε, ε_{nom}	-	nominal (engineering) strain	*mm/mm*
ε_{true}	-	true strain	*mm/mm*
$\varepsilon_{true,pl}$	-	true plastic strain	*mm/mm*
ε_y	-	nominal yield strain	*mm/mm*
θ	-	total tube/ring model rotation, central angle of an arc	*rad*
θ_{hinge}	-	plastic hinge rotation	*rad*
λ	-	imperfection (buckling mode) half-wavelength	*mm*
λ_s	-	section slenderness	*unitless*
ν	-	Poisson's ratio	*unitless*
ρ	-	radius of curvature	*mm*
σ, σ_{nom}	-	nominal (engineering) stress	*MPa*
σ_{true}	-	true stress	*MPa*
φ	-	plasticity angle, angle of rotation	*rad*
ψ_m	-	slope of the yield surface	*unitless*

1 Introduction

Combined sheet and pile walls, hereafter referred to as "combined walls", are an economical method of creating retaining walls when high forces are involved. Combined walls consist of primary load carrying elements spaced at regular intervals and connected by weaker intermediate elments. One type of combined wall, which consists of tubular primary elements (tubes) and secondary sheet piles, is shown in Figure 1.

Figure 1: Combined sheet and pile wall

Combined walls are economical solutions because they have much higher capacity than walls made out of sheet piling only, and because the manufacturing of tubular piles is very cost effective. These tubular sections are manufactured by longitudinally weldding or, more commonly, by spirally welding plates together.

1.1 Overview of Current Design Rules

The current European design rules for combined walls are given in EN1993 Part 5: Piling. According to these rules, primay elements of cross sectional classes 1-3 should be evaluated on a global level according to EN1993 Part 1-1: General Rules, and elements of class 4 should be evaluated for local buckling according to EN1993 Part 1-6: Strength and Stability of Shell Structures.

According to EN1993-1-1, cross section class can be determined based upon the D/t ratio and the yield stress of sections. For common tubular pile steel grades, the limiting D/t ratios above which the section should be classified as class 4 are shown in Table 1.

Table 1: Limiting D/t ratio for cross sectional classification of steel tubes

API Steel Grade	**f_y (MPa)**	**Class 4 D/t Limit**	**Class 4 λ_s Limit**
B	245	86	89.7
X42	290	72	88.9
X46	320	66	89.9
X52	360	58	88.9
X56	390	54	89.6
X60	415	50	88.3
X65	450	47	90.0
X70	485	43	88.7

In practice, D/t ratios between 60 and 150 are commonly used and available (*ArcellorMittal* 2010). Therefore, Table 1 shows that the primary elements of combined walls with a steel grade above X46 must always be checked according to EN1993-1-6, and the lower steel grades must often be checked as well.

It is also possible to compare results using a so-called section slenderness, as defined in Eqn. 1. EN1993-1-1 essentially uses this equation but solved for D/t, with a reference yield strength of 235 Mpa, as shwon in Eqn. 2. For consistency with the Eurocode, 235 MPa will also be used throughout this paper.

$$\lambda_s = \left(\frac{D}{t}\right)\left(\frac{f_y}{f_{y,ref}}\right) \tag{1}$$

$$\frac{D}{t} \leq \lambda_s \epsilon^2 \tag{2}$$

With:

$$\epsilon^2 = \sqrt{\left(\frac{235}{f_y}\right)} \tag{3}$$

The section slenderness is useful because it takes both yield stress as well as D/t ratio into account to classify sections. Using Eqn. 1, Table 1 can be summarised by stating that any sections where $\lambda_s > 90$ are class 4. The limiting section slendernesses for all section classes according to EN1993-1-1 are shown in Table 2.

Table 2: Section classification tubular sections

Section Class	λ_s
1	$\lambda_s \leq 50$
2	$50 < \lambda_s \leq 70$
3	$70 < \lambda_s \leq 90$
4	$90 < \lambda_s$

Experience has shown that the Eurocode gives overly conservative designs for the following reasons:

1. Previous versions of EN1993-1-6 limit the allowable membrane stress in the shell, effectively assuming that shells buckle elastically. This is an appropriate assumption for shells with a very high D/t ratio, such as tanks and silos, but tubular piles are expected to buckle inelastically with significant plastic strain capacity. This is currently being addressed in a new revision to the Eurocode.
2. Post buckling capacity provided by surrounding piles if one pile were to fail is not taken into consideration.
3. There is a significant jump in capacity between class 3 and class 4 sections at the limiting D/t ratio, depending on whether EN1993-1-1 or EN1993-1-6 is used. This likely leads to a significant underestimation of the capacity of class 4 sections near this limiting D/t value (Van Es et al. 2013).
4. The design rules are based on tests with significant scatter, resulting in the application of high safety factors (Gresnigt 1986).

1.2 State of Current Research

1.2.1 Theoretical Background

The minimum total potential energy principle states that a body will deform to a position which minimizes the total potential energy in the system. Translated into structural mechanics, this means that when a load is applied, a structural system will deform into a position which minimzes the total strain energy in the system. In other words, a structure will deform according to the path of least work into a state of least total strain energy.

A fundamental consequence of this principle is that for hollow shapes, bending does not result only in longitudinal and transverse strains, as it does for solid sections, but also in lateral deformation of the cross section (hereafter referred to as ovalization), because the section can dissipate energy by ovalizing. This can also be thought of from a purely mechanical point of view by realising that the forces directed along the length of the pipe due to bending will also have normal components directed towards the center of the pipe.

Brazier was the first to make use of this principle to study pipe bending (Brazier, 1927). Brazier allowed the cross section to deform and included this effect in the calculation of strain energy to derive a moment-curvature relationship for thin tubes bending in the elastic phase. Brazier also first described an instability known as limit point instability: the idea that an instability occurs when the moment-curvature relationship reaches a maximum, after which point the tube starts to collapse due to excessive ovalization. Brazier was also successfully able to verify his solutions for thin celluloid tubes in bending.

Brazier's derivation was refined by Reissner and Weinitschke (1963), who described both bending and ovalization in terms of a system of differential equations which were then solved to derive moment-curvature relations and ovalization-curvature relations for elastic tubes.

Limit point instability was further studied by Ades (1957) and Gellin (1980), who extended the previous analyses into the plastic range. Ades assumed that a round section would deform into an ellipse, and Gellin allowed the section to deform into an arbitrary oval shape. Neither author considered the effect of initial imperfections, however, both theorised that imperfections would have a significant effect on capacity as D/t ratio increases.

Another possible failure mode is bifurcation buckling, also known as axial wrinkling, which was not considered by Brazier or Ades. An early investigation into bifurcation buckling was conducted by Fabian in 1977, who investigated the relationship between the limit moment and the bifurcation moment in the elastic case. Fabian found that the limit moment and bifurcation moment almost coincide in the case of pure bending, and also showed that the bifurcation moment is bounded by the limit moment as the D/t ratio is decreased. Gellin extended Fabian's study by including the effects of plasticity, showing that even in this case the bifurcation and limit moments generally differ by no more than a few percent. Both authors only considered thick steel tubes, with D/t ratios between 15 and 50.

In 1972, Jirsa et al. performed full-scale 4 point bending tests on pipes which had D/t ratios between 30 and 80 and a yield stress of about 340 MPa ($43 < \lambda_s < 116$). The experimental results were then compared to results found using the theoretical method of Ades. They concluded that Ades' method accurately predicts the ultimate moment capacity for pipes in this D/t range, however, they also concluded that ovalization has very little effect on the ultimate capacity of pipes in bending, because all but one of the tubes buckled before significant ovalization occured.

Ju and Kyriakides (1992) attempted to unify bifurcation and limit point analysis into one numerical procedure. They performed experimental tests on aluminium tubes of various D/t ratios, and were able to identify several possible failure mechanisms that can occur in real tubes:

1. Thin tubes ($D/t>40$, $\lambda_s>50$): Axial wrinkling occurs, followed by catastrophic collapse of the tube. The limiting moment is never reached. This case was not investigated by Gellin or Fabian.
2. Thick tubes ($26<D/t<40$, $32<\lambda_s<50$): Axial wrinkling still occurs much closer to the limiting moment. The wrinkles form more slowly and progress into a single kink at the location of failure. There is still significant capacity after the bifurcation moment has been reached.
3. Very thick tubes ($D/t<26$, $\lambda_s<32$): The tube reaches the limiting moment and fails due to excessive ovalisation.

Ju and Kyriakides also mention that there is a strong interaction between bifurcation buckling and limit load instability in the case of intermediate tubes.

According to Ju and Kyriakides, it is likely that the tubes tested by Jirsa et al. were in the second thickness category, which means that according to Gellin, axial wrinkles must have formed during the tests. In general, possible reasons why axial wrinkling is often not observed during experiments include the following:

1. Since the bifurcation moment and limiting moment almost coincide in many cases (Gellin 1980), they may be indistinguishable during experimental testing.
2. There may be significant interaction between the two types of instability (Ju and Kyriakides 1992; Kyriakides and Ju 1992)
3. The presence of initial imperfections may cause one phenomena to dominate over the other (Reddy 1979).
4. Axial wrinkles are not always visible to the naked eye (Reddy 1979).
5. There is often significant additional capacity post-wrinkling (Hutchinson 1968; Ju and Kyriakides 1992; Kyriakides and Ju 1992).
6. Axial wrinkles may be forced to appear in certain locations due to initial imperfections.

In the case of Jirsa et al., it is most likely that they were simply not visible enough, especially since the theoretical foundations of bifurcation buckling in bending had not yet been developed.

In 1979, Reddy performed a very complete series of scale bending tests on steel and aluminium tubes with D/t ratios approximately between 10 and 20. Reddy used more sophisticated measuring equipment than Jirsa, and was able to both visually observe axial wrinkling, and also quantitatively measure it by measuring the longitudinal profiles of the tubes. Reddy was also able to measure ovalisation during the tests.

Reddy compared the experimental results to theoretical results obtained from two plasticity theories: J2 deformation theory and J2 flow theory (von Mises plasticity). Reddy found that the experimental strain capacities varied between 70-125% of that prediced by J2 deformation theory, and between 25-70% of that prediced by J2 flow theory.

Oddly, Reddy reported that the presence of axial wrinkles was surprising, and attributed their appearance to initial imperfections in the tube. Therefore, Reddy concluded that the discrepancy between the experimental and theoretical results was due to the presence of imperfections. Like Jirsa, Reddy also concluded that ovalization played little role in the bending capacity of the tubes.

However, it must be noted that it is possible that Reddy was not aware of Gellin's or Fabian's results, because they all published around the same time. Therefore, another possible interpretation of Reddy's results is that they simply demonstrate the weaknesses of theories which do not include ovalization or the possibility of axial wrinkling.

Spence and Toh (Spence and Toh, 1979) derived moment-curvature relationships for tubes in bending using a pure mechanics of materials approach, rather than an energy approach. They also performed small scale experimental tests on specimens with D/t ratios over 100. They showed reasonable agreement between the theory and experimental results at low curvatures, but were not able to predict the behavior closer to buckling. They also did not observe any axial wrinkling, and propose that this is due to the high length/diameter (L/d) ratios of the tested tubes. Although it is true that longer cylinders are less prone to axial wrinkling, because the end constraints in short tubes tend to prevent ovalization and force wrinkling, the authors themselves mention that their tubes were not long enough to be free of end effects, and also, because the cylinders failed by local buckling, it must be concluded that axial wrinkles formed at some point, which then progressed into a single local kink as described by Ju and Kyriakides. In reality then, the reasons why axial wrinkling was not observed are likely again due to the factors given above.

Elchalakani et al. (2002a) refined Ju and Kyriakides' classification after performing a series of tests on cold formed hollow sections with D/t ratios between 37 and 122. They characterised different failure mechanisms as follows, based upon a section slenderness defined in Eqn. 1.

1. Compact sections ($\lambda_s \leq 64$): The limiting moment is reached. The section fails due to excessive ovalization (a plastic hinge is formed).
2. Noncompact sections ($64 < \lambda_s \leq 146$): Local buckling and yielding occur around the same time. A localized kink is formed with most plastic deformation concentrated at this kink.
3. Slender sections ($\lambda_s > 146$): Local buckling occurs before the yield stress is reached. Buckling is very sudden and elastic.

It should be noted that the section slenderness limits vary for steel and aluminium, so the limits presented by Elchalakani cannot directly be compared to those presented by Ju and Kyriakides. In addition, the cold-forming process tends to introduce residual stresses which reduce stiffness, potentially resulting in a lower buckling capacity.

The goals of Elchalakani et al. were to improve the classification of sections for strength and rotation capacity, and in fact, if their recommendations were adopted, the issue of the jump in capacity between class 3 and class 4 sections in the Eurocode would be addressed. However, because they focused on rotation capacity, the exact buckling behavior of the different sections was only classified in a very broad sense.

Since pipe bending theories were first developed, many of the other experiments and analytical analyses have focused on thicker pipes, especially since they are more common in the petroleum industry. Some examples of experimental work regarding thick tubes include for example (Spinelli et al. 2011; Ueda 1985). Theoretical analyses and design recommendations for thick tubes have been published by many researchers including (Elchalakani et al. 2002b; Mamalis et al. 1989; Poonaya et al. 2009; Tatting et al. 1997; Wierzbicki and Sinmao 1997). Thick tubes have also recently been studied numerically by Wadee et al. (2006), who combined ovalization with Timoshenko beam theory, which allowed them to model the transition from global ovalization to final localised ovalization at the failure point. Good agreement was found with the experimental results of Ju and Kyriakides.

A complete analytical design procedure for pipes of any D/t ratio and any combination of loadings was presented by Gresnigt in 1986, which forms the basis of the current design rules used in EN1993 Part 4-3: Pipelines. This is a strain-based design procedure, which means that plastic deformation capacity is taken into account. The limit state of the pipe is defined in terms of a maximum deformation, in the form of a critical curvature. This is much preferable to the stress-based design found in EN1993-1-6, however, the applicability of this procedure to tubes of higher D/t ratios is in doubt (Gresnigt et al. 2010), and is currently being investigated experimentally by van Es.

1.2.2 Finite Element Analysis

In this section, a selection of papers published about the finite element modeling of tubes are presented. Karamanos (2002) compared ovalization instability and bifurcation buckling for tubes with D/t ratios over 100 using an in-house FEM formulation. Plasticity was not taken into account. Karamanos showed that ovalization alone cannot predict the actual behavior of bending tubes, and was also able to show that bifurcation buckling exhibits snap-back behavior under perfect conditions. In addition, Karamanos demonstrated that there is a very strong interaction between the two failure mechanisms, and that the exact behavior is strongly influenced by initial imperfections and initial out-of-straightness of the tubes. Karamanos also showed that for initially straight tubes under perfect conditions, bifurcation buckling will always occur before ovalization instability.

Houliara and Karamanos (2005) extended this investigation by considering the effect of internal pressure. The results found were largely similar. The limitation of both studies is that imperfections were not considered in detail, and plasticity was not taken into account, both of which are likely to have a significant impact on tubes in the D/t range considered in the present study. In addition, although the interaction between the two different instabilities was acknowledged, it was not fully investigated.

These issues were both addressed in a later paper (Houliara and Karamanos 2011), where the buckling behavior of thin-walled cylinders was addressed. In this paper, the results of Ju and Kyriakides, which were described above, were taken as a starting point for investigating the buckling behavior of thin-walled steel sections. A finite element analysis was performed on very thin elastic cylinders with D/t ratios of 120, 240, and 300. As expected, it was found that axial wrinkles formed and very quickly localized into a single local buckle. The limiting moment was never achieved.

Houliara and Karamanos also investigated the effect of initial imperfections on the moment-curvature diagram, introduced by superimposing the first buckling mode, scaled by various factors related to the thickness of the tube. They found that increasing imperfection amplitudes reduced the ultimate capacity of the tubes, but not by as much as imperfections reduce the capacity of tubes loaded in compression. They also found that increasing the imperfection amplitude led to a smoothening of the moment-curvature relation.

The inelastic case was also investigated. A thin-walled cylinder with a D/t ratio of 240 and yield strength of 483 MPa (λ_s=493) was investigated numerically. This cylinder was also found to behave in a very similar way to the elastic cylinders: axial wrinkles formed, which quickly progressed into a local buckle. The limiting moment was never reached. This result also agrees with the observations of Ju and Kyriakides, and is not unexpected, because the extreme slenderness of the tube makes it behave in a very similar way to an elastic tube.

Although the effect of imperfections was investigated, the weakness of this study is that only very thin-walled tubes were investigated, which are of much less importance in civil engineering applications. The extreme slenderness of the tubes also meant that they behaved in a very elastic way, even when plasticity was taken into account.

Lee et al. (2012) investigated the effect of girth welding on the mechanical behavior of cylinders in bending. Tubes with D/t ratios between 20 and 100 were considered, and the temperature dependence of the material properties E and f_y was included. An in-house FEM formulation was used to model the welding process, and the results of this thermal analysis were used as an initial thermal loading during a mechanical analysis. The effects of global initial imperfections were also considered.

Lee et al. found that the girth weld reduced ductility because the strain hardening capacity of the tubes was reduced. They also found that for thick tubes, local buckles formed near the girth welds, causing a change from a pure ovalization failure mode to a combined ovalization and buckling failure mode. Similar results were found for tubes with higher D/t ratios, but it was found that as D/t ratio increased, the effect of the girth weld on the capacity of the tube also increased. This is believed to be due to a larger relative plastic region near the girth weld for thinner tubes. Finally, they found that the tubes always buckled at the girth welds, but their global imperfections were symmetric, and they hypothesize that asymmetric initial imperfections might interact differently with the girth weld.

Finally, various methods of modeling boundary conditions have been investigated by several Italian researchers (Giordano et al. 2008; Guarracino et al. 2008). Three ways of modeling tubes to allow ovalization were investigated: increasing the length of the tubes, using a rigid plate to apply forces to the tube ends through contact elements, and using a coupling combined with a spherical or cylindrical coordinate system to allow free movement in the radial direction. In these papers, it was found that coupling the tube ends in such a way that ovalization is not prevented in the radial directions was the best solution. Increasing the tube length would introduce unwated plastic strain into the tubes, while using a rigid plate would induce local buckling at the tube ends.

1.3 Scope of Assignment

Despite being a popular research topic for nearly 100 years, the instability of shell structures is still a poorly understood phenomenon. The theory of elastic stability has been developed by authors such as Koiter and Timoshenko, and the specific case of the buckling of pipes in bending has been extensively investigated as detailed above, but the general consensus is that these types of instabilities are very difficult to investigate analytically, and current design codes are based on experimental testing. In recent years, the reliability of current design methods has increasingly been called into question, especially due to the fact that there is significant scatter in test results, and the fact that pipes of intermediate D/t ratios may experience significant plasticity before buckling, despite being designed according to elastic methods.

As computing power has increased, the finite element method has emerged as a viable way of investigating complex phenomena such as bifurcation buckling. The goal of the present study is to complement the physical testing that was carried out in Delft with finite element modeling to improve the understanding of the buckling behavior of spirally welded steel tubes with intermediate D/t ratios ($60<D/t<120$). Each tube which was investigated experimentally was recreated, and the available experimental data was used to calibrate these models. These models were then used to answer the following questions:

1. What is the influence of initial imperfections on the buckling capacity of the tubes, and how imperfection sensitive are the tubes?

2. Which additional parameters have the most significant influence on the capacity of the tubes?

In addition, a method to model any spirally welded tubes accurately and consistently has been developed, and it is expected that these types of models will be used for further research into this type of buckling behavior.

2 Description of Experimental Program

2.1 Full Scale Bending Tests

The experimental program carried out at Delft University of Technology involved full scale bending tests of 13 spirally welded steel tubes and 2 longitudinally welded steel tubes. The work described in this section was primarily carried out by ir. S.H.J. van Es of Delft University of Technology. Diagrams and photographs of the test setup are shown in Figures 2 and 3, respectively.

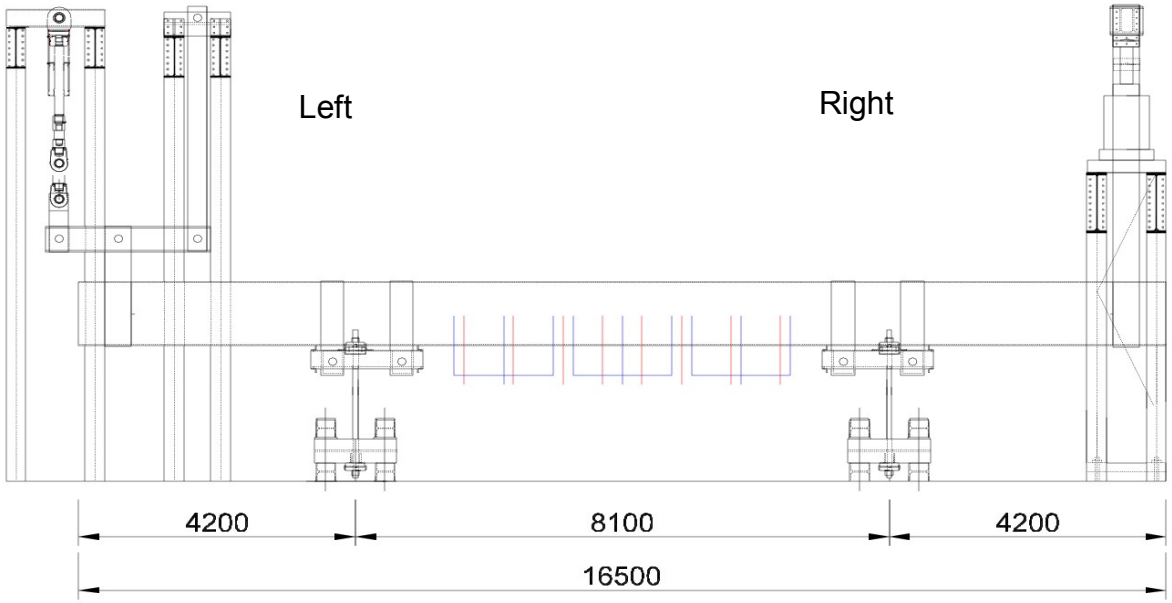

Figure 2: Shematic of test setup

Figure 3: Photograph of test setup

Each tube is characterized by its diameter, thickness, material properties, type of welding/production process, and imperfections. The imperfections will be discussed in more detail in Section 3.

The material properties were determined by carrying out a series of tensile and compressive tests. In this case, the tension tests will be described. They were carried out on specimens cut from the inside and outside faces of the tube walls in both the longitudinal and circumfrential directions, resulting in four tests per tube. An extensometer was used to measure strains up to 0.02 mm/mm, and strain gages were used to measure the overall strain throughout the test. The overall strain was corrected (to allow for 'seating' of the test specimen) by removing the difference between gage strain and extensometer strain at 0.02 mm/mm from all of the strain gage data.

The four nominal stress-strain curves found for each tube were used to generate average nominal stress-strain curves for each tube. These were then later converted to true stress-true plastic strain curves for insertion into ABAQUS®. The nominal stress-strain curves for Tubes 1, 2, 3, 4, 5, 8, 9, and 11 were generated by Daniel Vasilikis of the University of Thessaly, while the curves for the remaining tubes were generated by the author of this report. The curves for all tubes can be found in Appendix A.

In addition to the full stress-strain curves, each material was also characterized in terms of its yield stress. There is no set definition of yield stress, especially when the yield point is not well defined, but in this case, it has been decided to define the nominal yield stress f_y as the stress at 0.2% plastic strain.

Most of the tubes tested were spirally welded tubes, but some of the tubes also included girth or coil connection welds. Finally, Tubes 14 and 15 included longitudinal welds instead of spiral welds. Examples of each weld type are shown below.

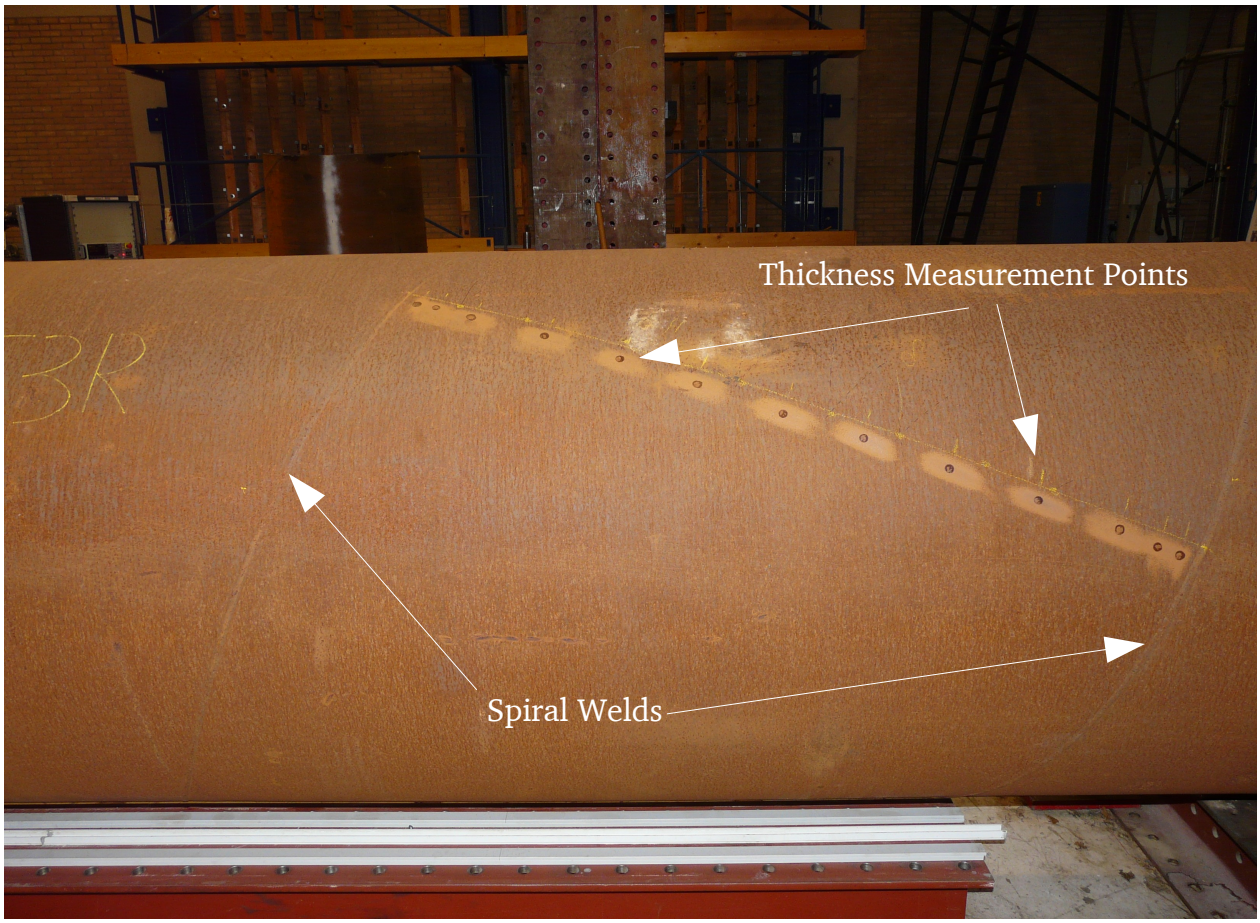

Figure 4: Example of spiral welds

Figure 4 shows the weld pattern of a plain spirally welded tube. The spiral welds run in a helix around the tube while the tube itself is formed out of a flat coil of steel, which is formed into a tubular shape and then continuously welded together. The spots visible in the figure are locations where thickness measurements were taken.

Figure 5 shows a girth weld, while Figure 6 shows a coil connection weld. Girth welds are used to join two separate pipes together, while coil connection welds are used to join two coils of steel together.

Finally, Figure 7 shows an example of a longitudinal weld.

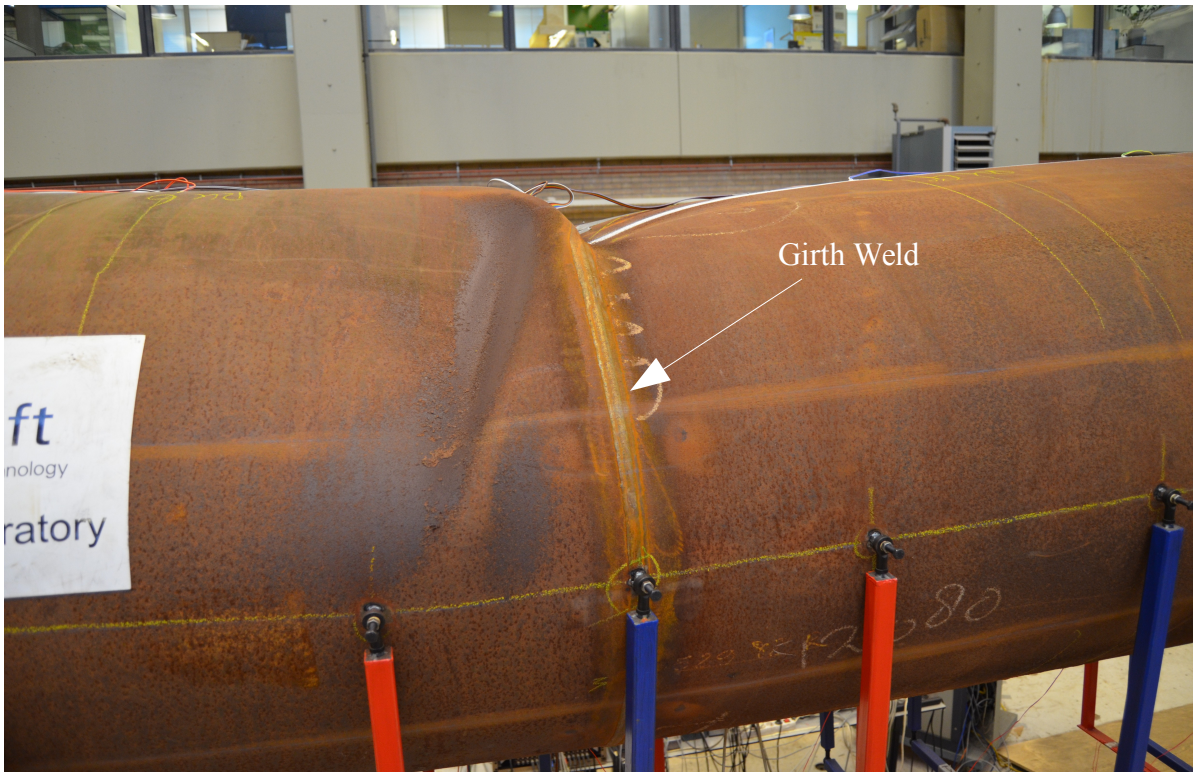

Figure 5: Example of girth weld

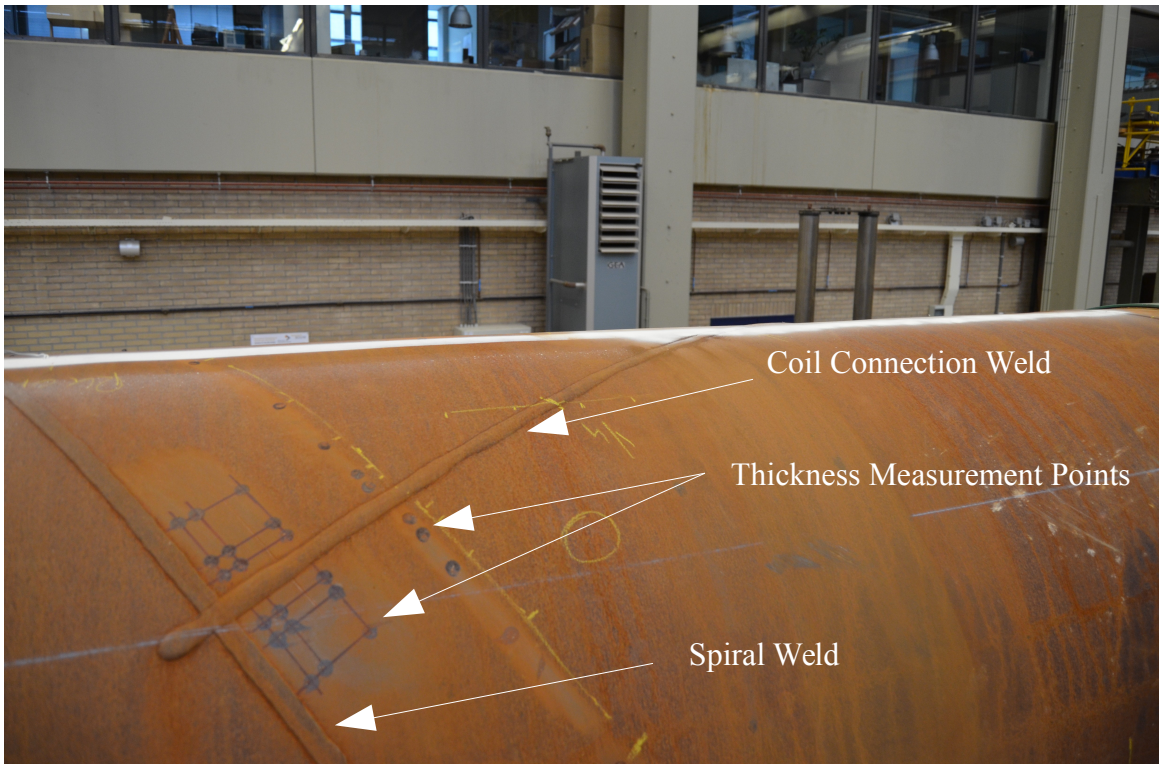

Figure 6: Example of coil connection weld

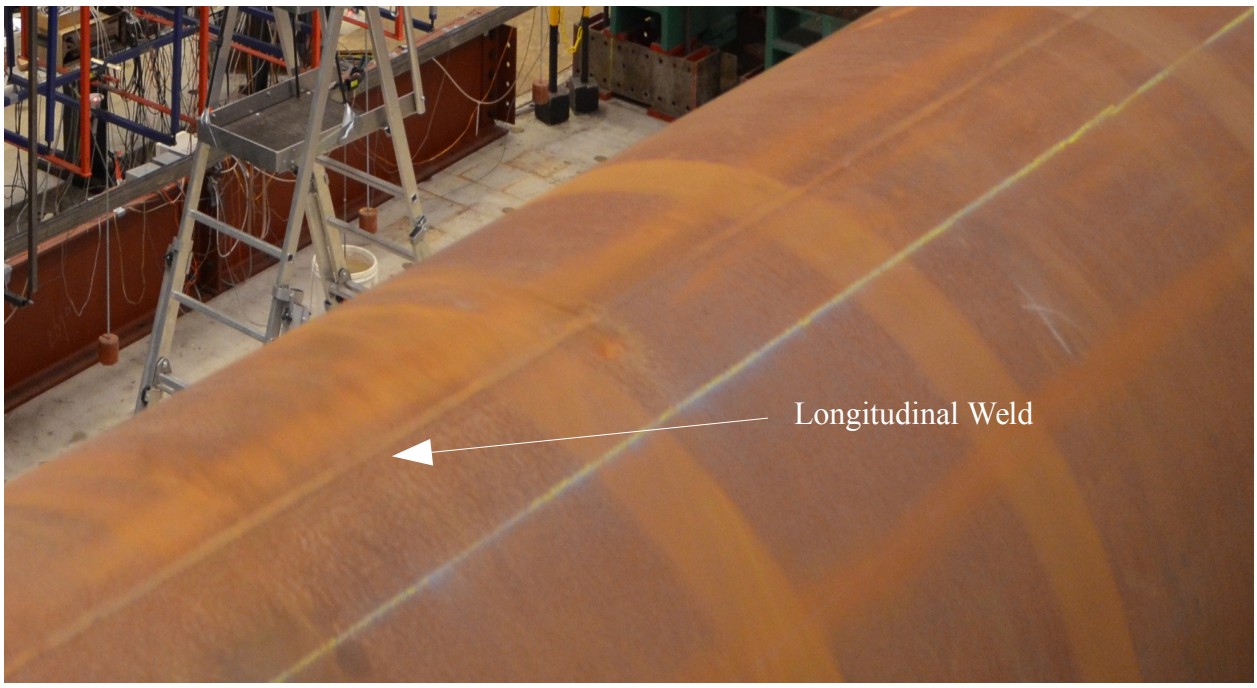

Figure 7: Example of longitudinal weld

A summary of all tubes tested in Delft is shown in Table 3. The tubes with girth or coil connection welds are divided into three sections: 'Left', 'Mid', and 'Right'. The notes "Left" and "Right" refer to the left most or right most sections, as viewed according to Figure 2, and the note "Mid" refers to the middle section, between the coil connection weld and the girth weld. For these tubes, the geometric and material properties were measured separately in each section.

Table 3: Summary of tubes used for experimental program

Tube #	**D (mm)**	**t (mm)**	**D/t**	**λ_s**	**$f_{y,avg}$ (MPa)**
1	1066	16.4	65	149	540
2	1067	9.0	119	150	390
3[1], Left	1067	8.8	121	193	375
3[1], Right	1070	9.2	116	202	410
4	1065	9.2	116	207	420
5	1070	9.0	119	202	400
6[2], Left	1067	16.1	66	147	525
6[2], Right	1066	16.4	65	151	545
7[1,2], Left	1067	16.4	65	159	575
7[1,2], Mid	1066	16.3	65	155	560
7[1,2], Right	1068	16.3	65	159	575
8	1068	9.1	117	217	435
9	1069	16.4	65	158	570
10[1,2], Left	1070	13.3	80	179	525
10[1,2], Mid	1070	13.3	80	165	485
10[1,2], Right	1069	12.8	84	116	325
11	1068	12.9	83	120	340
12[1,2], Left	1069	9.1	117	214	430
12[1,2], Mid	1067	9.2	116	242	490
12[1,2], Right	1069	9.1	117	214	430
13[1], Left	1070	9.1	118	213	425
13[1], Right	1071	9.2	116	220	445
14[3]	1068	9.8	109	244	525
15[3]	1070	14.8	72	164	535

[1]girth weld
[2]coil connection weld
[3]longitudinally welded

In addition to the full scale tests, measurements were also done to determine the following properties:

-wall thickness

-diameter

-initial ovalization

-material properties

-presence of residual stresses

-spiral pitch

The test setup itself was a four point bending test designed to give a constant moment in the center span. During testing, it was found that the reaction forces were always slightly higher on the left side, which was partially corrected during testing by adjusting the displacement of each cylinder manually while the tube was still elastic, and also accounted for during the analysis phase. This may be due to an asymmetry in the test setup, which is because identical hydraulic cylinders were not available to use at each end of the test setup.

The mid supports of the test set up were designed to introduce the load as smoothly as possible into the tube. The supports had the capacity to move and rotate slightly to follow the deformation of the tube, and two straps were used in order to smoothen the load introduction. The straps were also designed to allow for ovalization of the tubes, because the tubes were short enough that rigid supports may have had an influence on the test results.

Many data sets were collected during testing, including real-time measurement of strain, ovalization, and curvature at various locations. The locations of the curvature and ovalization brackets are shown in Figure 8. The blue lines indicate the curvature brackets, while the red lines indicate the ovalization brackets.

In addition, measurements of the imperfections were also periodically collected. These measurements were collected via two laser cars, remote controlled cars fitted with lasers to measure the distance from the car to the tube wall (see Figures 10 and 11). One car drove through the tube, collecting circumfrencial profiles of the tube at 200mm intervals via a rotating laser, as well as a scan of the top inside surface of the tube to measure the imperfections. There was also a car which drove along a beam suspended above the tube, making a downward measurement of the outside profile of the top of the tube to measure the imperfections.

Along with the experimental program in Delft, an experimental program was also carried out at Karlsruhe Institute of Technology, where the effect of normal forces was also investigated, and additional numerical modeling has been carried out at the University of Thessaly and the University of Edinburgh.

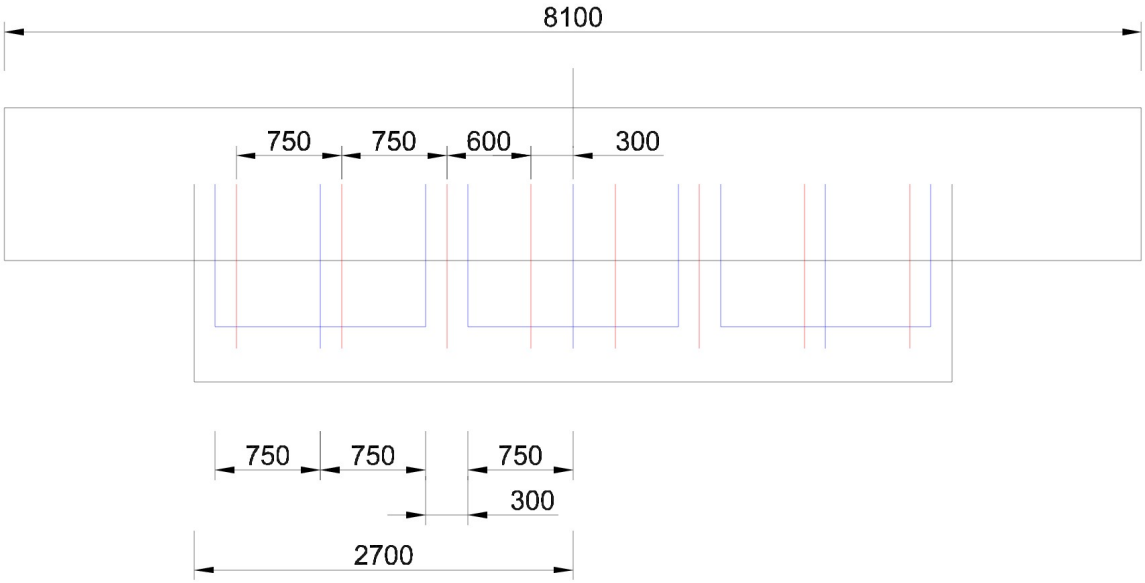

Figure 8: Locations of measurement brackets

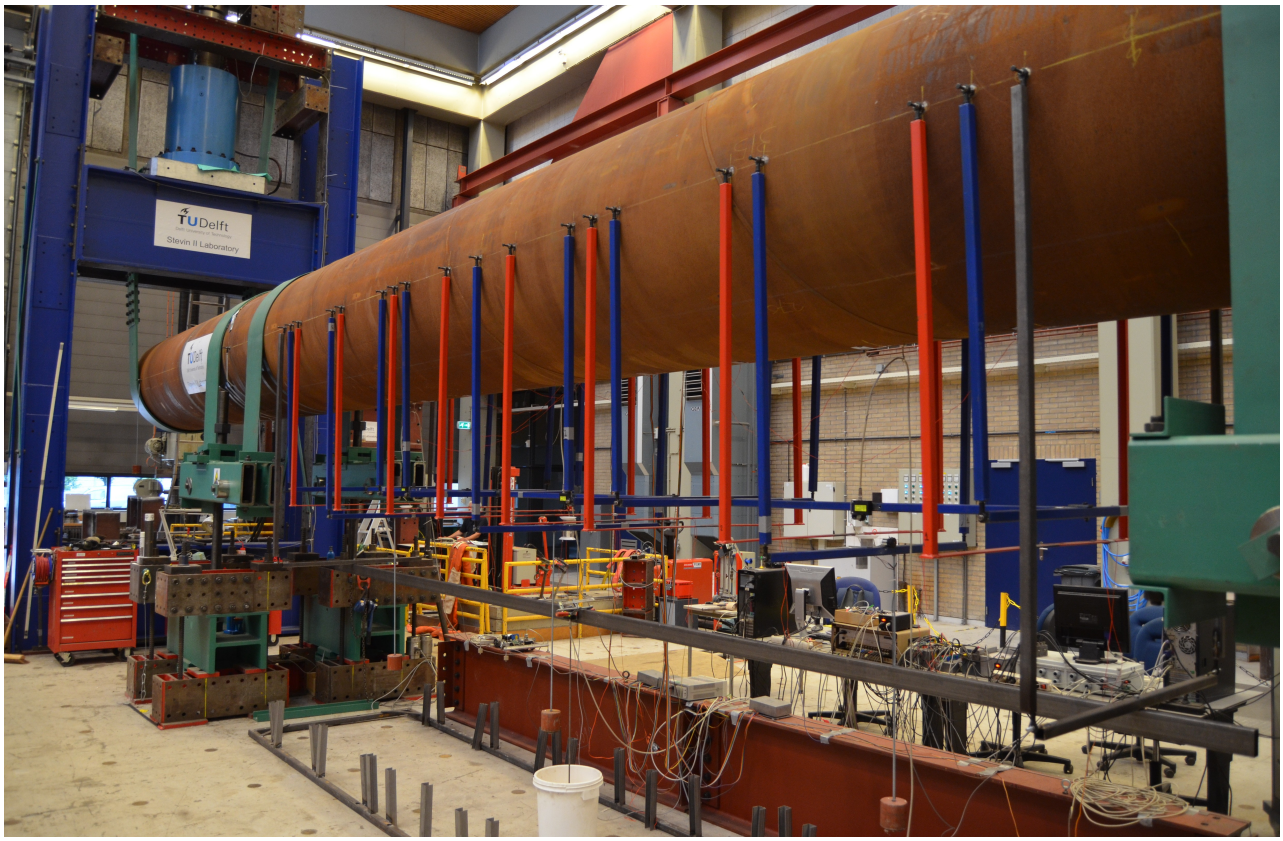

Figure 9: Detail of measurement brackets

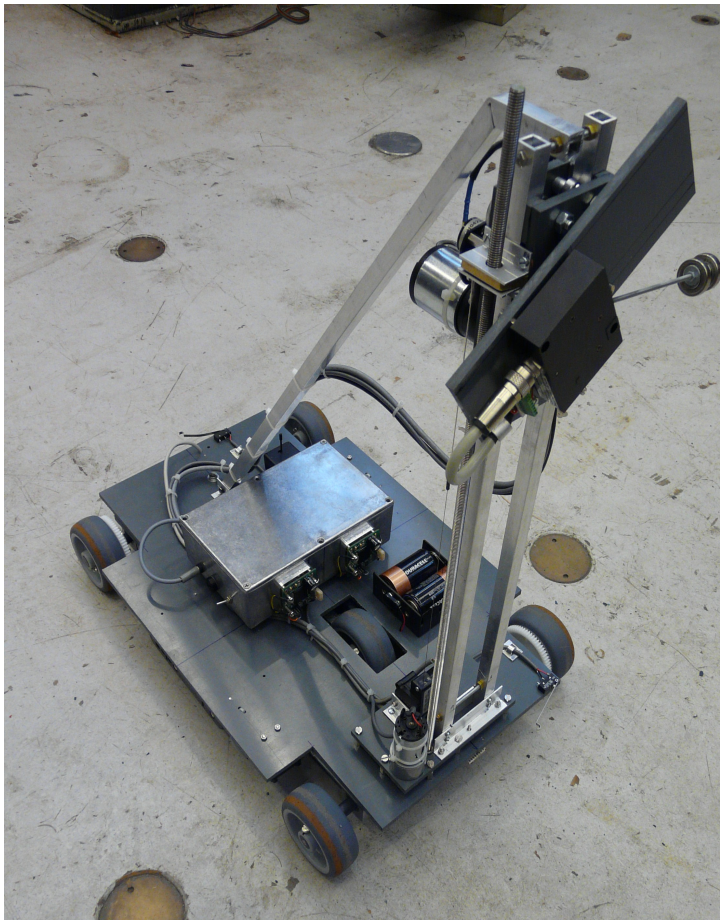

Figure 10: Laser car 1

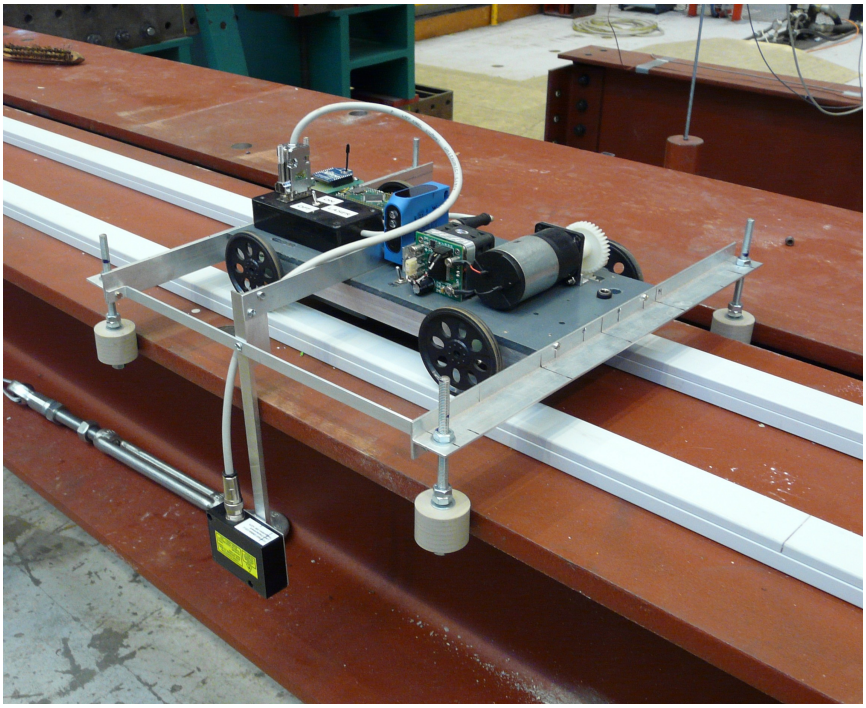

Figure 11: Laser car 2

2.2 Definition and Measurement of Curvature

Curvature can be defined in several ways. In an elastic beam, the definition is straightforward and comes from basic geometric relationships.

According to the theory of elasticity, in the elastic range, the moment is given by:

$$M = EIk_{elastic} \tag{4}$$

Where:
M = section moment
E = modulus of elasticity
I = moment of inertia
$k_{elastic}$ = elastic curvature

This curvature is defined as follows, where ρ is the radius of curvature (see Figure 12):

$$k_{elastic} = \frac{1}{\rho} \tag{5}$$

The relationship between the central angle of an arc θ and the arc length s is given by:

$$s = \rho\,\theta \tag{6}$$

The central angle is equal to the total rotation of the beam, which is always given by:

$$\theta = \alpha_1 + \alpha_2 \tag{7}$$

Finally, inserting Eqns. 5 and 7 into Eqn. 6, as well as setting s = L, the following definition of elastic curvature can be derived:

$$k_{elastic} = \frac{\alpha_1 + \alpha_2}{L} \tag{8}$$

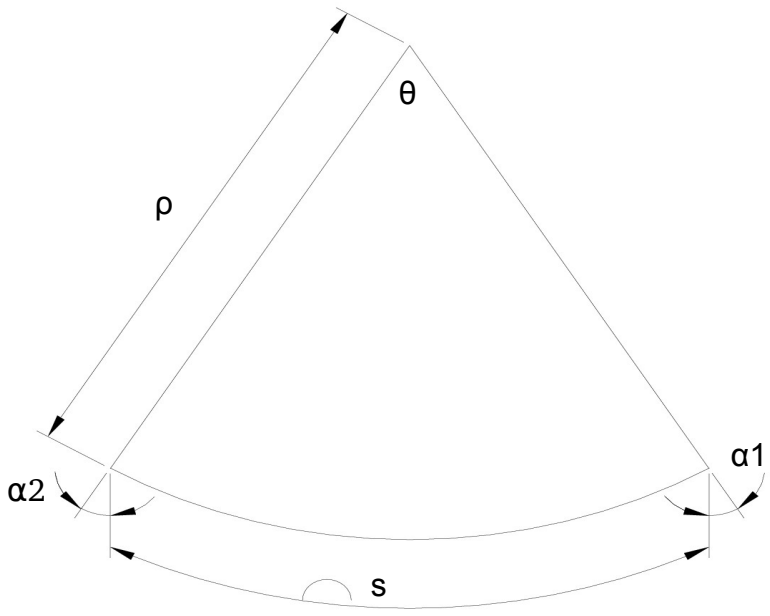

Figure 12: Definition of curvature

Once yielding occurs, the rotation in the beam will slowly localize to the location of a plastic hinge. The curvature contribution due to the rotation of the hinge is given by:

$$k = \frac{\theta_{hinge}}{L_{hinge}} \tag{9}$$

In an ideally plastic section, the beam will bend according to Figure 13. In that case, the hinge rotation can be defined as follows:

$$\theta_{hinge} = \alpha_1 + \alpha_2 \tag{10}$$

This gives the following definition of plastic curvature:

$$k_{plastic} = \frac{\alpha_1 + \alpha_2}{L_{hinge}} \tag{11}$$

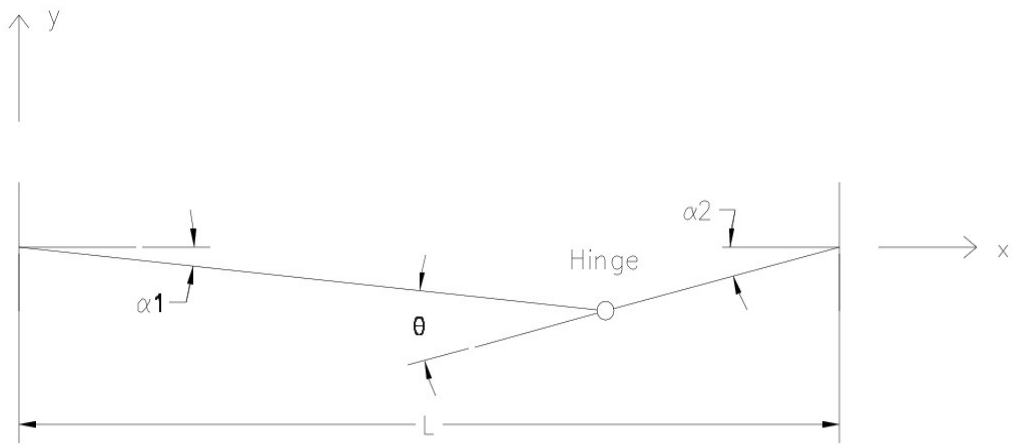

Figure 13: Geometry of buckled tube

By comparing Eqns. 8 and 11, it can be seen that the difference between elastic and ideally plastic curvature is that the length over which the curvature is distributed is different. As an approximation, the plastic hinge rotation may also be distributed over the length of the entire tube, giving one unified definition of curvature:

$$k = \frac{\alpha_1 + \alpha_2}{L} \tag{12}$$

Three other curvatures are now defined based on this definition:

k_y = curvature at first yield

k_{crit} = curvature at maximum moment

k_{buck} = curvature at buckling (bifurcation point)

In many cases, $k_{crit} = k_{buck}$. They are only expected to differ in very ductile tubes with low D/t ratios, in which case tube may have significant rotation capacity after the limiting moment is reached before failure.

This basic curvature k is the main curvature that is used to compare the results of the FEM analyses with the experimental results. During the experimental program, the rotations of the end supports α_1 and α_2 could be measured based on the displacement of the end supports. This curvature is also refered to as 'Kappa', to differentiate it from the other curvatures measured during testing.

These other curvatures were measured using special brackets attached to the tubes (see Figure 18). A laser was used to measure the distance between the inner and outer brackets, and this distance was used to calculate the curvature, which follows according to Figures 12 and 14.

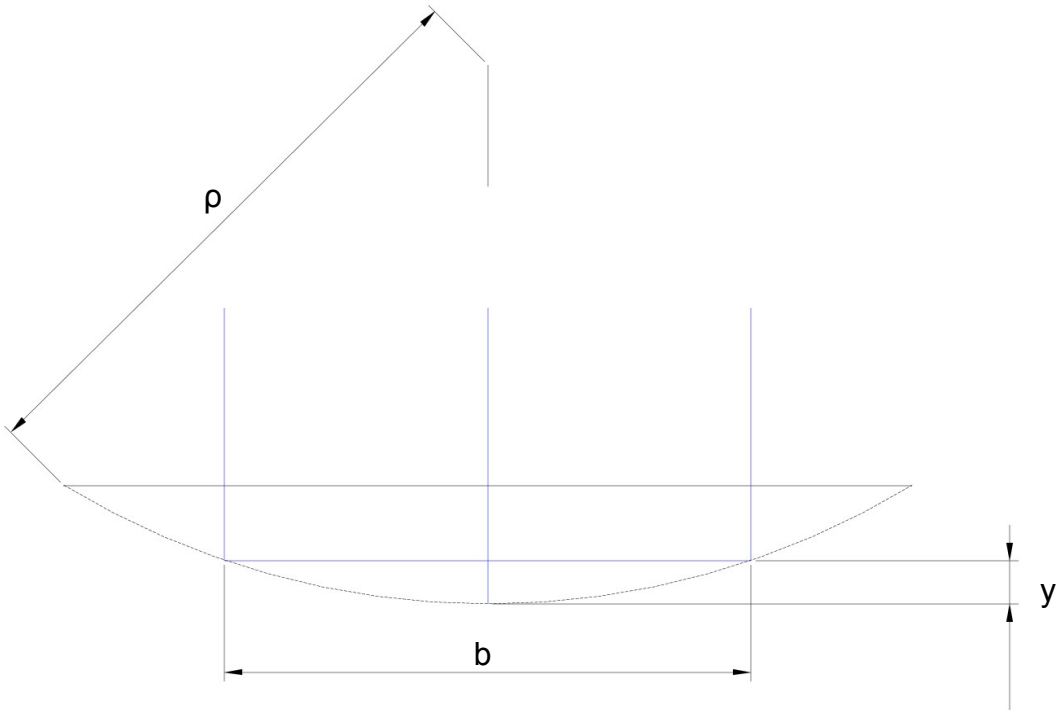

Figure 14: Geometry of curvature bracket

Given a change in distance between brackets y, a bracket length b, radius of curvature ρ, and curvature k, the total curvature is given by the following equations:

$$(\rho - y)^2 + \left(\frac{b}{2}\right)^2 = \rho^2 \tag{13}$$

$$2\rho y = y^2 + \frac{b^2}{4} \tag{14}$$

Since $y^2 << b^2$:

$$\rho = \frac{b^2}{8y} \tag{15}$$

Finally:

$$k = \frac{1}{\rho} = \frac{8y}{b^2} \tag{16}$$

Three 1.5m brackets were used to measure local curvature (referred to as 'curv1', 'curv2', and 'curv3', starting from the left end of the tube), and one 5.4m bracket was used to measure overall curvature (refered to as 'curvall'). The overall curvature bracket was not used during the first three experiments.

3 Analysis and Characterization of Initial Imperfections

3.1 Approach and Methods

The initial imperfections of the tubes were measured via a laser car which made a measurement of the outside surface of the tubes at 22.5° intervals. The results were used to decide how to orient the tubes in the test setup and to determine the size of the imperfections to introduce into the FEM models. The measurement length approximately corresponds to the length of the mid span of the tubes.

In this section, the imperfections are analyzed and grouped into several categories. It is explained how the imperfection heights were derived for each tube, and the results are reported for each tube.

3.2 Results

The critical imperfections could be grouped into several distinct types:

1. Characteristic humps. Most tubes buckled at locations with a characteristic 'hump' imperfection, including all plain spirally welded tubes except for Tube 9, as well as Tube 12. These humps are likely marks due to the tooling used to bend flat plates into a tubular shape. The characteristic imperfection was taken as the height of this 'hump', which was then introduced into the FEM models by scaling one of the elastic buckling modes to this value. Figure 15 shows the profile of a typical hump-type imperfection.

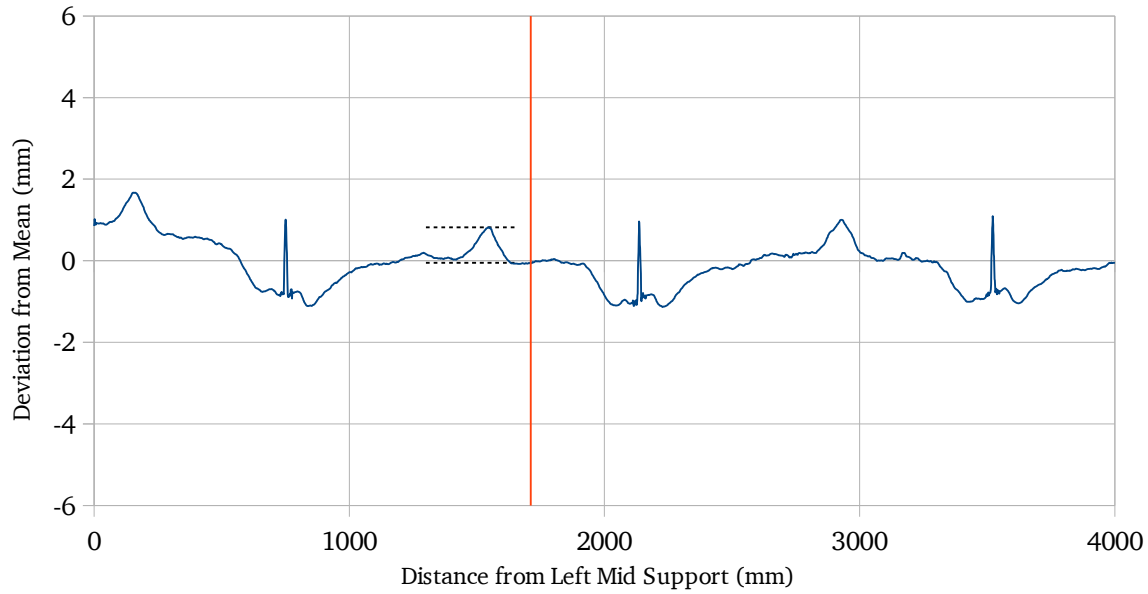

Figure 15: Characteristic hump imperfection of Tube 2

2. Weld Features. Tubes 3, 10, and 13 failed at the of girth welds and Tube 6 failed at a coil connection weld. Although Tubes 12 also featured both types of welds, it failed at a hump type imperfections. Tubes 7 and 9 are the only tubes which failed at a spiral weld instead of at a hump or other weld feature. In reality, the tubes did not fail at the welds themselves but at large imperfections very close to the welds caused by the fabrication process.

Girth welds are generally characterized by an offset at the weld location, as well as an additional imperfection at the weld. Both features were incorporated into the FEM models. The coil connection welds did not appear to be associated with an offset, but they were characterized by a much shallower and wider weld profile than the other types of welds. For these welds, the imperfections were taken as the height of the largest imperfection near the weld.

Typical weld profiles are shown in Figures 16-18.

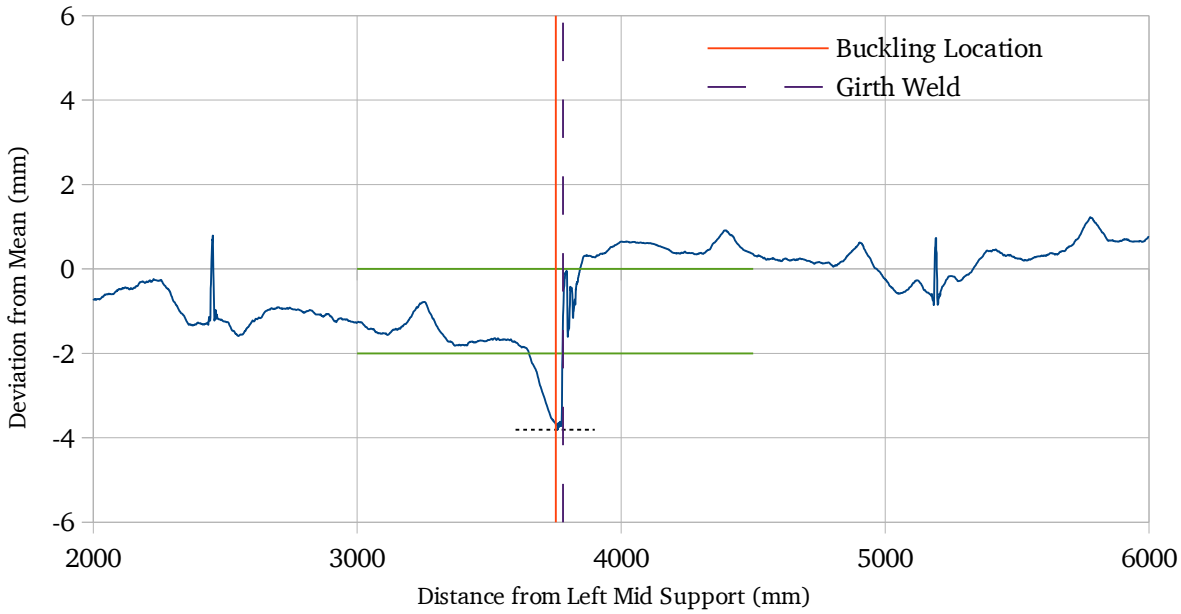

Figure 16: Offset at girth weld of Tube 3

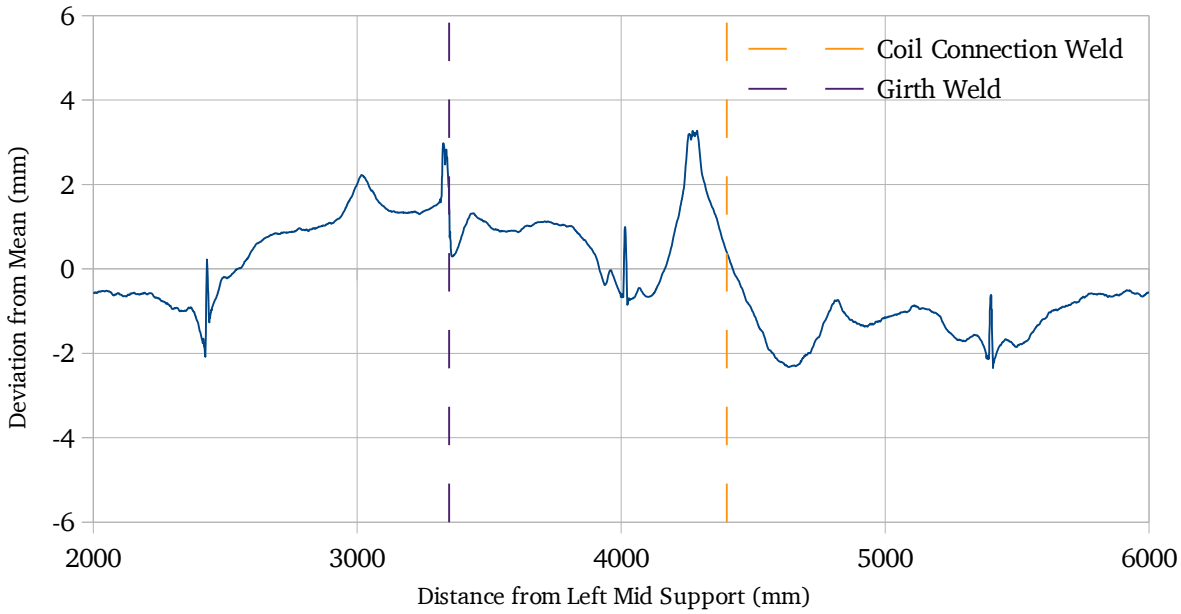

Figure 17: Girth and coil connection weld profiles of Tube 12

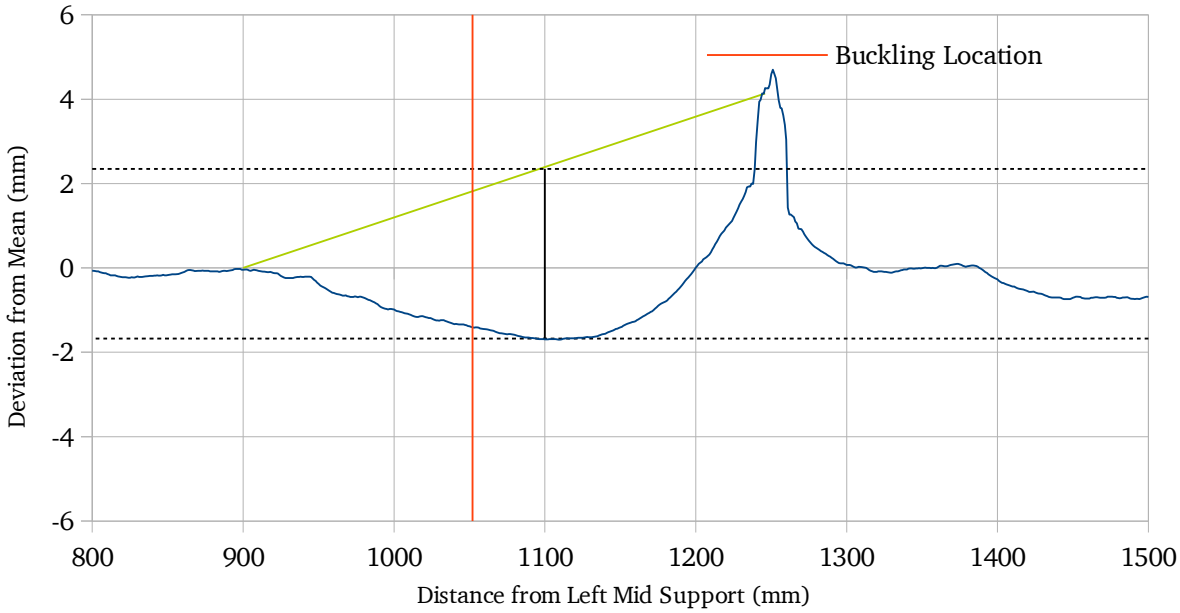

Figure 18: Spiral weld profile of Tube 9

3. Longitudinally welded tubes. The initial profiles of Tubes 14 and 15 are very different from the other other tubes because the production process is quite different. There are no welds or tooling marks in the profiles. The profile of Tube 14 does not appear to have a regular pattern, while Tube 15 is characterized by a series of waves with a long wavelength.

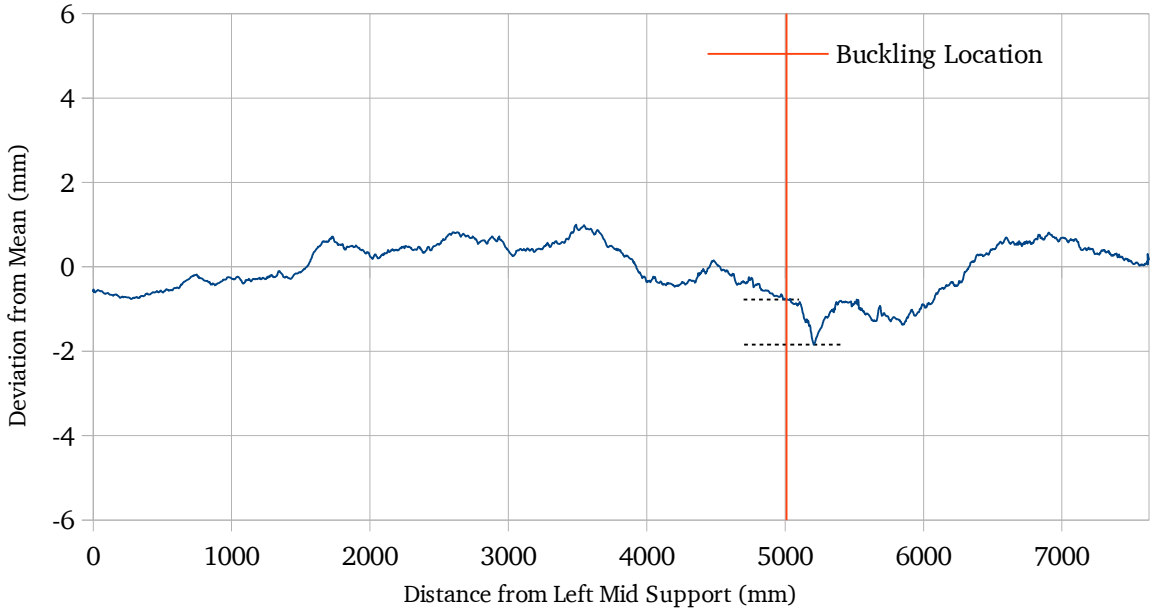

Figure 19: Irregular profile of Tube 14

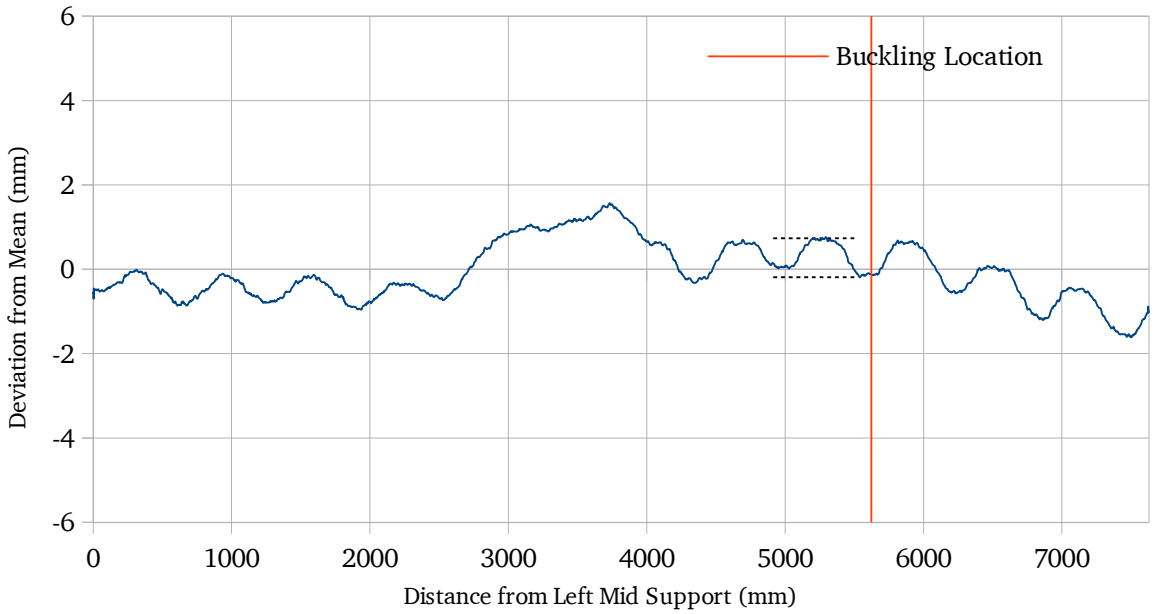

Figure 20: Wavy profile of Tube 15

3.3 Discussion

The analysis of imperfections shows that all plain spirally welded tubes aside from Tube 9 buckled at an initial 'hump' type imperfection, thought to be caused by tooling. These measured imperfections were directly incorporated into the FEM models, as described in Section 5.4. Tube 9 was the only plain spirally welded tube which buckled at a spiral weld. For this tube, an intermediate imperfection was used based on the two imperfections observed near the location of buckling.

The girth and coil connection welded tubes generally failed at the location of girth welds, although Tube 12 failed at a hump-type imperfection and Tube 7 failed at a spiral weld. For all of these tubes, any observed offset was included in the models. For Tubes 3, 6, and 10, any additional imperfection measured at the weld was included, while for Tube 12, an imperfection was also introduced into the left part of the tube equal to the size of the hump measured at the buckling location, and for Tube 7, an intermediate imperfection was introduced similar to the imperfection used for Tube 9.

Tubes 14 and 15, which are longitudinally welded tubes, showed no similarity to the other tubes or to each other. For these tubes, it was simply decided to introduce imperfections scaled to the largest characteristic imperfection observed near the buckling location.

Table 4 shows the measured imperfections which were included in the FEM models, including the offset at any girth welds. Graphs of all initial tube profiles are found in Appendix B.

Table 4: Summary of imperfection heights

Tube	2w (mm)	$2w/t_{avg}$	Offset (mm)
1	0.645	0.039	-
2	0.871	0.097	-
3[1]	1.700	0.189	2
4	0.636	0.069	-
5	0.718	.078	-
6[2]	3.100	0.191	-
7[1,2]	2.450	0.150	-
8	1.070	0.117	-
9	2.010	0.123	-
10[1,2]	1.200	0.091	3
11	0.465	0.036	-
12[1,2]	1.160	0.127	-
13[1]	1.500	0.163	0.5
14[3]	1.066	0.109	-
15[3]	0.926	0.063	-

[1]girth weld
[2]coil connection weld
[3]longitudinally welded

3.4 Conclusions and Recommendations

In this section, the imperfections measured in the tubes were analyzed, and the characteristic imperfections were described for each tube type. For the plain spirally welded tubes with the exception of Tube 9, the imperfections were introduced into the FEM models based on characteristic hump-type imperfections observed near the buckling locations. For Tube 9, imperfections was chosen based on two characteristic imperfections observed near the buckle.

For the Tubes 3, 6, 10, and 13, any offset at the weld was measured and incorporated into the models, and any additional imperfections were included based on the measured imperfections at the welds. For Tube 12, an imperfection was introduced based on the characteristic hump-type imperfection observed at the buckling location, while for Tube 7, an imperfection was introduced similar to that used for Tube 9 based on the tube profile near the spiral weld.

Finally, for the longitudinally welded tubes, imperfections were simply introduced based on the initial profiles observed near the buckles.

4 Bending and Ovalization Models

4.1 Ovalization Models

Ovalization is defined as the change in diameter of an initially round tube during bending, as shown in Figure 21. Figure 22 shows the forces which cause this ovalization, which are the vertical components of the bending forces. Most authors utilize the classic elastic ovalization model first proposed by Reissner and Weinitschke (1963), although plastic ovalization models do exist, the one derived by Gresnigt (1986) being of particular interest.

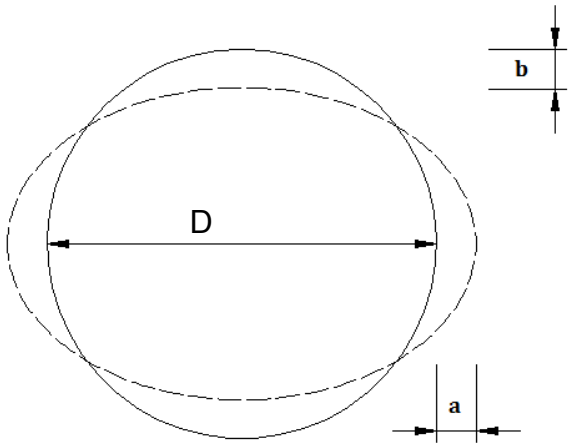

Figure 21: Ovalization of tube during bending

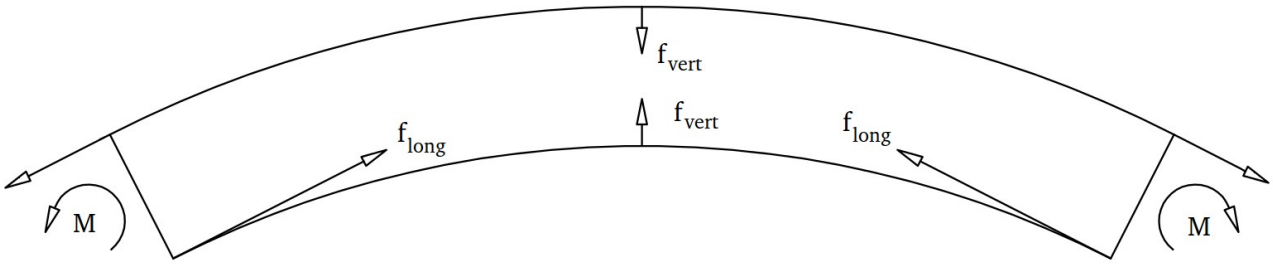

Figure 22: Ovalization forces

4.1.1 Elastic Ovalization

The classic ovalization model derived by Reissner and Weinitschke is a closed form solution for the elastic ovalization at any given curvature. It is given by the following infinite series, where a and b are the horizonal and vertical half-ovalizations of the tube, respectively:

$$a_{i,\,elastic} = r\left(\frac{\alpha_i^2}{12} + \frac{\alpha_i^4}{960} - 2059\frac{\alpha_i^6}{168*7200} + \ldots\right) \tag{17}$$

$$b_{i,\,elastic} = r\left(\frac{\alpha_i^2}{12} + 71\frac{\alpha_i^4}{8640} + 44551\frac{\alpha_i^6}{7560*7200} + \ldots\right) \tag{18}$$

With:

$$\alpha_i = \frac{k_i r^2}{t}\sqrt{12} \tag{19}$$

In the elastic range of combined walls, α is on the order of .05-0.5, which means the higher order terms can be neglected, leading to:

$$a_{i,\,elastic} = b_{i,\,elastic} = r\left(\frac{\alpha_i^2}{12}\right) \tag{20}$$

4.1.2 Plastic Ovalization

An analytical ovalization model for tubes in the plastic range was derived by Gresnigt in 1986. This is an iterative solution, so it is best suited for implementation in a computer program or a spreadsheet. The ovalization model is briefly presented below, slightly simplified since the cases where internal pressure or torsion are present will not be considered.

First some definitions are given:

a = horizontal half ovalization of the tube

E = modulus of elasticity

f_y = yield stress of the steel

i = current load step

k = current curvature of the tube

r = radius of the tube

t = thickness of the tube

The elastic moment M_e is given by:

$$M_e = \pi r^2 t f_y \tag{21}$$

The plastic moment M_p is given by:

$$M_p = 4r^2 t f_y \tag{22}$$

The maximum moment that can be resisted is reduced from the plastic moment M_p to a value M_m, which depends on the stress distribution across the section. This equation is derived by assuming a stress distribution (which satisfies equilibrium), and then applying the yield criterion of von Mises:

$$M_{m,i} = h_i g_i M_p \tag{23}$$

With:

$$h_i = 1 - \frac{2}{3}\frac{a_i}{r} \tag{24}$$

$$g_i = \frac{c_{1,i}}{6} + \frac{c_{2,i}}{3} \tag{25}$$

$$c_{1,i} = \sqrt{4 - 3\left(\frac{n_{y,i}}{n_p}\right)^2 - 2\sqrt{3} * \left|\frac{m_{y,i}}{m_p}\right|} \tag{26}$$

$$c_{2,i} = \sqrt{4 - 3\left(\frac{n_{y,i}}{n_p}\right)^2} \tag{27}$$

$$n_p = tf_y \tag{28}$$

$$n_{y,i} = 0.2\frac{M_{m,i-1} k_i}{r} \tag{29}$$

$$m_p = .25 t^2 f_y \tag{30}$$

$$m_{y,i} = 0.071 \mathrm{M}_{m,i-1} k_i f_{0,i} \tag{31}$$

$$f_{0,i} = 1 + \frac{a_i}{r} \tag{32}$$

The plate forces are defined as (see Figure 23):

n_y = plate normal force
n_p = plastic plate normal force
m_y = plate moment
m_p = plastic plate moment

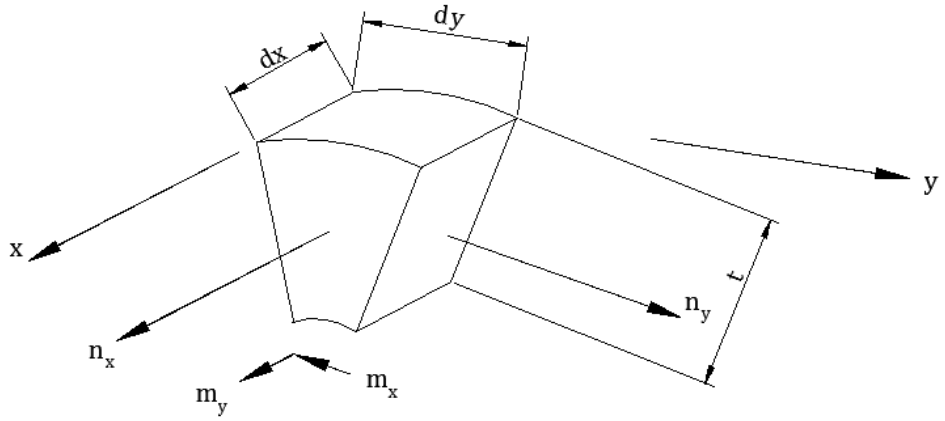

Figure 23: Sign convention for plate forces

The current section moment M assuming an elastoplastic stress strain relation is given by:

$$M_i = M_{m,i} * 0.5\left(\frac{\varphi_i}{\sin(\varphi_i)} + \cos(\varphi_i)\right) \tag{33}$$

The plasticity angle φ due to pure bending (See Figure 24) is given by:

$$\varphi_i = \arcsin\left(\frac{k'_{e,i}}{k_i}\right) \tag{34}$$

Where k'_e is a reduced curvature due to the reduction in stiffness caused by ovalization and is given by:

$$k'_{e,i} = \frac{M'_{e,i}}{EI_{\text{red,i}}} \tag{35}$$

And:

$$EI_{\text{red,i}} = E\,\pi r^3 t\left(1 - 1.5\frac{a_i}{r}\right) \tag{36}$$

$$M'_{e,i} = \frac{M_e}{M_p} M_{m,i} \tag{37}$$

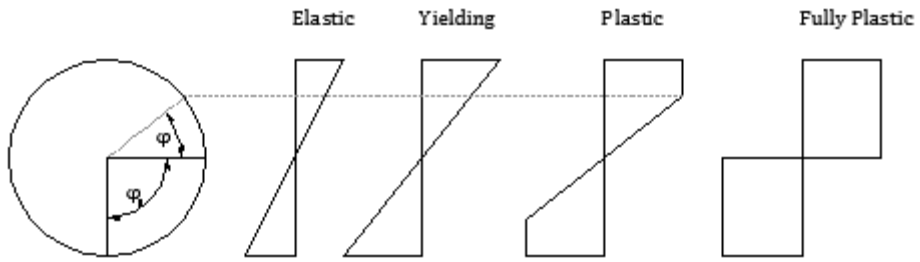

Figure 24: Definition of plasticity angle

The ovalization is calculated by assuming an elasto-plastic stress distribution. This results in a different expression for the moment used to calculate ovalization. The current moment M_{ep} assuming an elastic perfectly plastic stress-strain relation is given by:

$$M_{ep,i} = g_i M_p \tag{38}$$

Finally, the additional half ovalization after an increase in curvature δk is given by:

$$\delta a_{i,\,plastic} = \frac{-r^3}{t}\left(2\,\psi_{m,i-1}\right) * \delta k \tag{39}$$

And the total ovalization in the current load step is given by:

$$a_{i,\,plastic} = a_{i-1,\,plastic} + \delta a_{i,\,plastic} * \frac{M_{i-1}}{M_{m_{i-1}}} \tag{40}$$

Where ψ_m is the slope of yield surface, which is defined by:

$$\left(\frac{M}{M_p}\right)^2 - g^2 = 0 \tag{41}$$

In a computer implementation, the yield surface may be plotted in an easier way by simply plotting the calculated values of M_{ep}/M_p vs. the calculated values of m_y/m_p, and ψ_m can be calculated with a finite difference approximation.

As in the elastic ovalization model, the horizontal and vertical ovalization of the tube is assumed to be equal, leading to:

$$b_{i,\,plastic} = a_{i,\,plastic} \tag{42}$$

The factor M/M_m used in Eqn. 40 is a factor which approximates the ovalization in the elastoplastic range. Therefore, the correct procedure to implement this ovalization model is to use the elastic ovalization model until yielding, and then to increase the ovalization by $\delta a_{plastic}$ after each increase in curvature δk. The criteria used to determine whether or not the section has yielded is given below:

$$\begin{aligned} \Re(\varphi) \geq \frac{\pi}{2} &\rightarrow Elastic \\ \Re(\varphi) < \frac{\pi}{2} &\rightarrow Plastic \end{aligned} \tag{43}$$

4.1.3 FEM Ring Model

In addition to the analytical ovalization models, another tool used to verify these models is a ring model, as suggested by Van Es et al. (2013). This is simply a FEM model of a thin section of pipe, which is constrained in such a way that it is free to move in the transverse directions. One side of the strip is restrained in the longitudinal direction, and a bending moment is applied to the other side, via a reference point. The resulting undeformed and deformed shapes are shown in Figures 25-26.

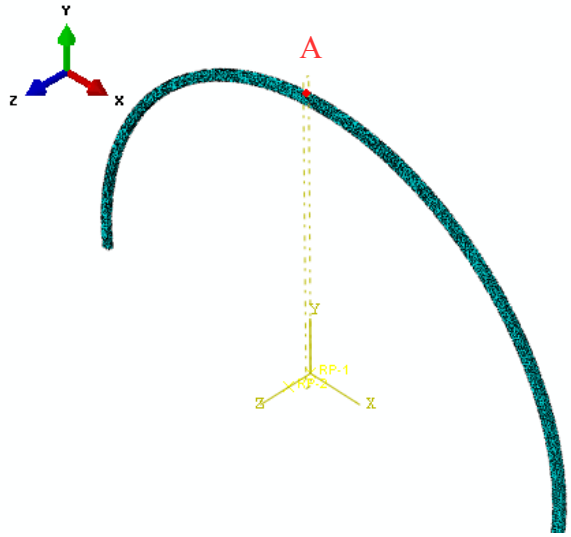

Figure 25: Undeformed ring model

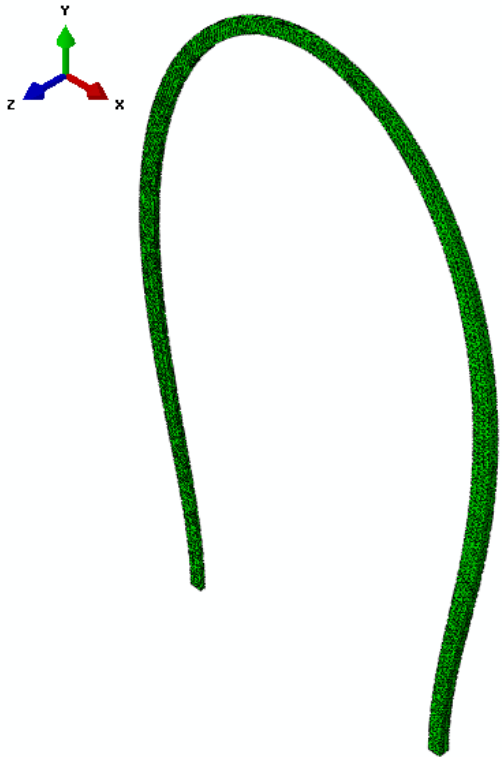

Figure 26: Deformed ring model

The ovalization can simply be determined from the transverse deflection of point A, and the corresponding curvature is given by:

$$k = \frac{\theta}{L} \tag{44}$$

Where θ is the rotation of the reference point, and L is the width of the strip, which was taken as 10mm.

4.2 Analytical Bending Model

The problem of pipe bending, not to mention pipe buckling, is very complex. So far, no analytical expressions exist for the critical strain (curvature) for inelastic tubes, although limiting strain values based on experimental tests are available in Gresnigt (1986). A full analytical solution for the moment-curvature relationship has also been derived in this paper.

In this derivation, the curvature k is defined as follows:

$$k = \frac{\theta}{L} \tag{45}$$

For a fully plastic section, the moment in the section is given by:

$$M_i = g_i M_p \tag{46}$$

The maximum moment M_m (as a function of the current curvature and ovalization) is given by:

$$M_{m,i} = h_i M_i = h_i g_i M_p \tag{47}$$

Equations for g_i, h_i, and M_p are given in Eqns. 25, 24 and 22, respectively.

The following approximation is made in the elasto-plastic range:

$$M_i = M_{m,i} * 0.5\left(\frac{\varphi_i}{\sin(\varphi_i)} + \cos(\varphi_i)\right) \tag{48}$$

This approximation assumes that the stiffness of the section slowly decreases after yielding. It is also valid over the full moment-curvature range, because it includes a yield criteria in the form of a plasticity angle φ. This model has been implemented in Matlab, and can be found in Appendix C.

5 Finite Element Modeling

5.1 Approach and Methods

Finite element models were created of all 15 tubes which were investigated experimentally using the commercial FEM package ABAQUS®. These models were calibrated according to available experimental data, and then they were used to perform parameter studies to investigate the sensitivity of the tubes to various changes in the models. A full description of how the models were created in ABAQUS® can be found in Appendix D.

In fact, two models were created for this project. Model 1 represents the mid section of each tube only, with a length of 8,100mm. Bending moments were applied to each end of the tube to simulate the constant moment situation created by the 4-point bending tests. This model accurately represents the geometry of the physical tubes, but does not allow ovalization at the tube ends. Therefore, a second model was created, which is a tube of length 12,500mm. In this model, the mid span of the physical tubes is represented by an 8,100mm section in the center of the model. The ends of the tube are still restrained but due to the additional length the ends of the 8,100mm central section are much less restrained. Both tubes have the same loading situation, with a constant moment along the entire length of the model.

The girth and coil connection welds were incorporated by simply partitioning the tube geometry into sections and applying the relevant material and geometric properties to each section separately. In the case of girth welds, any measured offset was incorporated, and then the nodes at the partitions were tied together so that they acted as one assembly. The material properties of the welds themselves were not considered. Both girth and coil connection welds were modeled as being normal to the longitudinal axis, even though coil connection welds are angled in reality.

For both FEM models, the full measured material models were applied as well as representative residual stress distributions. Imperfections were also applied to both models by performing elastic buckling analyses and applying the resulting deformations as initial conditions, scaled to the heightss of the measured imperfections. For Model 1, the elastic buckling analysis was carried out by applying bending moments to the tube ends, while for Model 2, bending moments were applied to an 8,100mm section in the middle of the tube, in order to generate the same buckling shape. This was done to keep the conditions between the two models as similar as possible.

5.2 Model Parameters

5.2.1 Load Introduction

The end conditions of tubes during bending may have a significant effect on their behavior. If the ends of the tube are supported improperly, the ovalization of the tubes may be restrained at these locations. These end effects will propagate from the supports of the tubes and will affect ovalization some distance away from the supports. In the experimental program, this was allowed for by using thin steel strips to support the tube at the mid support. This thin strips are strong enough to act as supports, but flexible enough to allow the tube to ovalize.

There are two basic ways to account for end effects in a finite element model. One way is to use end conditions that allow ovalization, and the second way is to ensure that the tube is long enough so that end effects may be ignored. The second alternative is simpler and was considered in this case. It is a valid solution because there is a constant moment throughout the entire length of the tube, so the moment-curvature response does not depend on the actual length of the tube.

A criteria to ensure the exclusion of end effects has been derived by Akselrad (taken from Spence and Toh (1979)):

$$\frac{L}{2r}\left(\frac{3}{1-\nu^2}*\frac{t^2}{r^2}\right)^{1/4} > 2 \qquad (49)$$

This relation has been solved for the minimum length L given υ=0.3, r=533.5mm, and various tube diameters. The results are reported in Table 5.

Table 5: Minimum tube length to avoid end effects

Thickness	**Minimum Length**
9 mm	12,194 mm
12 mm	10,560 mm
16 mm	9,145 mm
30 mm	6,679 mm
100 mm	3,658 mm

Despite these results, Model 1 was created with a length of 8,100mm for all tubes, because this matches the geometry of the test setup. However, based on these results, it was also decided to create a second model (Model 2) with a length of 12,500 mm. In order to ensure that 12,500mm was sufficient, Tube 5 (t = 9mm) was modeled with a length of 12,500mm, 15,000mm, and 20,000mm. The results are shown in Figures 27 and 28. These results include all of the imperfections, residual stresses, and material data which are further described in the following sections.

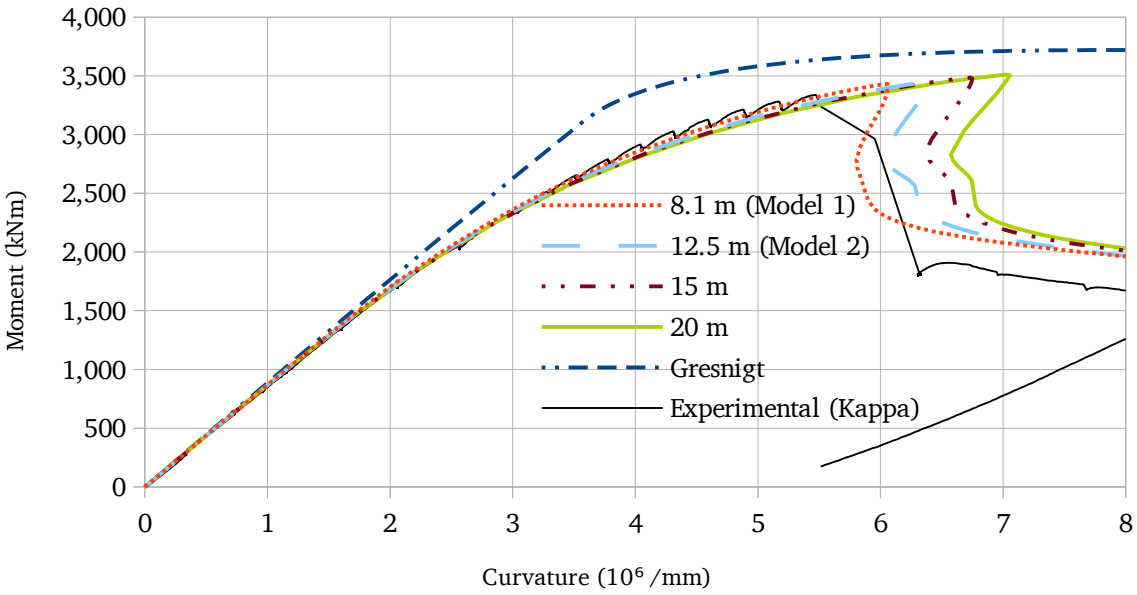

Figure 27: Effect of length on equilibrium path of Tube 5

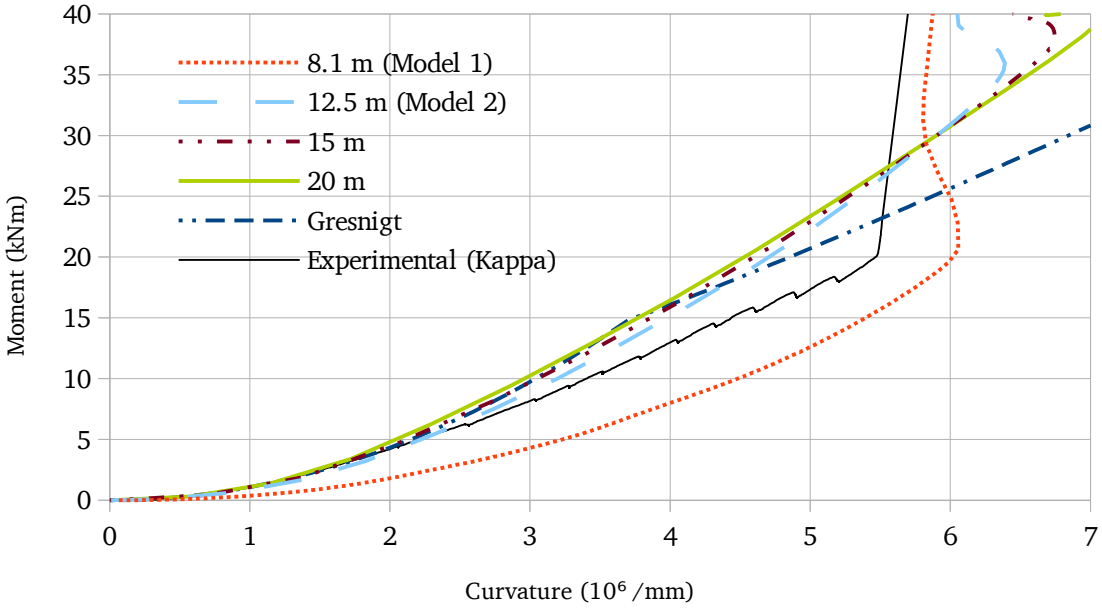

Figure 28: Effect of length on ovalization path of Tube 5

These figures show that although the ovalizations measured in the 15 and 20 meter models match the analytical solution almost perfectly, the critical curvature keeps increasing. This is a very unexpected result, because a more ovalized pipe is expected to buckle at a lower critical curvature.

It is thought that this is due to the way the tubes 'straighten' between the point when the curvature is elastic and the point when the buckle is fully localized. In particular, it is thought to be due to the fact that a global curvature measure is used as a measure of strain in the buckle. When the buckle is fully localized (see Figure 13), the regions of the tube away from the buckle straightens, in which case the measured curvature should not depend on the length of the tube, and there should be a linear relationship between strain and curvature for both models. This can be seen in Figure 27, because the post buckling equilibrium paths eventually converge if the tube is curved far enough. Similarly, while the tube is still elastic, each tube takes on the shape of a perfect arc. In fact, there is always a linear relationship between curvature and strain for any elastic tube. This can also be seen in Figure 27, where it is shown that the equilibrium paths matched in call cases until close to the point of buckling.

In the curvature range between these two extremes, it is thought that the strain corresponding to a given curvature is higher for shorter tubes than for longer tubes. It was attempted to confirm this theory by plotting the strains in the main buckle for Models 1 and 2. The von Mises stresses at buckling were also investigated. The results are shown below.

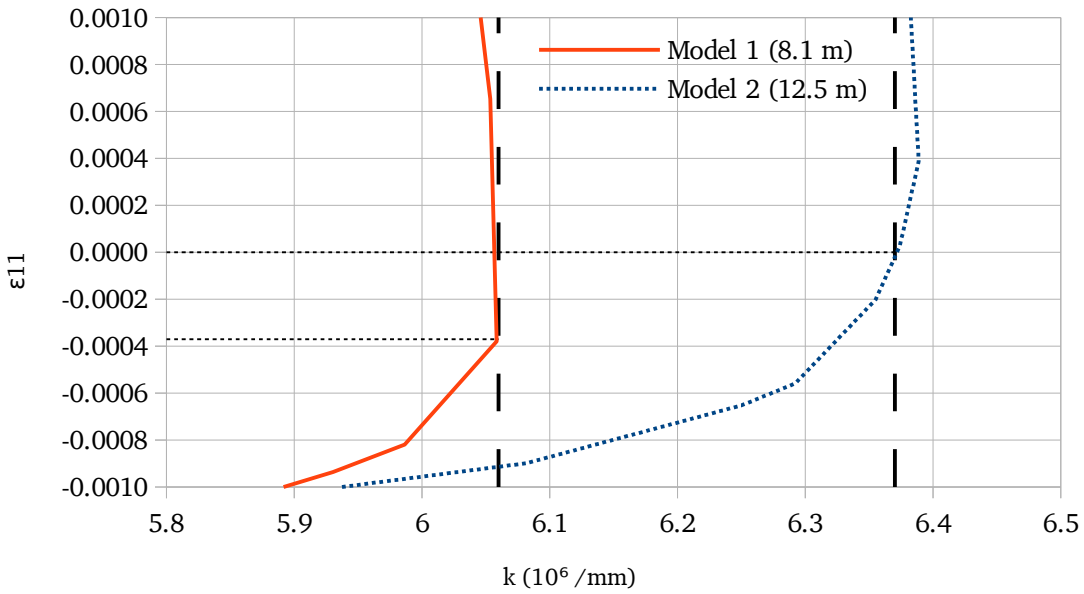

Figure 29: Comparision of first principle strain ε_{11}

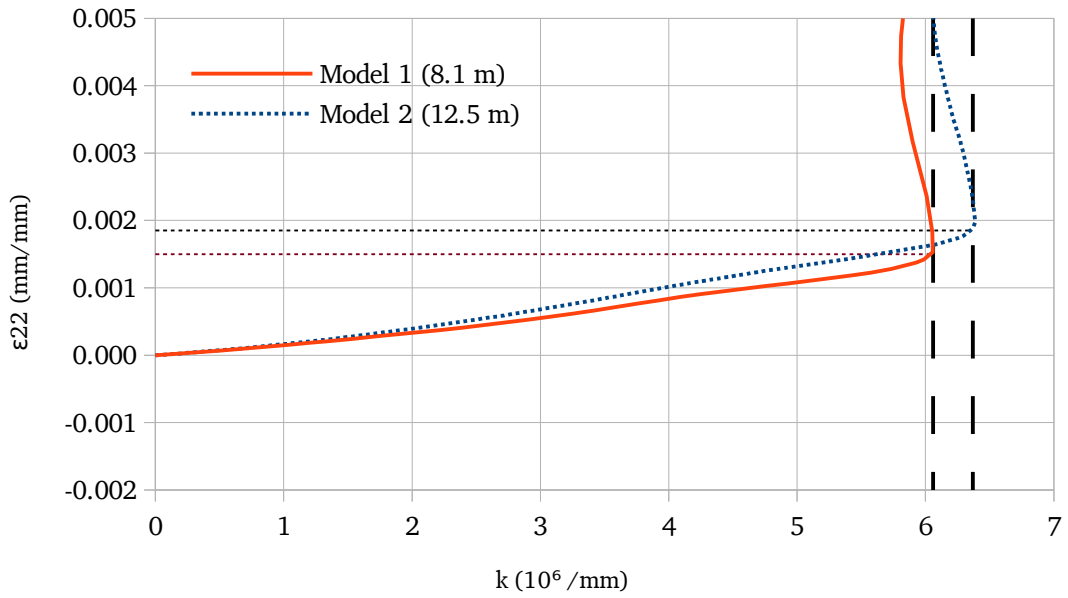

Figure 30: Comparison of second principle strain ε_{22}

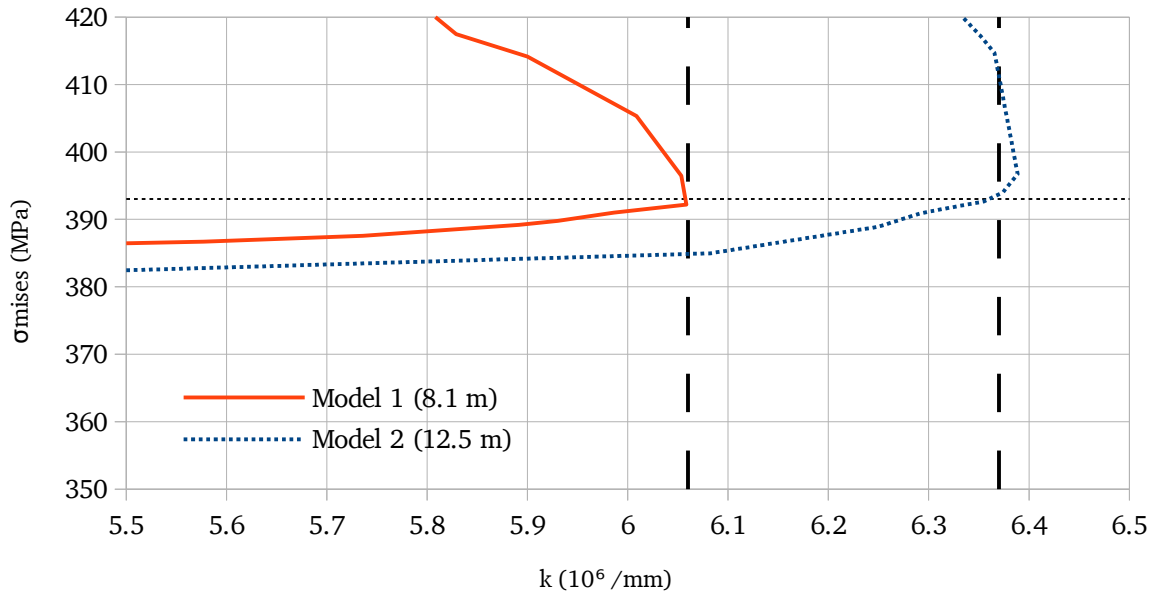

Figure 31: Comparision of von Mises stresses

These figures provide evidence supporting the theory that the difference between the models is geometrical in nature. In Figure 29, it can be seen that the axial strain close to buckling is greater for Model 1 than for Model 2. However, this does not explain the fact that the actual strain at buckling is lower for Model 2 than for Model 1. The reason for this is uncertain, but in Figure 31 it can be seen that the von Mises stress is nearly the same for Models 1 and 2 at buckling, and easily within the error in measurement location caused by element size. This suggests that even if some yielding occurs, buckling may in fact still depend on a critical stress rather than a critical strain.

Finally, Figure 30 shows a slight difference in the strain in the transverse direction between the two models. This discrepancy is thought to be due to the ovalization restraint caused by the length of Model 1.

Although this analysis is very preliminary and theoretical, it is suggested that Model 2 should be used with extreme caution, because it is thought that geometrical length effects outshadow any potential end effects. In addition, due to the fact that no shear stresses were observed (meaining that ε_{11} is a measure of the true true axial strain and ε_{22} is a measure of the true transverse strain), it is also suggested that ovalization restraint influences ε_{22} much more strongly than it does ε_{11}. It is also thought that perhaps buckling depends on the critical stress rather than critical strain.

5.2.2 Boundary Conditions and Geometry

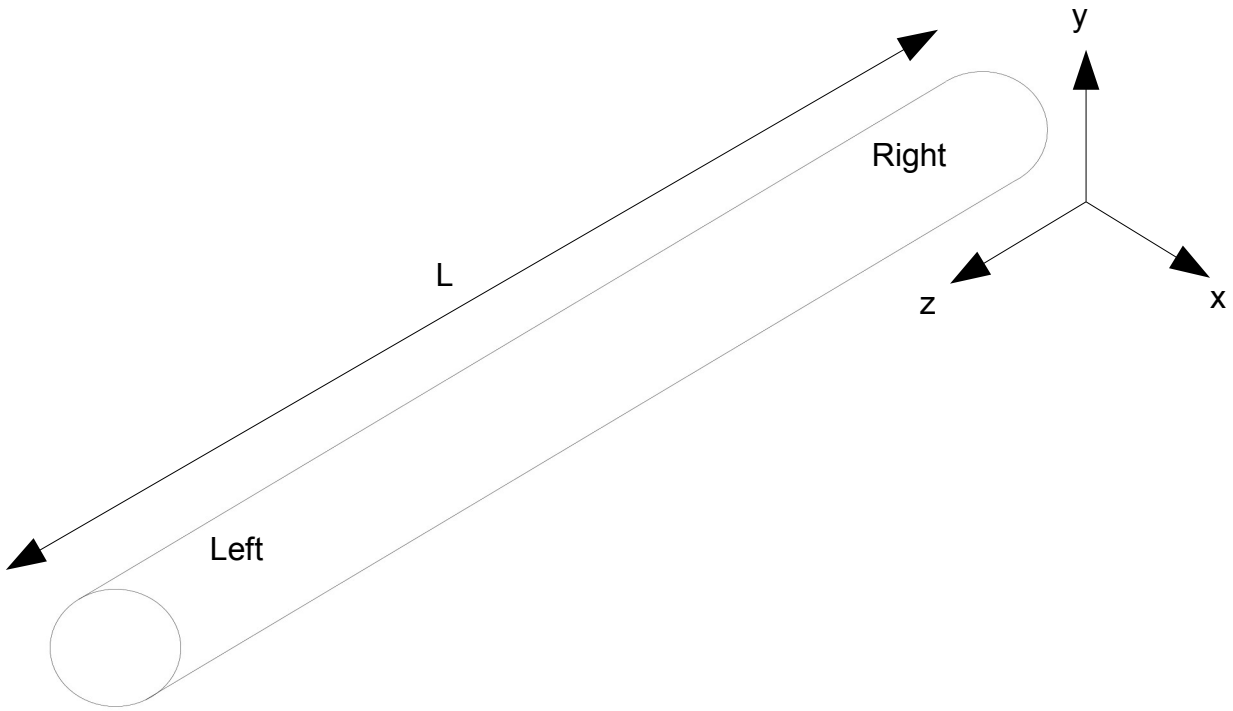

Figure 32: Geometry of finite element models

Figure 32 shows the basic geometry of the finite element models, including the global x-y-z coordinate system in which all models were created, as well as the adopted definitions of "Left" and "Right". ABAQUS® uses a numbering system for its coordinate systems with x, y, and z referred to as directions 1, 2, and 3, respectively, and rotations 1, 2, and 3 defined as the rotations about these axes according to the right hand rule..

The tubes were modeled as if each end was fixed to a very stiff plate. At each end, a kinematic coupling was used to tie the edge of the tube opening to a reference node at the center of the tube. This is a type of coupling which transfers the forces or displacements applied to the reference node to the tube ends in a rigid way.

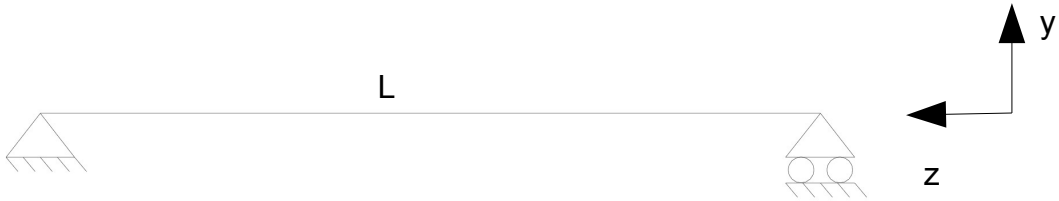

Figure 33: Boundary conditions of FEM models

Figure 33 shows the boundary conditions of the tubes. The ends of the tube were pinned in the x and y (transverse) directions, and one end was also pinned in the z (longitudinal) direction in order to provide longitudinal support. The tube was also restrained from rotating about the y and z axes at both supports, although it was found that there was no tendency for the tube to rotate in these directions during analysis. It was also found that vertical reaction forces would develop at the supports, but they were on the order of 0.5 N, and so could be neglected.

5.2.3 Element Type

For computational efficiency, shell elements were used to model the tubes. ABAQUS® provides several types of shell elements for various applications. Due to the large rotations expected, especially post buckling, finite-strain elements are most appropriate, restricting the choice to three types of linear elements:

-S3, a general purpose triangular shell element

-S4/S4R, general purpose quadrilateral shell elements with full or reduced integration

The choice of element type was found to affect both critical curvature and maximum moment, as shown in Figure 34.

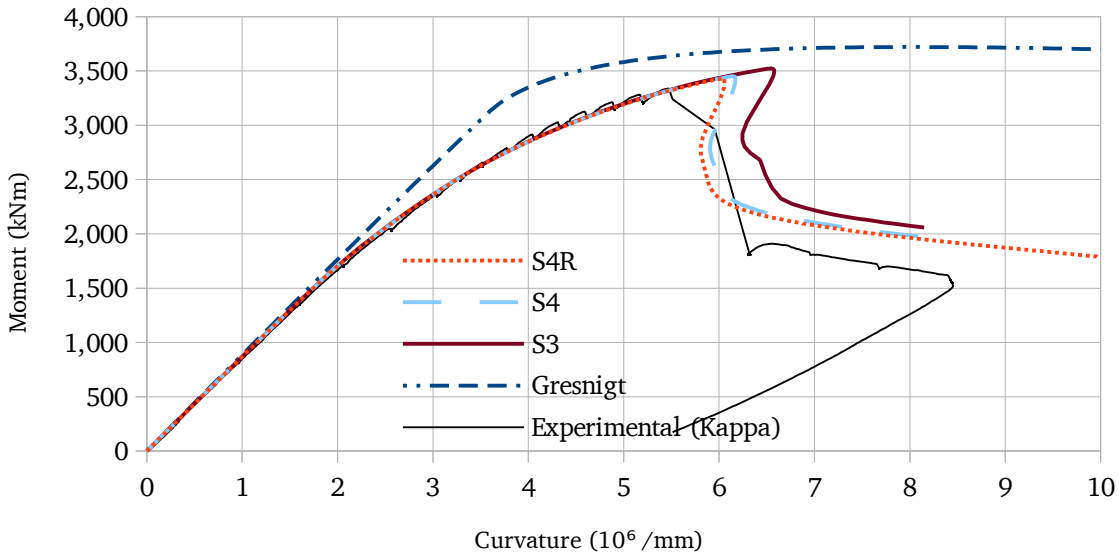

Figure 34: Effect of element type on behavior of Tube 5

Table 6: Effect of element type on capacity

Element type	**k_{crit} (10^6 /mm)**	**M_{max} (kNm)**
S4R	6.06	3,431.7
S4	6.14	3,451.1
S3	6.55	3,523.0

As shown in Figure 34 and Table 6, element type has a significant effect on the capacity of the tubes. S4 elements showed a 1.3% increase in k_{crit} and a 0.6% increase in M_{max} over S4R elements, while S3 elements showed an 8% increase in k_{crit} and a 2.7% increase in M_{max} over S4R elements.

S3 elements are very stable because their formulation is not susceptible to spurious modes, and they are preferable when local mesh refinement is used, but they were found to introduce asymmetries into the model. It was also found that local mesh refinement affected the results of the elastic buckling calculations, which were used to introduce imperfections, so it was decided to only employ global mesh refinement.

Therefore, the final choice was a choice between S4 and S4R elements. Although S4 elements are susceptible to locking, this was not observed in any of the FEM analyses, which means that the final choice is rather arbitrary. In the end it was decided to use S4R elements simply because they are the default shell element used in ABAQUS®.

5.2.4 Solution Procedures

Many different potential solution procedures are available in ABAQUS® to solve buckling problems, including:

-Static General

-Static Riks

-Implicit Dynamic

The standard static solution procedure, when used with displacement control, was often able to find the limiting moment, but was generally not able to trace the post-buckling equilibrium path, depending on its stability. On the other hand, the static riks procedure is capable of tracing the entire equilibrum path, but was found to be less robust because it sometimes was not able to converge past the limiting moment, especially for very smooth equilibrium paths or for longer tubes.

The implicit dynamic procedure was found to be the most robust, and was always able to converge, but when displacement control was used, there were issues with the kinematic response of the models, drastically affecting the results. This phenomenon was not observed when force control was used, but of course, equilibrium could not be found beyond the limiting moment with this method.

Based on these experiences, the static riks analysis was used for most analyses, although the static general solution procedure was used for some initial verification.

5.2.5 Output Parameters and Failure Criteria

Three different output parameters were taken from the initial FEM models, defined according to the global x-y-z system:

1. Rotation at the end supports/rotation 4,050mm from the tube center (UR1)
2. Applied moment at the end supports (CM1)
3. Horizontal displacement in the center of the tube (U1)

The applied moment could be used to calculate moment-curvature curves directly, and the horizontal displacement in the center of the tube simply had to be multiplied by 2 in order to give the total horiziontal ovalization. The rotation at the end supports could be converted into the curvature in the tube via Eqn. 49.

Since there are two possible fialure modes (limit point instability and bifurcation), two failure different failure points can be defined. M_{max} simply corresponds to the maximum moment in the moment-curvature diagram, and M_{buck} corresponds to the point right before a sudden drop in moment occurs, which is the bifurcation point. The curvatures at these points are labeled k_{crit} and k_{buck}, respectively. In an imperfection sensitive structure, these moments are expected to occur at the same point, but in a structure that is not imperfection sensitive, it is possible that there is a significant gap between k_{crit} and k_{buck}, even if $M_{max} \approx M_{buck}$. This difference has also been discussed in the introduction.

For all models created for this report, however, it was found that $M_{max} = M_{buck}$. Therefore, when failure is discussed, M_{max} and k_{crit} are generally implied.

5.2.6 Material Models

As described in Section 2.2, material data was available for all test specimens. For the creation of the finite element models, the material model was either taken as elastic perfectly plastic with the yield stress at 0.2% plastic strain, in the case where the FEM models are directly compared to the analytical solution of Gresnigt, or as the average stress-strain relation, converted from a nominal stress-strain curve to a true stress-true plastic strain curve, which is the form required by ABAQUS®. This conversion is accomplished by the following formulas:

$$\sigma_{true} = \sigma_{nom}(1+\epsilon_{nom}) \tag{50}$$

$$\epsilon_{true} = \ln(1+\epsilon_{nom}) \tag{51}$$

$$\epsilon_{true,\,pl} = \epsilon_{true} - \frac{\sigma_{true}}{E} \tag{52}$$

For Tubes 1, 2, 3, 4, 5, 8, 9, and 11, the conversion from the test data to average nominal stress/strain and finally to average true stress-true plastic strain was done by Daniel Vasiliks of the University of Thessaly. For the remaining tubes, the conversion was done by the author of this report.

5.2.7 Residual Stresses

Residual stresses have many sources in spirally welded steel tubes: uneven heating and cooling, cooling after welding, and the manufacturing process, among others. In these models, only the residual stresses due to the manufacturing process were considered.

The process of bending a plate into a tubular shape was modeled in ABAQUS® by Vasilikis and Karamanos (2014). The result is a normalized residual stress distribution across the thickness of the tube, which was adapted to each specific tube my multiplying by the yield stress. In this case the average stress at 0.2% plastic strain was used. This distribution could then be applied directly to each tube as an initial stress state (see Appendix D).

The stress distribution used to model the residual stresses is shown in Figure 35 (compression positive).

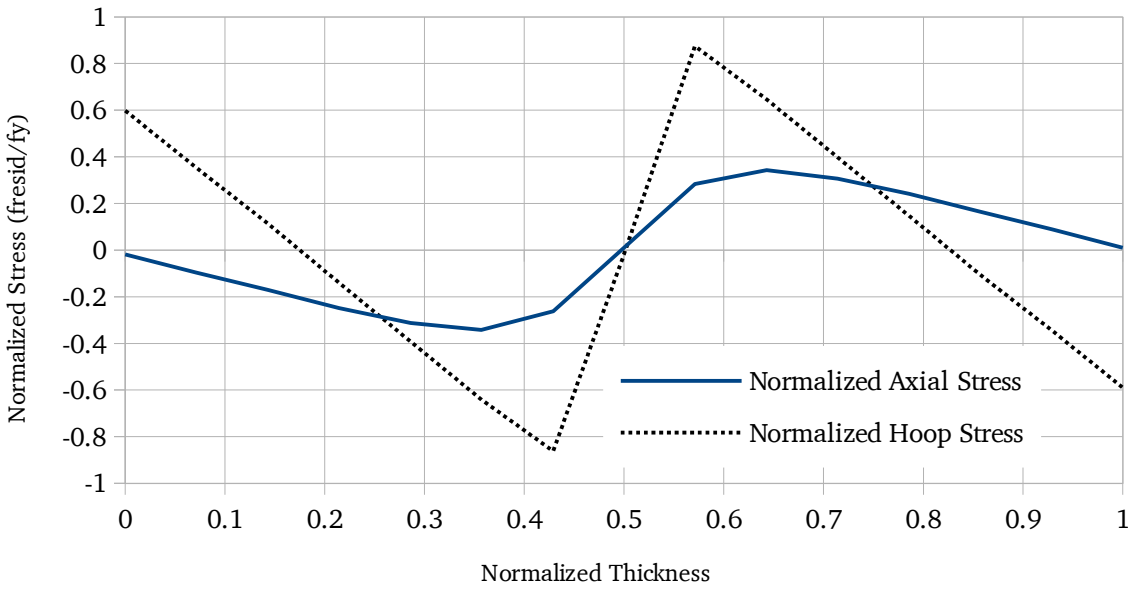

Figure 35: Residual stress distribution

The residual stress distribution was calculated using 15 thickness integration points, and the raw data is shown in Table 7. The integration points are numbered from the inside to the outside of the tube wall.

Strictly speaking, the residual stress distribution presented in Figure 35 is not valid for Tubes 14 and 15 because longitudinally welded tubes are produced using a different forming process. In fact, longitudinally welded tubes are expected to have higher residual stresses in the hoop direction and lower residual axial stresses. Despite this, the stress distribution of Figure 35 has been applied to the longidunially welded tubes as a first approximation.

Table 7: Residual stress distribution

Integration Point	Normalized Axial Stress	Normalized Hoop Stress
1	-0.018	0.598
2	-0.096	0.354
3	-0.171	0.114
4	-0.248	-0.139
5	-0.312	-0.392
6	-0.342	-0.641
7	-0.262	-0.862
8	-0.01	-0.017
9	-0.284	0.875
10	-0.343	0.646
11	-0.307	0.398
12	-0.241	0.146
13	-0.165	-0.106
14	0.089	-0.345
15	0.01	-0.590

5.3 Mesh Refinement Study

5.3.1 Approach and Methods

There are two aspects to mesh refinement: the actual size of the elements, and the number of thickness integration points. Several mesh sizes were used to perform a mesh refinement study, as shown in Table 8.

Table 8: Mesh sizes

Nominal Mesh Size	Total Degrees of Freedom
60mm	45,708
40mm	102,671
30mm	182,665
25mm	261,382
20mm	409,554
12mm	1,129,235

Model 1 of Tube 9, meshed with S4R elements, was used to investigate the influence of mesh size, which included the full material model, the residual stresses, and the measured imperfection height. The tube was meshed with each of the meshes described in Table 8, and an imperfection was introduced in the form of the third pair of eigenmodes (see Section 5.4), scaled to 2w = 2.01mm. Both M_{max} and k_{crit} were used as convergence criteria.

In order to investigate the effect of the number of thickness integration points, the mesh size was held constant and the number of thickness integration points was varied from 3 to 17. Once again the resulting influences on M_{max} and k_{crit} were extracted.

5.3.2 Results

The results of the mesh refinement study are shown in Figures 36 and 37.

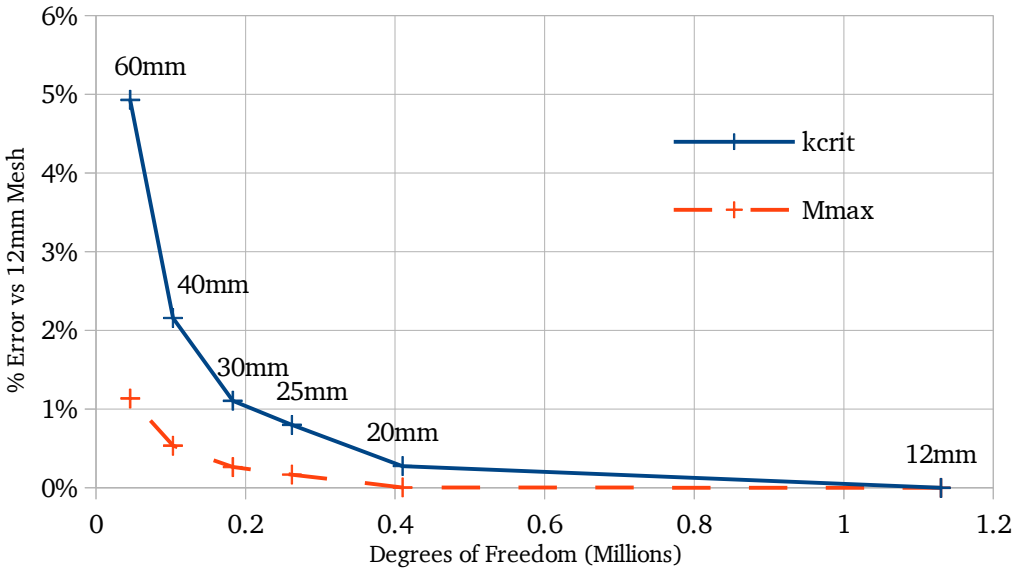

Figure 36: Mesh refinement study for Tube 5

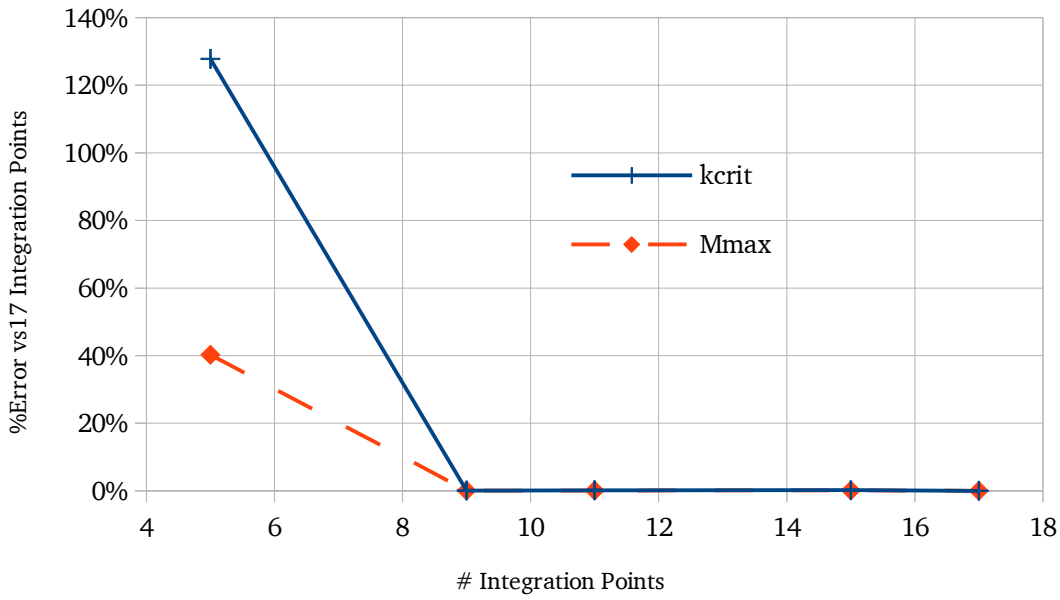

Figure 37: Effect of integration points on the behavior of Tube 5

5.3.3 Discussion

The influence of mesh size on the tube capacity shown in Figure 36. This figure shows a logarithimically decreasing trend for both k_{crit} and M_{max}. Mesh size was found to influence k_{crit} significantly more than $M_{max.}$

Although there is still a noticable increase in accuracy when going to a 12mm mesh, due to the fact that computing time increases exponentially with decreased mesh size, this was found to be unrealistic. In particular, it was found that decreasing mesh size from 25mm to 12mm resulted in a 1.7% decrease in k_{crit} at the expense of a 20 fold increase in computing time. It was therefore decided that the increase in accuracy was not worth the additional computing time, especially considering the fact that simply switching from S4 to S4R elements also resulted in a change in k_{crit} on the order of 1-2%.

On the other hand, Figure 37 shows that there is virtually no benefit to using more than 9 integration points. However, the residual stress distribution that was used was based on 15 integration points, therefore 15 integration points were used to model all tubes.

5.3.4 Conclusions and Recommendations

In this section, a basic mesh refinement study has been performed. In terms of mesh size, it was found that a 25mm mesh provided a good balance between accuracy and efficiency. In terms of integration points, it was found that 9 integration points were sufficient for accuracy, but 15 integration points were used for compatibility with the residual stress distribution.

5.4 Elastic Buckling Analysis

5.4.1 Approach and Methods

Imperfections in the form of elastic buckling modes are often used for analysis purposes because structures are generally most sensitive to imperfections in the form of a buckling mode. However, the most significant buckling mode may not be the lowest buckling mode, especially if the eigenvalues are closely spaced-an indication that the structure is imperfection sensitive.

An elastic buckling analysis was performed on all tubes using ABAQUS®. The nature of the eigenmodes and eigenvalues was qualitatively observed for all tubes and investigated in detail for Tube 5. This was done by incorporating imperfections into Model 1 of Tube 5 in the form of several critical single buckling modes and combinations of the buckling modes. The imposed imperfections were scaled based on the actual measured imperfections according to Table 4. The results of the study were used to identify the most critical combination of buckling modes, which was used in the final models of all plain spirally welded and longitudinally welded tubes. The girth and coil connection welded tubes have not been considered in this section. Instead, the shape of the initial imperfections has been described individually for each of these tubes in Section 5.5.

5.4.2 Results

Figures 38-41 show some of the eigenmodes of both Model 1 and Model 2, taken directly from ABAQUS®.

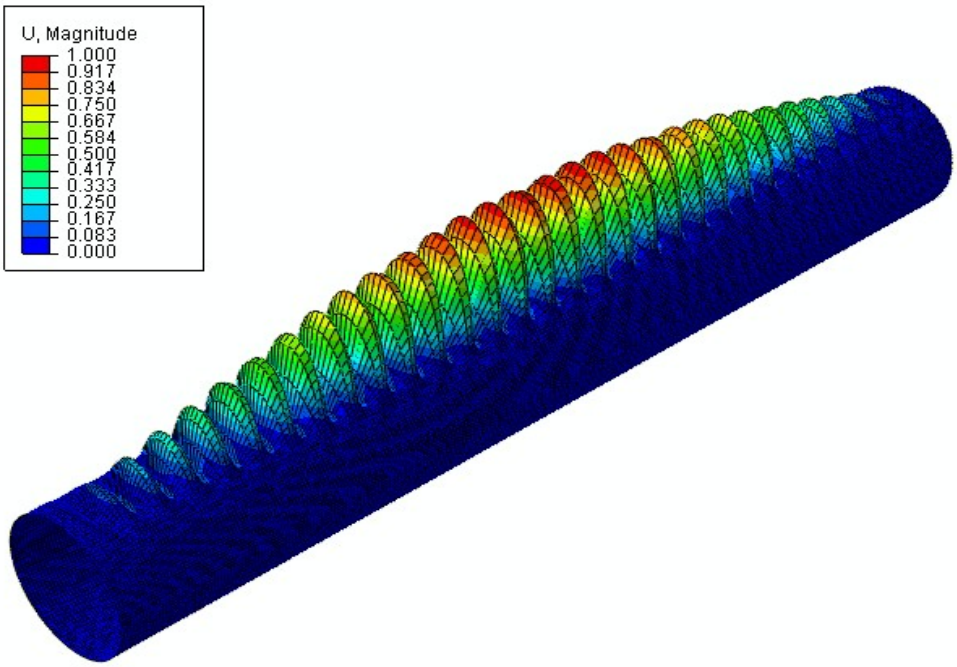

Figure 38: 1st eigenmode of Model 1

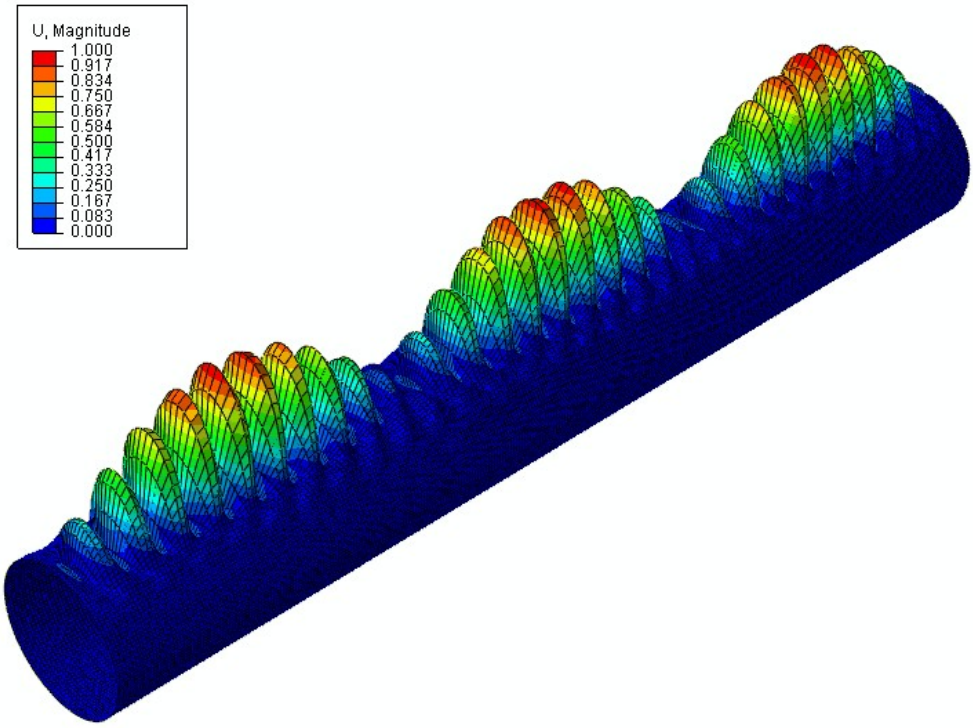

Figure 39: 5th eigenmode of Model 1

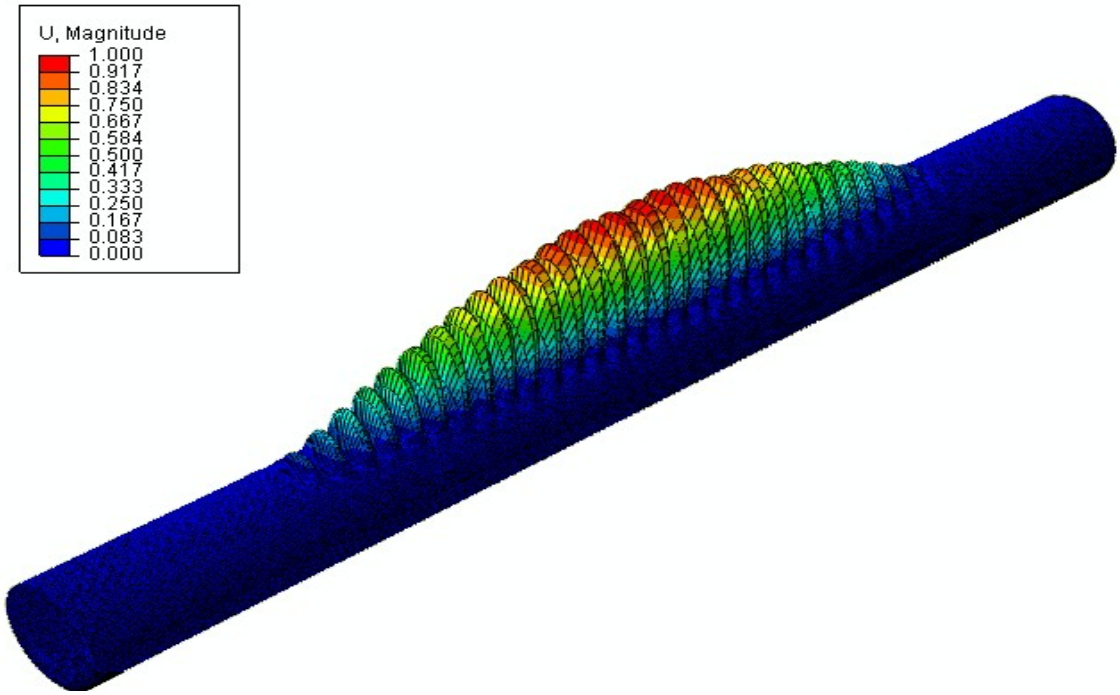

Figure 40: 1st eigenmode of Model 2

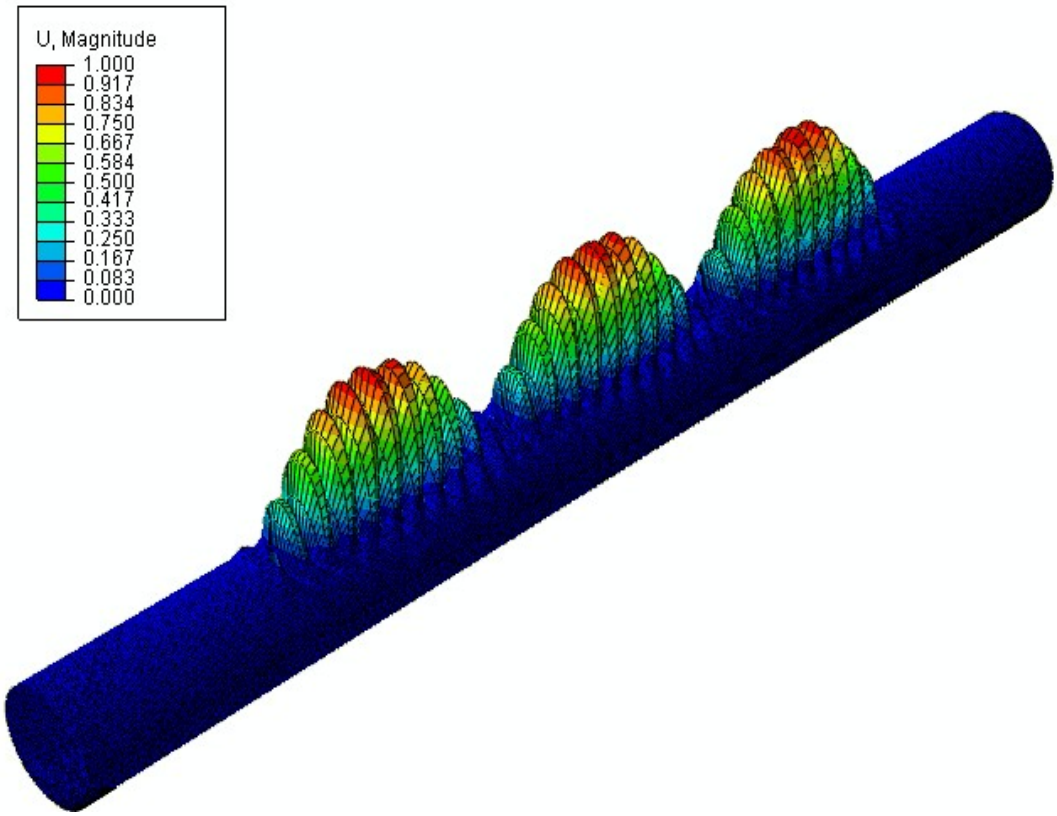

Figure 41: 5th eigenmode of Model 2

All 12 buckling modes of Tube 5 are shown in detail in Figure 43. The dashed blue lines represent the center of the compression face of the tube, and the black lines represent the deviation from the centerline, normalized to a maximum of 1mm. The red line represents the center of the tube. The other plain tubes were found to have similar buckling modes.

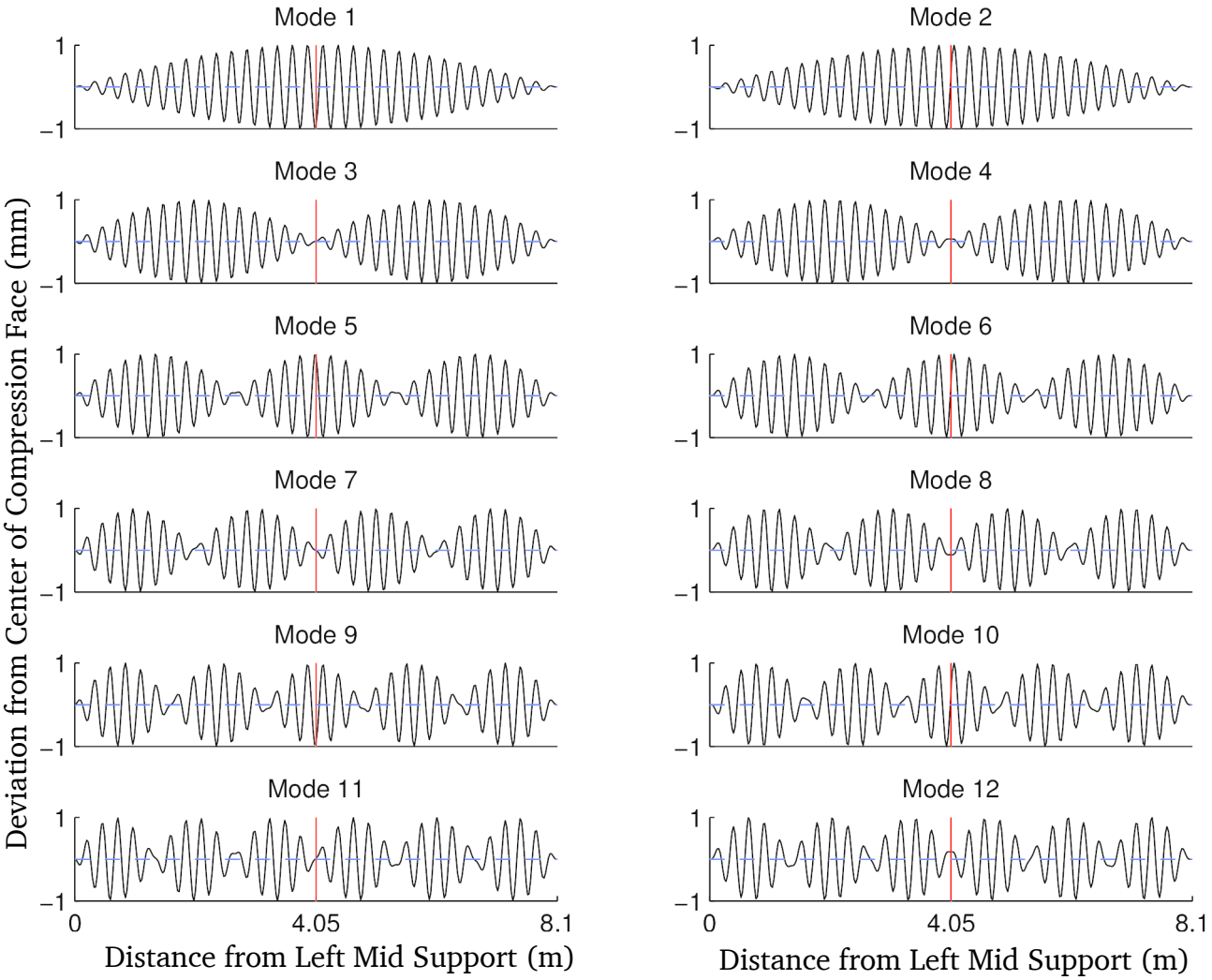

Figure 42: Buckling modes of Tube 5

The elastic buckling modes were found to occur in pairs of symmetric and antisymmetric modes. In other words, one buckling mode was found to be a cosine function, which is an even (symmetric) function and one was found to be a sine function, which is odd (antisymmetric). Sine and cosine functions have the property that they are added together according to the following identity:

$$\cos(x)+\sin(x)=\sqrt{(2)}\sin\left(\frac{\pi}{4}+x\right) \tag{53}$$

It can be seen from this equation that when a sine function is added to a cosine function, a phase shift occurs and the amplitude increases from 1 to √2. This is illustrated in the following figure. The result of adding a symmetric function to a antisymmetric function is always a function that is neither symmetric nor antisymmetric.

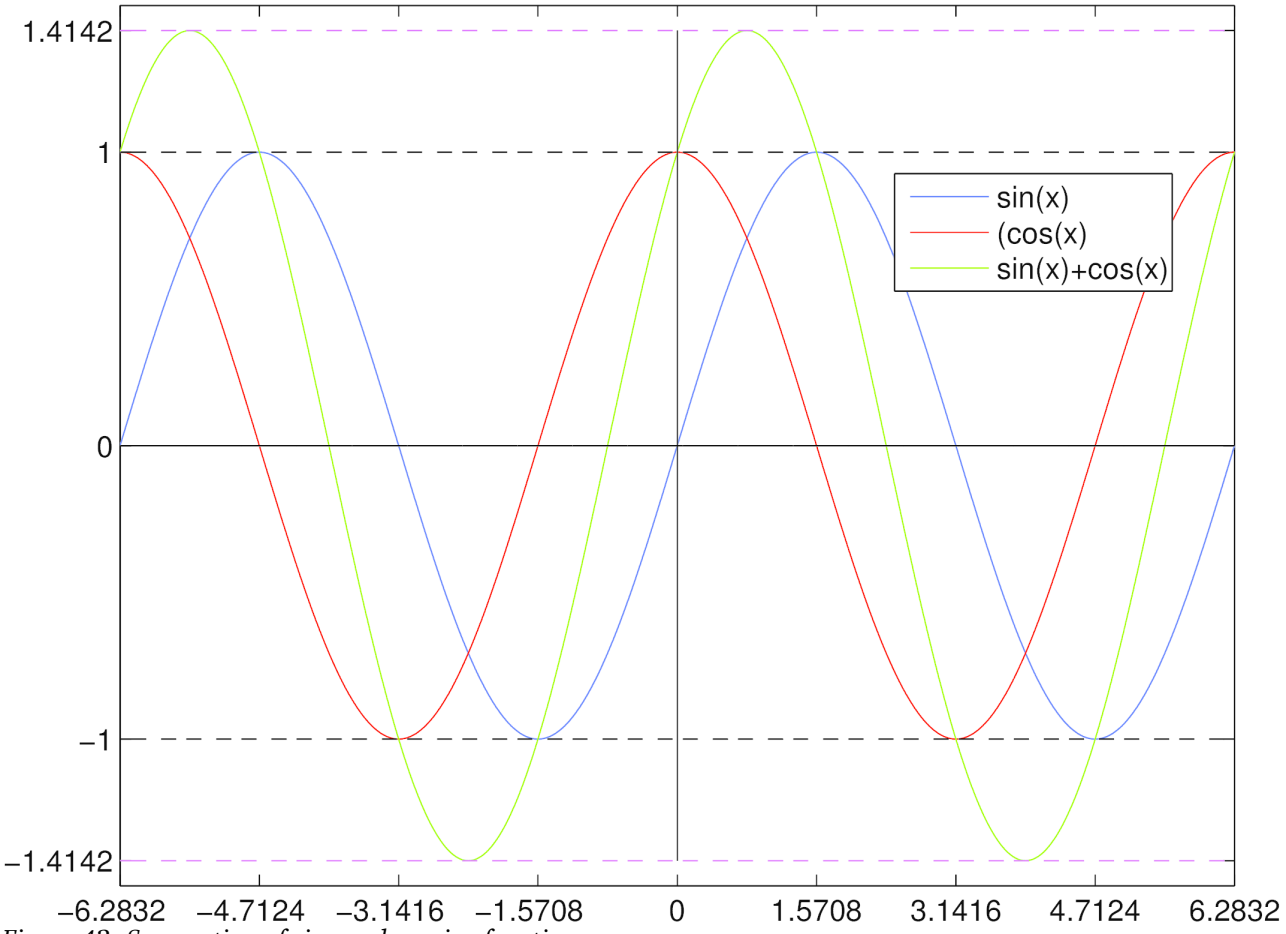

Figure 43: Summation of sine and consine functions

The same thing was observed in the buckling modes of these tubes. Each base mode has an amplitude of 1 but when a mode pair is added together the resulting amplitude is √2. This is shown in Figure 44, where Modes 1 and 2 have been added together.

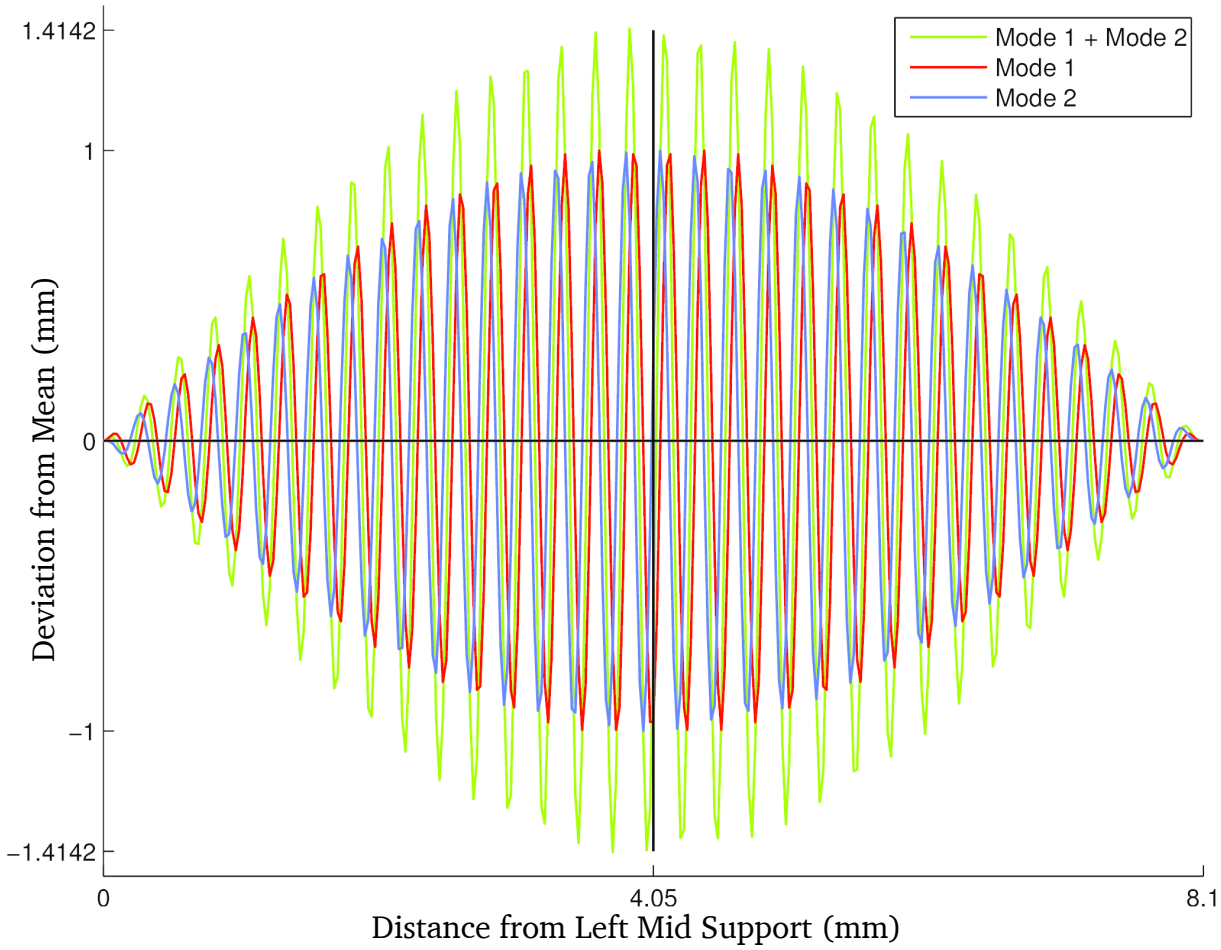

Figure 44: Mode pair 1 of Tube 5

All buckling modes were found to be the superposition of a wave with half-wavelength λ_{local} of L/64 and a wave with half-wavelength λ_{global} of L/n, where n corresponds to the set of pairs (e.g. Modes 1 and 2 belong to pair 1). Each pair of modes can also be characterized by having an even or odd number of peaks. Table 9 shows a summary of the eigenvalues and types of buckling modes found for Tube 5. The eigenmodes of the other tubes shared the same characteristics, including the same wavelengths, but the eigenvalues varied depending on the tube geometry.

Table 9: Eigenvalues of Tube 5

Mode	**Eigenvalue (kNm)**	**Global # Peaks**	λ_{global} **(mm)**	λ_{local} **(mm)**
1	17,039.9	Odd	8,100.0	126.6
2*	17,040.0	Odd	8,100.0	126.6
3*	17,061.7	Even	4,050.0	126.6
4	17,062.1	Even	4,050.0	126.6
5	17,097.7	Odd	2,700.0	126.6
6*	17,098.6	Odd	2,700.0	126.6
7*	17,147.9	Even	2,025.0	126.6
8	17,149.5	Even	2,025.0	126.6
9	17,211.9	Odd	1,620.0	126.6
10*	17,214.3	Odd	1,620.0	126.6
11*	17,289.0	Even	1,350.0	126.6
12	17,292.5	Even	1,350.0	126.6

*Antisymmetric Mode

The eigenvalues corresponding to each of these modes are very closely spaced, which suggests that Tube 5 may be imperfection sensitive, meaning that buckling is unstable. To understand the exact ways in which the various buckling modes influence the behavior of the structure, each of the first 12 odd modes was applied to Tube 5 independently as an initial condition, scaled to 10% of the tube thickness. In addition, the effect of combining and normalizing each mode pair was also investigated. The tube was then analyzed using a Static Riks procedure, and the resulting responses are shown in Figures 45-48. The buckling modes with an even number of peaks were not investigated because they always resulted in two buckles forming away from the center, resulting in a skewed curvature measurement. They were also of less interest for introducing actual imperfections into the models.

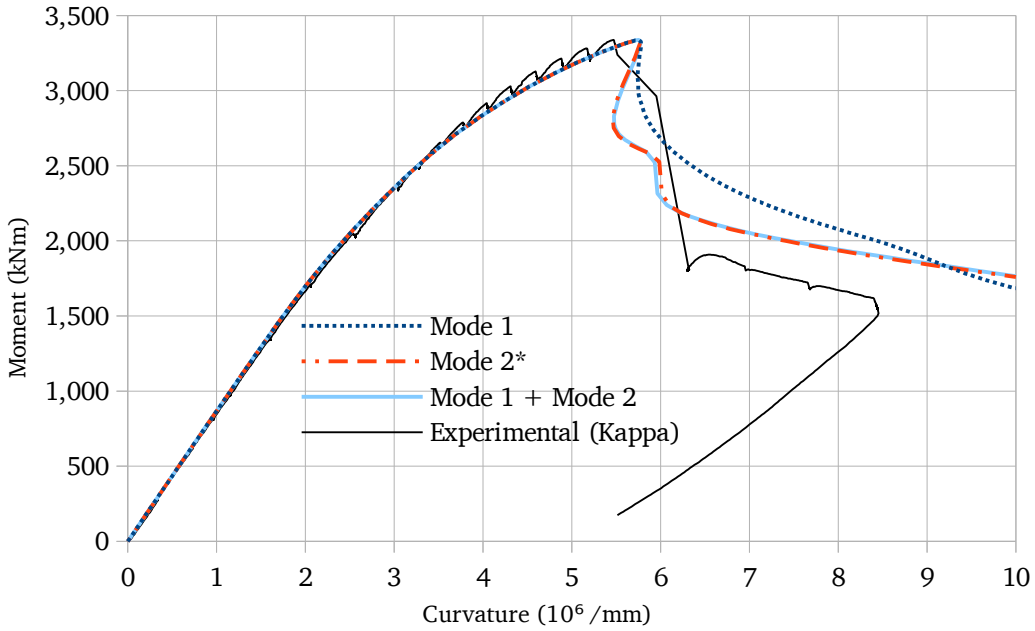

Figure 45: Buckling behavior of Mode Pair 1, Tube 5

*Antisymmetric Mode

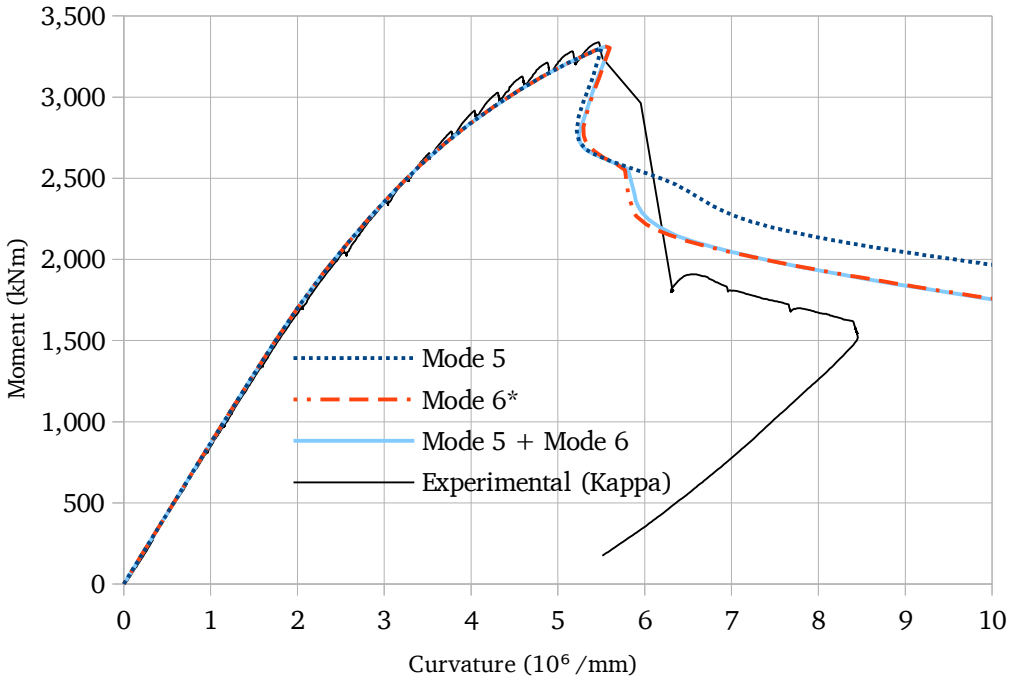

Figure 46: Buckling behavior of Mode Pair 3, Tube 5

*Antisymmetric Mode

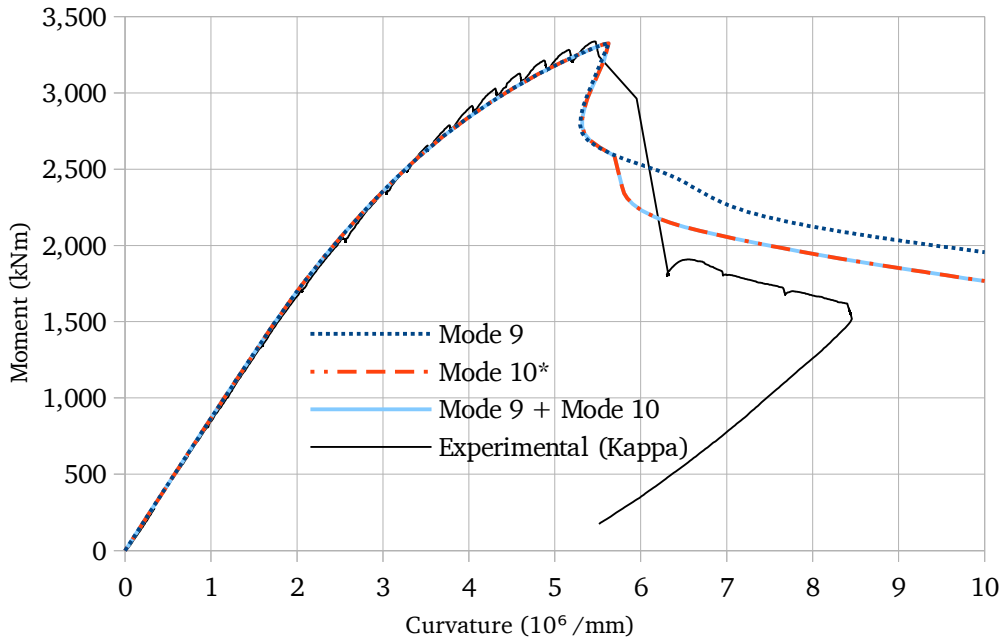

Figure 47: Buckling behavior of Mode Pair 5, Tube 5

*Antisymmetric Mode

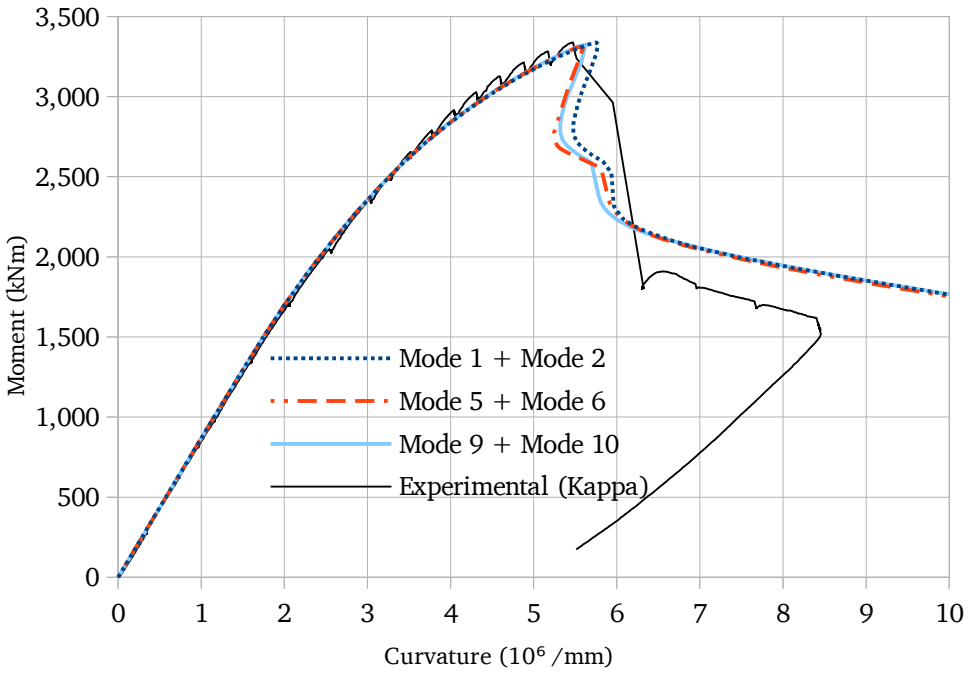

Figure 48: Imperfection sensitivity of Tube 5

5.4.3 Discussion

Based on these results, it can be seen that Tube 5 is sensitive to imperfections, due to the fact that the eigenvalues are closely spaced. In addition, it was found there is no clear distinction between the bifurcation point and the limiting moment, implying that there is no additional post-buckling moment capacity higher than M_{buck} (although the tube can still carry a significant portion of M_{buck} as strain increases). In addition, snap-back behavior occurs in every case, which means that the structure buckles even if the applied curvature is not increased beyond k_{buck}.

It can also be seen that Tube 5 is much more sensitive to mode pairs 3 and 5 than mode pair 1. Mode pairs 3 and 5 produced almost identical responses. The symmetric mode of each mode pair resulted in a different post-buckling behavior, but the antisymmetric and combined modes resulted in similar postbuckling plateaus, which also matched the experiment better. Finally, it can be seen that the buckling capacity was the same for each mode as well as for the combined mode within each mode pair.

The two types of post-buckling behavior corresponded to two buckled shapes, hereafter refered to as shape 1 and shape 2. Shape 1 occured when a symmetric buckling mode was applied and shape 2 occured when an antisymmetric or combined mode was applied.

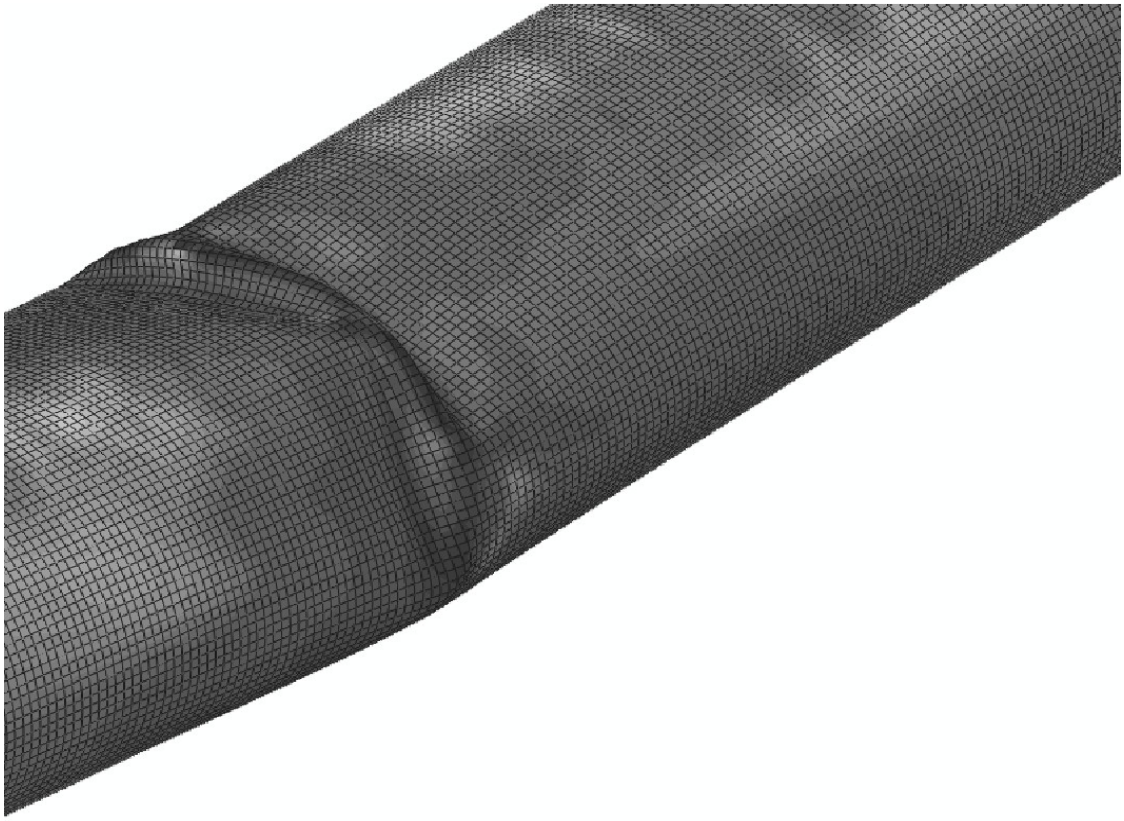

Figure 49: FEM buckle shape 1

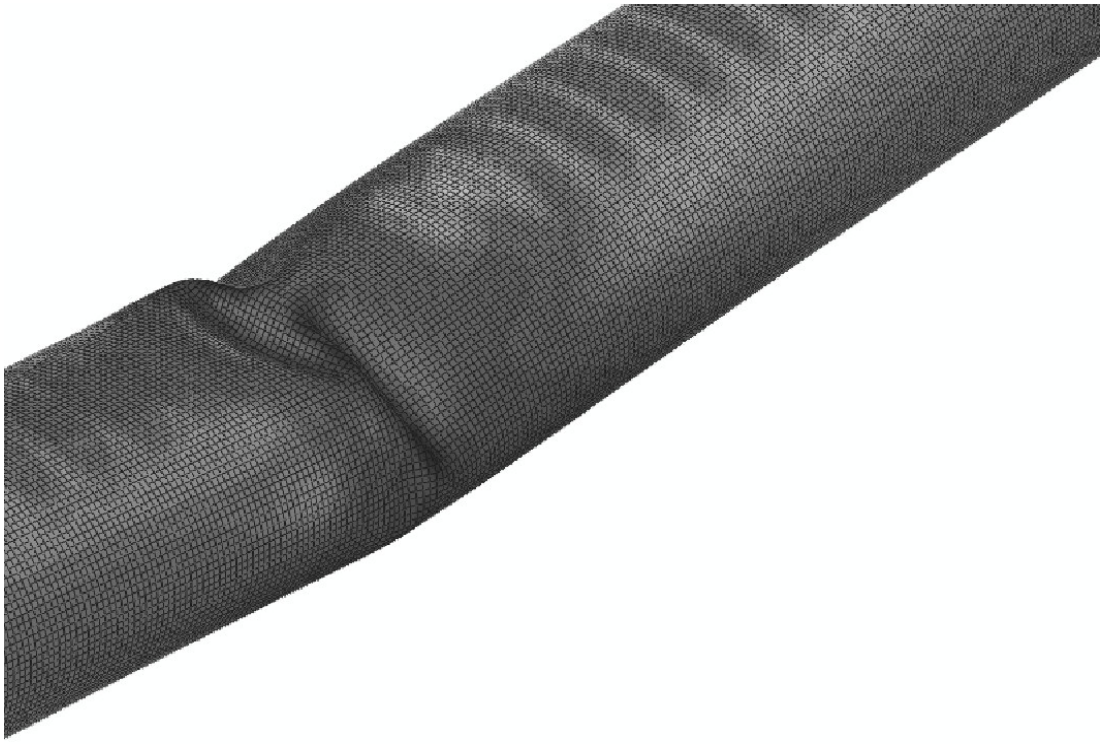

Figure 50: FEM buckle shape 2

For comparison, the actual buckled shape of Tube 5 is shown in Figure 51.

Figure 51: Physical buckled shape of Tube 5

This physical buckled shape corresponds to FEM shape 2, although it has been slightly skewed due to the presence of the spiral weld. In fact, all experimental tubes buckled according to shape 2, suggesting either that the antisymmetric buckling mode is dominant, or that the symmetric and antisymmetric modes are coupled into one combined mode.

A similar investigation was repeated for all tubes, but only the effect of the mode pairs was investigated. In all cases, the results were the same. It was always found that the tubes responded similarly to imperfections in the form of mode 5 + mode 6 or mode 9 + mode 10, and that the tubes were more sensitive to these mode pairs than to mode pair 1: mode 1 + mode 2.

An initial imperfection in the form of an elastic buckling mode can be used to not only take into account initial geometric imperfections, but also any other imperfections, including variations in geometry or material properties. However, in order to relate the imperfection to the physical tubes, it was decided to scale the imperfection to the magnitude of the initial imperfection at the location where the physical tubes buckled during testing.

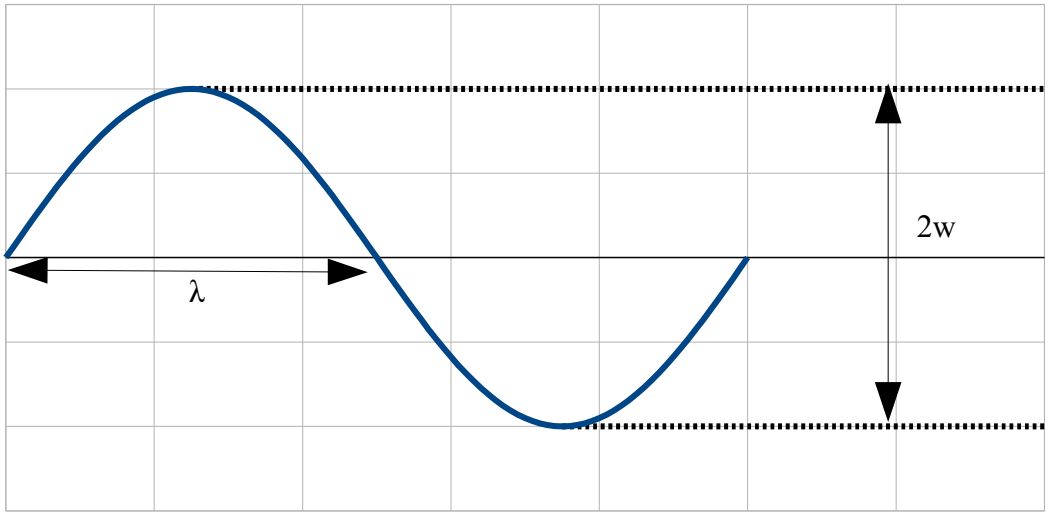

Figure 52: Translation of measured imperfection height to buckling mode amplitude

Figure 52 shows how the measured imperfection size was related to the amplitude of the applied buckling modes. The measured imperfection height is designated as 2w. This value is then related to the amplitude of the imperfection by scaling each buckling mode by the factor $w/\sqrt{2}$. Since the buckling modes were applied in pairs, this results in a total amplitude of w and a total imperfection height of 2w being applied to the models. The total imperfection heights 2w for each tube are given in Table 4.

Another imperfection parameter which influences the buckling capacity is the imperfection half wavelength λ, but this effect was not considered in this study.

5.4.4 Conclusions and Recommendations

In this section, the influences of various elastic buckling modes on the buckling behavior of Tube 5 have been investigated in detail. Based on the results, the least favorable combination of buckling modes was identified and used to introduce imperfections into Tube 5. It was also assumed that this analysis was valid for all of the other plain spirally welded and longitudinally welded tubes.

The results of this study show that the elastic buckling modes always occur in pairs of symmetric and antisymmetric shapes. It was found that the symmetric mode resulted in a different buckled shape than the antisymmetric or combined modes. The symmetric shape did not correspond to the physical buckled shapes, so it was decided to always use the combined shapes to incorporate imperfections into the tube models.

It was also found that the plain tubes are most sensitive to mode pairs 3 and 5, but less sensitive to mode pair 1. Therefore, it was decided to introduce imperfections into the plain tubes based on mode pair 3.

For Model 1, moments were applied to the tube ends to generate the buckled shapes, while for Model 2, moments were applied to an 8,100mm section of tube in order to generate the same buckling shapes as were found for model 1. This was done in order to better separate the effect of ovalization from the effect of a different buckling shape when comparing the two models. A full study was not performed using Model 2 but it was assumed that the results of the analysis described above were also valid for Model 2.

The girth and coil connected tubes were handled differently, but the behavior of these tubes was not investigated in this section. Instead, the imperfection shapes of these tubes is described separately in Section 5.5.

5.5 Results

In this section, the results of the modeling are presented for all tubes. First, the tubes are described, and in the case of the girth and coil connection welded tubes, the imperfection shapes are shown and described.

Next, moment-curvature relations are presented based on the FEM analyses, the analytical solution, and the experimental results. Model 1 was used to model every tube, while Model 2 was also used to model the tubes without girth or coil connection welds. For each tube, curvature has been calculated in two ways. First, the curvature has been calculated based on the rotation of each end support, a la Eqn. 12. This curvature is also known as Kappa. Second, the curvatures curv1, curv2, curv3, and curvall have been calculated in the way described in Section 2.3. During the experiments, these curvatures were calculated directly based on the deflection of the curvature brackets. In the FEM models, the corresponding locations of the brackets first had to be calculated, based on the difference between the buckling location observed during testing and the buckling location in the models. Because the buckles did not occur in the same location in the models and in the test setup, for some tubes, the corrected location of the curvature brackets was beyond the end of the tube. Therefore, not all curvatures are presented for all tubes.

After the moment-curvature relations, ovalization-curvature relations are presented. First, they are presented based on the ovalization at the buckling location. In the FEM models, this ovalization was measured directly, and for the experimental data, it was calculated based on the two ovalization brackets closest to the buckle. Then, the ovalization-curvature relations are also presented for each tube based on the ovalization brackets. As mentioned before, the locations of the brackets were related to the location of the buckle in the physical tube, and this information was used to locate the measurement points correctly in the models.

Finally, an analysis of the ovalization of the tube along the tube length is presented. In addition, images of the evolution of the deformed shape can be found in Appendix E.

5.5.1 Tube 1 Results

Tube 1 is a plain spirally welded tube with D/t = 65, f_y = 540 MPa, and 2w = 0.645mm.

Table 10: Tube 1 results

	k_{buck} (10^6 /mm)	k_{crit} (10^6 /mm)	M_{buck} (kNm)	M_{max} (kNm)
Model 1	9.62	9.62	9,072	9,072
Model 2	10.55	10.55	9,143	9,143
Gresnigt	-	12.0	-	9,280
Experimental	10.08	9.61	8,430	8,840

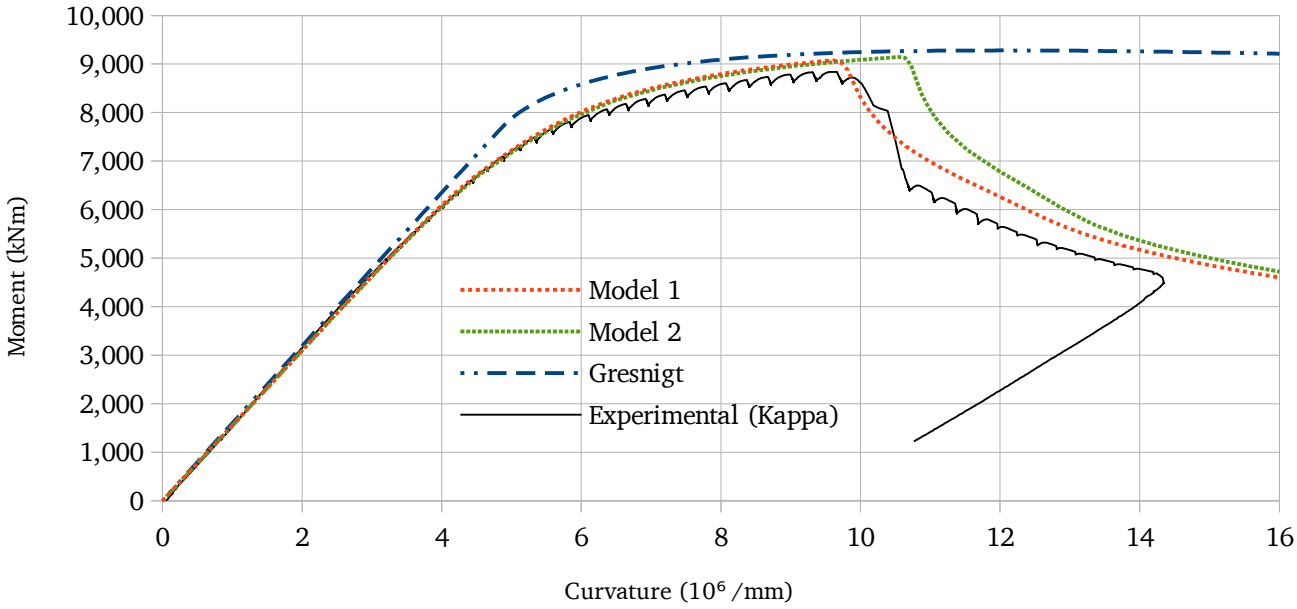

Figure 53: Moment-curvature relations for Tube 1: Kappa

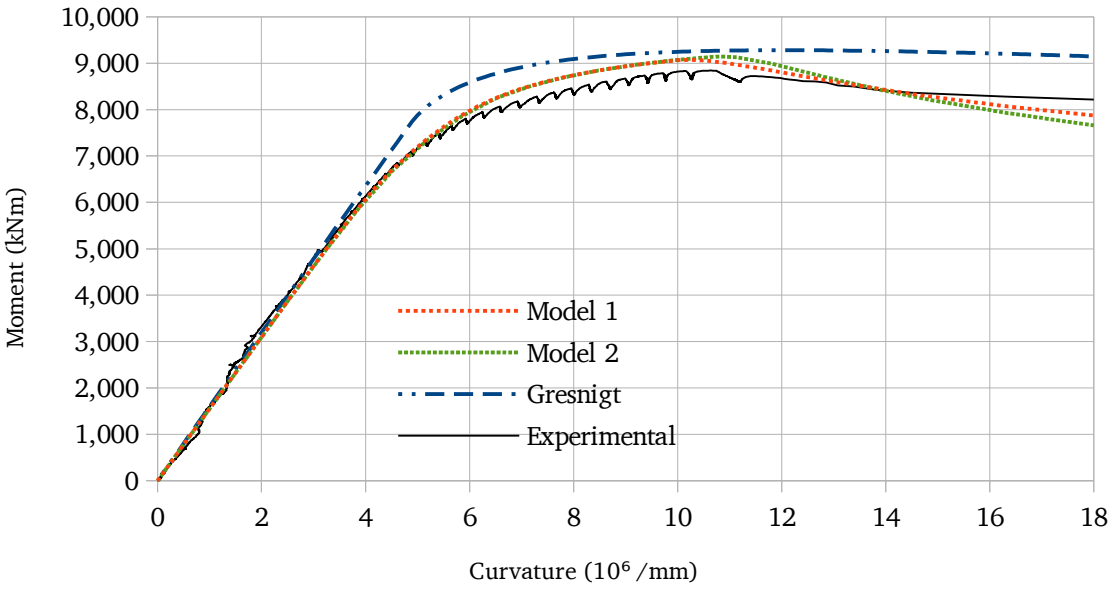

Figure 54: Moment-curvature relations for Tube 1: curv1

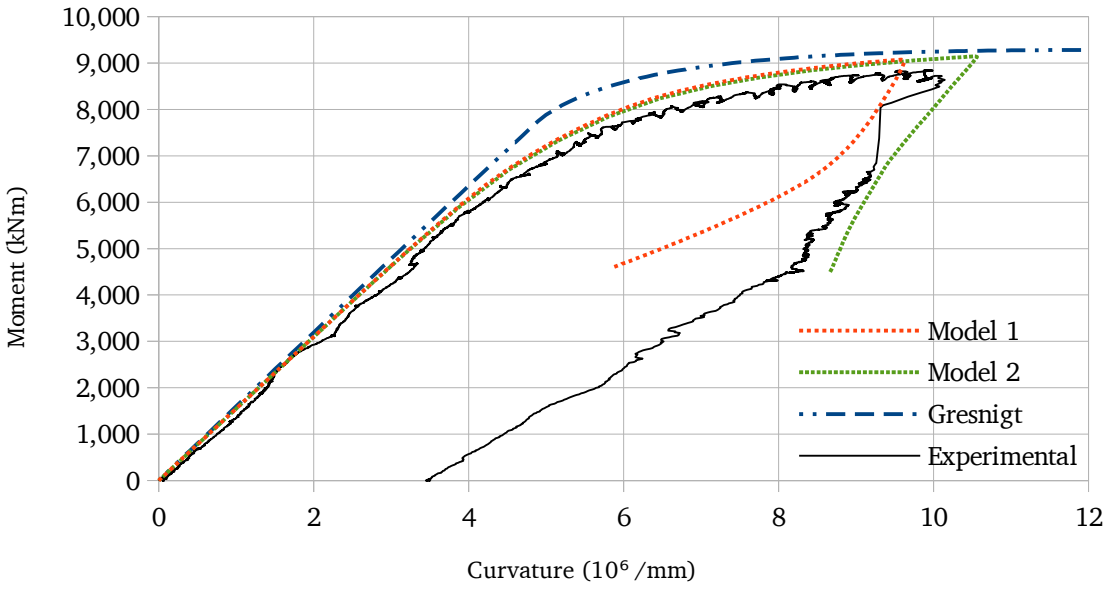

Figure 55: Moment-curvature relations for Tube 1: curv2

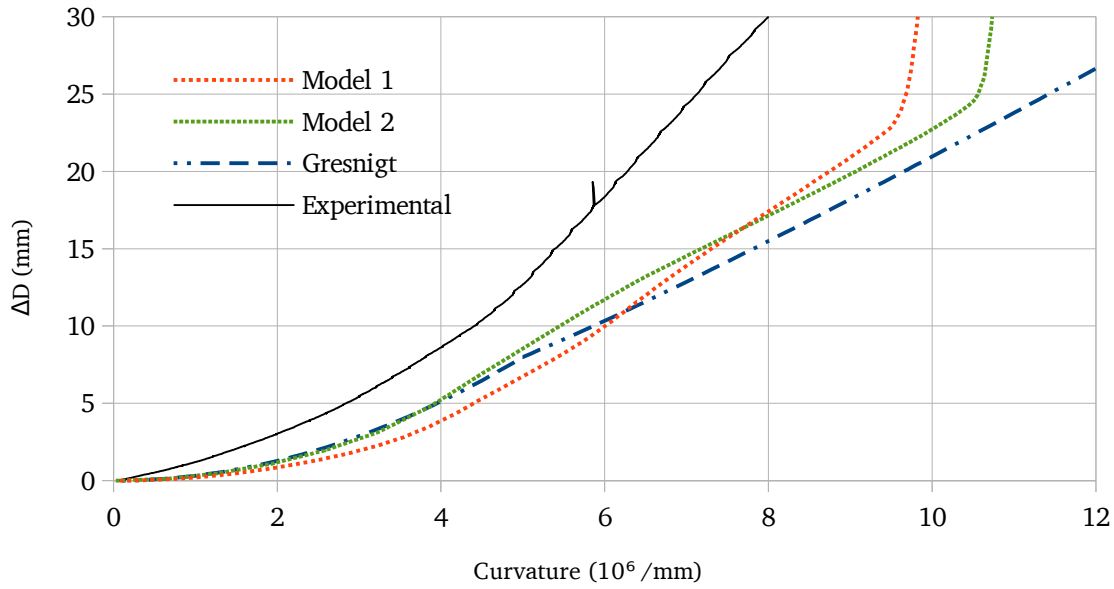

Figure 56: Ovalization-curvature relations for Tube 1: Buckling location (Kappa)

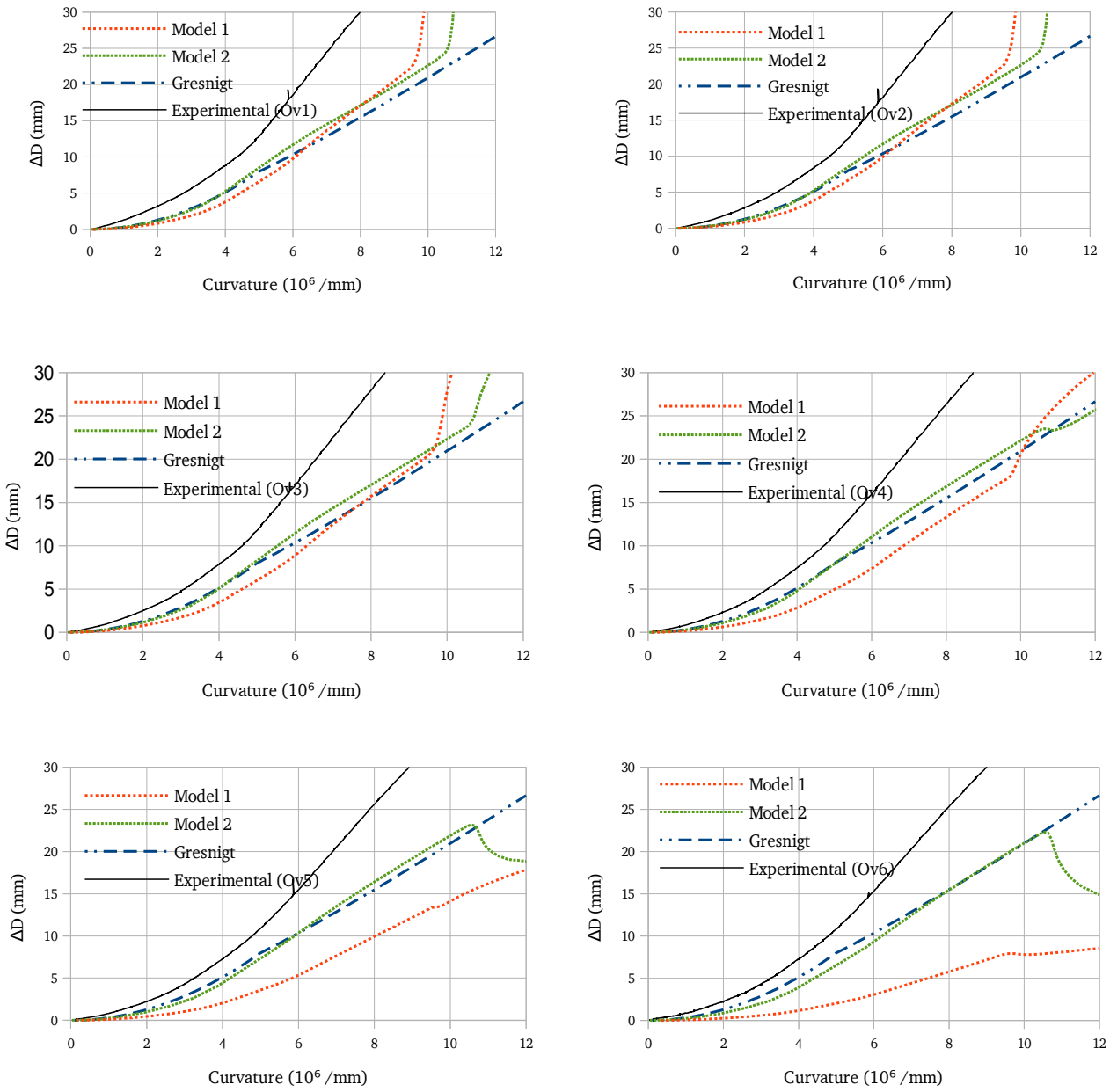

Figure 57: Curvature-ovalization relations for Tube 1: Ovalization brackets (Kappa)

5.5.2 Tube 2 Results

Tube 2 is a plain spirally welded tube characterized by D/t = 119, f_y = 390 MPa, and 2w = 0.871mm.

Table 11: Tube 2 results

	k_{buck} (10^6 /mm)	k_{crit} (10^6 /mm)	M_{buck} (kNm)	M_{max} (kNm)
Model 1	4.53	4.53	3,248.2	3,248.2
Model 2	4.77	4.77	3,381.6	3,381.6
Gresnigt	-	7.9	-	3,615.9
Experimental	4.94	4.51	2,812.5	3046.7

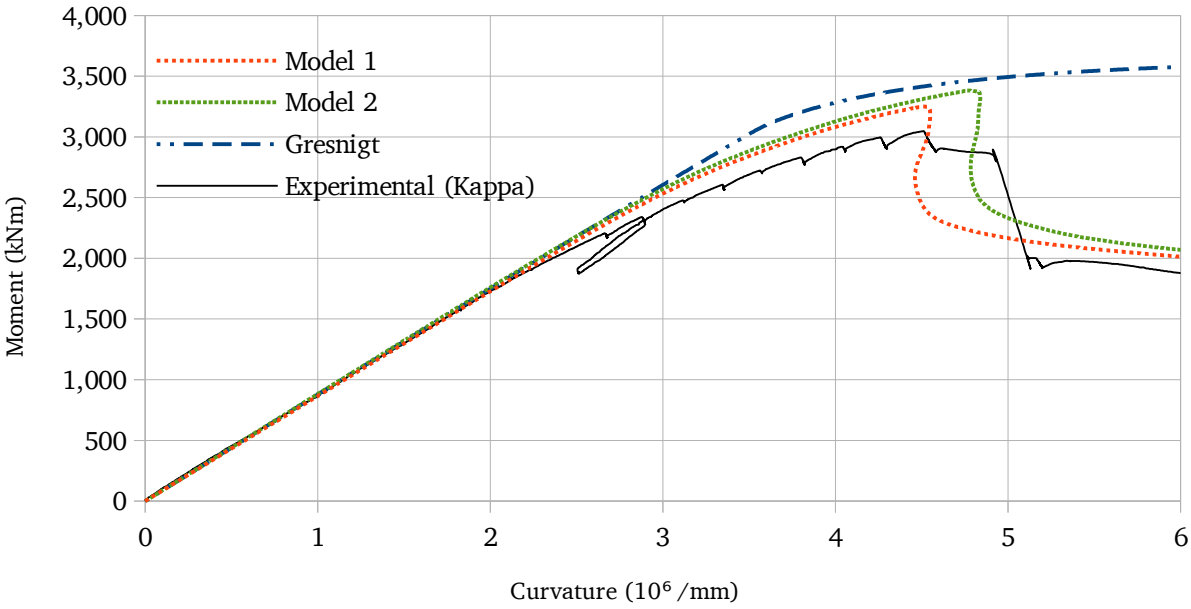

Figure 58: Moment-curvature relations for Tube 2: Kappa

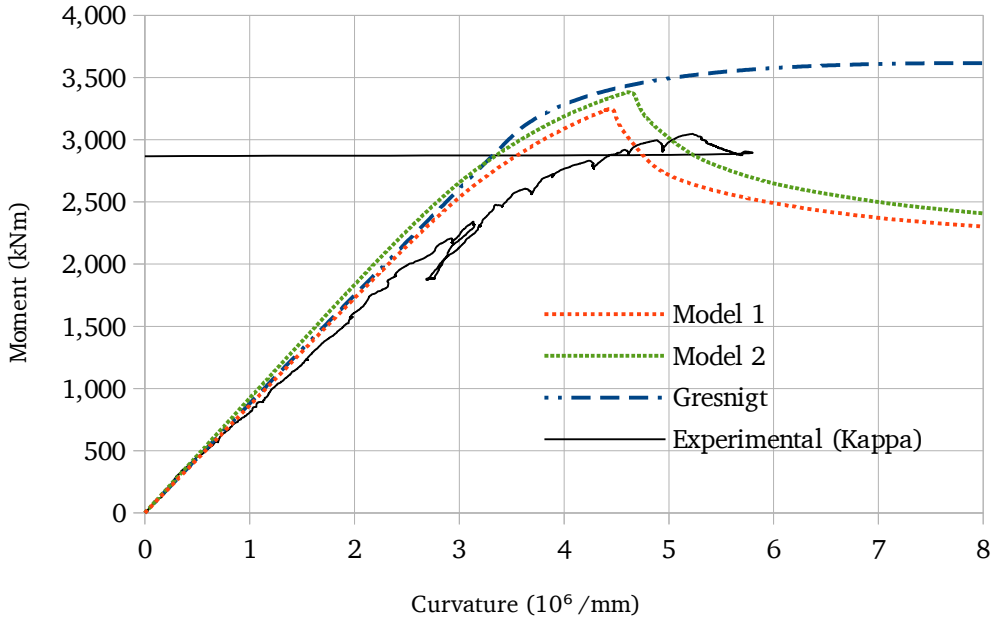

Figure 59: Moment-curvature relations for Tube 2: curv1

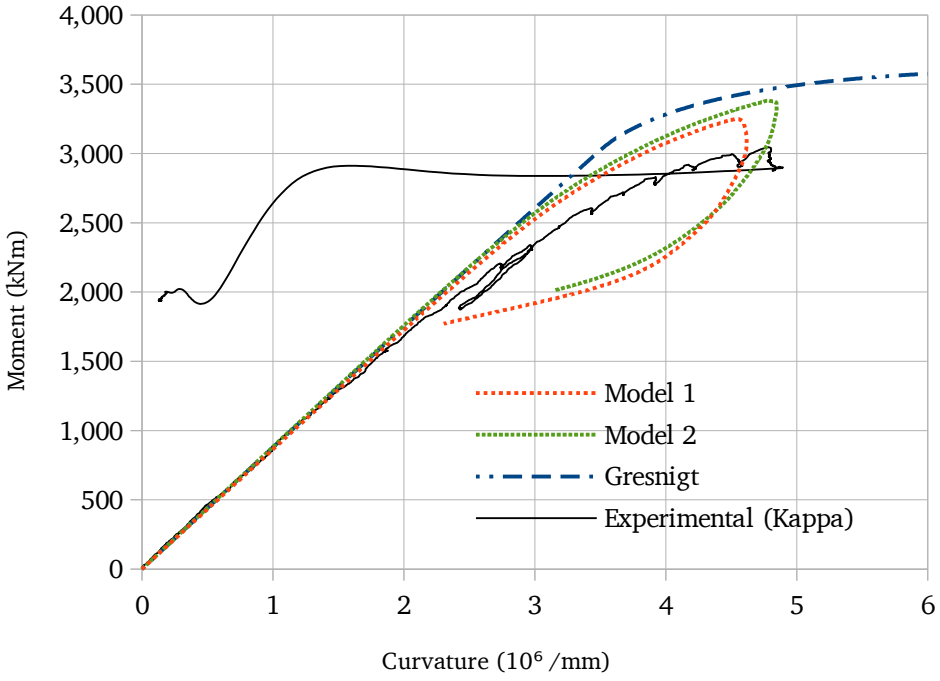

Figure 60: Moment-curvature relations for Tube 2: curv2

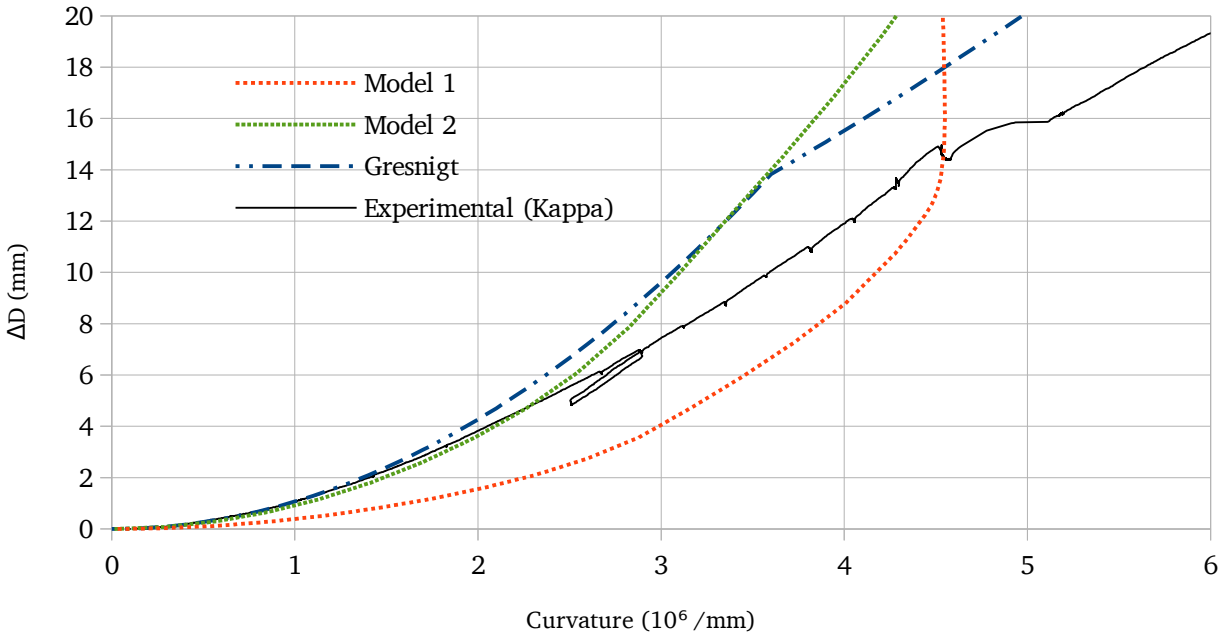

Figure 61: Ovalization-curvature relations for Tube 2: Buckling location (Kappa)

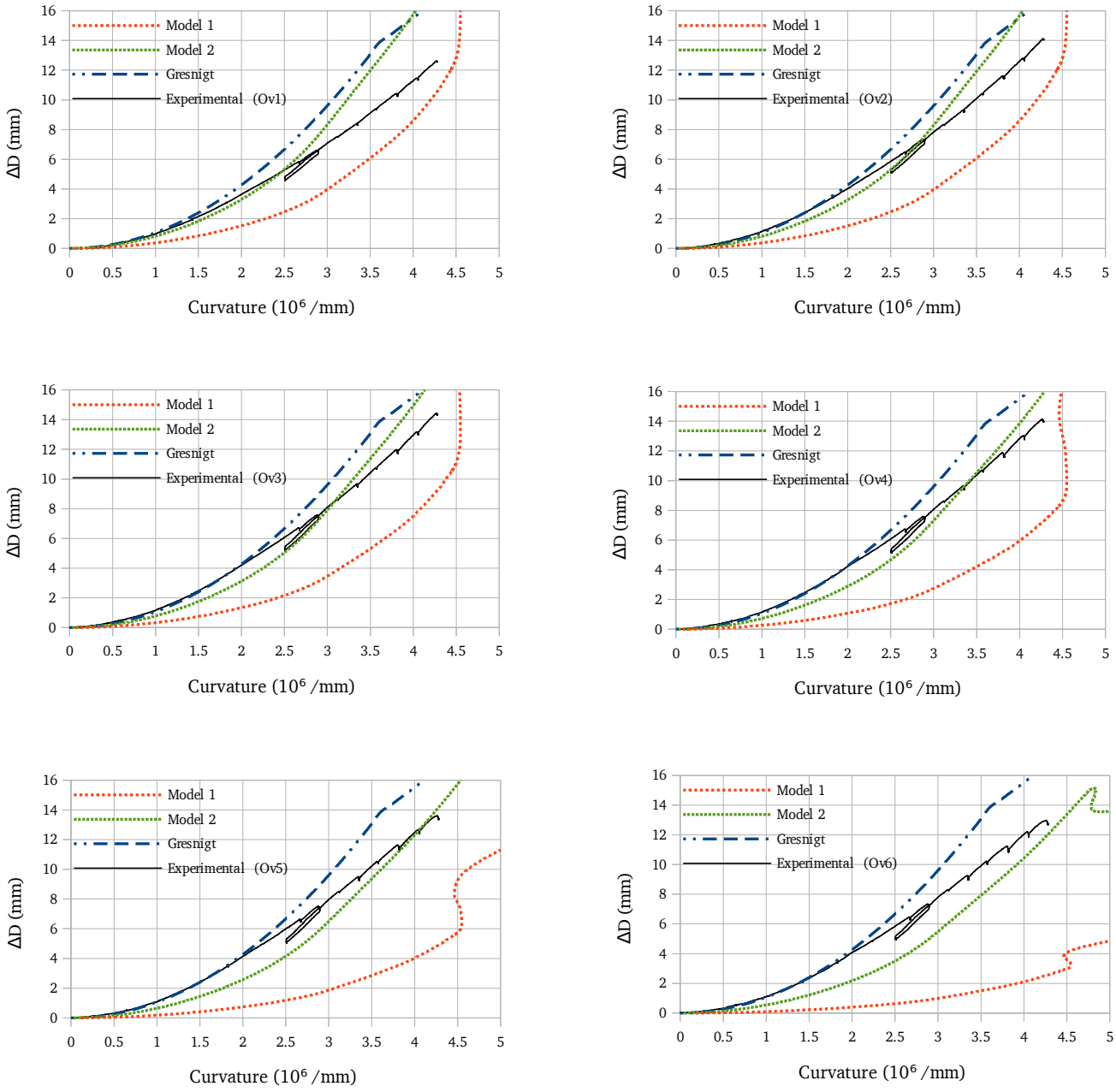

Figure 62: Curvature-ovalization relations for Tube 2: Ovalization brackets (Kappa)

5.5.3 Tube 3 Results

Tube 3 is a plain spirally welded tube with a girth weld in the center of the tube. The left side is characterized by D/t = 121 and f_y = 375 MPa, and the right side is characterized by D/t = 116 and f_y = 410 Mpa. The girth weld is characterized by an offset of 2mm and an additional imperfection of 2w = 1.81mm.

Table 12: Tube 3 results

	k_{buck} (10^6 /mm)	k_{crit} (10^6 /mm)	M_{buck} (kNm)	M_{max} (kNm)
Model 1	5.20	5.20	3,139.4	3,139.4
Gresnigt	-	8.0	-	3,647.2
Experimental	3.44	3.41	2,809.9	2,878.7

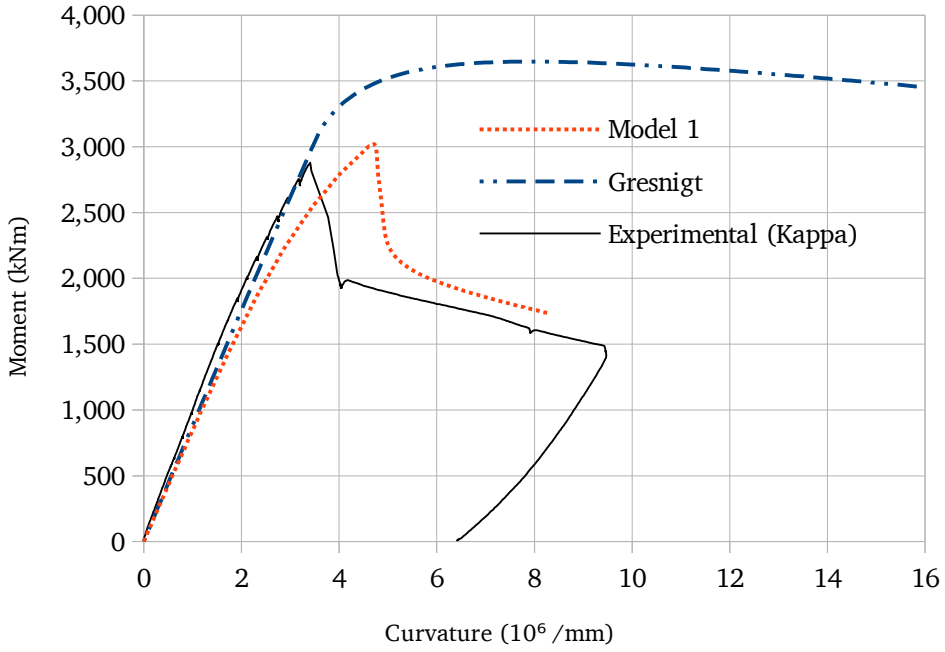

Figure 63: Moment-curvature relations for Tube 3: Kappa

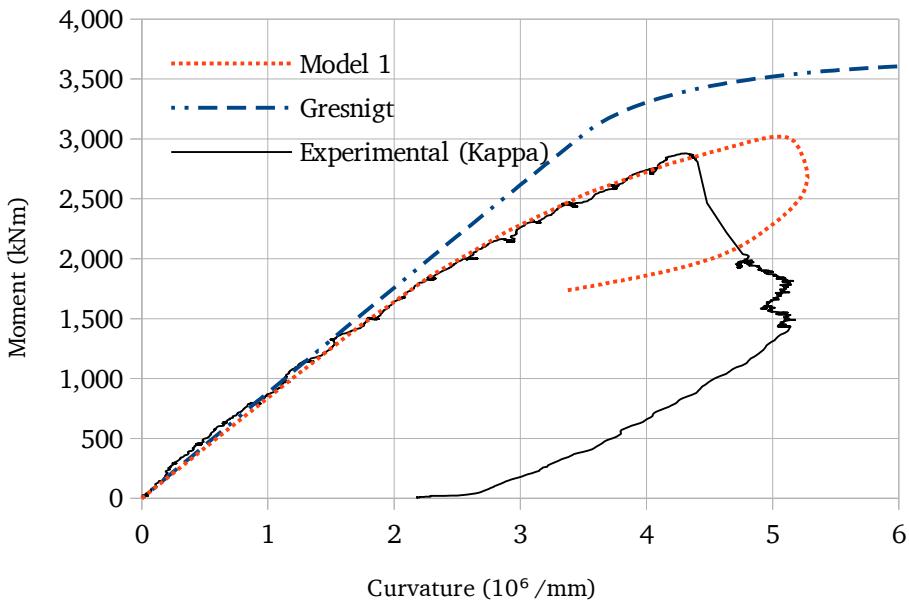

Figure 64: Moment-curvature relations for Tube 3: curv1

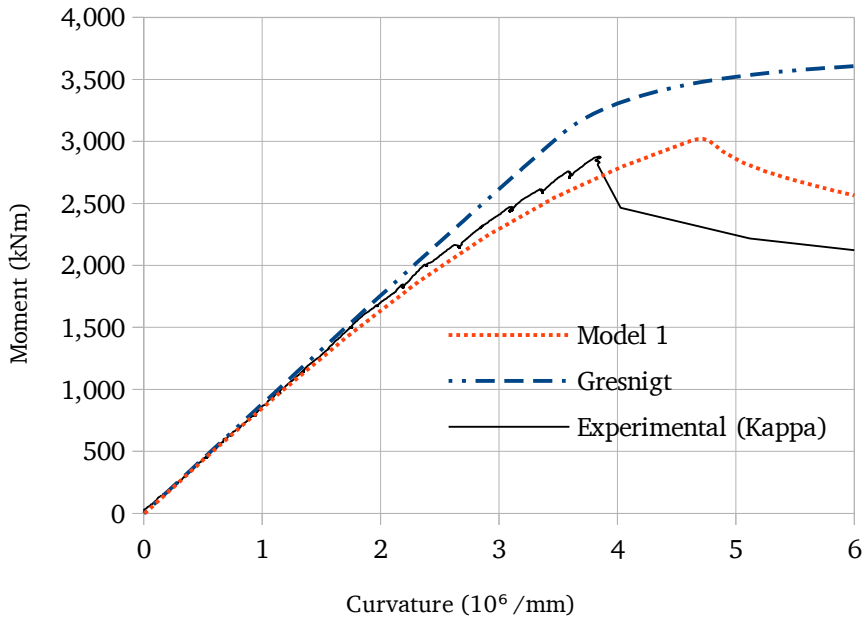

Figure 65: Moment-curvature relations for Tube 3: curv2

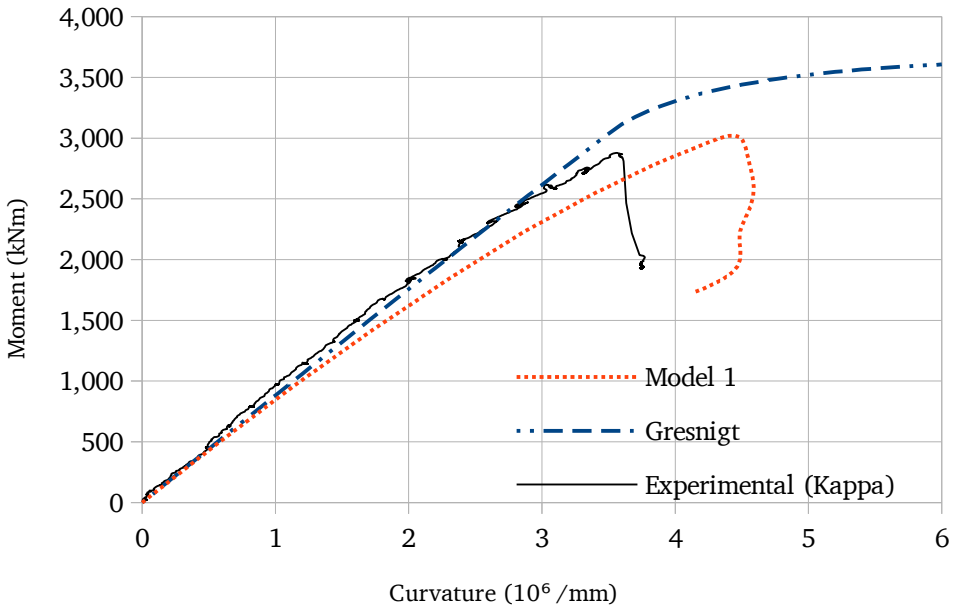

Figure 66: Moment-curvature relations for Tube 3: curv3

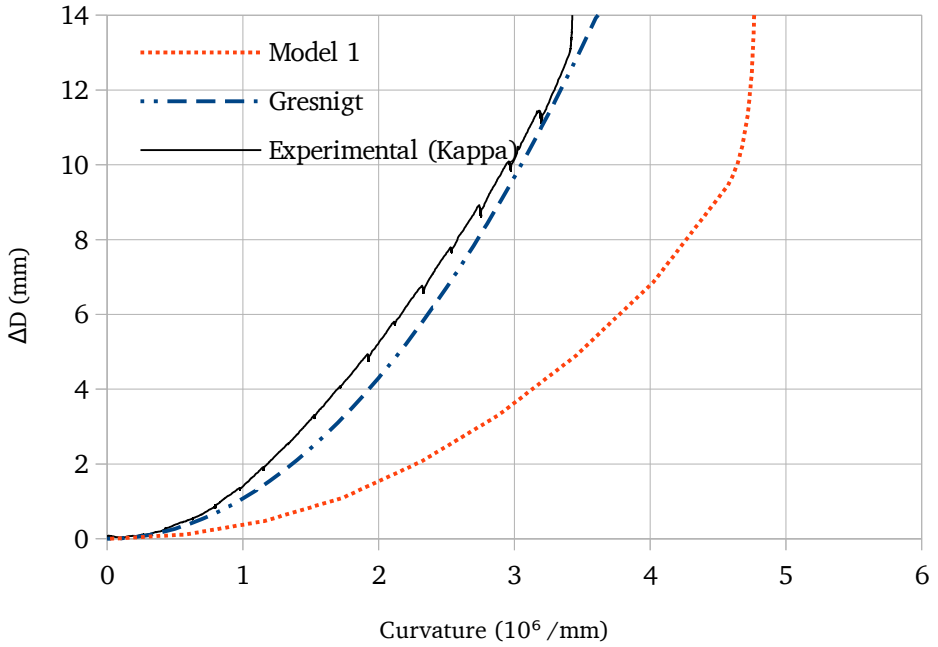

Figure 67: Ovalization-curvature relations for Tube 3: Buckling location (Kappa)

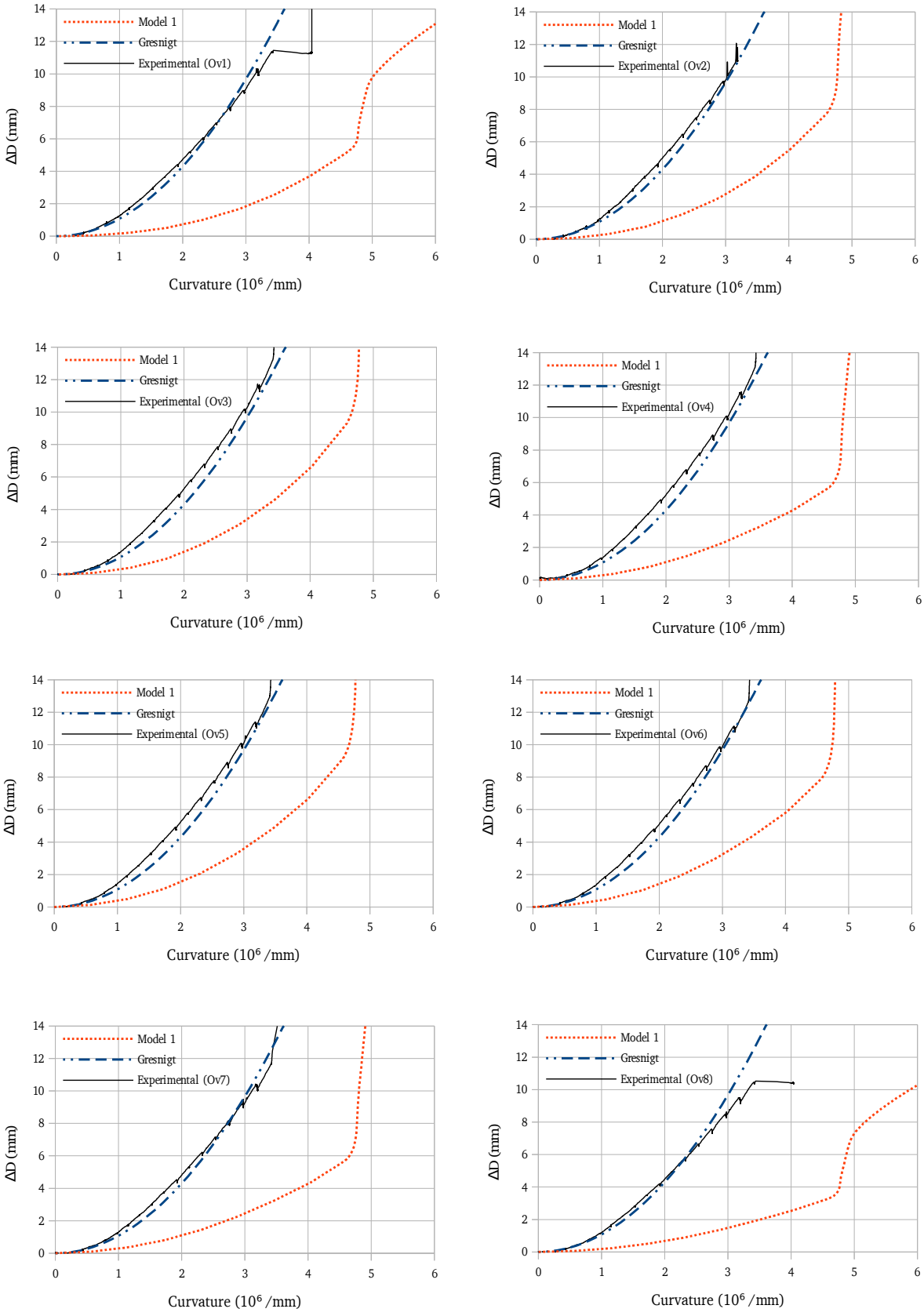

Figure 68: Curvature-ovalization diagrams for Tube 3: Ovalization brackets (Kappa)

5.5.4 Tube 4 Results

Tube 4 is a plain spirally welded steel tube characterized by D/t = 116, f_y = 420 MPa, and 2w = 0.636mm.

Table 13: Tube 4 results

	k_{buck} (10^6 /mm)	k_{crit} (10^6 /mm)	M_{buck} (kNm)	M_{max} (kNm)
Model 1	5.71	5.71	3,582.4	3,582.4
Model 2	6.19	6.19	3,639.4	3,639.4
Gresnigt	-	8.4	-	3,949.5
Experimental	6.31	6.27	3,730.9	3,716.4

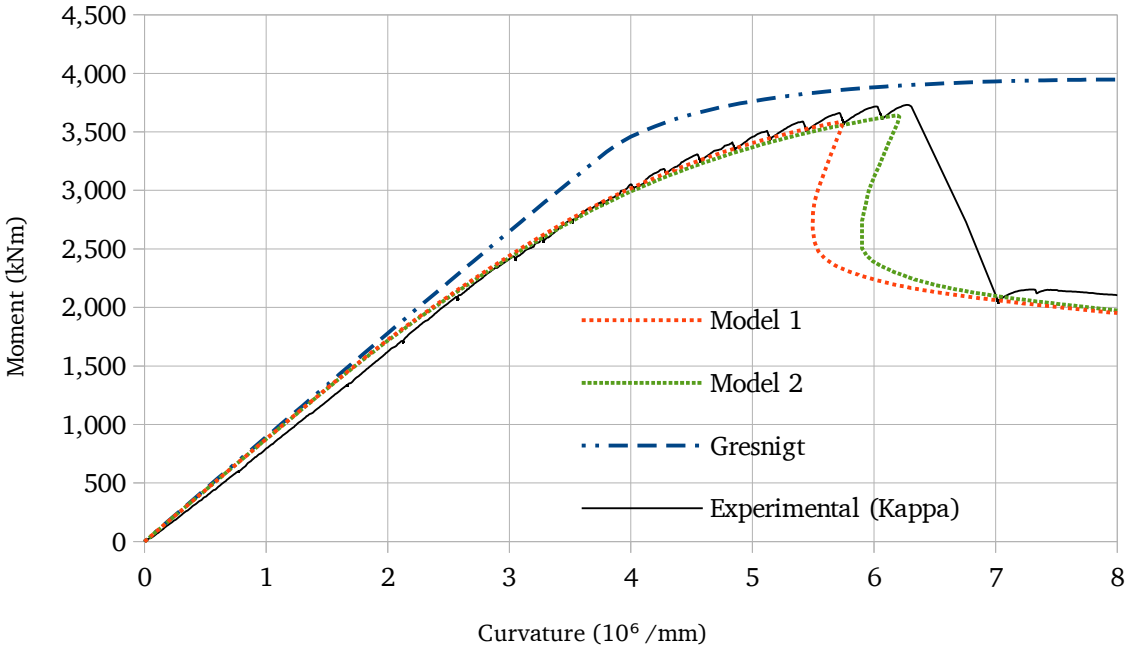

Figure 69: Moment-curvature relations for Tube 4: Kappa

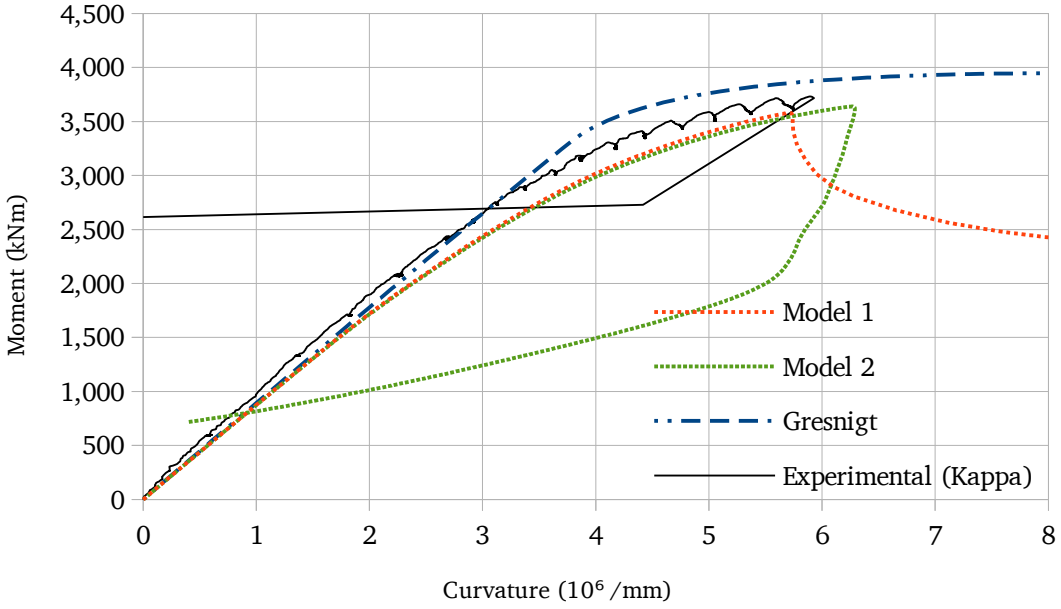

Figure 70: Moment-curvature relations for Tube 4: curv1

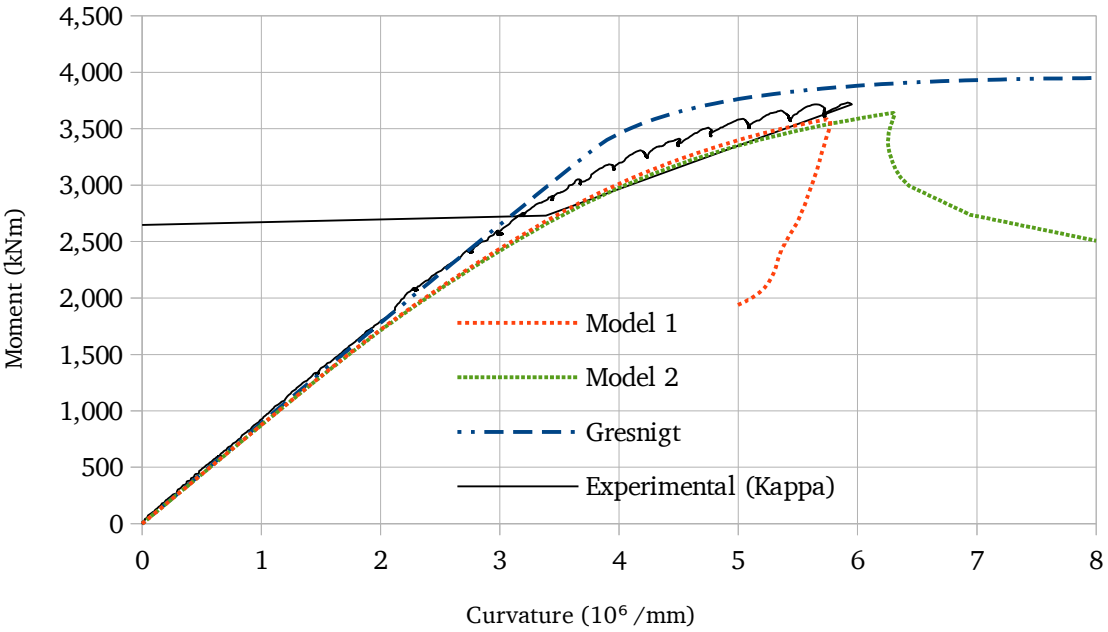

Figure 71: Moment-curvature relations for Tube 4: curv2

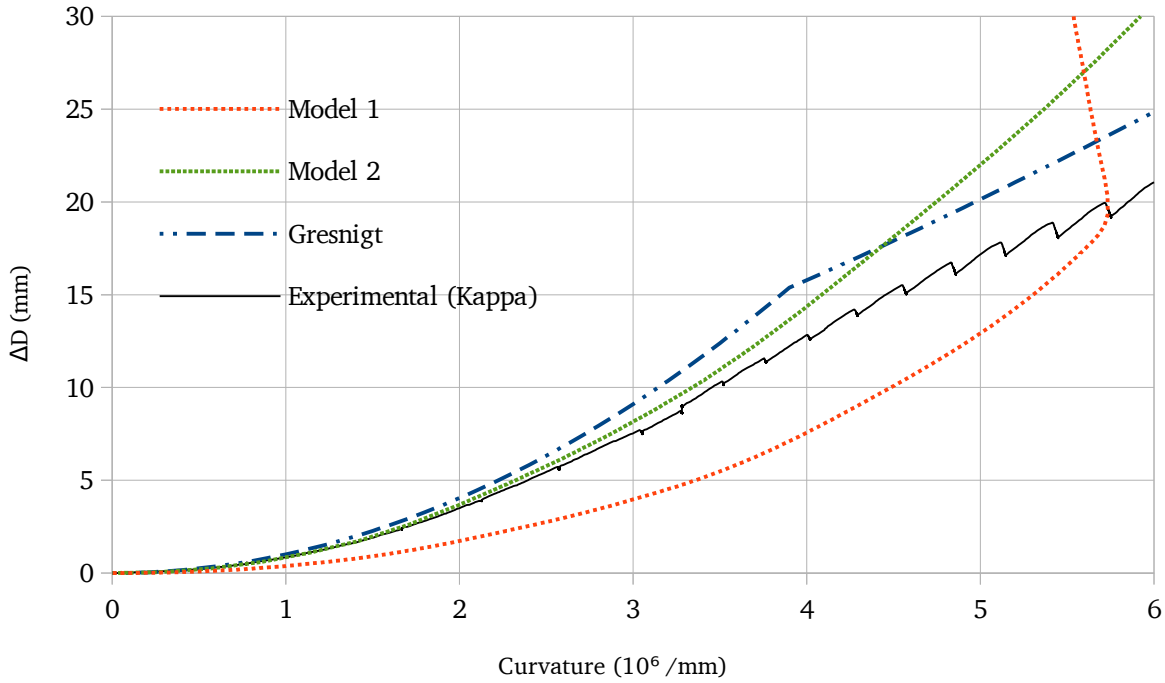

Figure 72: Ovalization-curvature relations for Tube 4: Buckling location (Kappa)

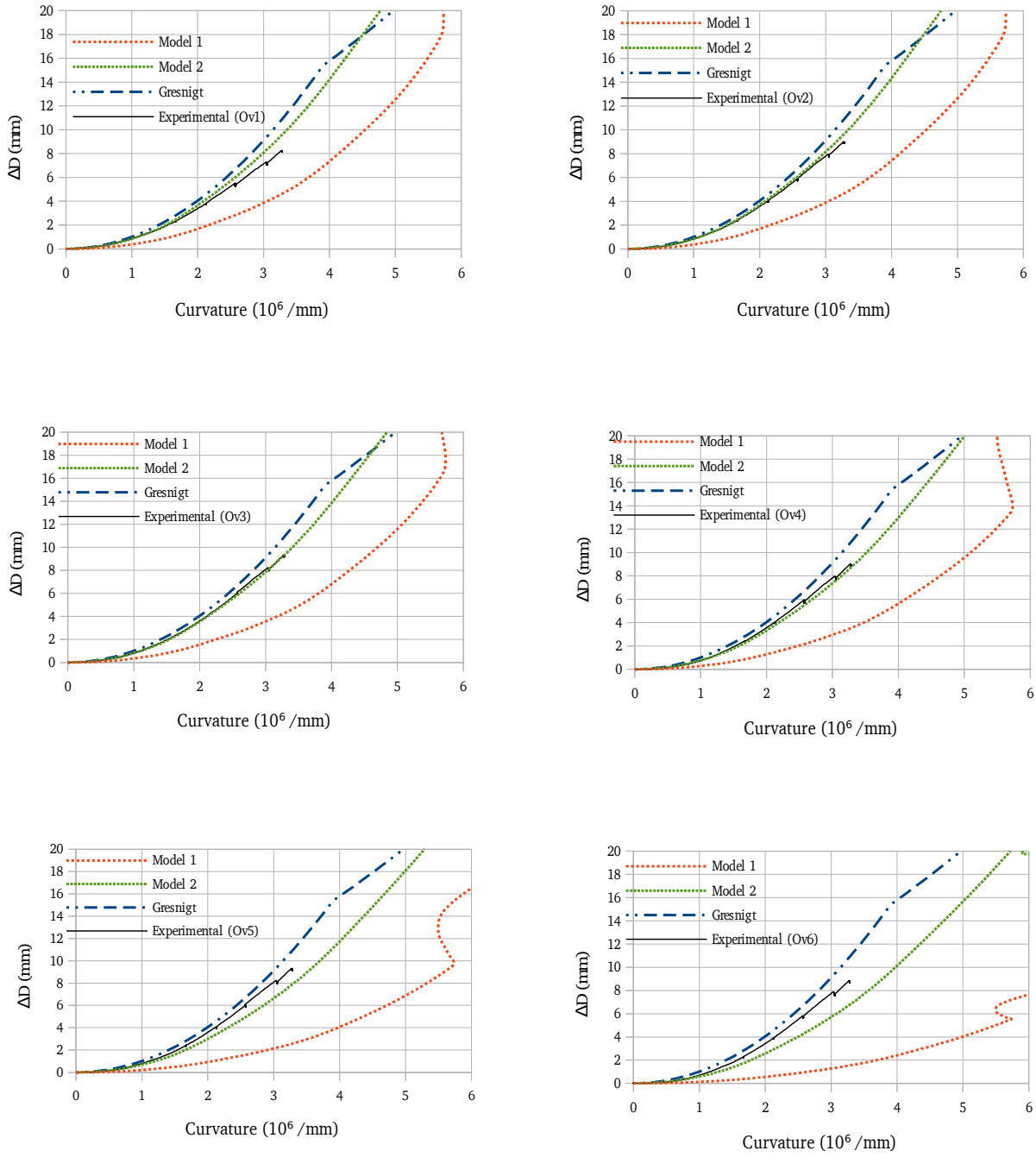

Figure 73: Ovalization-curvature relations for Tube 4: Curvature brackets (Kappa)

5.5.5 Tube 5 Results

Tube 5 is a plain spirally welded tube characterized by D/t = 119, f_y = 400 MPa, and 2w = 0.718mm.

Table 14: Tube 5 results

	k_{buck} (10^6 /mm)	k_{crit} (10^6 /mm)	M_{buck} (kNm)	M_{max} (kNm)
Model 1	6.06	6.06	3,431.7	3,431.7
Model 2	6.37	6.37	3,443.5	3,443.5
Gresnigt	-	8.0	-	3,721.0
Experimental	5.47	5.51	3,238.5	3,338.2

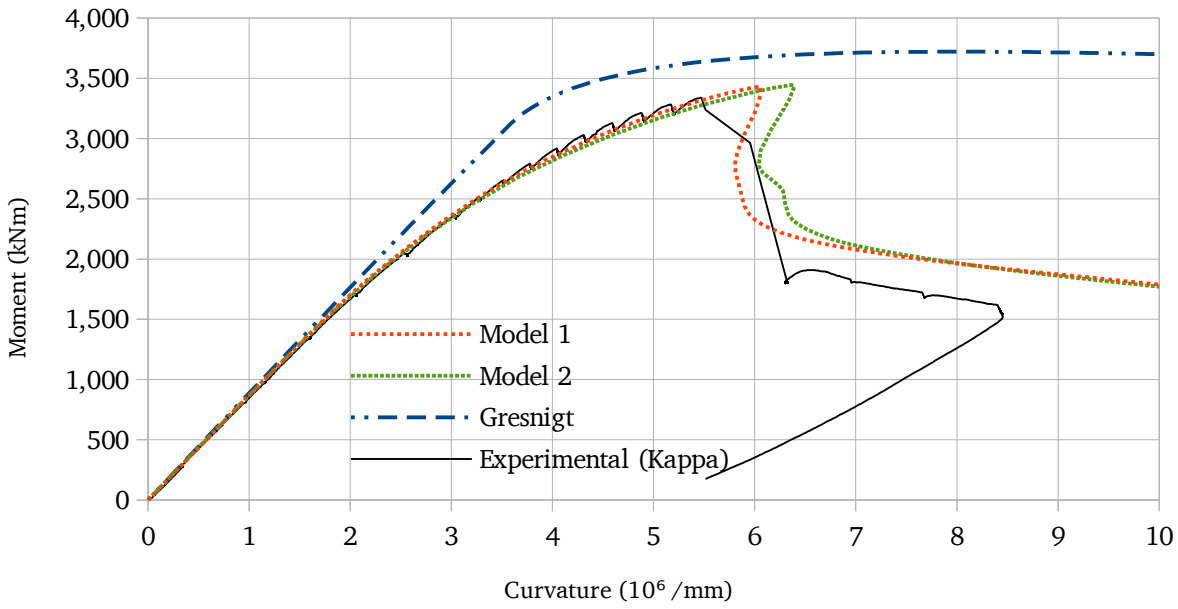

Figure 74: Moment-curvature relations for Tube 5: Kappa

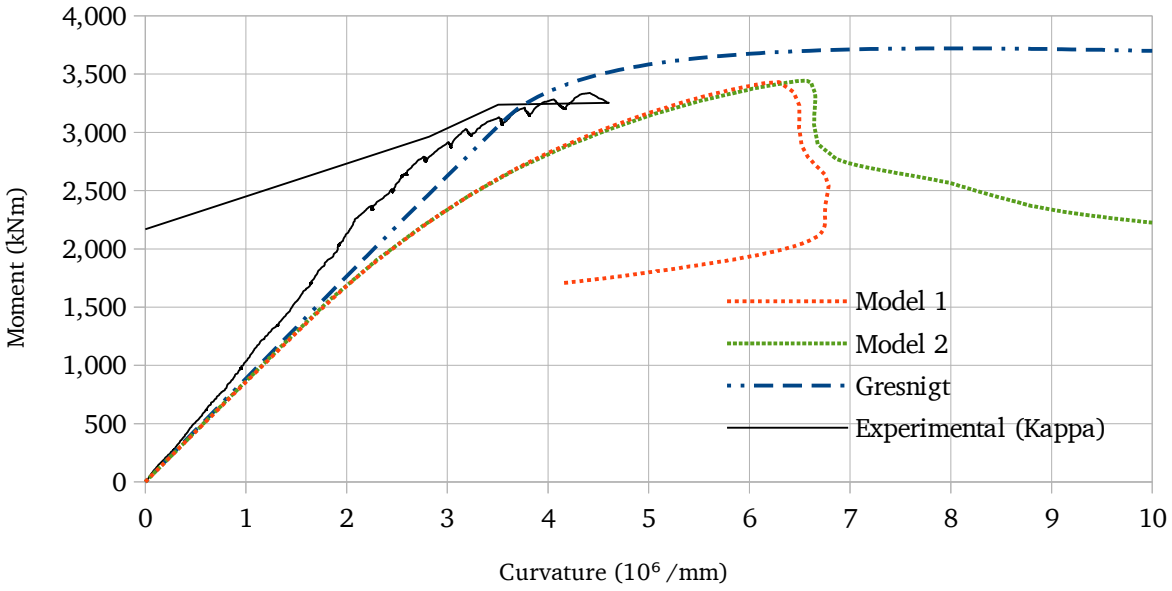

Figure 75: Moment-curvature relations for Tube 5: curv1

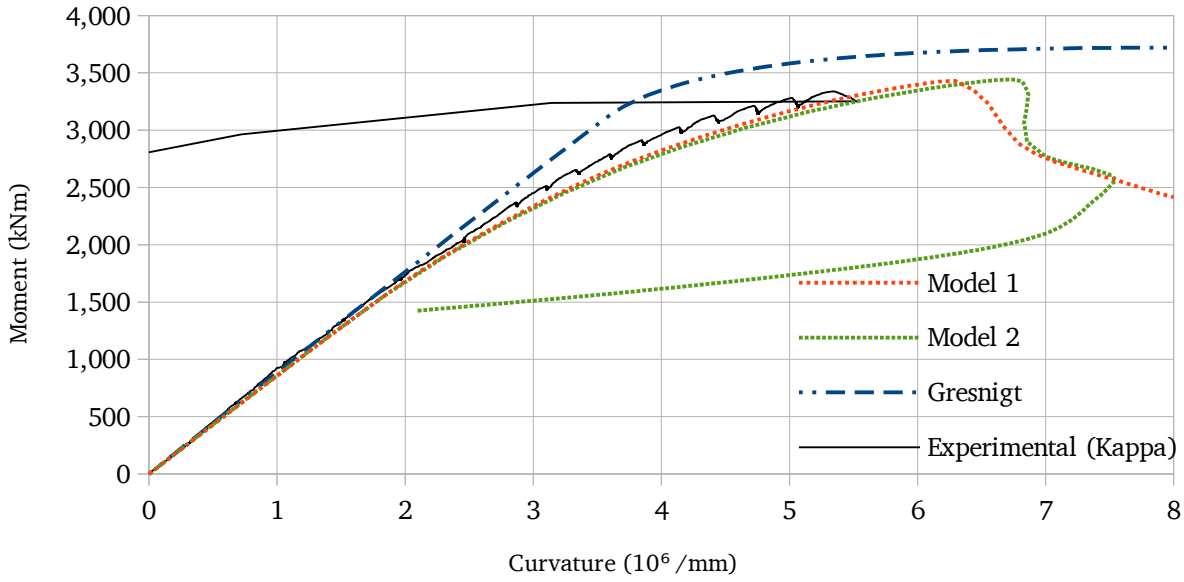

Figure 76: Moment-curvature relations for Tube 5: curv2

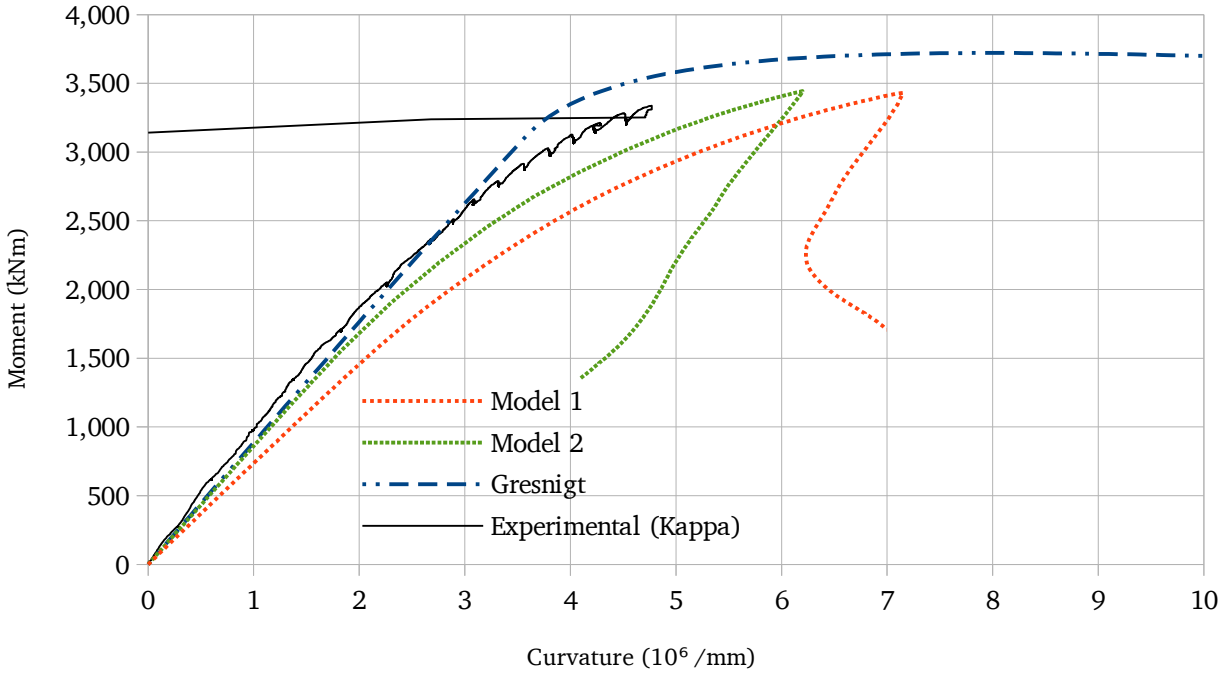

Figure 77: Moment-curvature relations for Tube 5: curv3

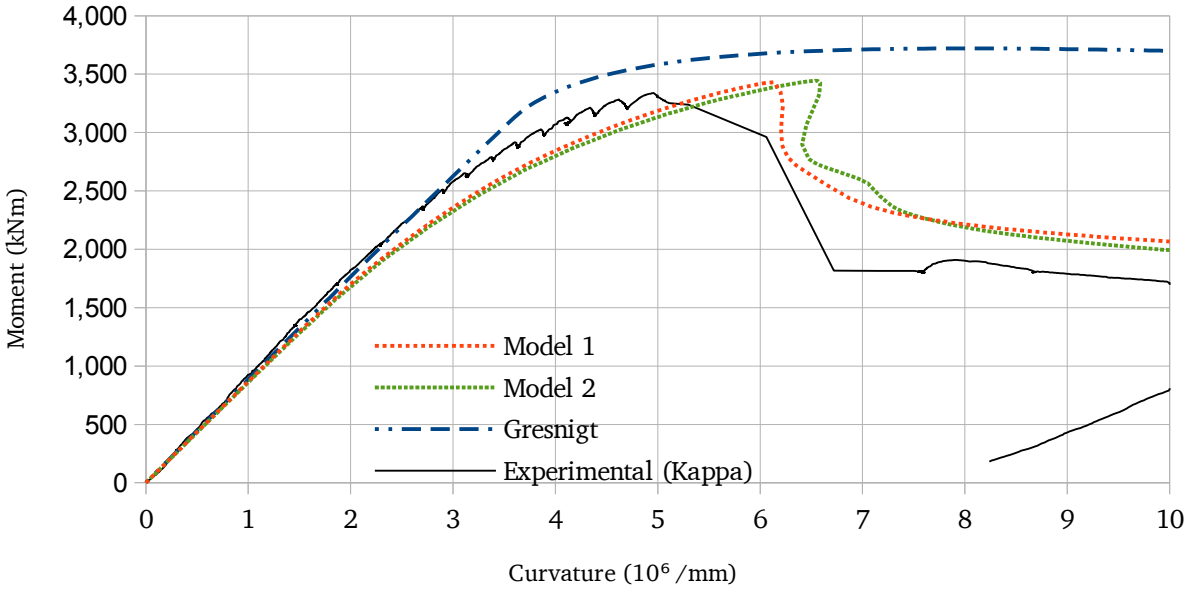

Figure 78: Moment-curvature relations for Tube 5: curvall

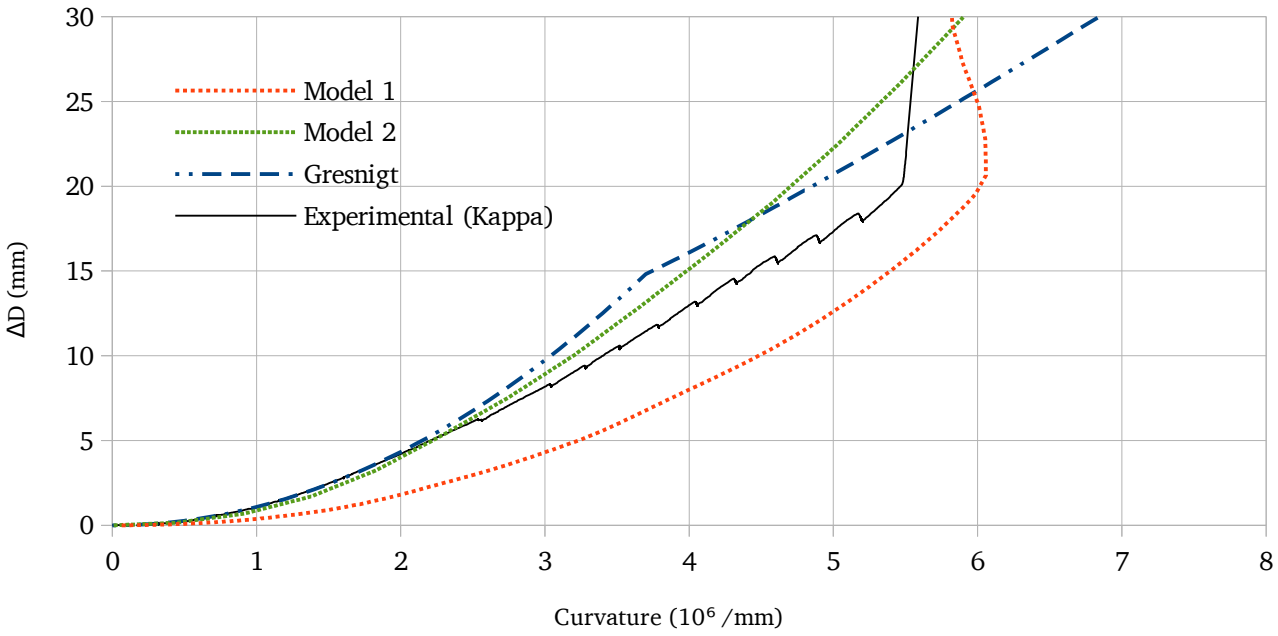

Figure 79: Ovalization-curvature relations for Tube 5: Buckling location (Kappa)

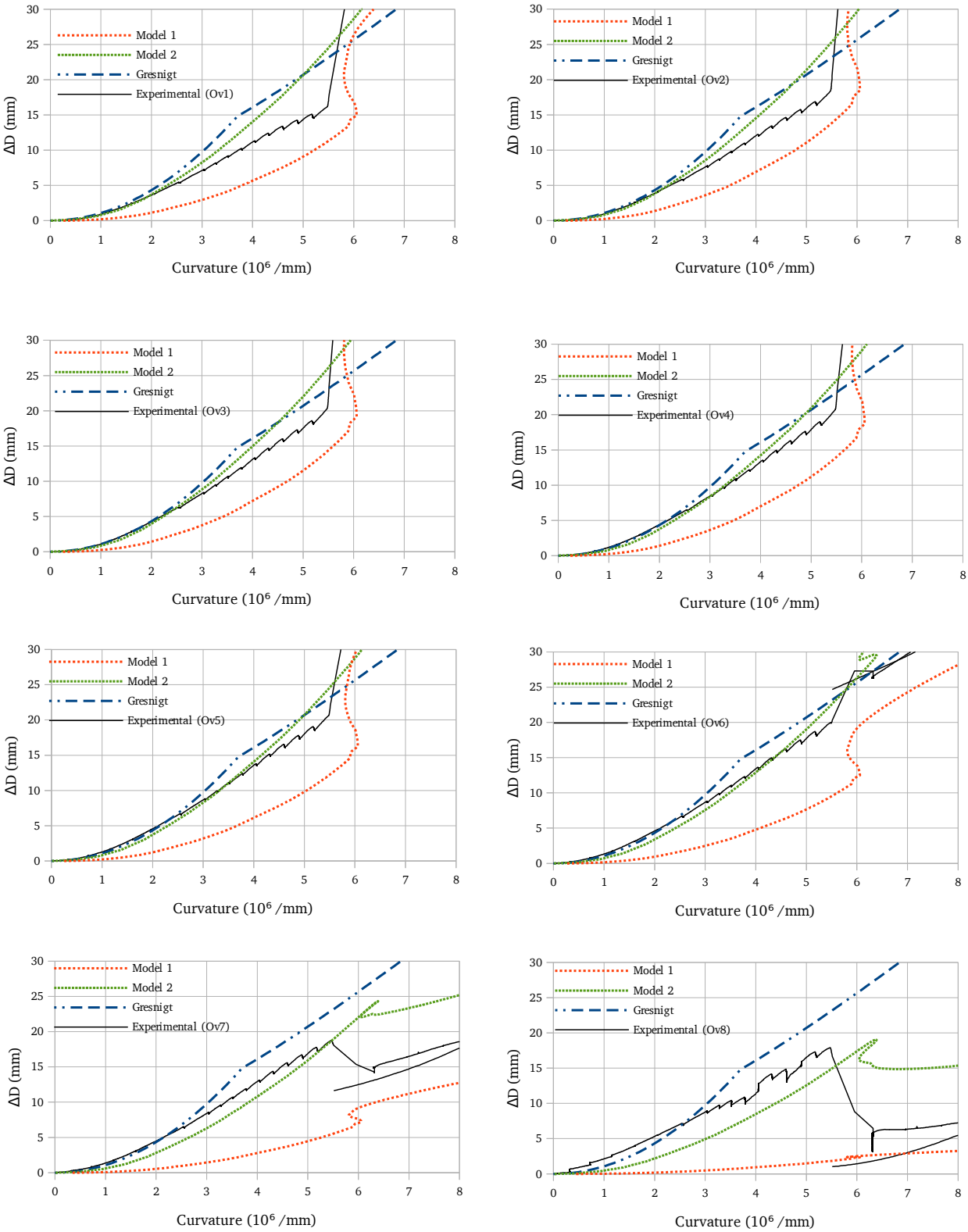

Figure 80: Ovalization-curvature relations for Tube 5: Ovalization brackets (Kappa)

5.5.6 Tube 6 Results

Tube 6 features a coil connection weld but no girth weld. The left side is characterized by D/t = 66 and fy = 525 MPa. The right side is characterized by D/t = 65 and fy = 545 MPa. The girth weld is characterized by an additional imperfection of 2w = 3.1mm, which was induced according to Figure 81. The final deformed shape is shown in Figure 82.

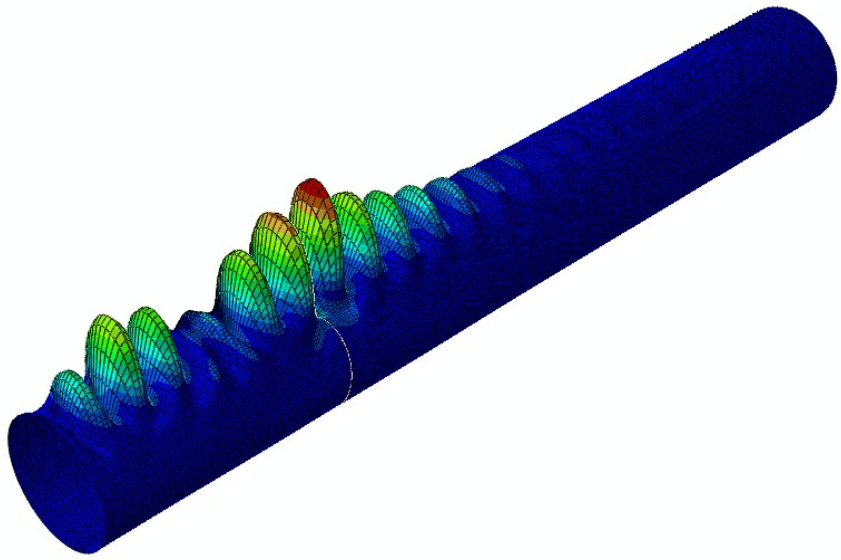

Figure 81: Imperfection shape of Tube 6

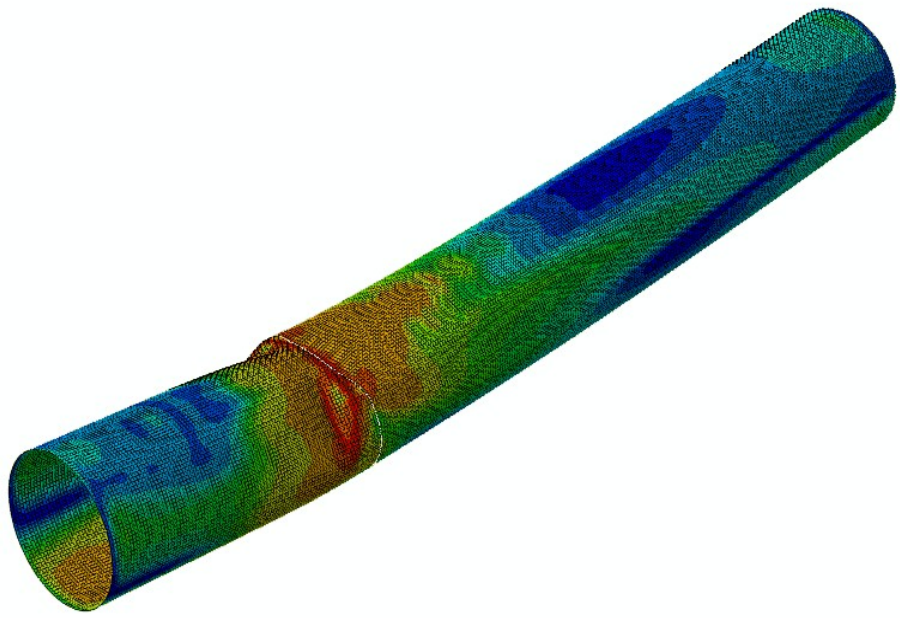

Figure 82: Deformed shape of Tube 6

Table 15: Tube 6 results

	k_{buck} (10^6 /mm)	k_{crit} (10^6 /mm)	M_{buck} (kNm)	M_{max} (kNm)
Model 1	8.09	8.09	6,490.7	6,490.7
Gresnigt	-	11.8	-	9,151.8
Experimental	9.30	8.84	7,667.9	8,160.4

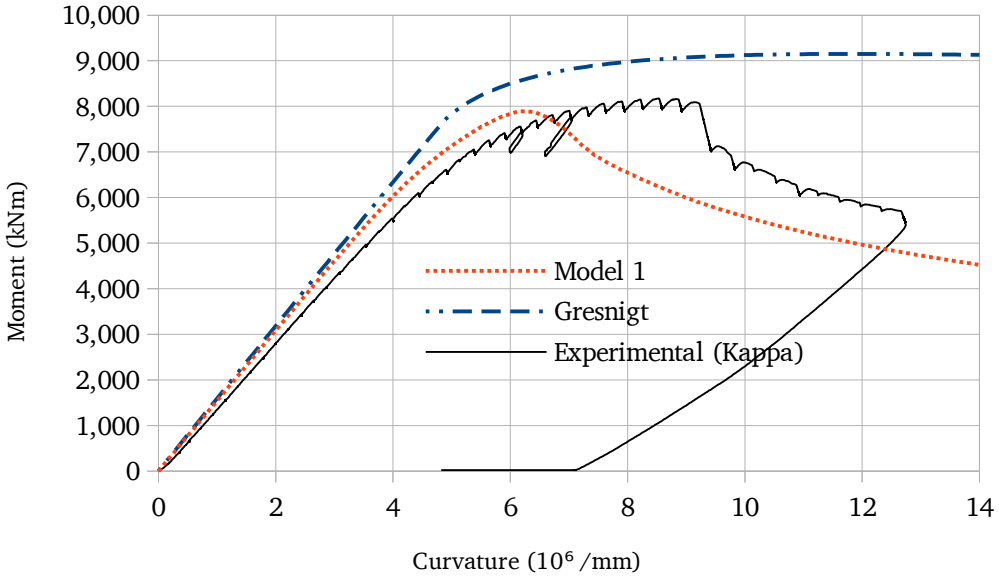

Figure 83: Moment-curvature relations for Tube 6: Kappa

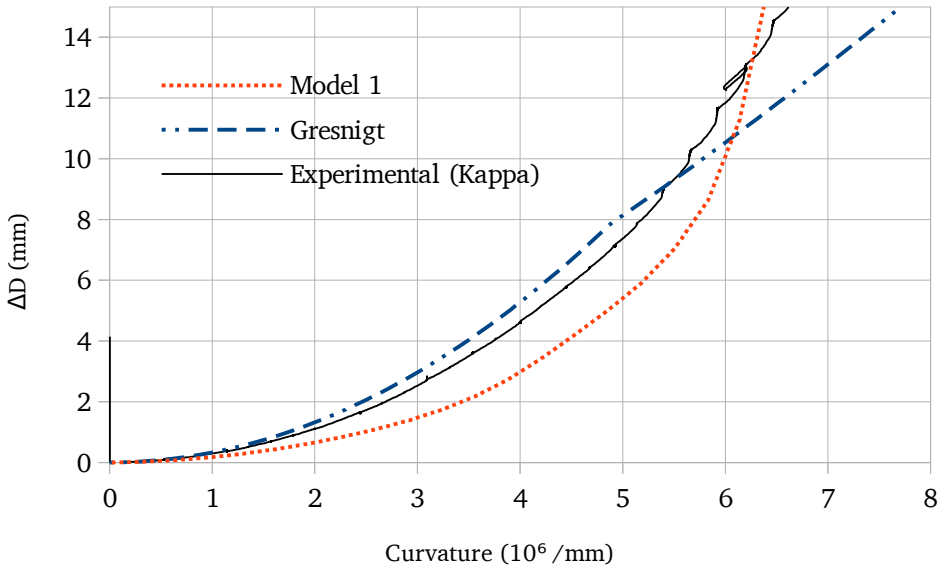

Figure 84: Ovalization-curvature relations for Tube 6: Kappa

5.5.7 Tube 7 Results

Tube 7 is a tube featuring a girth weld and a coil connection weld. All sections are characterized by D/t = 65. The left section is characterized by f_y = 545 MPa, the middle section by f_y = 575 MPa, and the right section by f_y = 560 MPa. The imperfection amplitude is 2w = 2.45mm and occured in the left section. The buckling mode used to induce an imperfection into Tube 7 is shown in Figure 85. The deformed shape is shown in Figure 86.

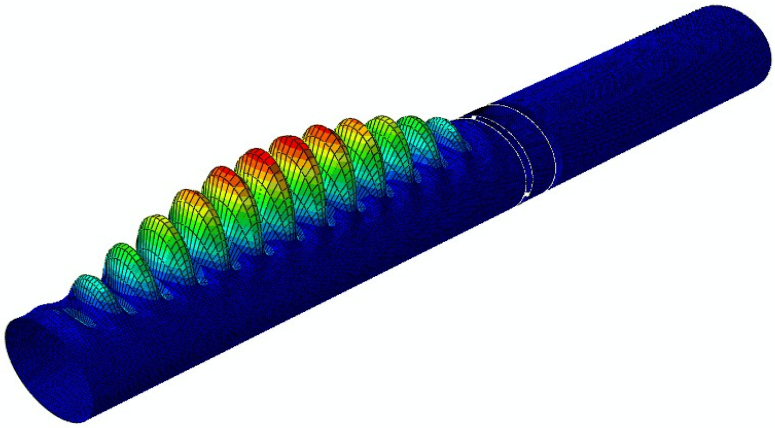

Figure 85: Imperfection shape of Tube 7

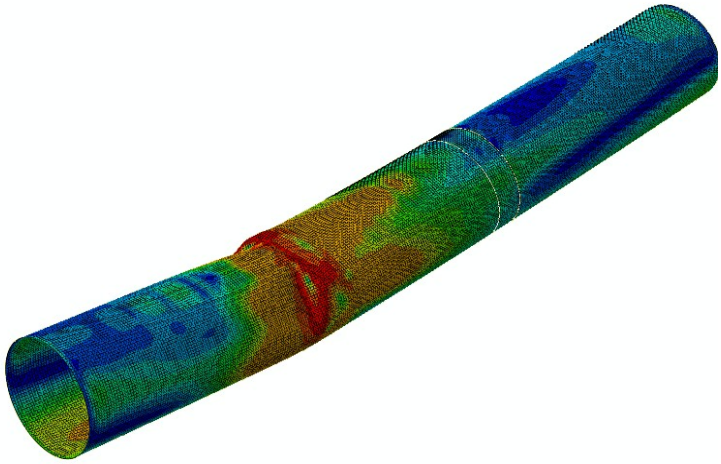

Figure 86: Deformed shape of Tube 7

Table 16: Tube 7 results

	k_{buck} (10^6 /mm)	k_{crit} (10^6 /mm)	M_{buck} (kNm)	M_{max} (kNm)
Model 1	10.64	10.64	9,649.2	9,649.2
Gresnigt	-	12.5	-	9,736.9
Experimental	8.20	7.88	8,096.2	7,722.1

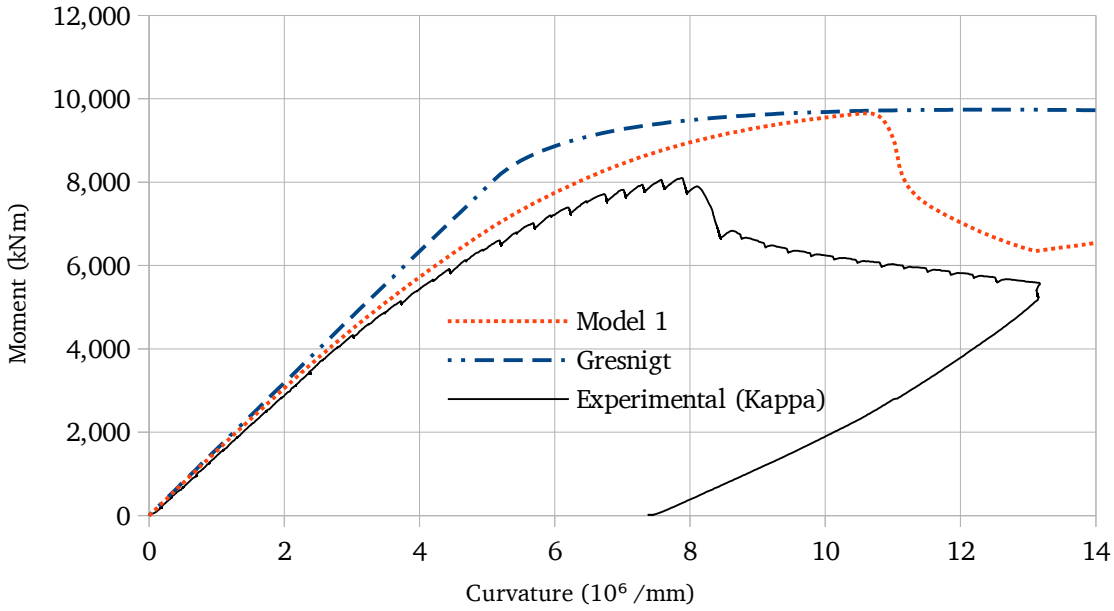

Figure 87: Moment-curvature relations for Tube 7: Kappa

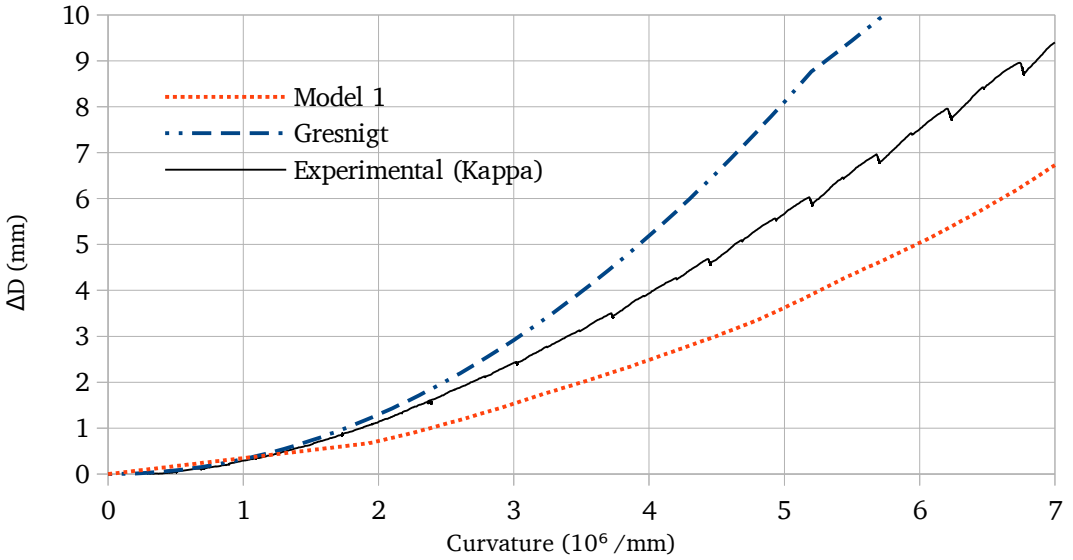

Figure 88: Ovalization-curvature relations for Tube 7: Kappa

5.5.8 Tube 8 Results

Tube 8 is a plain spirally welded tube characterized by D/t = 117, f_y = 435 MPa, and 2w = 1.070mm.

Table 17: Tube 8 results

	k_{buck} (10^6 /mm)	k_{crit} (10^6 /mm)	M_{buck} (kNm)	M_{max} (kNm)
Model 1	5.14	5.14	3,579.1	3,579.1
Model 2	5.36	5.36	3,599.5	3,599.5
Gresnigt	-	8.5	-	4052.4
Experimental	5.70	5.66	3,469.1	3,347.1

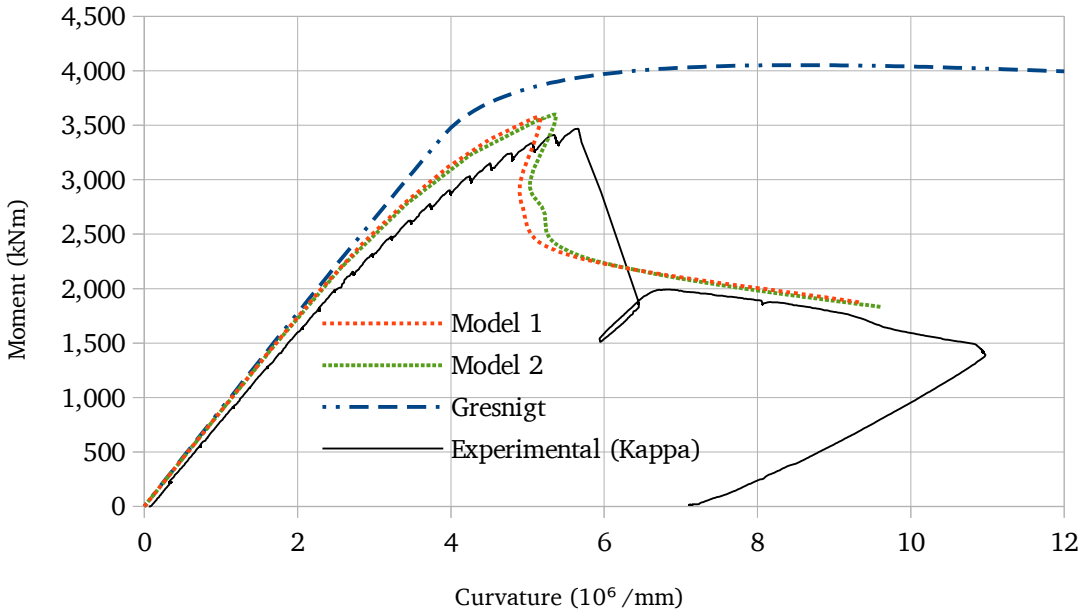

Figure 89: Moment-curvature relations for Tube 8: Kappa

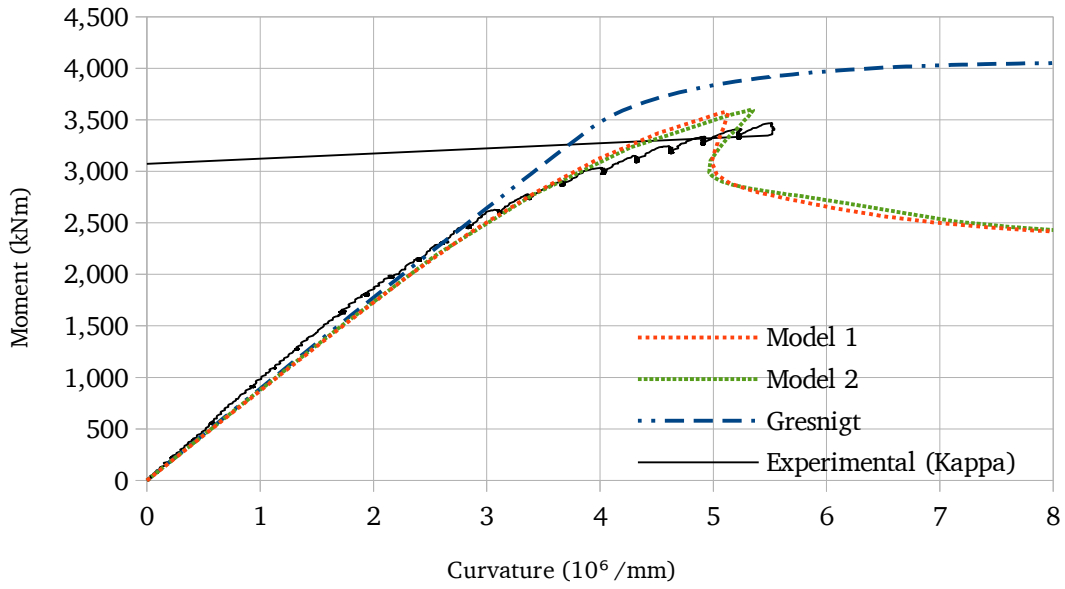

Figure 90: Moment-curvature relations for Tube 8: curv1

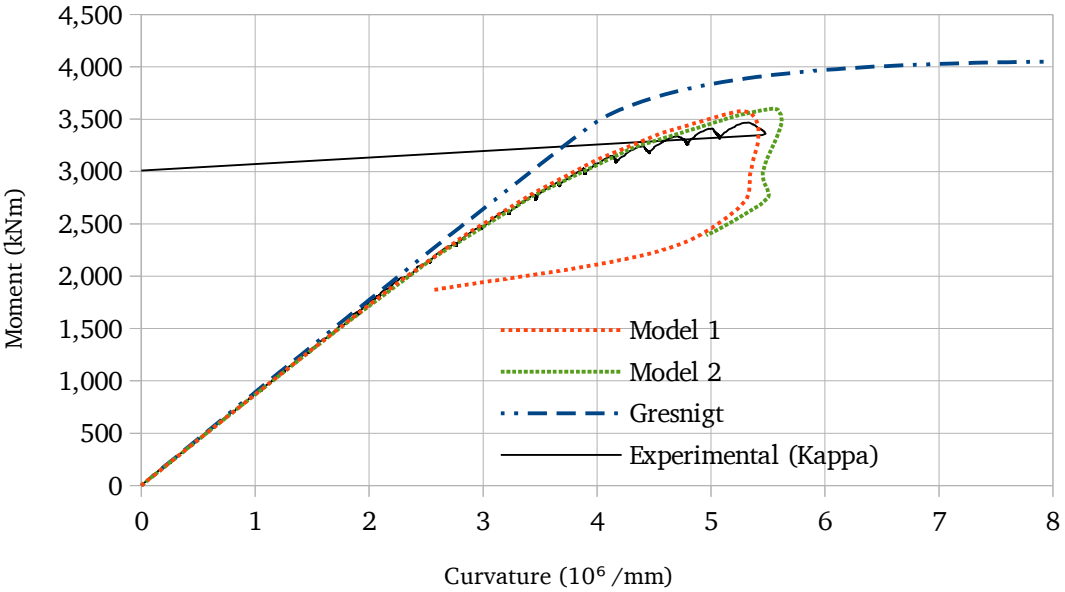

Figure 91: Moment-curvature relations for Tube 8: curv2

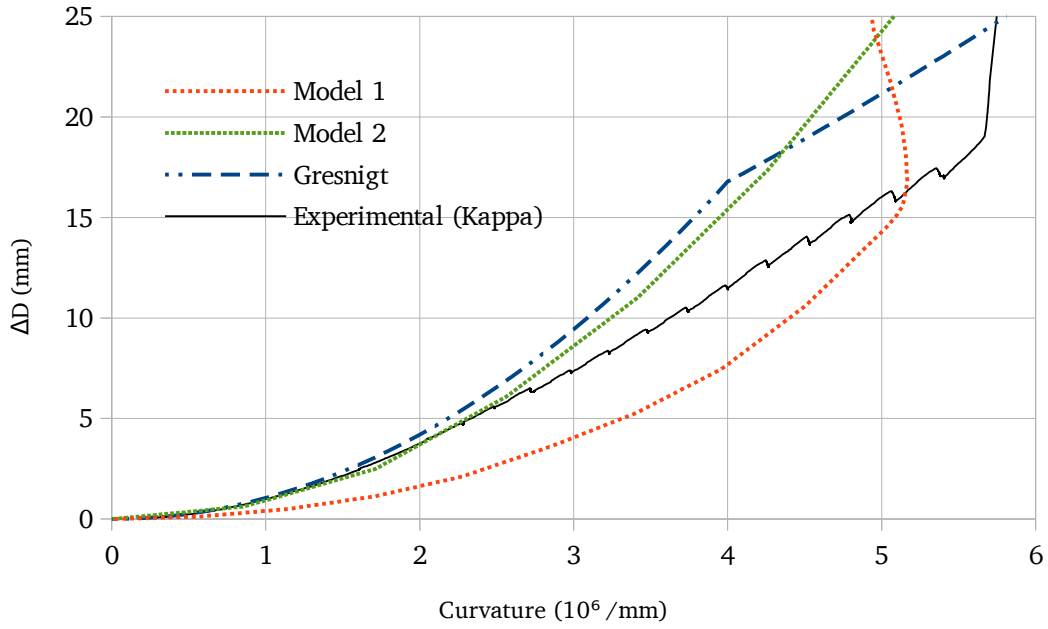

Figure 92: Ovalization-curvature relations for Tube 8: Buckling location (Kappa)

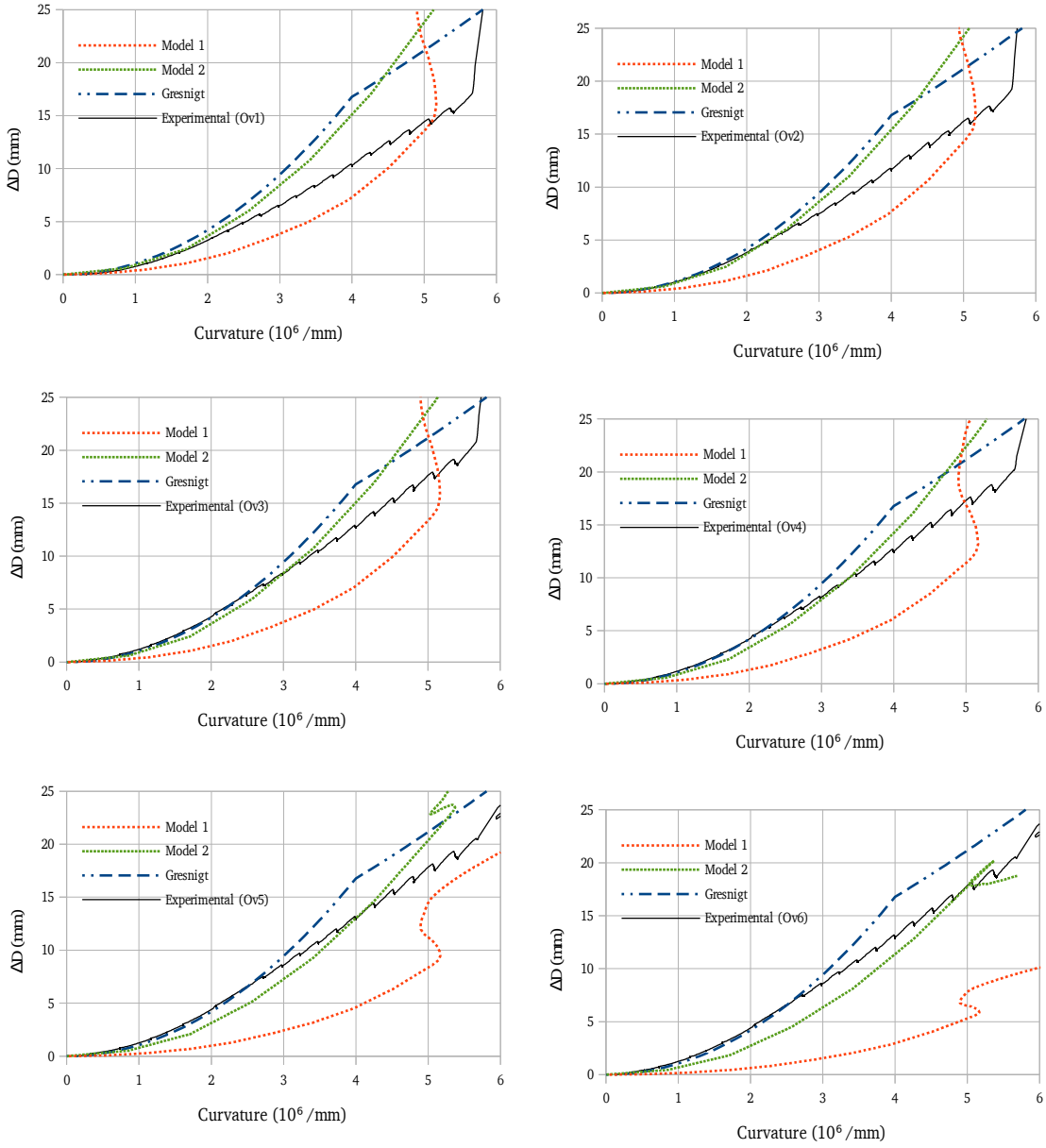

Figure 93: Ovalization-curvature relations for Tube 8: Ovalization brackets (Kappa)

5.5.9 Tube 9 Results

Tube 9 is a plain spirally welded tube characterized by D/t = 65 and f_y = 570 MPa and 2w = 2.01mm.

Table 18: Tube 9 results

	k_{buck} (10^6 /mm)	k_{crit} (10^6 /mm)	M_{buck} (kNm)	M_{max} (kNm)
Model 1	10.85	10.85	9,665.4	9,665.4
Model 2	12.04	12.04	9,808.2	9,808.2
Gresnigt	-	12.4	-	9,816.5
Experimental	9.90	9.22	8.770.0	8,978.0

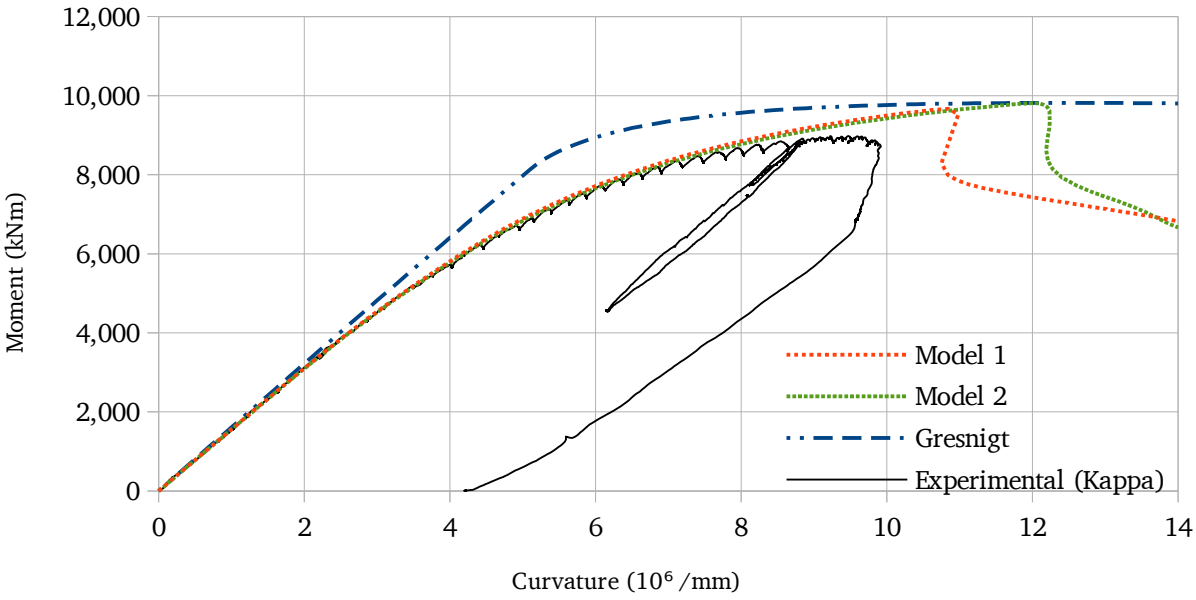

Figure 94: Moment-curvature relations for Tube 9: Kappa

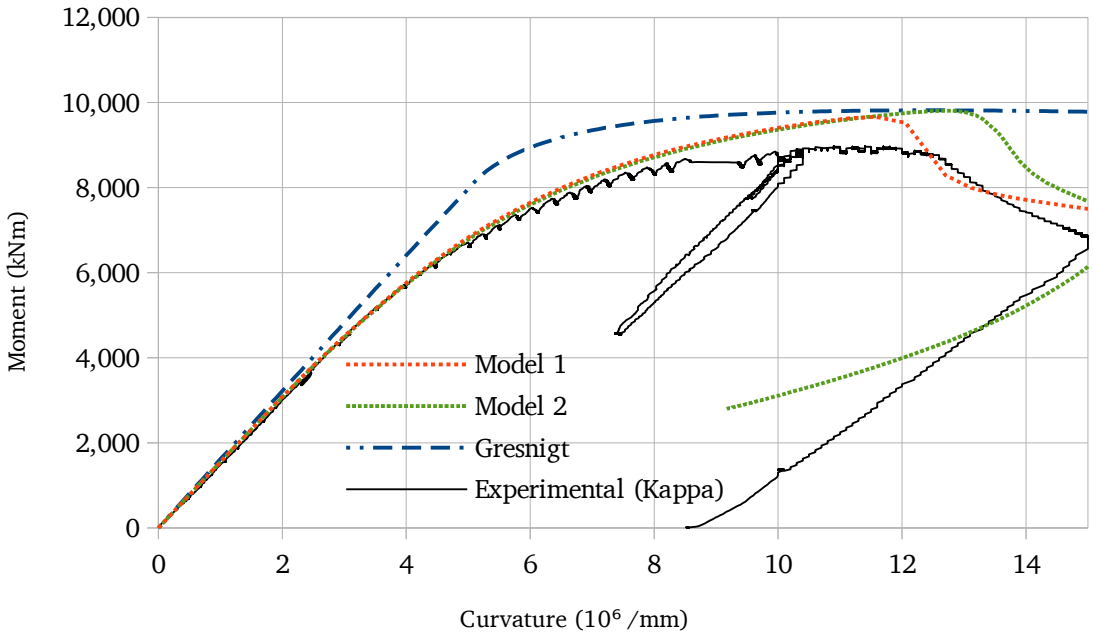

Figure 95: Moment-curvature relations for Tube 9: curv1

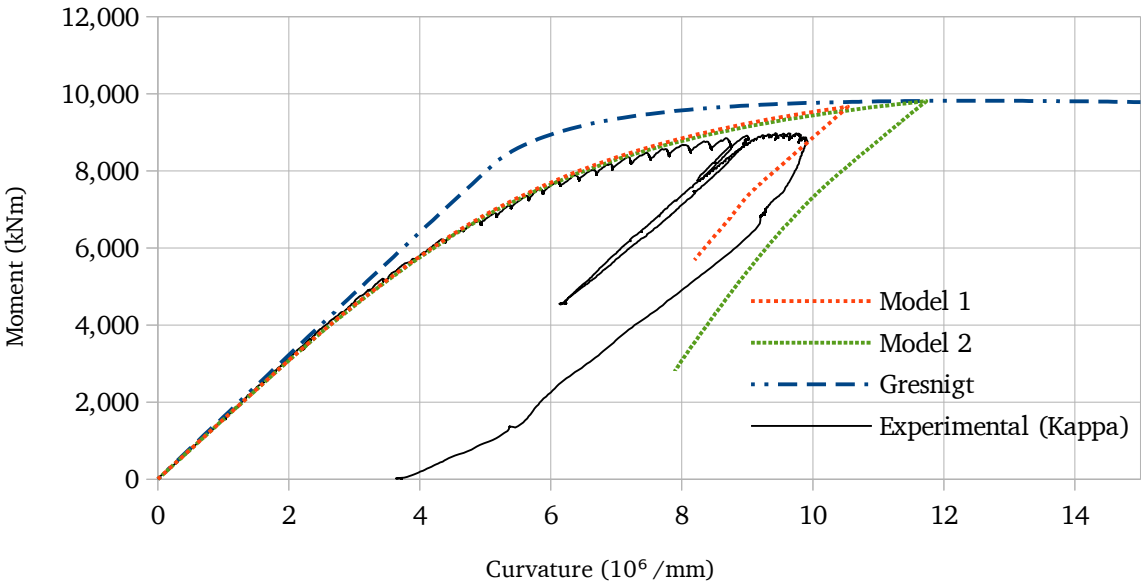

Figure 96: Moment-curvature relations for Tube 9: curv2

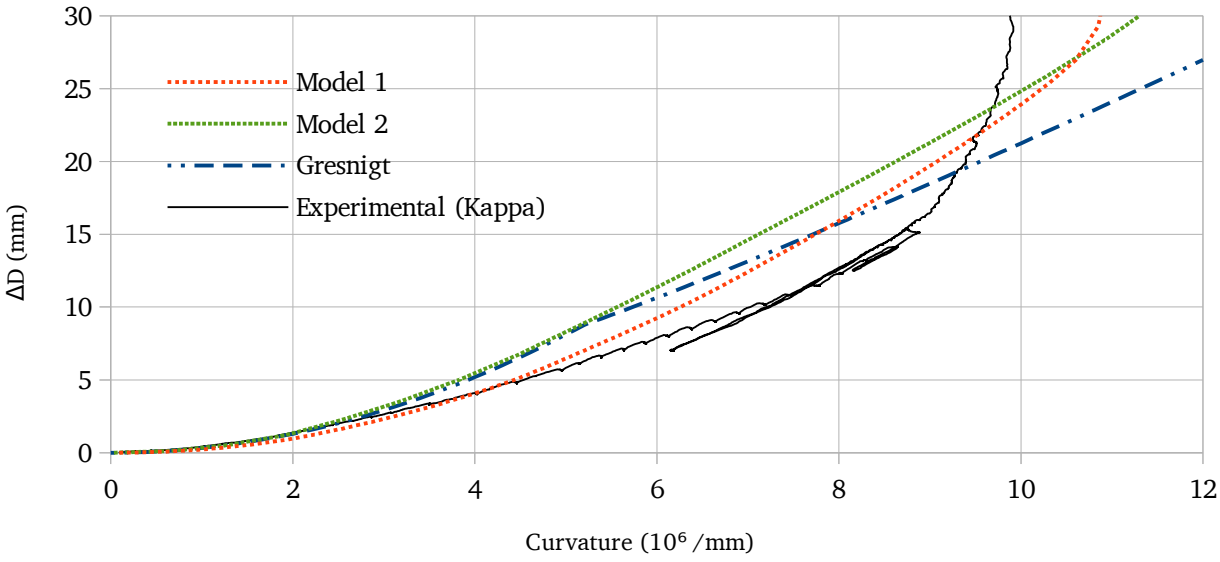

Figure 97: Ovalization-curvature relations for Tube 9: Buckling location (Kappa)

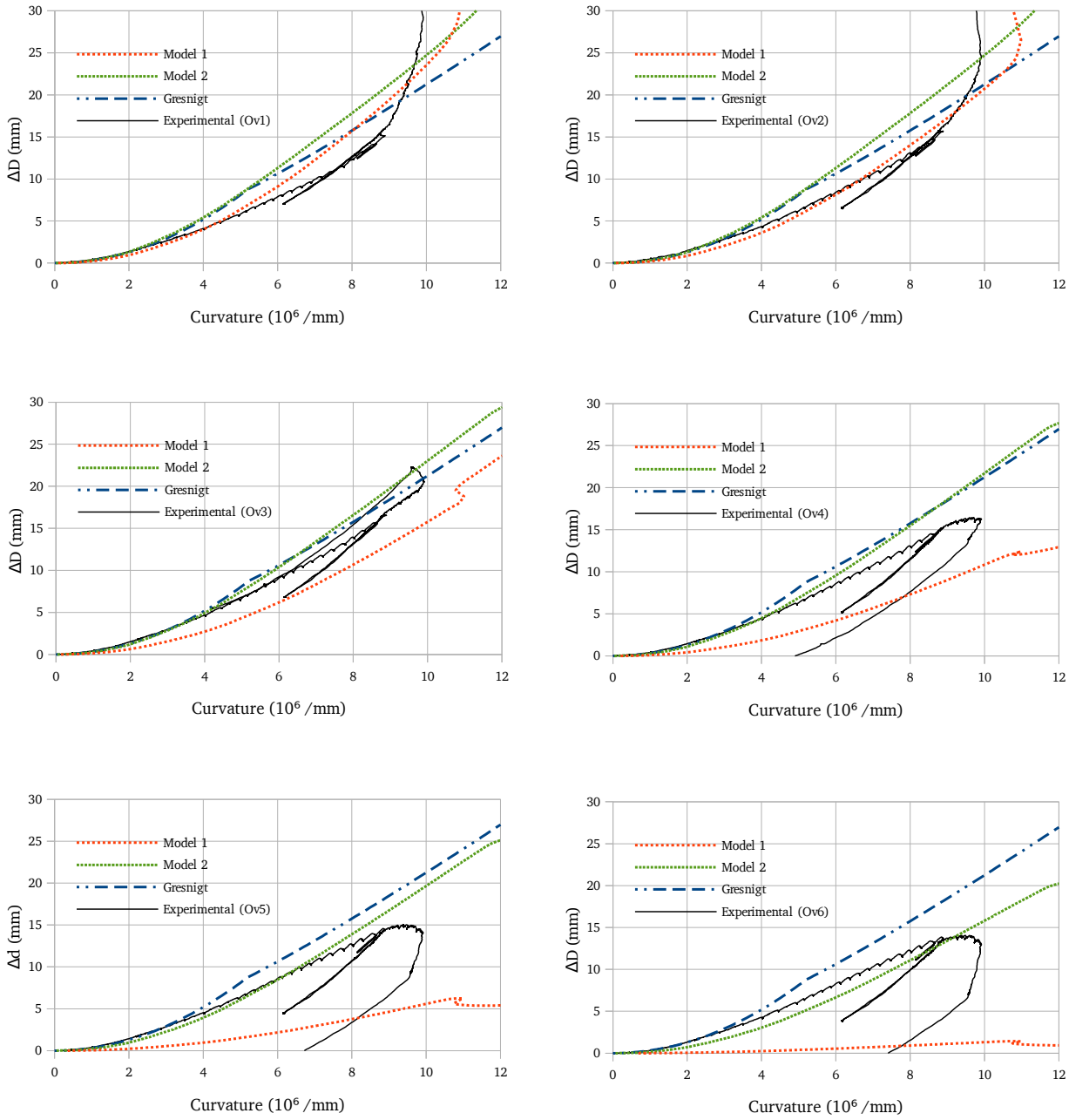

Figure 98: Ovalization-curvature relations for Tube 9: Ovalization Brackets (Kappa)

5.5.10 Tube 10 Results

Tube 10 includes both girth and coil connection welds. The left section is characterized by D/t = 80 and f_y = 525 MPa, the mid section is characterized by D/t = 80 and f_y = 485 MPa, and the right section is characterized by D/t = 84 and f_y = 325 MPa. An imperfection was introduced at the girth weld based on the imperfection shape shown in Figure 99.

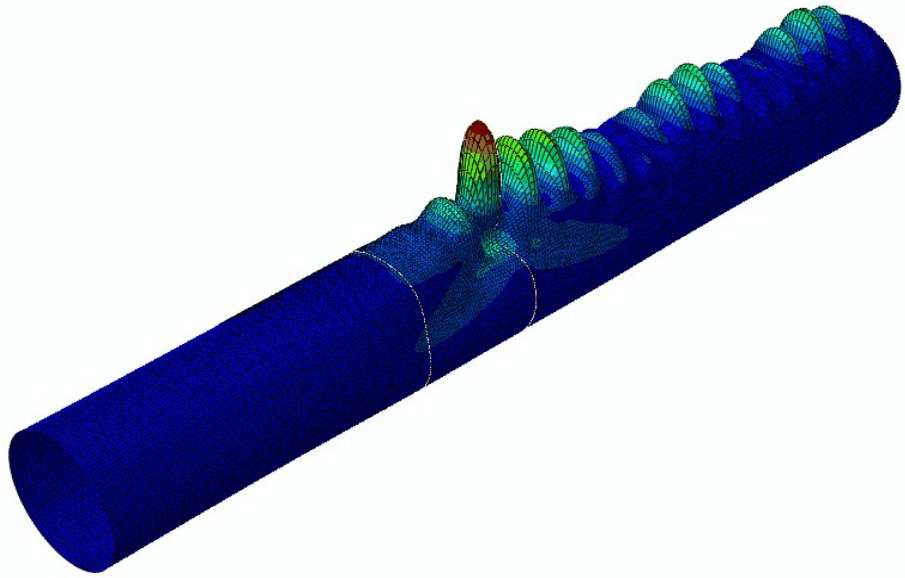

Figure 99: Imperfection shape for Tube 10

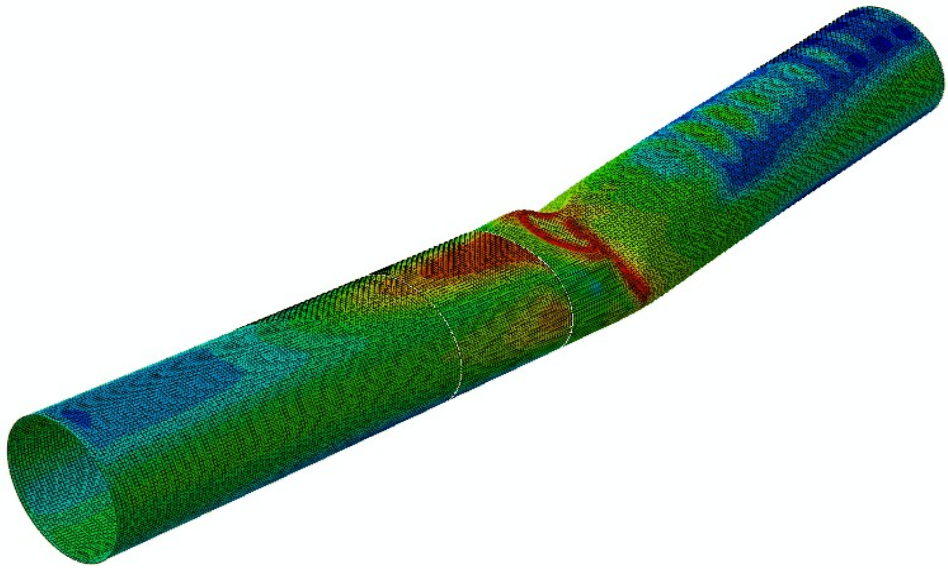

Figure 100: Deformed shape of Tube 10

Table 19: Tube 10 results

	k_{buck} (10^6 /mm)	k_{crit} (10^6 /mm)	M_{buck} (kNm)	M_{max} (kNm)
Model 1	7.20	7.20	4,445.8	4,445.8
Gresnigt	-	9.8	-	6,155.1
Experimental	6.00	5.57	3,982.9	4,270.2

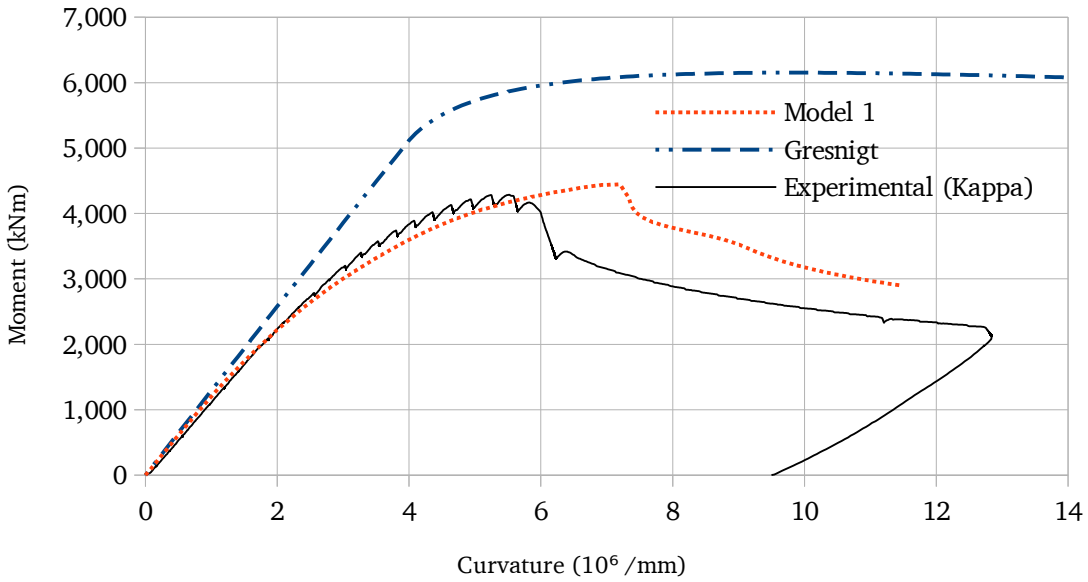

Figure 101: Moment-curvature relations for Tube 10: Kappa

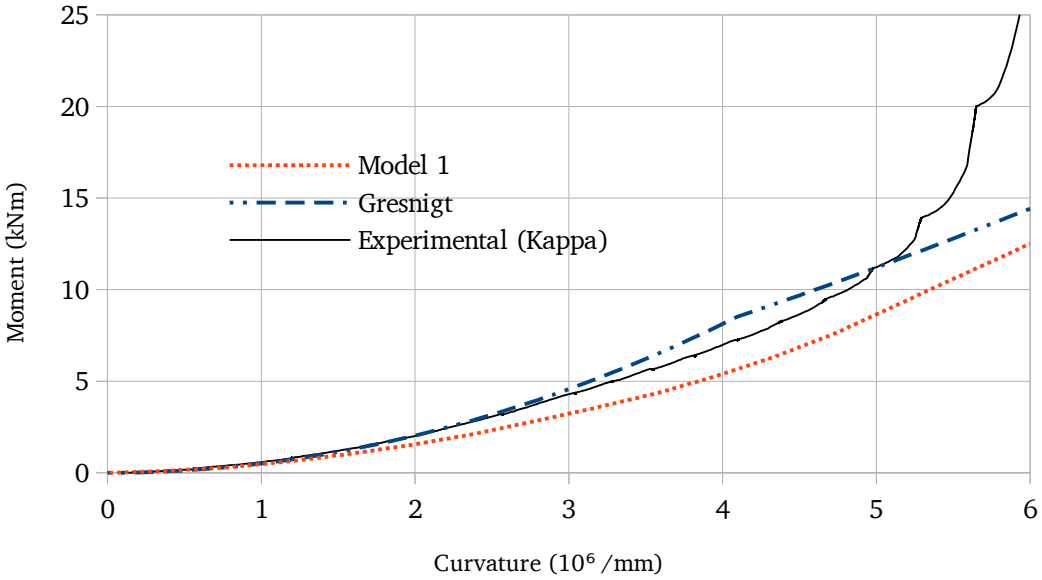

Figure 102: Ovalization-curvature relations for Tube 10: Buckling location (Kappa)

5.5.11 Tube 11 Results

Tube 11 is a plain spirally welded tube characterized by D/t = 83, f_y = 340 MPa, and 2w = 0.465mm.

Table 20: Tube 11 results

	k_{buck} (10^6 /mm)	k_{crit} (10^6 /mm)	M_{buck} (kNm)	M_{max} (kNm)
Model 1	8.06	8.06	4,649.7	4,649.7
Model 2	9.26	9.26	4,687.0	4,687.0
Gresnigt	-	8.1	-	4,677.9
Experimental	9.03	9.53	3,724.5	4,172.9

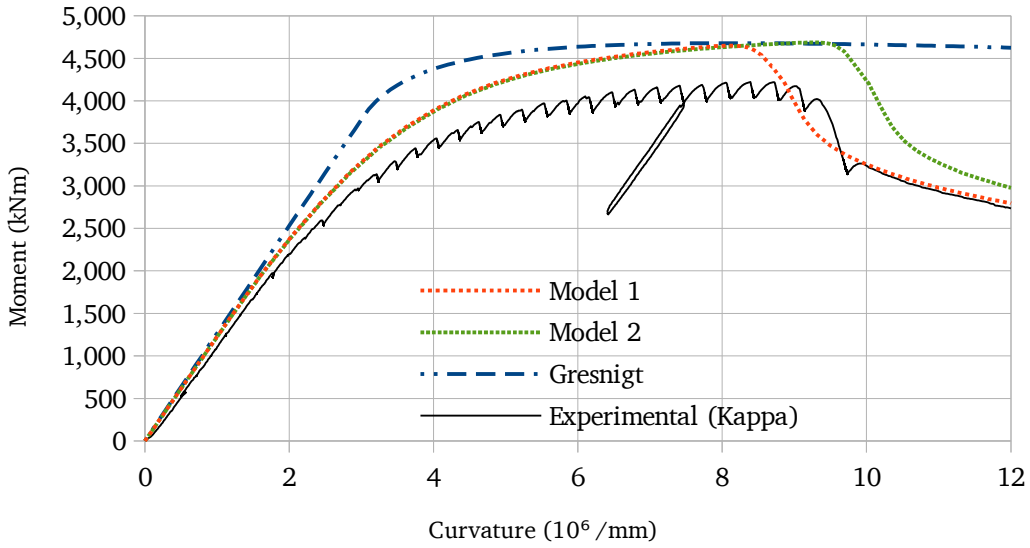

Figure 103: Moment-curvature relations for Tube 11: Kappa

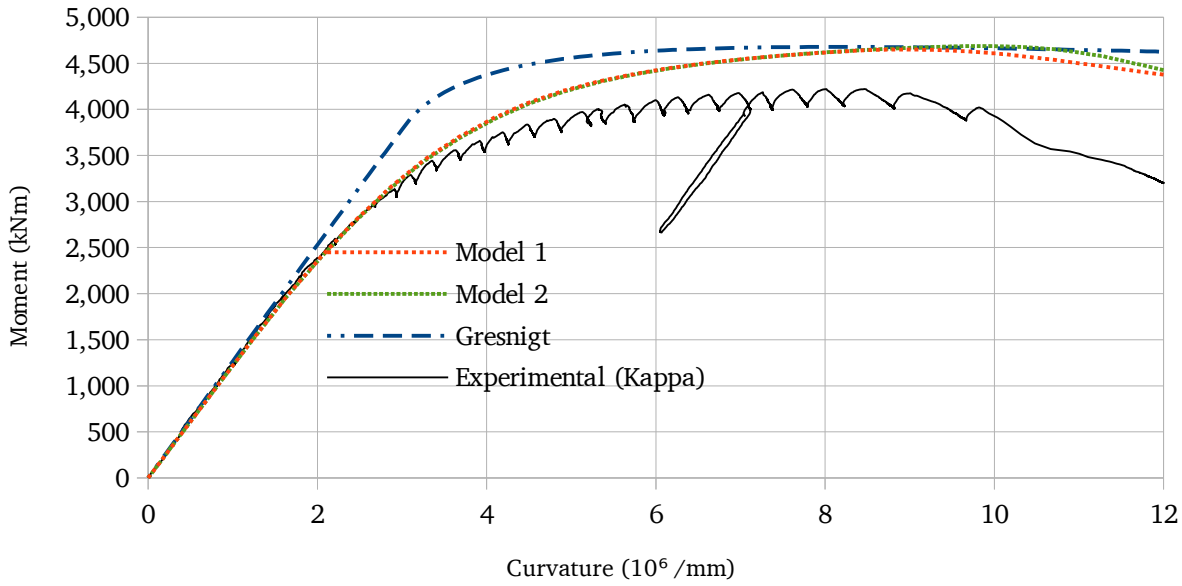

Figure 104: Moment-curvature relations for Tube 11: curv1

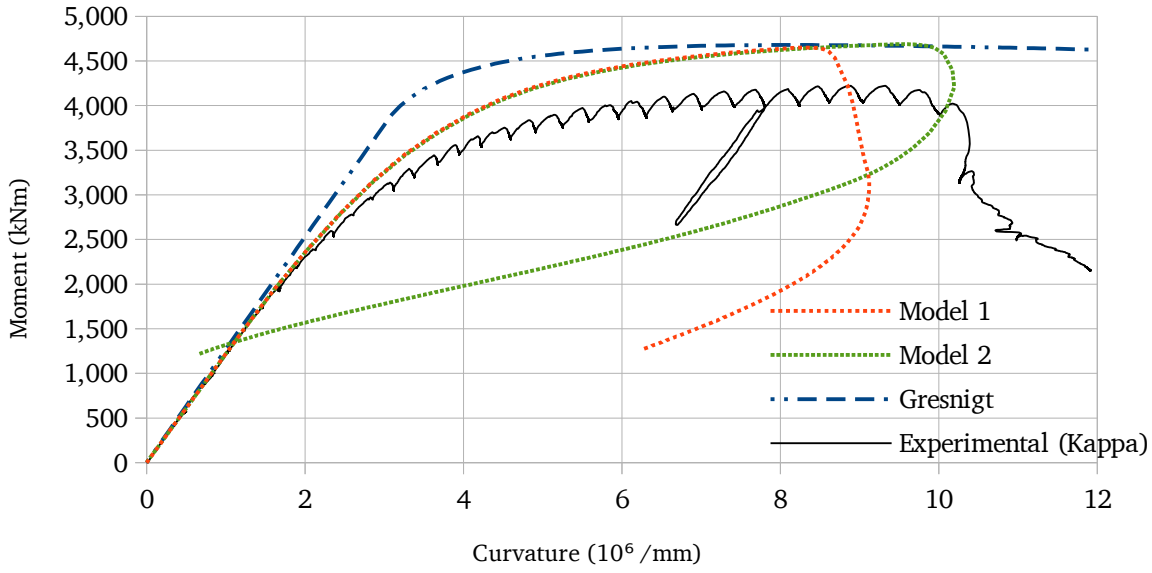

Figure 105: Moment-curvature relations for Tube 11: curv2

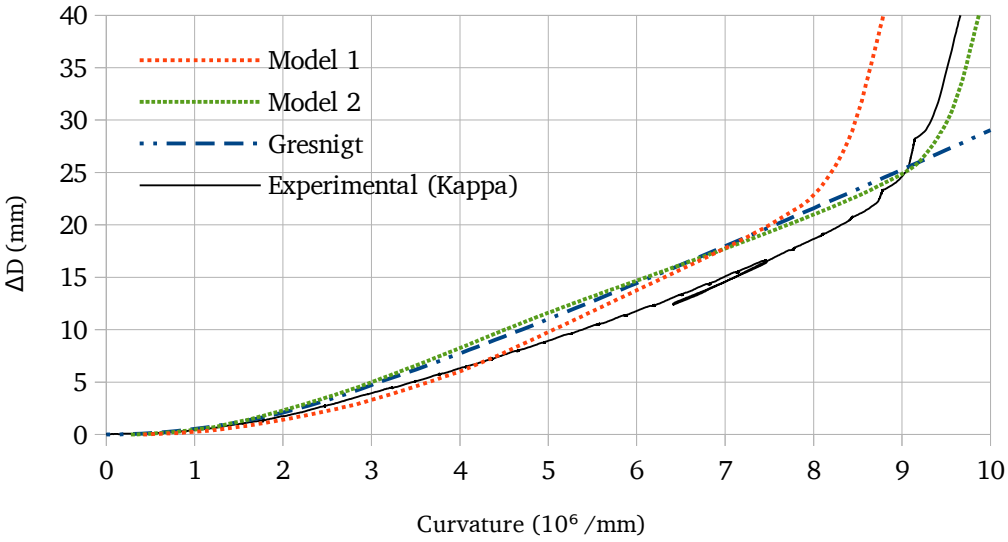

Figure 106: Ovalization-curvature relations for Tube 11: Buckling location (Kappa)

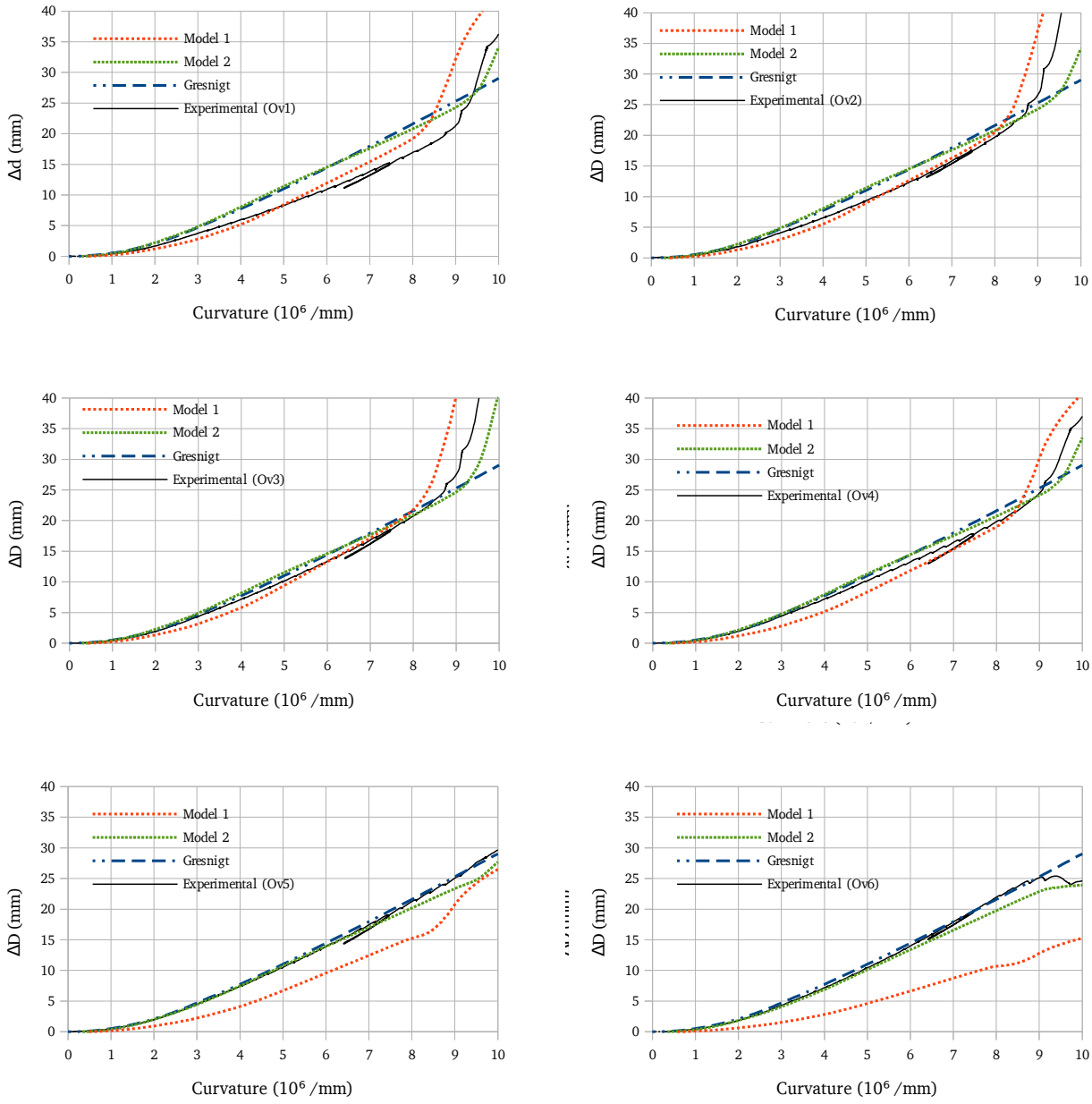

Figure 107: Ovalization-curvature relations for Tube 11: Ovalization brackets (Kappa)

5.5.12 Tube 12 Results

Tube 12 features both girth and coil connection welds. The left section is characterized by D/t = 117 and f_y = 430 MPa, the mid section is characterized by D/t = 116 and f_y = 116 MPa, and the right section is characterized by D/t = 117 and f_y = 430 MPa. An imperfection was introduced into the left section according to the shape shown in Figure 21 and 2w = 1.16mm. The final deformed shape is shown in Figure 108.

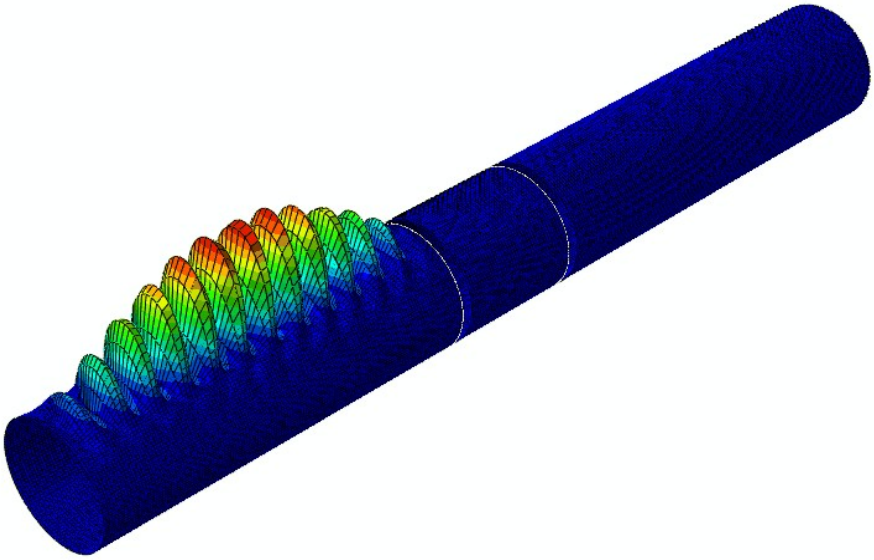

Figure 108: Imperfection shape of Tube 12

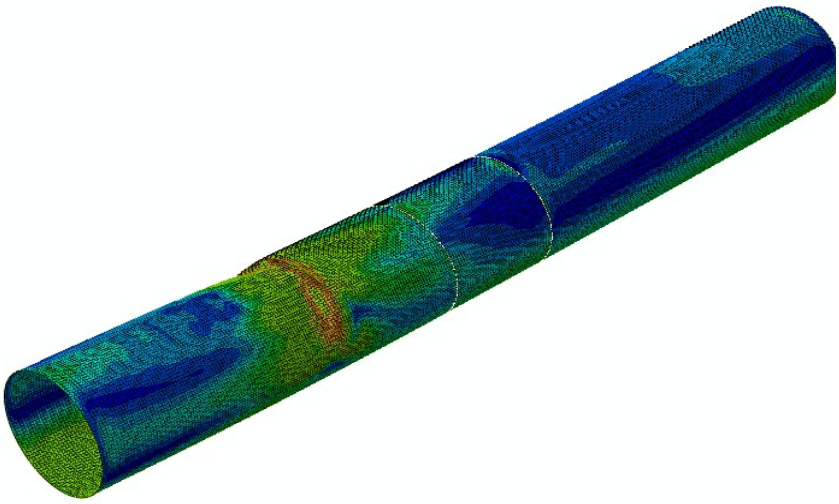

Figure 109: Deformed shape of Tube 12

Table 21: Tube 12 results

	k_{buck} (10^6 /mm)	k_{crit} (10^6 /mm)	M_{buck} (kNm)	M_{max} (kNm)
Model 1	6.03	6.03	3,722.8	3,722.8
Gresnigt	-	8.5	-	4,054.3
Experimental	5.59	5.59	3,435.3	3,435.3

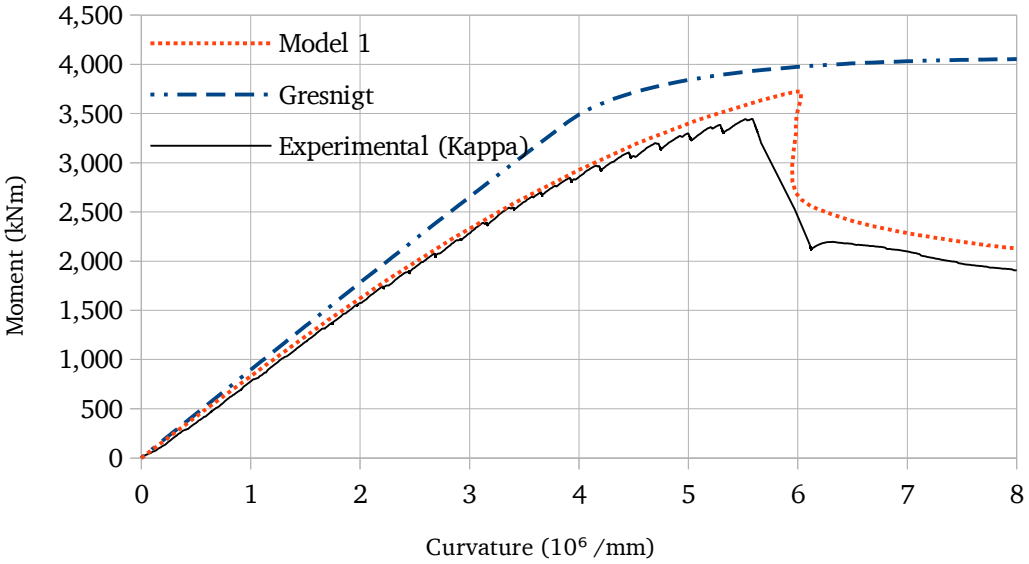

Figure 110: Moment-curvature relations for Tube 12: Kappa

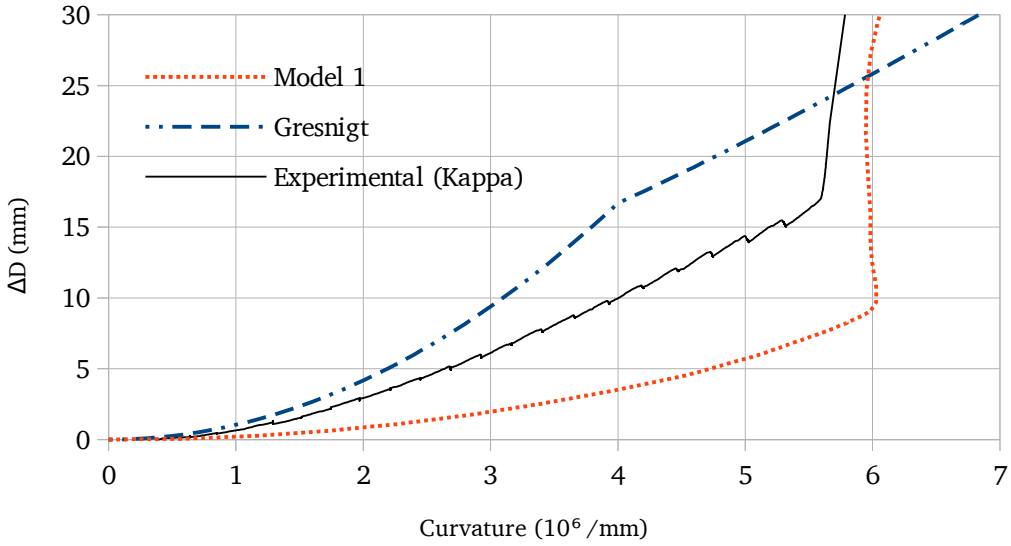

Figure 111: Ovalization-curvature relations for Tube 12: Buckling location (Kappa)

5.5.13 Tube 13 Results

Tube 13 is a spirally welded tube with a girth weld in the center. The left side is characterized by D/t = 118 and f_y = 425 MPa, and the right side is characterized by D/t = 116 and f_y = 445 Mpa. The tube is characterized by an offset of 0.5mm at the girth weld and an additional imperfection of 2w = 1.65mm.

Table 22: Tube 13 results

	k_{buck} (10^6 /mm)	k_{crit} (10^6 /mm)	M_{buck} (kNm)	M_{max} (kNm)
Model 1	5.54	5.54	3,628.0	3,628.0
Gresnigt	-	8.5	-	4,094.7
Experimental	5.15	5.15	3,393.2	3,393.2

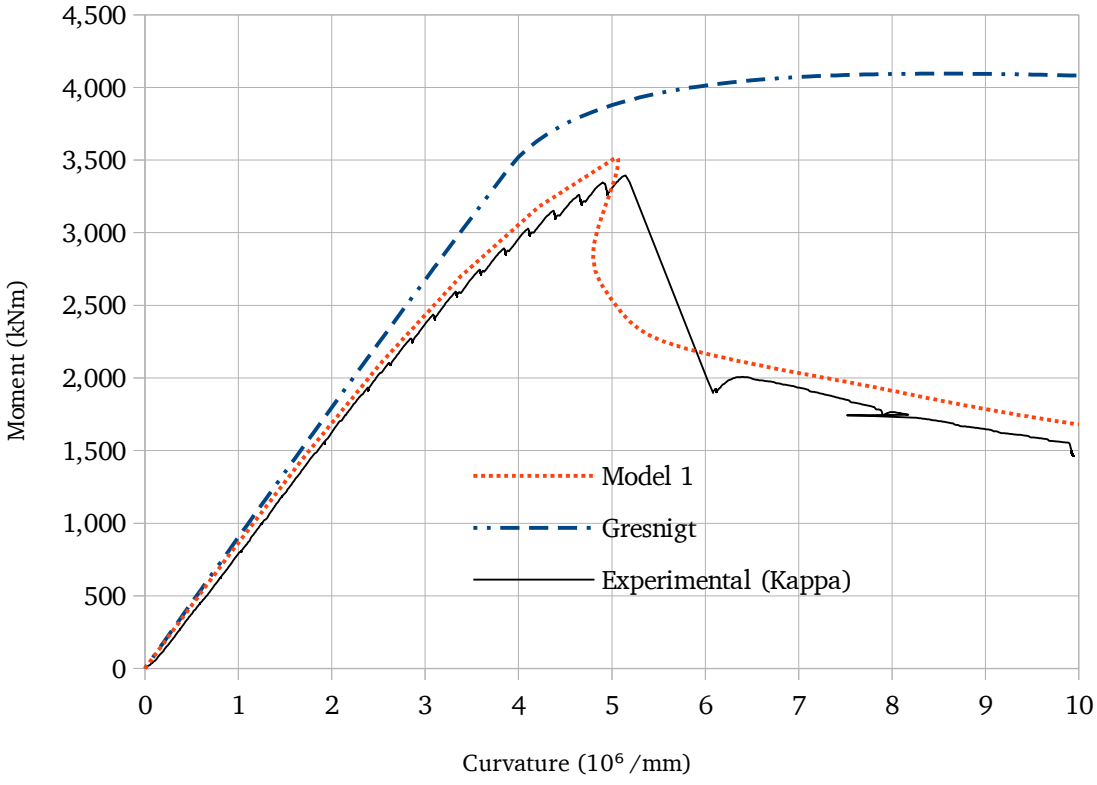

Figure 112: Moment-curvature relations for Tube 13: Kappa

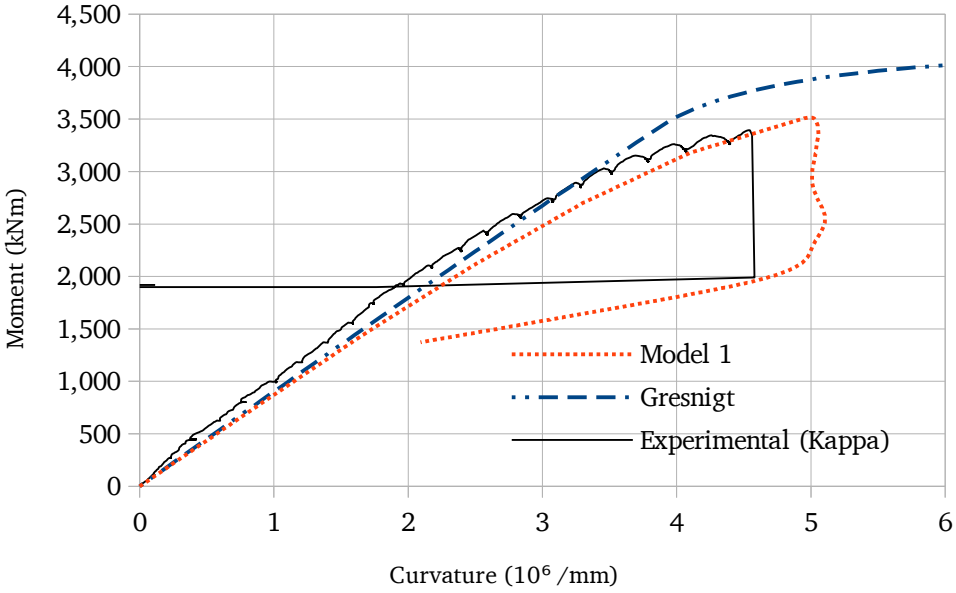

Figure 113: Moment-curvature relations for Tube 13: curv1

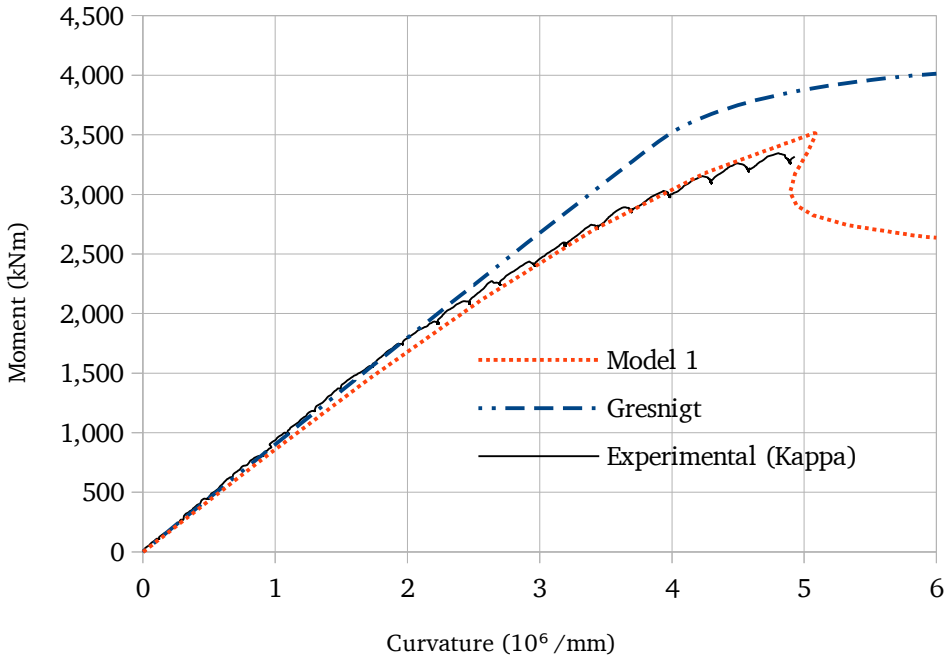

Figure 114: Moment-curvature relations for Tube 13: curv2

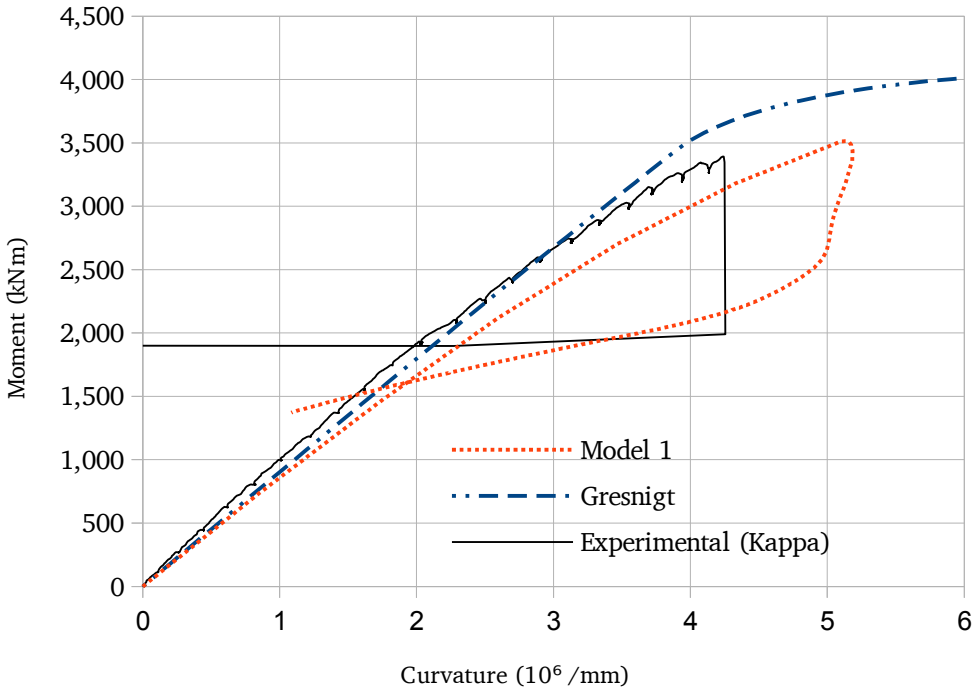

Figure 115: Moment-curvature relations for Tube 13: curv3

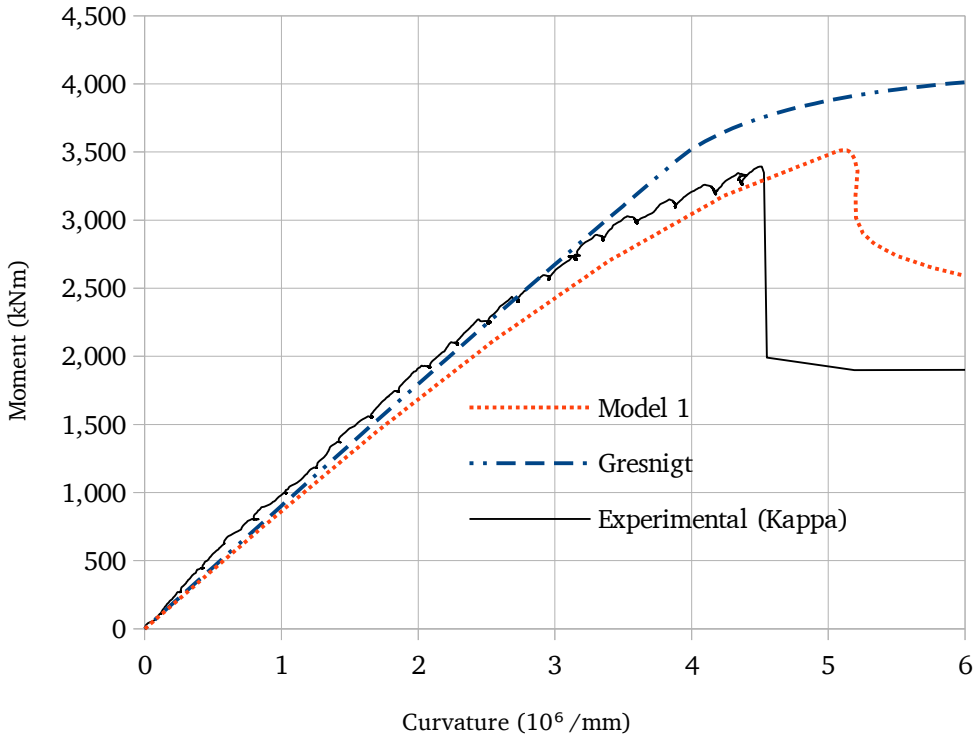

Figure 116: Moment-curvature relations for Tube 13: curvall

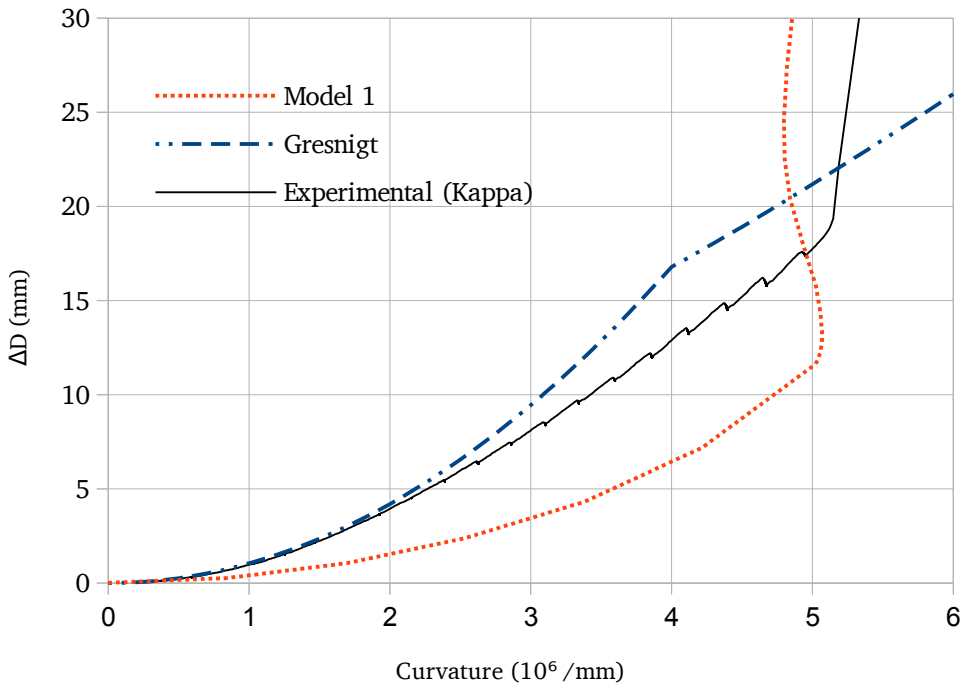

Figure 117: Ovalization-curvature relations for Tube 13: Buckling location (Kappa)

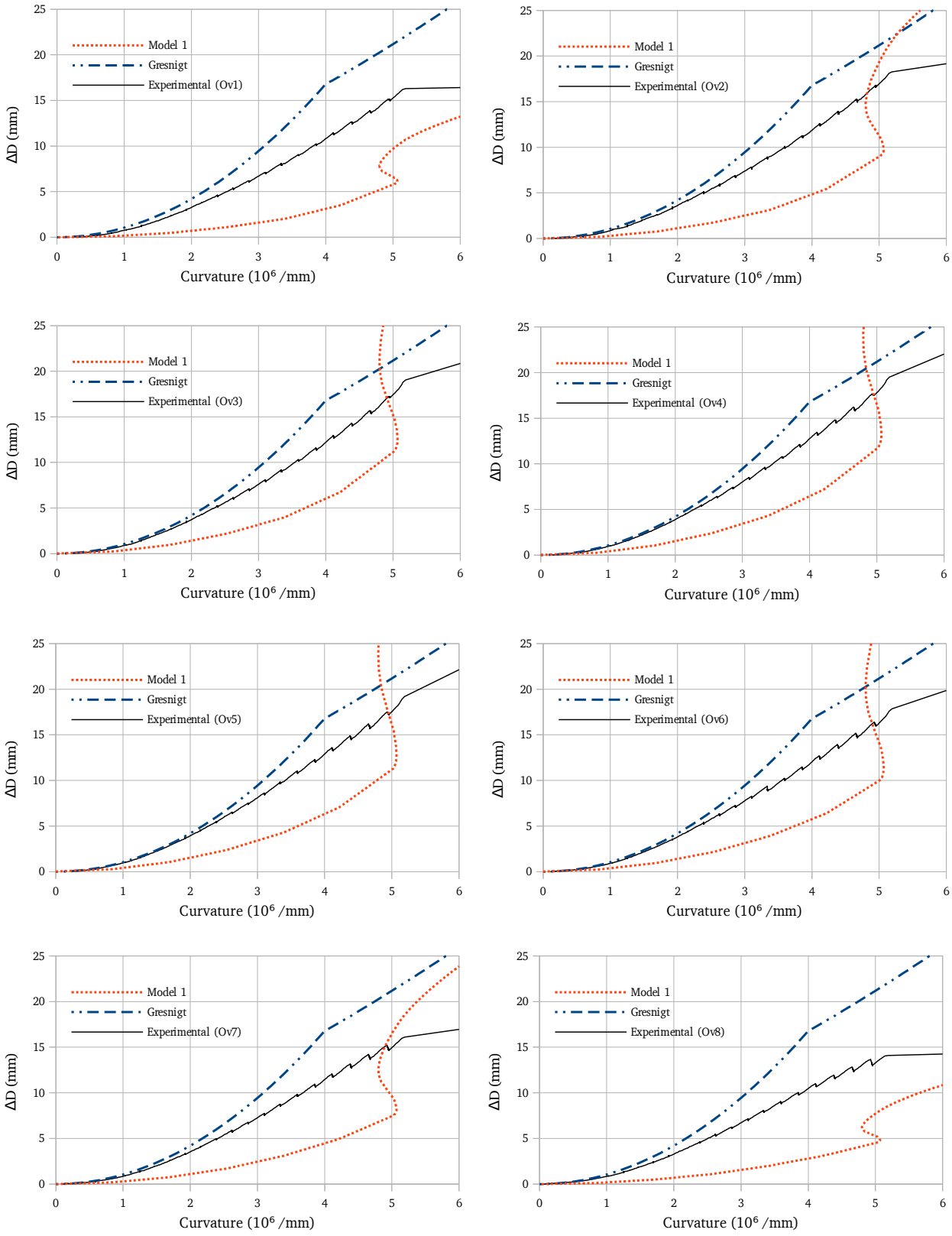

Figure 118: Ovalization-curvature relations for Tube 13: Ovalization brackets (Kappa)

5.5.14 Tube 14 Results

Tube 14 is a longitudinally welded tube characterized by D/t = 109, fy = 525 MPa, and 2w = 1.066mm.

Table 23: Tube 14 results

	k_{buck} (10^6 /mm)	k_{crit} (10^6 /mm)	M_{buck} (kNm)	M_{max} (kNm)
Model 1	6.65	6.65	4,532.8	4,532.8
Model 2	6.90	6.90	4,533.1	4,533.1
Gresnigt	-	9.9	-	5,212.2
Experimental	5.75	5.75	4,357.5	4,357.5

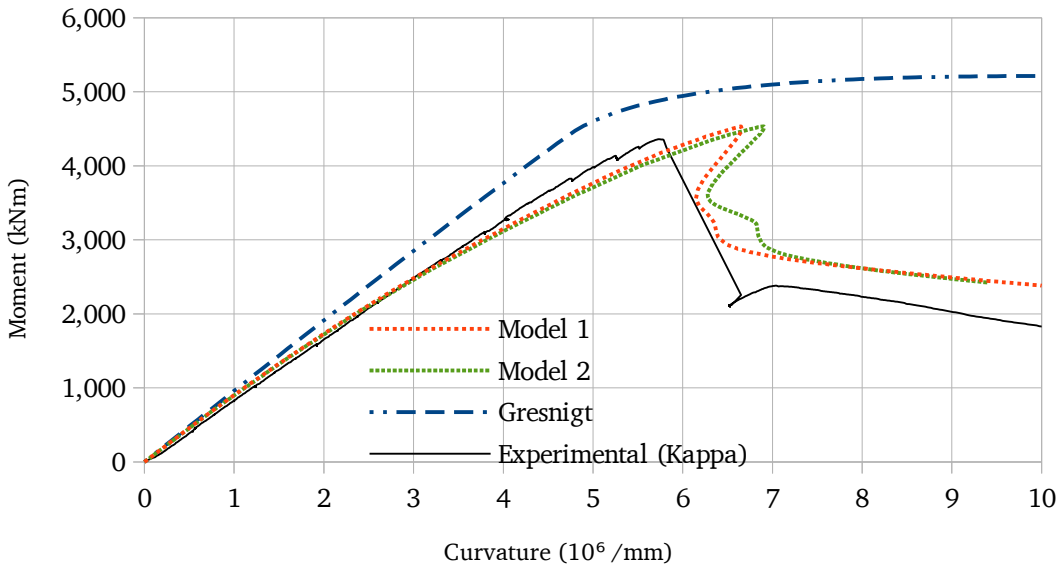

Figure 119: Moment-curvature relations for Tube 14: Kappa

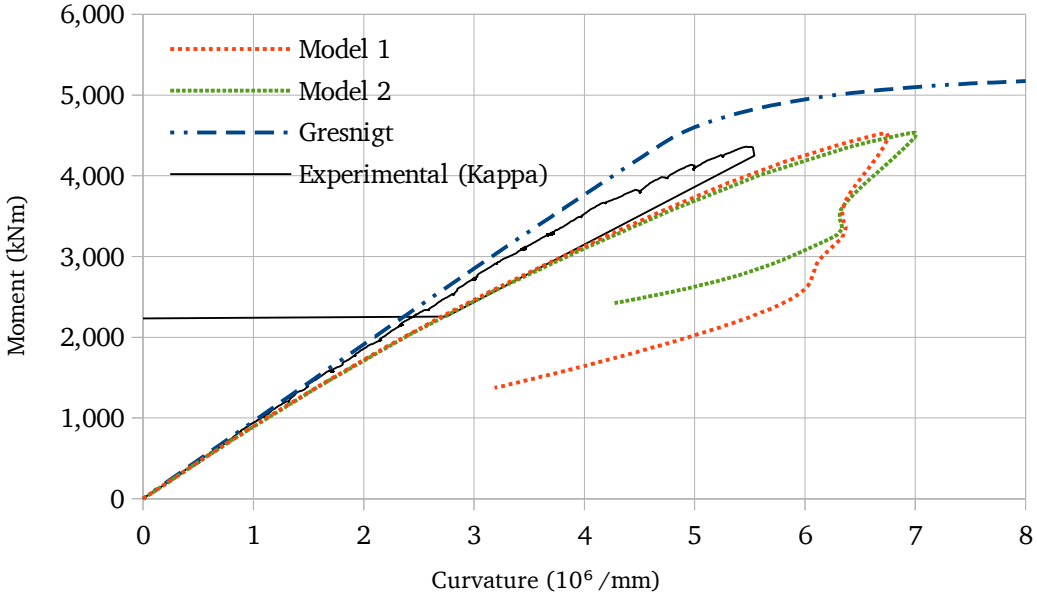

Figure 120: Moment-curvature relations for Tube 14: curv2

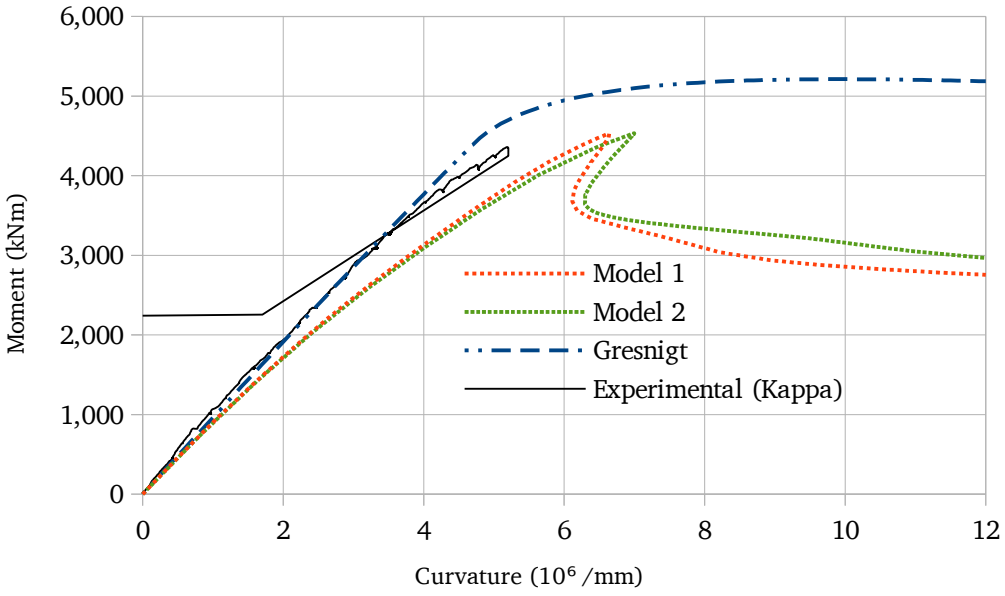

Figure 121: Moment-curvature relations for Tube 14: curv3

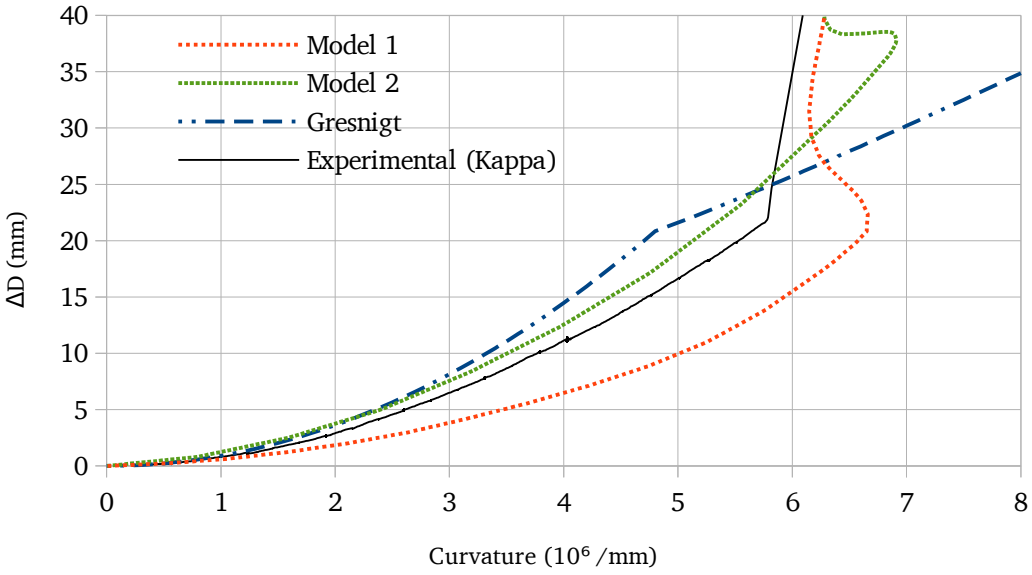

Figure 122: Ovalization-curvature relations for Tube 14: Buckling location (Kappa)

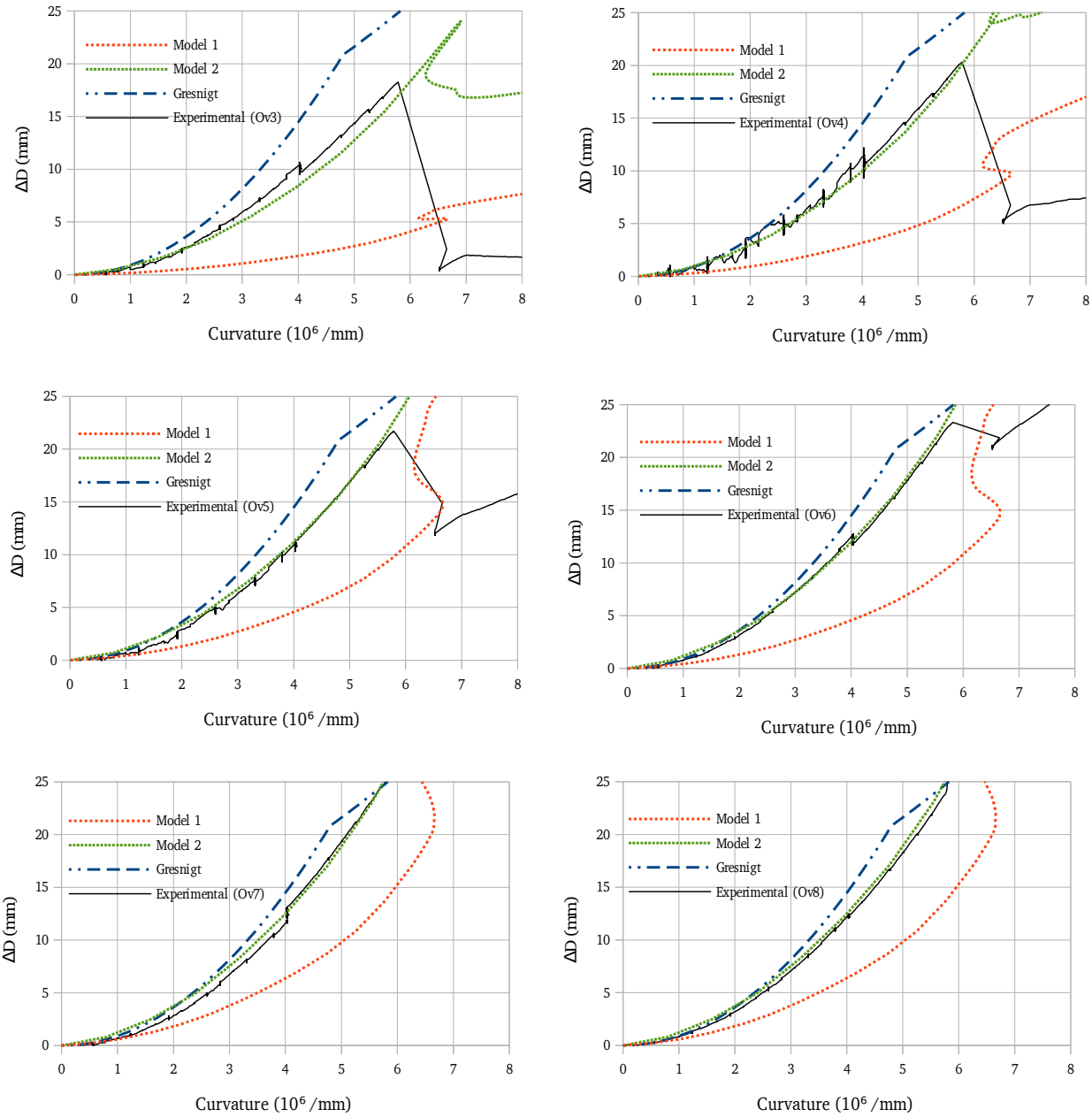

Figure 123: Ovalization-curvature relations for Tube 14: Ovalization brackets (Kappa)

5.5.15 Tube 15 Results

Tube 15 is a longitudinally welded tube characterized by D/t = 72, fy = 535 MPa, and 2w = 0.926mm.

Table 24: Tube 15 results

	k_{buck} (10^6 /mm)	k_{crit} (10^6 /mm)	M_{buck} (kNm)	M_{max} (kNm)
Model 1	10.26	10.26	8,076.8	8,076.8
Model 2	11.66	11.66	8,196.5	8,196.5
Gresnigt	-	11.5	-	8,308.9
Experimental	12.50	12.11	7,305.0	7,665.7

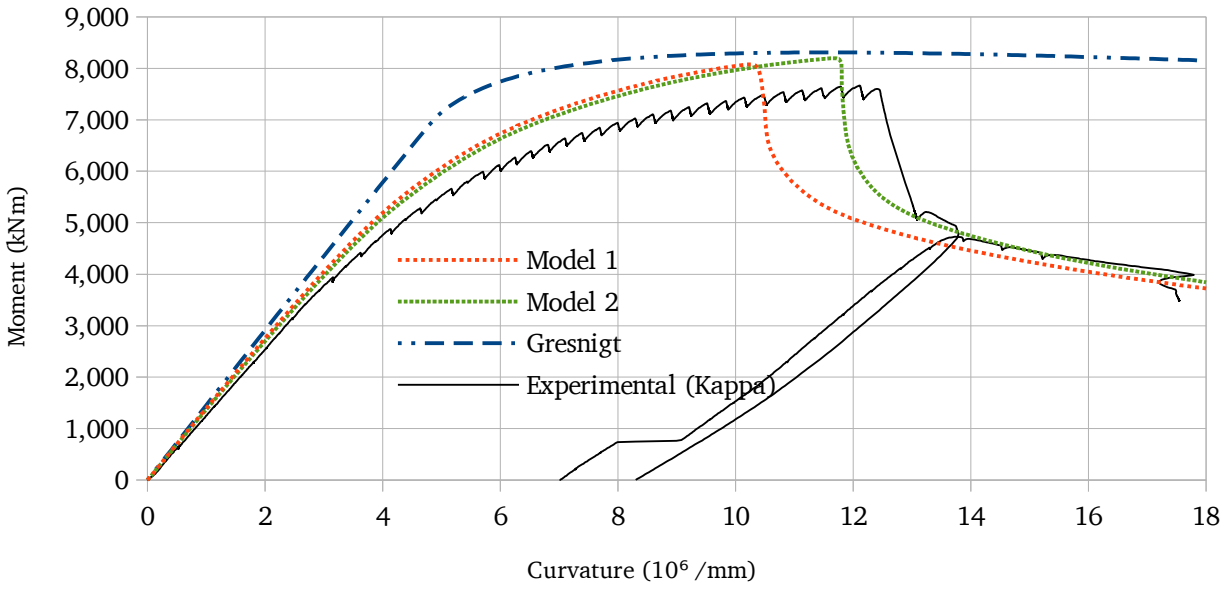

Figure 124: Moment-curvature relations for Tube 15: Kappa

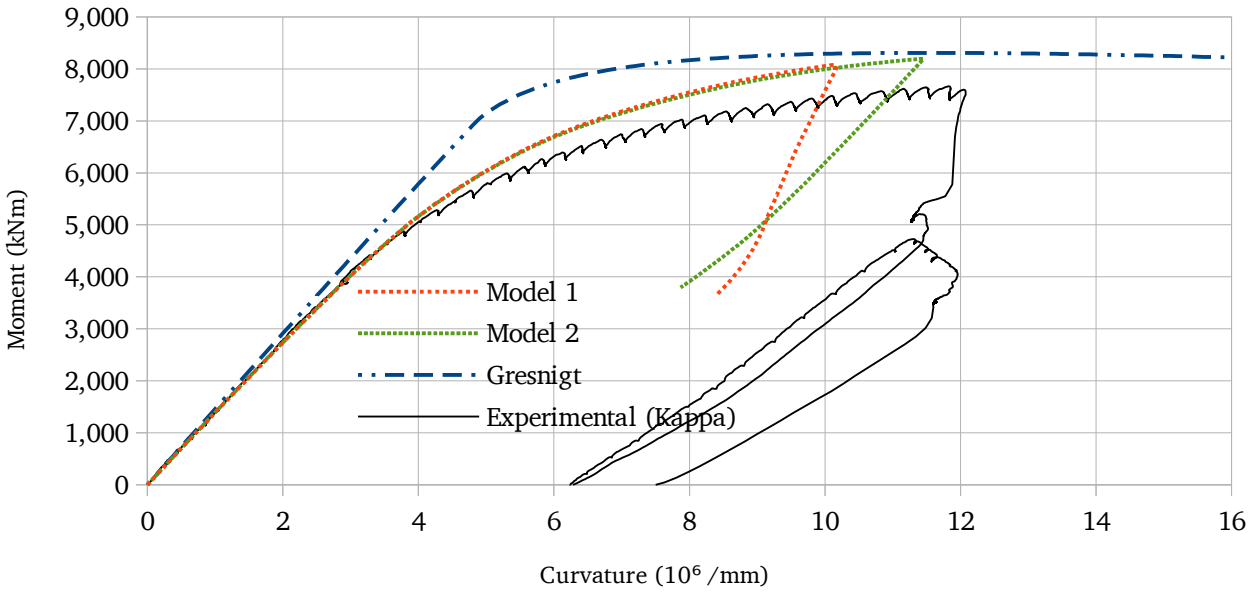

Figure 125: Moment-curvature relations for Tube 15: curv2

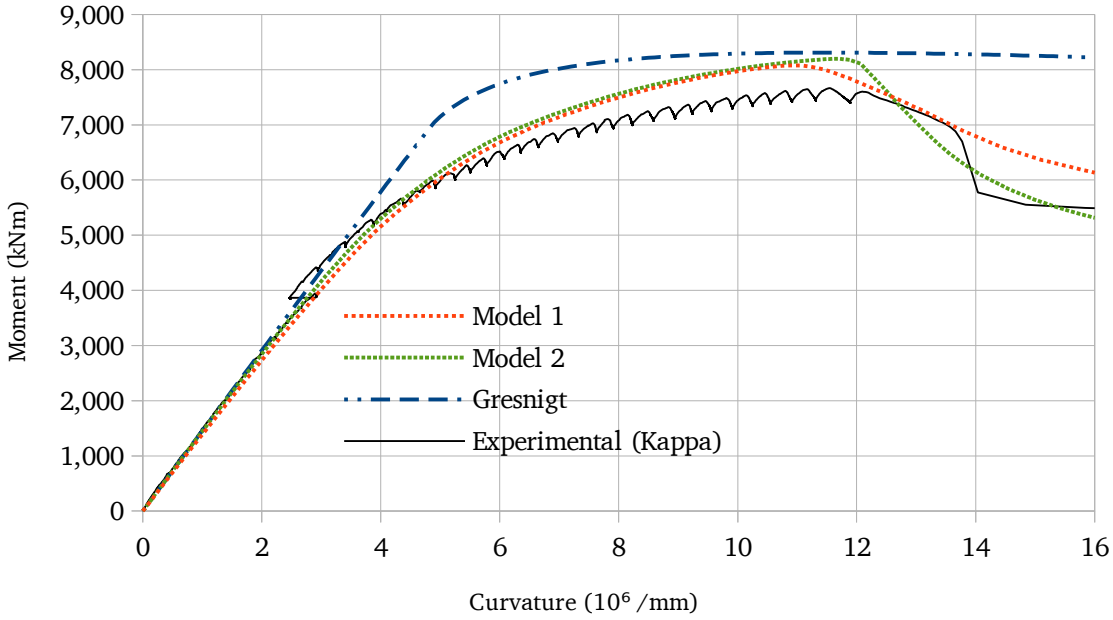

Figure 126: Moment-curvature relations for Tube 15: curv3

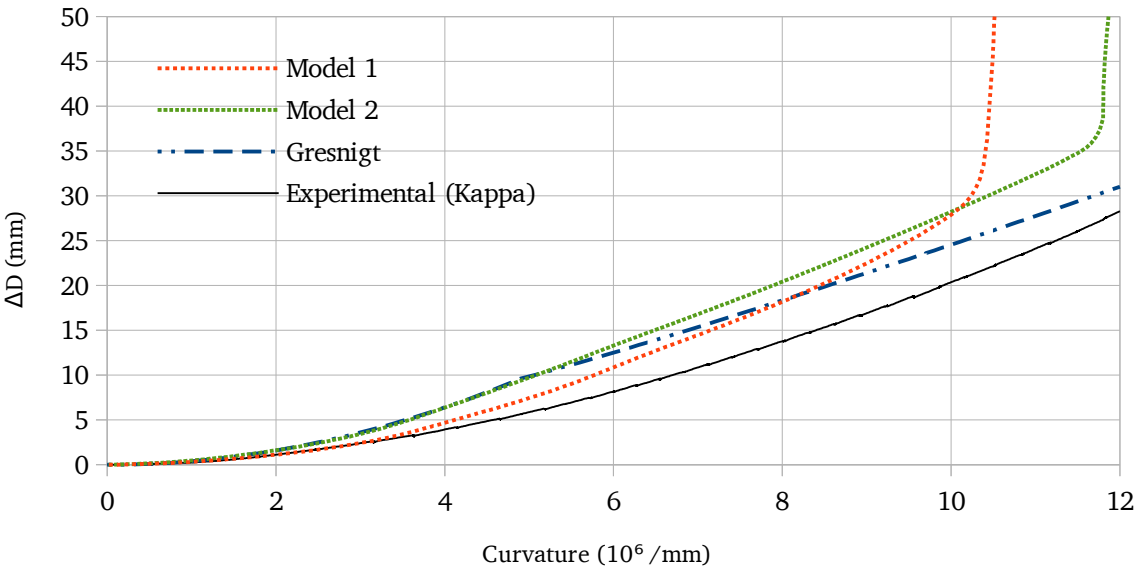

Figure 127: Ovalization-curvature relations for Tube 15: Buckling location (Kappa)

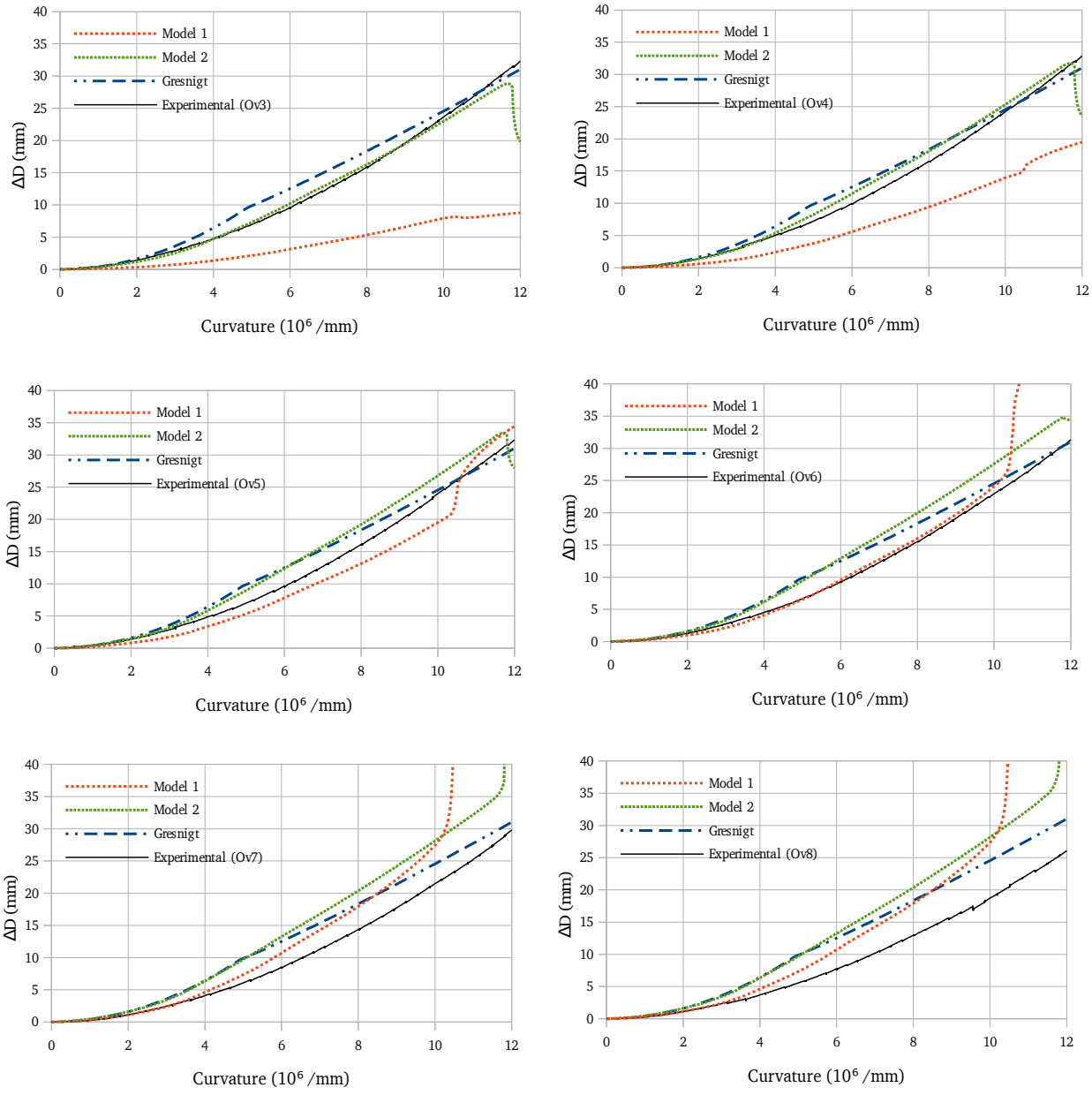

Figure 128: Ovalization-curvature relations for Tube 15: Ovalization brackets (Kappa)

5.5.16 Statistical Analysis of Results

In this section, the accuracies of the two FEM models as well as the analytical model are investigated. Figure 129 shows a plot of the predicted value of k_{crit} vs the experimental value for each model, and Table 25 shows the results of a regression analysis. Table 26 shows the results of a regression analysis from which the girth and coil connection welded tubes have been excluded.

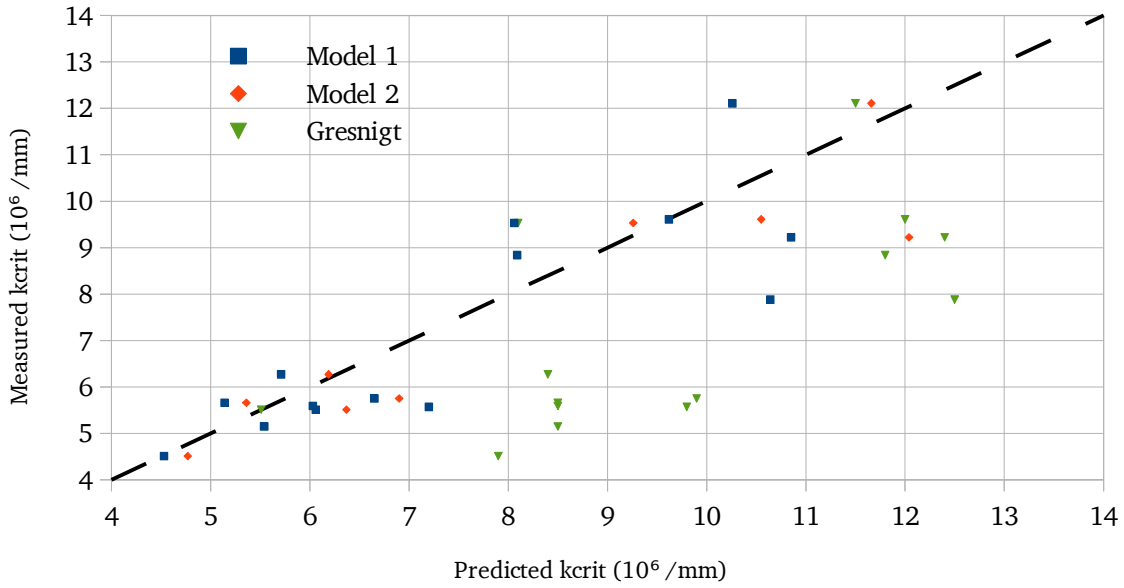

Figure 129: Accuracy of models for k_{crit}

Table 25: Regression analysis for k_{crit}: all tubes

	Model 1	**Gresnigt**
R^2	0.722	0.241
Standard Error (10^6 /mm)	1.32	1.88

Table 26: Regression analysis for k_{crit}: plain tubes

	Model 1	**Model 2**	**Gresnigt**
R^2	0.818	0.562	0.461
Standard Error (10^6 /mm)	1.18	1.67	2.03

The same data is presented below for M_{max}.

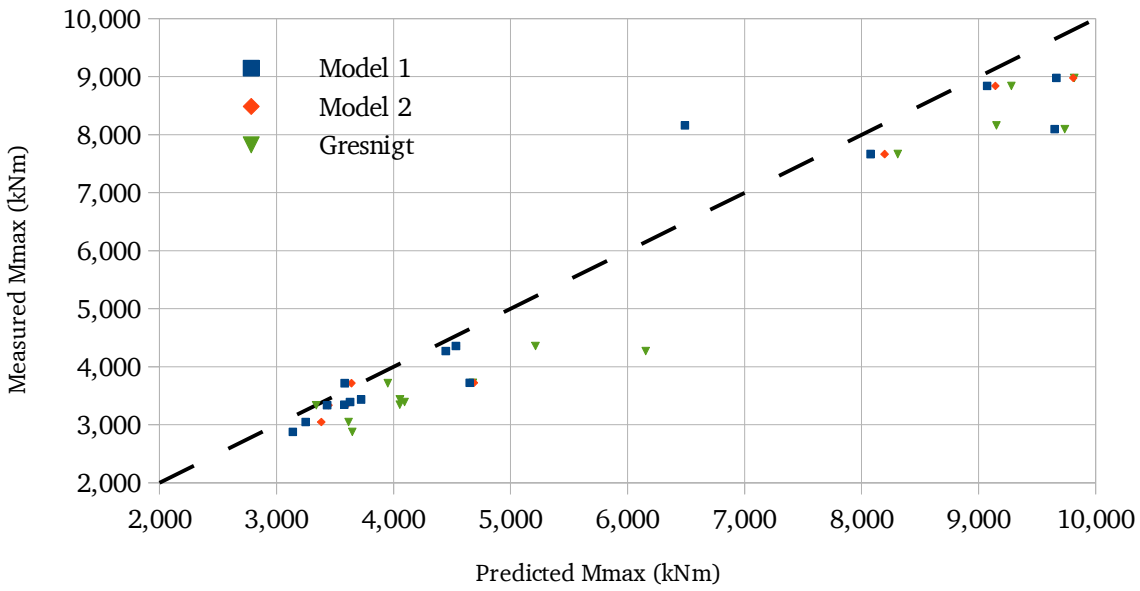

Figure 130: Accuracy of models for M_{max}

Table 27: Regression analysis for M_{max}: all tubes

	Model 1	**Gresnigt**
R^2	0.928	0.967
Standard Error (kNm)	666.4	450.9

Table 28: Regression analysis for M_{max}: plain tubes

	Model 1	**Model 2**	**Gresnigt**
R^2	0.987	0.986	0.986
Standard Error (kNm)	309.3	314.6	316.9

5.5.17 Propagation of End Effects

In this section, the ovalization of the tube in the FEM model is compared to the ovalization measured during testing. The data from the curvature brackets and the FEM models has been used to plot the ovalization of the tubes along the length of the tube for Tubes 1, 5, and 11. The ovalization profiles have been plotted for two curvatures: first at k=1.5 *10^6 /mm and then at k=3.6 *10^6 /mm.

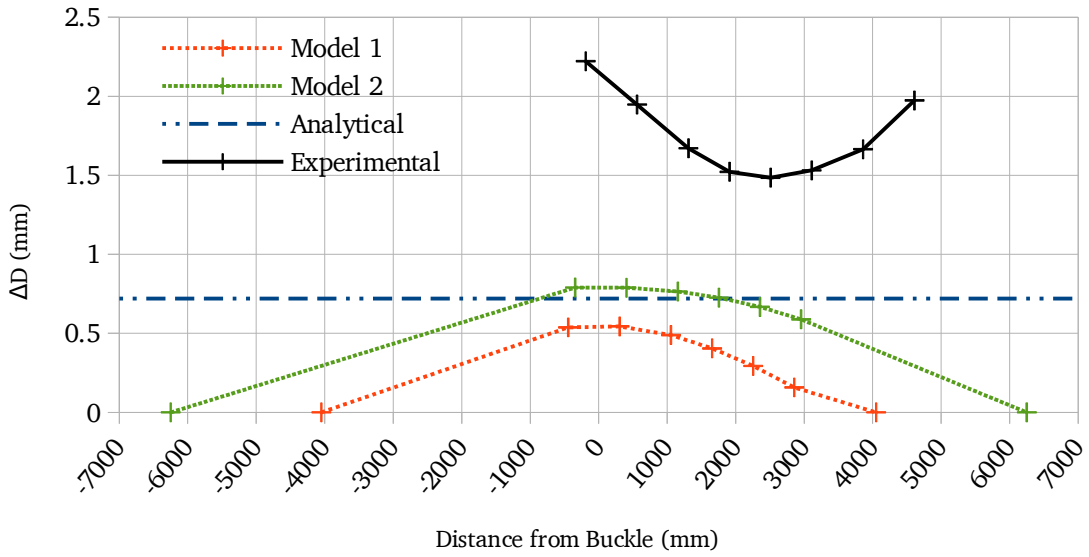

*Figure 131: Ovalization profile of Tube 1 at k=1.5 *10^6 /mm*

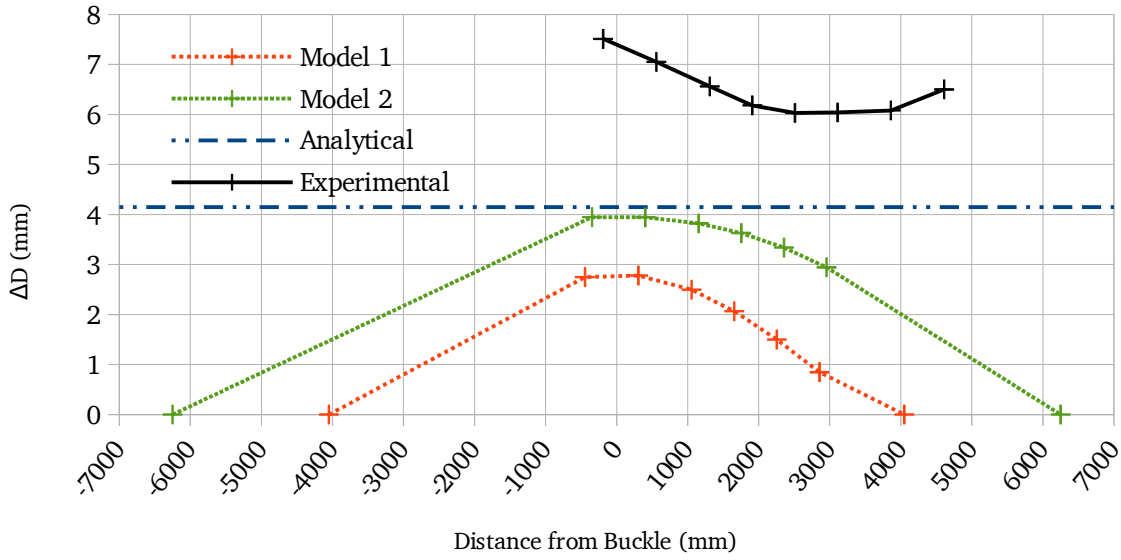

*Figure 132: Ovalization profile of Tube 1 at k=3.6 *10^6 /mm*

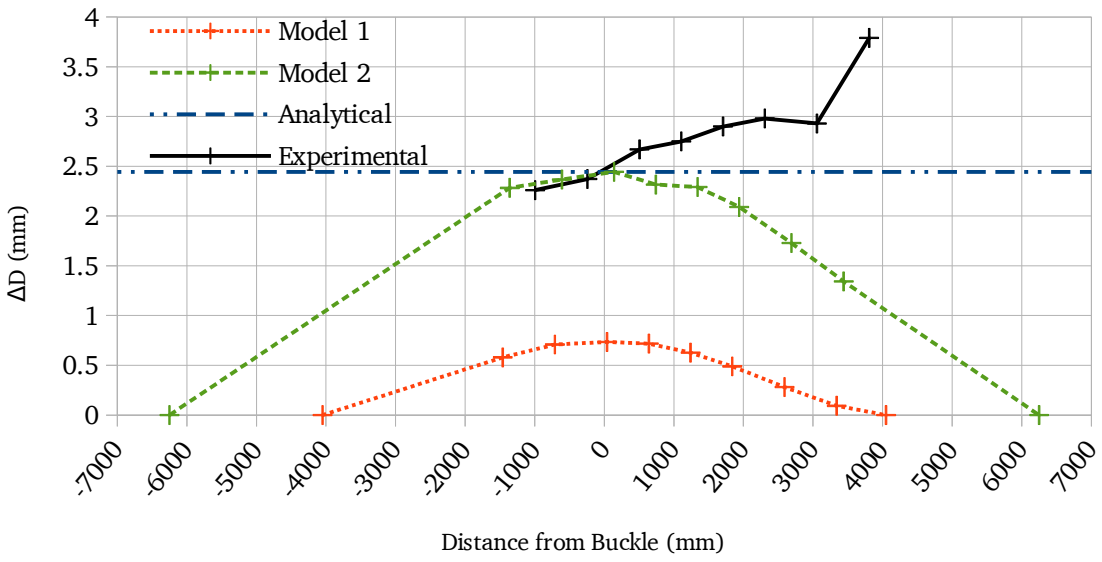

*Figure 133: Ovalization profile of Tube 5 at k=1.5 *10⁶ /mm*

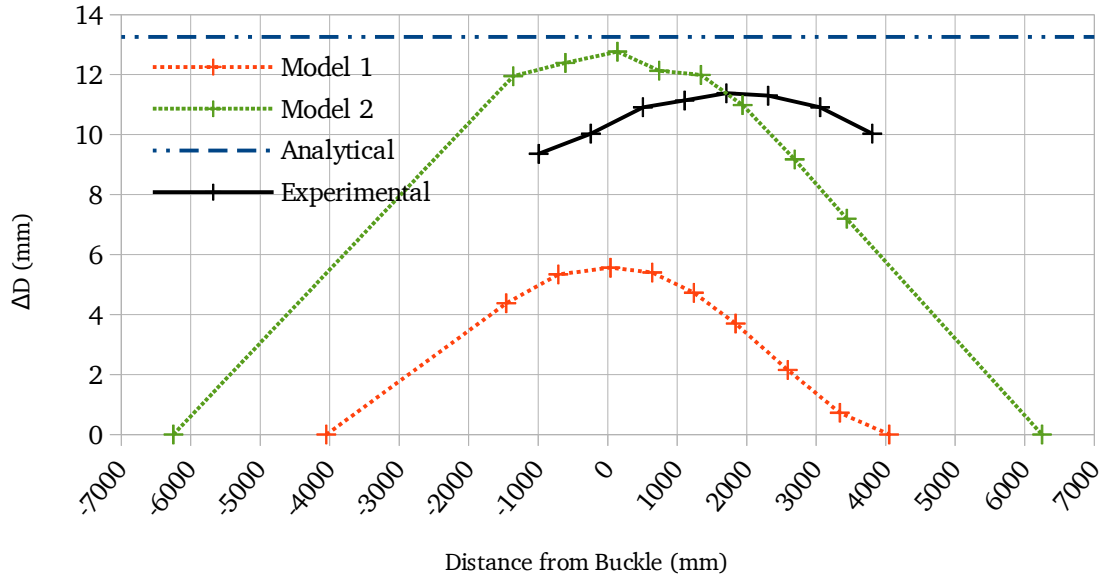

*Figure 134: Ovalization profile of Tube 5 at k=3.6 *10⁶ /mm*

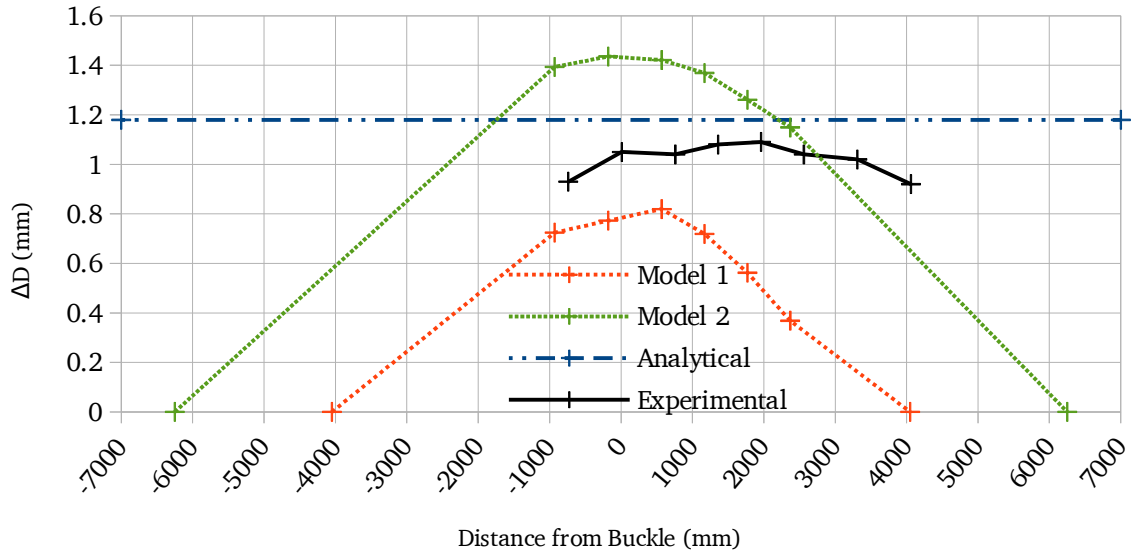

*Figure 135: Ovalization profile of Tube 11 at k=1.5 *10⁶ /mm*

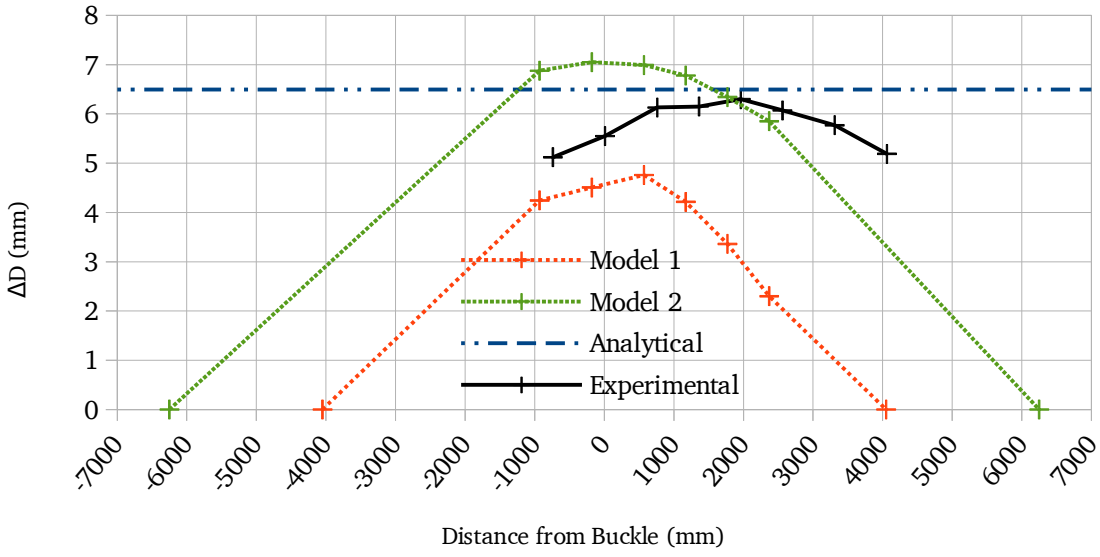

*Figure 136: Ovalization profile of Tube 11 at k=3.6 *10⁶ /mm*

5.5.18 Discussion

For Tube 1, there is excellent agreement between the models and the experimental data in the pre-buckling equilibrium path. Model 1 shows good agreement with k_{crit} and M_{max}, while Model 2 overestimates the buckling point. There is also very good agreement with both models in terms of curv1 and curv2. In terms of ovalization, Model 1 slightly underestimates the analytical solution, Model 2 matches it almost perfectly, and all models underestimate the measured ovalization. This is because for Model 1, the support straps were oriented in such a way that increasing force actually increased the ovalization rather than supporting the tube neutrally. Finally, the ovalization bracket data shows that the end effects are insignificant for Model 2 because the ovalization matches the analytical solution very closely in all cases, while for Model 1 the ovalization is significantly affected, especially for OV5 and OV6.

For Tube 2, the accuracy of the FEM models is also generally good in terms of moment and curvature. There is good agreement in the pre-buckling equilibrium path, but k_{crit} is slightly underestimated by Model 1 and M_{max} is overestimated by both models. The agreement is relatively good in terms of the curvature brackets. The ovalization is much more restrained at the buckle than it was for Tube 1, so end effects may be at play here. Ovalization is significantly underestimated by Model 1 at all ovalization bracket locations, while it is also slightly underestimated by Model 2 at OV1-OV4 and significantly understimated by Model 2 at OV5 and OV6. Tube 2 has a much higher D/t ratio than Tube 1 so it is expected that ovalization is more restrained.

For Tube 3, only Model 1 was considered. The FEM model deviates from the elastic solution at a relatively low curvature, which may indicate that the material properties, and thus the residual stress ratio, may not accurately represent the properties of the tube. It may also indicate that there is an interaction between the properties on either side of the girth weld. Since Tube 3 has a high D/t ratio, the ovalizations are also significanty under-estimated at all locations. However, the equilibrium paths generall show good agreement, although the ovalization is significantly restrained in the FEM model. The analytical and experimental ovalization-curvature curves agree well.

Tube 4 shows very good pre-buckling moment-curvature agreement, but k_{crit} is underestimated by Model 1. Interestingly, the post-buckling behavior is different between the models for curv1 and curv2. End effects are again evident, because the experimental ovalization is significantly underestimated by Model 1 at all locations. Model 2 shows quite good agreement in terms of both moment-curvature and ovalization-curvature.

For Tube 5, the overall moment-curvature agreement is good for both models, however, k_{crit} is significantly overestimated by both models in curv1, curv2, curv3, and curvall. Model 1 also shows a significant deviation from the elastic line in curv3. It was thought that this may have been due to an error in the measurement locations in the FEM model, but these locations were double-checked and found to be accurate. It is therefore unclear where this deviation comes from. In terms of ovalization, Model 2 shows excellent agreement while Model 1 shows significant end effects.

For Tube 6, the FEM model buckled at the coil connection weld just as it did during the experiment. However, the k_{crit} is significantly underestimated by the model. For this tube, an intermediate imperfection was chosen at the coil connection weld, and this result shows that this imperfection is likely an overestimate. The analytical solution significantly overestimates the experimental solution, which again may be due to the fact that the properties on either side of the girth weld were averaged together to do the calculation, which is an urealistic but necessary assumption.

For Tube 7, the FEM buckling location matches the experimental buckling location, and the pre-buckling equilibrium path shows good agreement. The FEM model significantly overestimates both k_{crit} and M_{max}. This suggests that the intermediate imperfection amplitude chosen likely underestimates the actual imperfection at the buckling location. It is thought that perhaps setting the imperfection amplitude equal to the height of the spiral weld would give better results.

For Tube 8, the two FEM models show good agreement with each other as well as with the experimental results. Both models also show good agreement in terms of the curvature brackets. However, significant end effects are evident in Model 1, as shown in the ovalization-curvature diagrams in Figure 92. The fact that the moment-curvature curves agree well despite the fact that ovalization is restrained in Model 1, combined with the fact that the behavior of the models does not stabilize when the tube length increases (Figure 39), strongly suggests that the difference between Models 1 and 2 is not only due to end effects, but due to other effects as well, likely geometrical.

More evidence for this is seen with Tube 9, where there is a very significant deviation between the two FEM models in terms of moment and curvature, but a small difference in terms of ovalization. For this tube, both models overestimate k_{crit}, but Model 2 overestimates it much more than Model 1 does. Model 1 generall shows good agreemenet with the experimental data for this tube, while Model 2 overestimates k_{crit} and M_{ma} somewhat.

For Tube 10, the pre-buckling agreement is very good, but k_{crit} is once again overestimated. This is likely due to the chosen imperfection height. The analytical solution also significantly overestimates the experimental one, once again likely due to the fact that the analytical solution cannot take two different yield strenghts into account. Low ovalization restraint is observed at the buckling location.

For Tube 11, all models overestimate the experimental equilibrium path in terms of moment. Tube 11 had very poor material properties and significant pitting due to rust, which may explain the poor agreement for this tube. However, the ovalization was found to agree well at the buckling location.

For Tube 12, the FEM model shows very good agreements in terms of moment and curvature, but poor agreement in terms of ovalization. The analytical solution also over-estimates the ovalization of the physical tube. It is unclear why this occurred but it is possible that it is due to ovalization restraint during experimental testing.

Tube 13 shows excellent agreement between the FEM model and the experimental moment-curvature data, although the elastic line is underestimated for curv1 and curv3. As with Tube 5, it is unclear why this occurred. The ovalization restraint observed with Tube 13 is significant.

For Tube 14, as with Tube 8, there is good agreement between the two FEM models in terms of moment and curvature. There is also good agreement between the models and the experimental data, although both models underestimate the experimental data for curv1 and curv2. Ovalization is restrained at all locations for Model 1 but not significantly restrained for Model 2.

For Tube 15, there is again a significant difference between the behavior of the two models. The overall pre-buckling equilibrium paths agree relatively well, but k_{crit} and M_{max} are underestimated by both models. Ovalization is somewhat restrained with Model 1 and not significantly restrained with Model 2.

In general, both models could predict k_{crit} significantly better than the analytical solution could, but neither model provided any improvement in terms of predicting M_{max}. When all tubes were considered, Model 1 actually performed worse than the analytical solution, even though the analytical solution was based on average material and geometrical properties. In the case where all tubes were considered, the standard error for k_{crit} was improved from 1.88 $*10^6$ /mm to 1.32 $*10^6$ /mm and the correlation R^2 was improved from 0.241 to 0.722. The standard error for M_{max} was reduced from 450.9 kNm to 666. kNm and the correlation worsened from 0.967 to 0.928.

When only the plain tubes were considered, the standard error for k_{crit} improved from 2.03 to 1.18 $*10^6$ /mm for Model 1 and to 1.67 $*10^6$ /mm for Model 2. R^2 improved from 0.461 to 0.818 and 0.562, respectively. For M_{max} the standard error was reduced from 316.9 kNm to 309.3 kNm for Model 1 and to 314.6 kNm for Model 2. The improvements in M_{max} are virtually insignificant.

The accuracy of the predictions for M_{max} were strongly influenced by three outliers: Tubes 6, 11, and 15. Tube 6 buckled near a coil connection weld, and an intermediate imperfection was introduced based on the overall imperfection profile near the buckle (see Figure 231). The result for Tube 6 suggests that this is not the most representative way to introduce imperfections in this case, and it is thought that if a larger imperfection were introduced, the accuracy of the prediction would increase.

For Tubes 11 and 15, the over-estimation is simply due to the material model used, because it is known that variations in the material model shift moment-curvature curves up or down. It is noted that for Tube 11, the quality of the material was very poor, with significant rusting and pitting, which likely contributes to the error.

The propagation of end effects section shows that Model 1 underestimates the ovalization at the buckle for Tubes 1, 5, and 11, but the distribution of ovalization along the tube length is similar for both models. In other words, the ovalization of both models is restrained away from the buckle. The results in this section also confirm that end effects depend on D/t. Figures 133 and 134 show a very significant difference between Models 1 and 2 for Tube 5, while Figures 131 and 132 show a much lower difference for Tube 1, which is thicker. Finally, it can be seen that the experimental solution is close to the analytical solution for all tubes except for Tube 1, where the measured experimental ovalizations are significantly greater. This is due to the fact that for Tube 1 the mid support straps were oriented in such a way that they actually increased the ovalization upon an increase in reaction force rather than supporting the tube neutrally.

5.6 Conclusions and Recommendations

Judging by the individual results of the FEM models, they appear to be quite good. The pre-buckling equilibrium paths agree well with the experimental data. In terms of k_{crit}, the standard error was reduced from 1.88 $*10^6$ /mm with the analytical solution to 1.32 $*10^6$ /mm with Model 1 when all tubes were considered. When only the plain tubes were considered, the improvement was from 2.03 to 1.18 $*10^6$ /mm with Model 1 and to 1.67 $*10^6$ /mm with Model 2. The correlations R^2 also increased significantly, suggesting that the FEM models can predict the experimental results more accurately than the analytical solution.

The improvement in k_{crit} is significant, especially with Model 1, but a standard error of 1.32 $*10^6$ /mm is still quite poor, especially considering that many of the thin tubes failed at curvatures around 5 $*10^6$ /mm. In order to improve the model further, it is thought that the initial imperfections would have to be incorporated in a more representative way, especially for the girth welded and coil connection welded tubes and the tubes which buckled at spiral welds. It is also thought that the model may be improved by modeling the residual stresses more accurately and accounting for the effects of residual stresses other than those caused by the forming process.

In terms of M_{max}, when all tubes were considered, the standard error was increased from 450.9 kNm to 666.4 kNm with Model 1. When only plain tubes were considered, it improved from 316.9 kNm to 309.3 kNm with Model 1 and to 314.6 kNm with Model 2. This result suggests that the FEM model provides no improvement in estimating M_{max} over the analytical model, and that it is actually worse at estimating M_{max} for girth and coil connection welded tubes. This is a surprising result given that the material and geometric properties were simply averaged for the analytical solution, however, it was found that Model 1 was affected by a significant outlier: Tube 6. If this tube were removed from the results, Model 1 would estimate M_{max} more accurately than the analytical solution. In any case, all models provided sufficient accuracy in terms of M_{max}.

Overall, it is shown that Model 1 performs better than Model 2, because a higher correlation and a lower standard error is found in all cases. It is also concluded that M_{max} is much easier to predict than k_{crit}. Due to the fact that the analytical solution was just as accurate as the FEM models in estimating M_{max}, it is suggested that elastic-perfectly-plastic material models may be sufficient to estimate M_{max} accurately, although this was not investigated with the FEM models.

It is also thought that end effects do not significantly influence M_{max} or k_{crit}. No pattern was observed in the accuracy in the ovalization-curvature relations as compared to the moment-curvature relations, and, as suggested in Section 5.2.2, it is thought that Model 2 suffers from serious geometrical effects and should be used with caution. However, it is acknowledged that further investigation is necessary to confirm this; in particular, it is suggested that a model should be designed with supports that allow for free ovalization at the ends.

Finally, it is suggested that there may be an inconsistency in the correlation between strain and curvature, and therefore an error in using curvature as a measure of strain. It is shown that Models 1 and 2 buckled at different strains but at very similar stresses, suggesting that a critical stress may be more relevant than a critical strain, even if yielding occurs.

6 Parameter Studies

Parameter studies were carried out by varying some of the geometrical and material parameters used to describe spirally welded tubes. The goals of these studies were to identify which parameters have the largest effect on the behavior and to characterize the sensitivity of the tubes to these parameters.

In the first part of this section, the effects of the imperfection height 2w, the residual stresses f_{resid}/f_y, and D/t are investigated by varying these parameters for three of the real tubes: Tubes 1, 5 and 11. These tubes were chosen becaues they represent a wide range of D/t ratios and material properties. The properties of these tubes are summarized in Table 29.

Table 29: Properties of physical tubes used for parameter studies

Tube	**D/t**	**f_y (MPa)**	**k_y (10^6 /mm)**	**M_p (kNm)**
1	65	540	4.94	9,757.1
5	118	400	3.65	4,052.7
11	83	340	3.11	4,882.9

In the second part of this section, a three-variable parameter study is conducted, based on wide range of D/t ratios, imperfection heights, and yield stresses in various combinations. The results were also used to determine the most favorable combinations and the parameters which have the most significant influence on the capacity of the tubes.

In this section, the overall curvature Kappa is always used, and all ovalizations are reported at the buckling location. Moments and curvatures are generally normalized with M_p and k_y.

6.1 Influence of Residual Stresses

6.1.1 Approach and Methods

Residual stresses were investigated by varying the yield stress used to calculate the residual stress distribution (see Figure 35). For each tube, the residual stress ratios f_{resid}/f_y were varied between 0 and 1.2. The actual material properties of the tubes were not varied: the yield stresses were only used to vary the residual stress distribution.

First, a selection of results has been used to plot moment-curvature and ovalization-curvature paths for each tube in order to qualitatively show the effect of residual stresses. Then, the effects of residual stresses on k_{crit} and M_{max} specifically are shown by plotting the residual stress ratios f_{resid}/f_y against k_{crit}/k_y and M_{max}/M_p.

6.1.2 Results

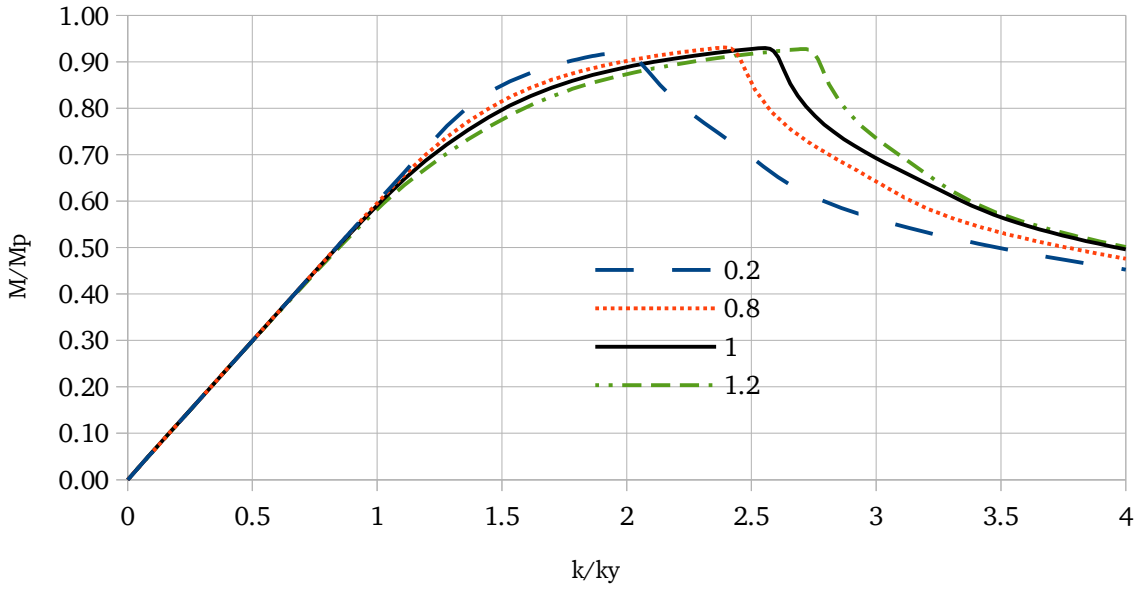

Figure 137: Effect of residual stresses on equilibrium path of Tube 1

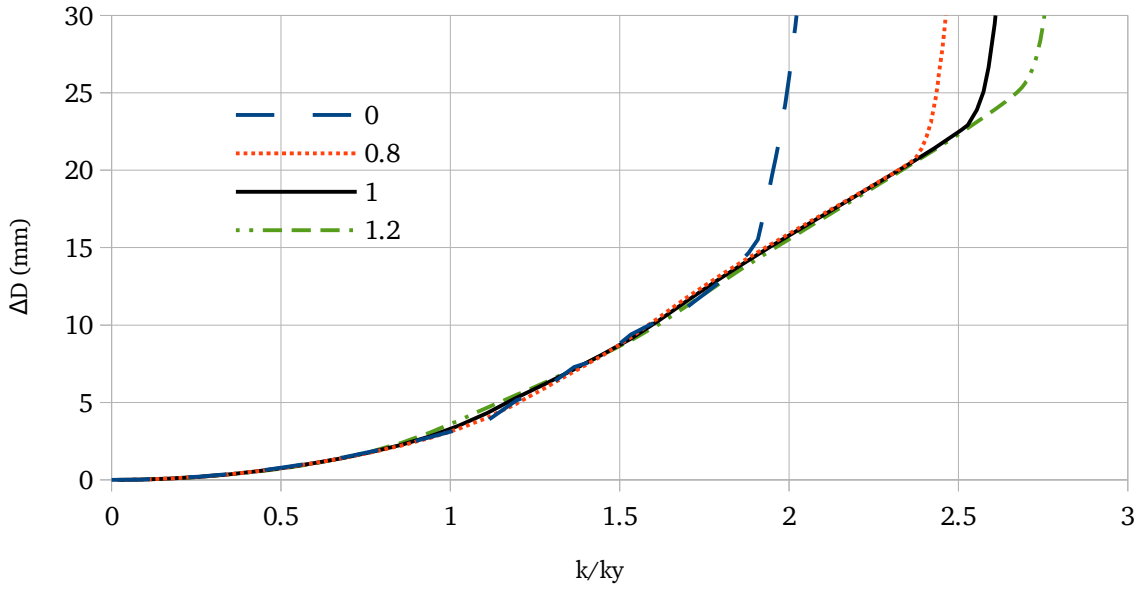

Figure 138: Effect of residual stresses on ovalization of Tube 1

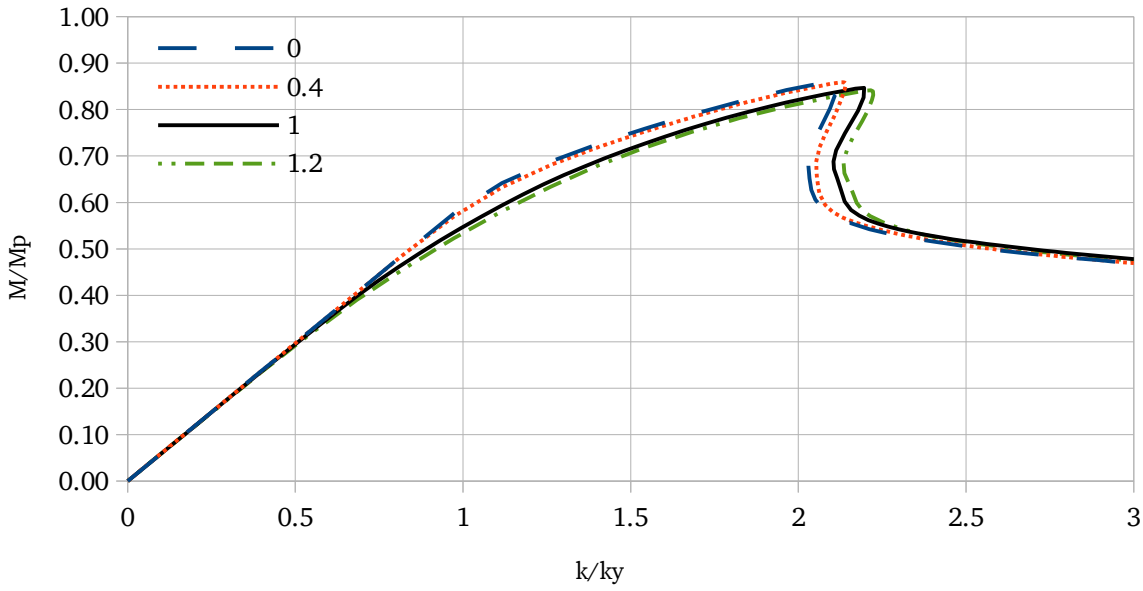

Figure 139: Effect of residual stresses on equilibrium path of Tube 5

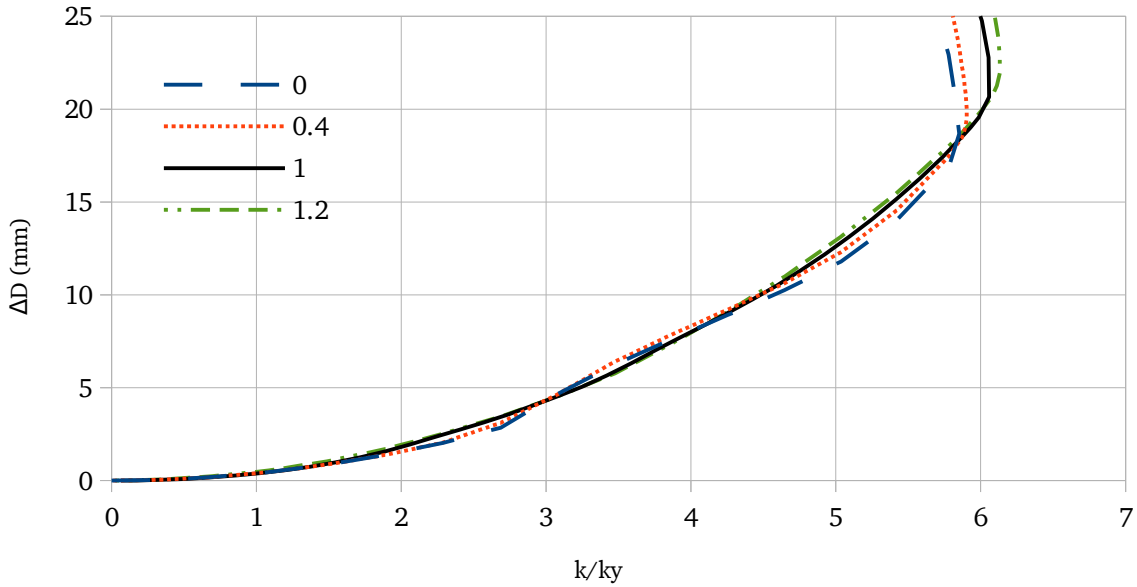

Figure 140: Effect of residual stresses on ovalization of Tube 5

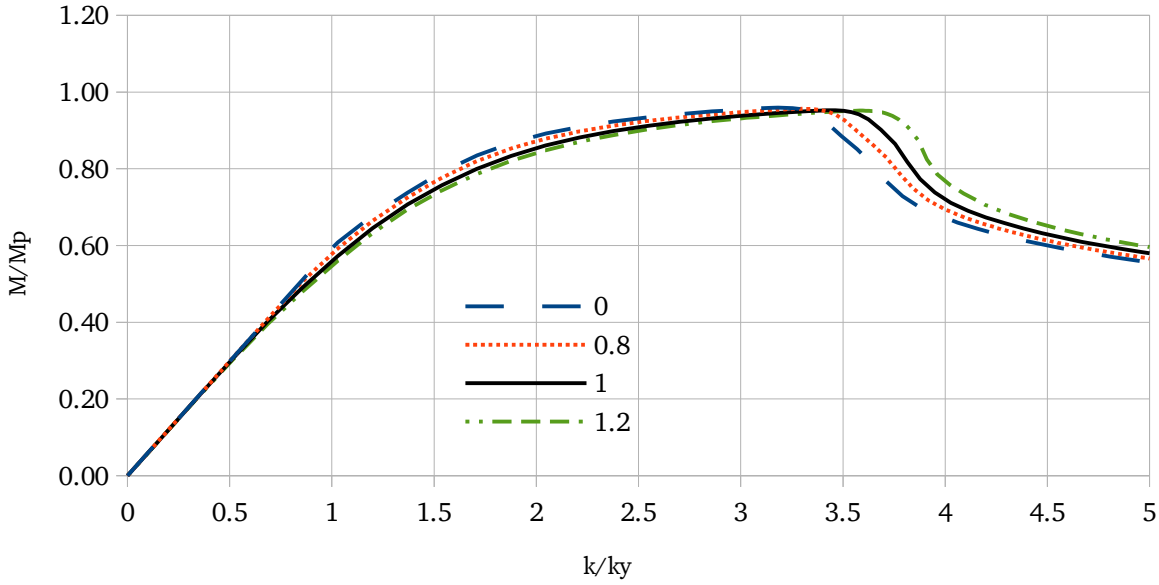

Figure 141: Effect of residual stresses on equilibrium path of Tube11

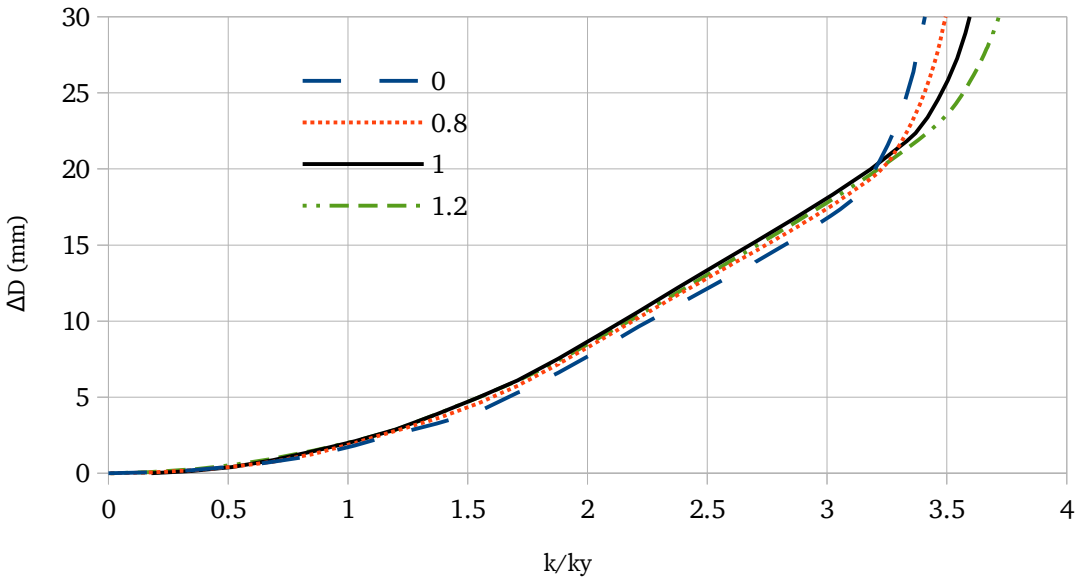

Figure 142: Effect of residual stresses on ovalization of Tube 11

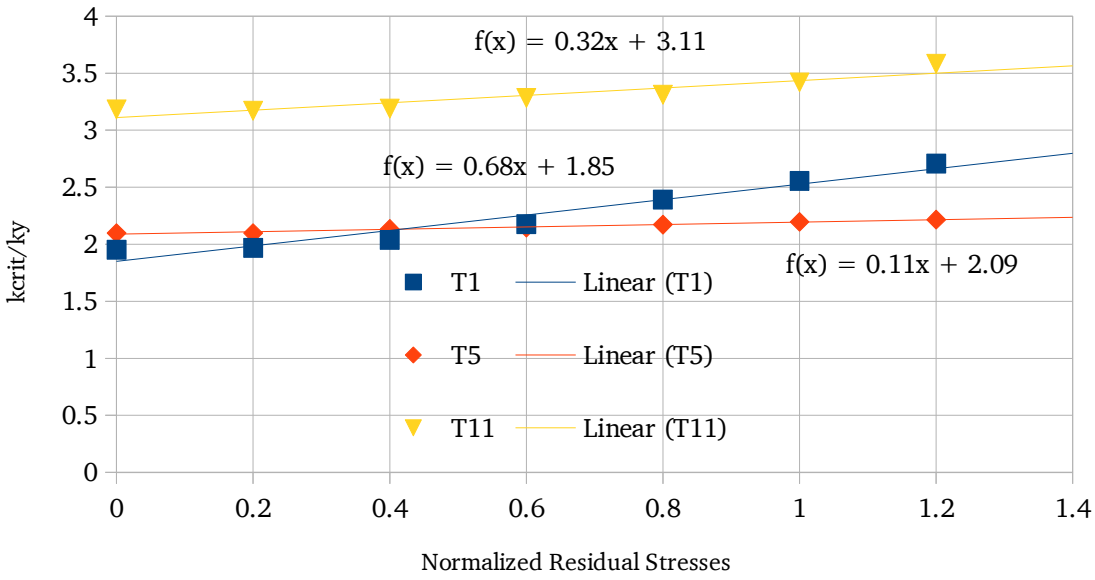

Figure 143: Effect of residual stresses on critical curvature of real tubes

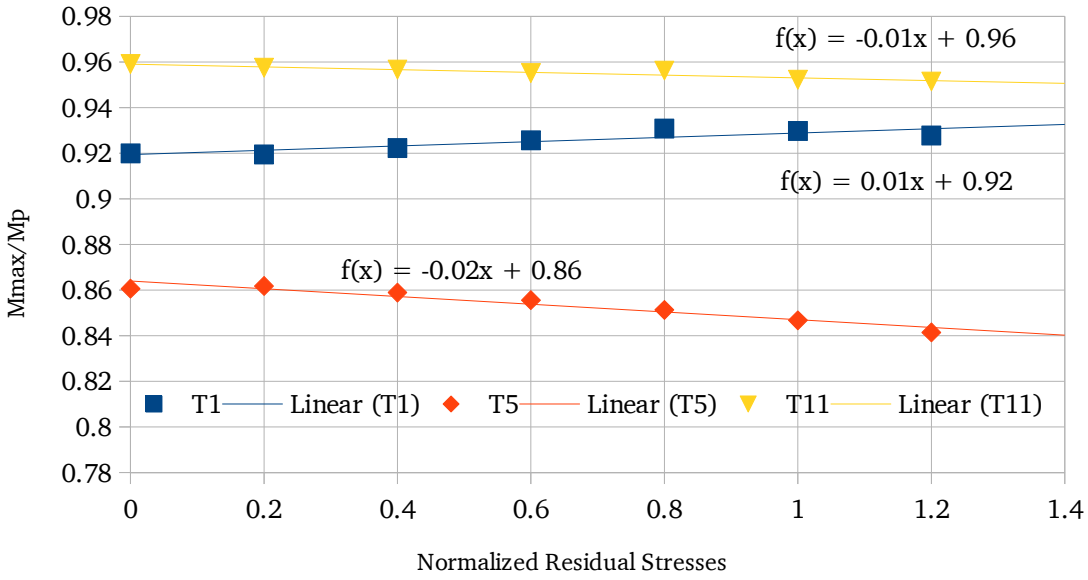

Figure 144: Effect of residual stresses on maximum moment of real tubes

6.1.3 Discussion

The results of this study show that residual stresses have a significant effect on the moment-curvature relation of the tubes, especially for Tube 1. As shown in Figures 137, 139, and 141, the equilibrium paths of the tubes tend to become smoother after yielding as residual stresses increase, and k_{crit} tends to increase. On the other hand, the pre-buckling ovalization paths of the tubes remained unchanged, as shown in Figures 138, 140, and 142. k_y itself does not appear to change.

Figure 143 shows the effect of residual stresses on k_{crit}, and Figure 144 shows the effect on M_{max}. For all tubes, linear trendlines were used of the following form:

$$y = ax + b \tag{54}$$

These trendlines are summarized in Table 30.

Table 30: Effect of residual stresses on behavior of real tubes

	k_{crit}		M_{max}			
Tube	**a**	**b**	**a**	**b**	**D/t**	**f_y**
1	0.68	1.85	0.01	0.92	65	540
5	0.32	2.09	-0.02	0.86	119	400
11	0.11	3.11	-0.01	0.96	83	340

This table shows that in terms of k_{crit}, all tubes benefit from higher residual stresses. In terms of moment capacity, M_{max} increased for Tube 1 but decreased for Tubes 5 and 11. Overall, residual stresses were found to affect k_{crit} much more significantly than M_{max}.

It is also thought that residual stresses may depend on D/t, which is a measure of ductility. Table 30 shows the highest slopes for Tube 1, which has the lowest D/t ratio, and the lowest slopes for Tube 5, which has the highest D/t ratio. This was true for both k_{crit} and M_{max}, and suggests that residual stresses may have a higher effect as D/t is decreased.

6.1.4 Conclusions and Recommendations

This study shows that residual stresses have a significant effect on the behavior of steel tubes, especially in terms of the smoothness of the equilibrium paths and in terms of k_{crit}. The effect varied widely between the tubes, but it was found that the effect on both k_{crit} and M_{max} was greatest for Tube 1 and least for Tube 5, suggesting a dependence on D/t. However, the sample size was very small and there are other differences between the tubes, such as the imperfection heights and the material models, so further work is needed to exclude these variables and confirm that the effect of residual stresses depend on D/t.

6.2 Influence of Imperfection Amplitude

6.2.1 Approach and Methods

In this section, Tubes 1, 5, and 11 were used to carry out a sensitivity study based on the applied imperfection amplitude. The applied imperfection amplitudes were varied between 10% and 300% of the measured imperfections. The results are shown by plotting the resulting effect on the moment-curvature and ovalization-curvature relations, as well as by plotting the influence of 2w on k_{crit} and M_{max}.

6.2.2 Results

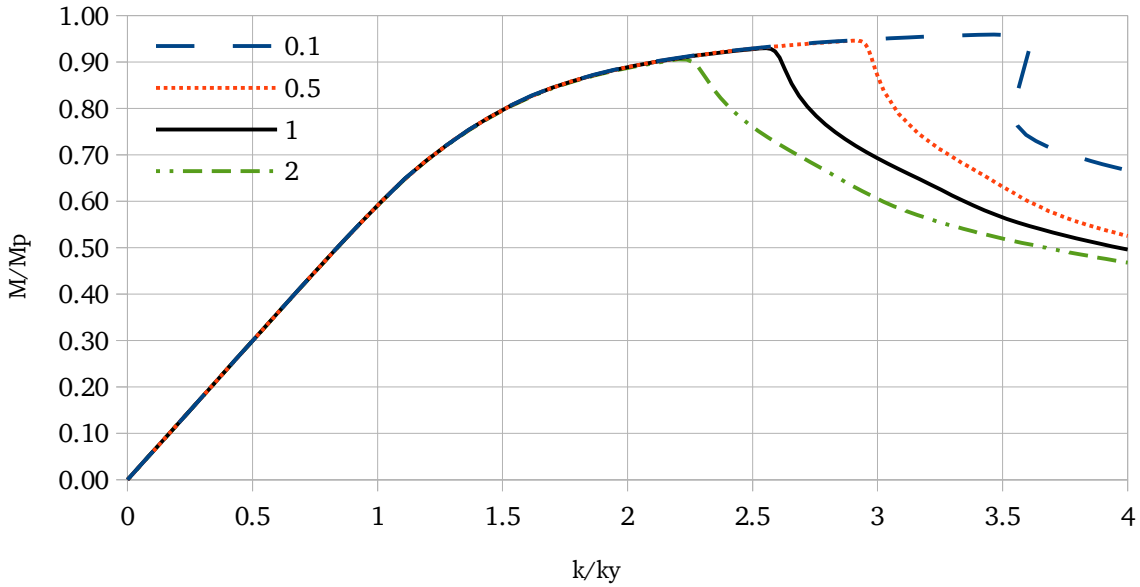

Figure 145: Effect of 2w on the equilibrium path of Tube 1

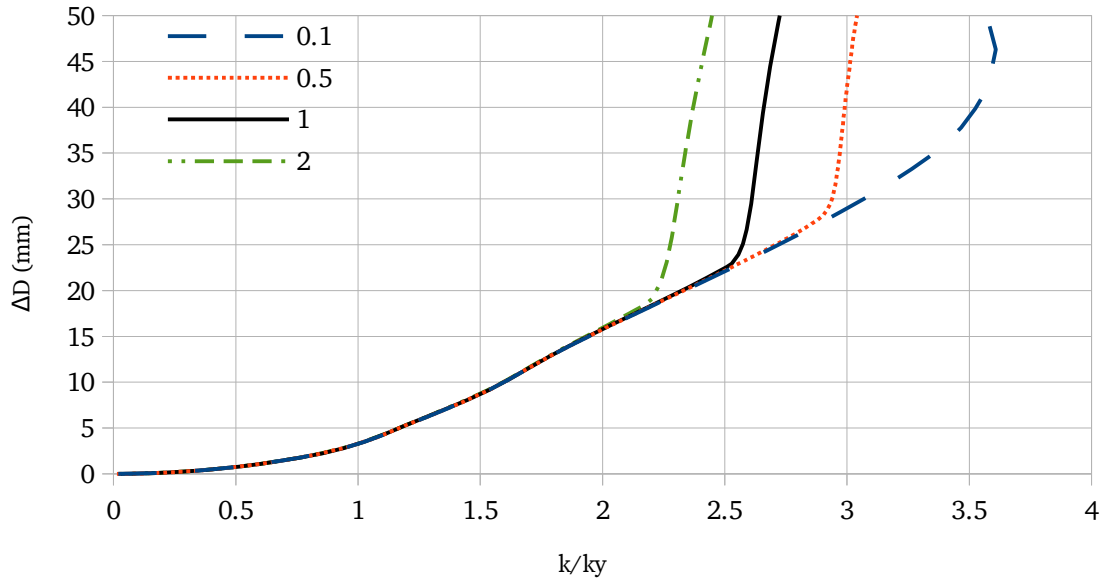

Figure 146: Effect of 2w on the ovalization of Tube 1

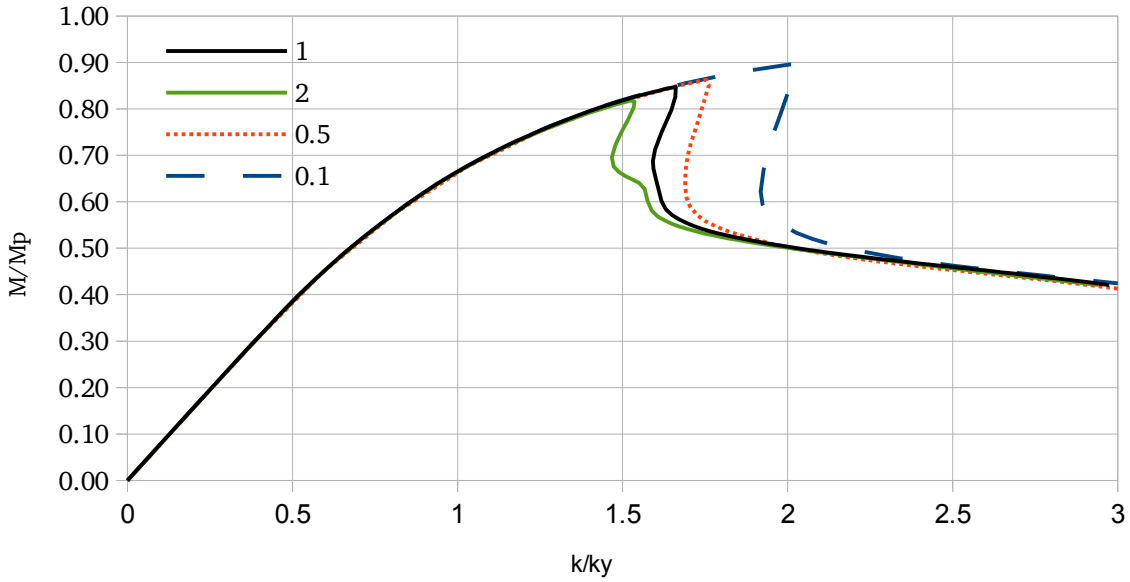

Figure 147: Effect of 2w on the equilibrium path of Tube 5

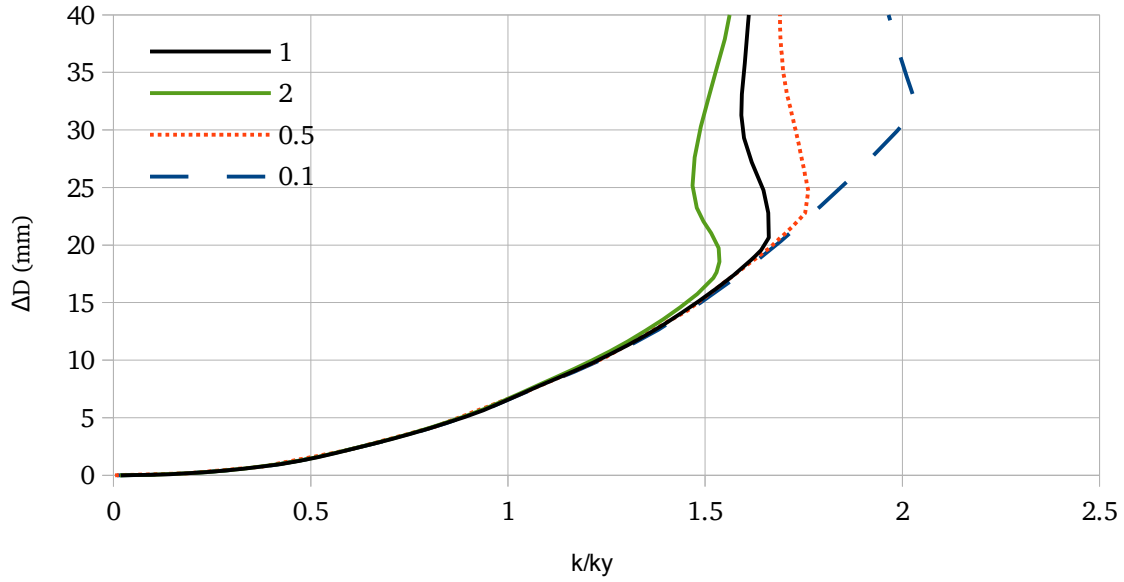

Figure 148: Effect of 2w on the ovalization of Tube 5

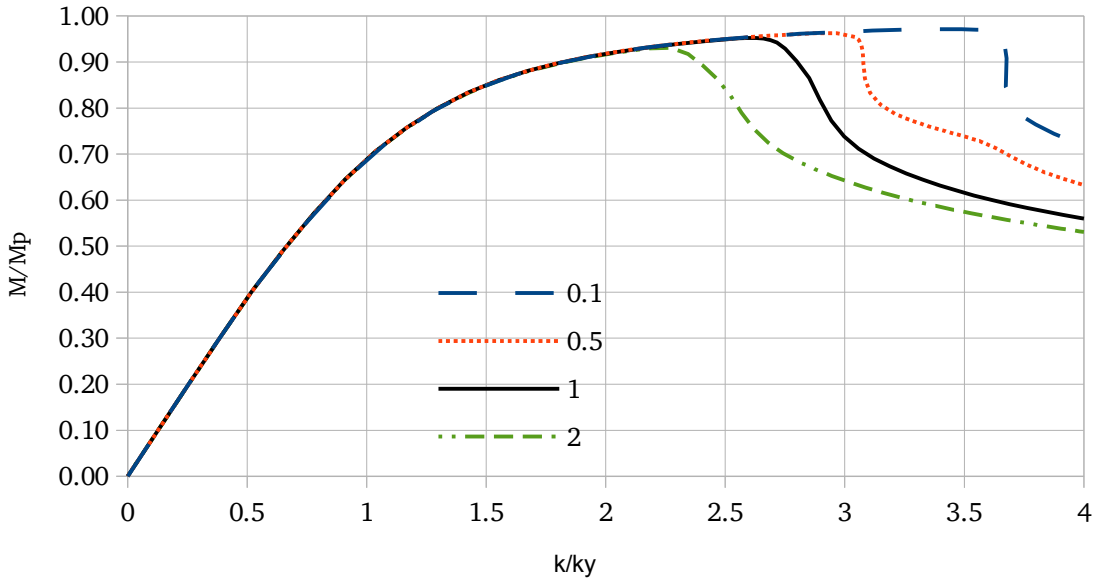

Figure 149: Effect of 2w on the equilibrium path of Tube 11

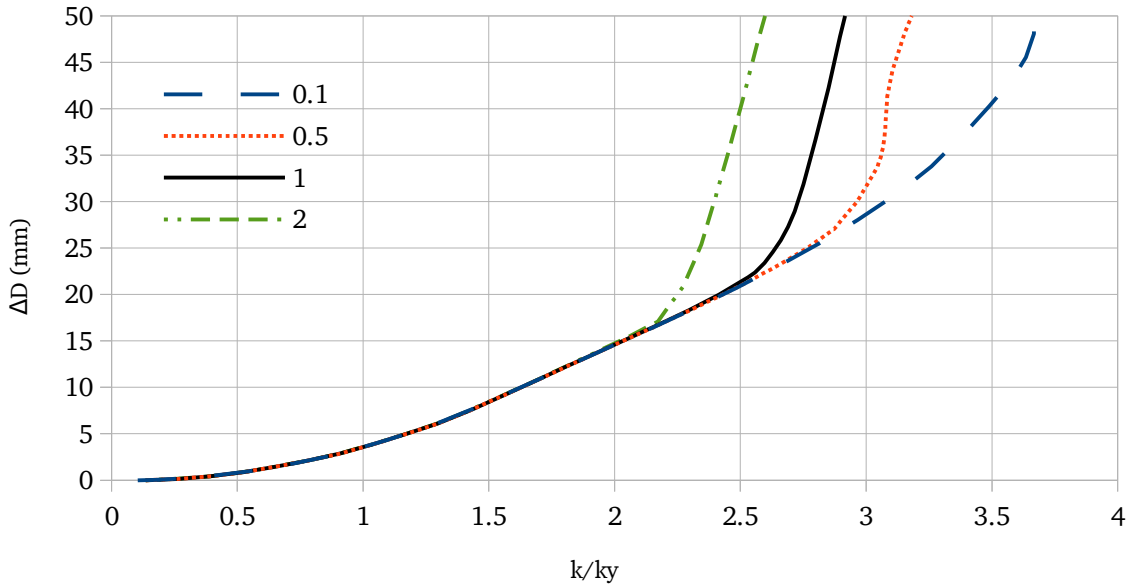

Figure 150: Effect of 2w on the ovalization of Tube 11

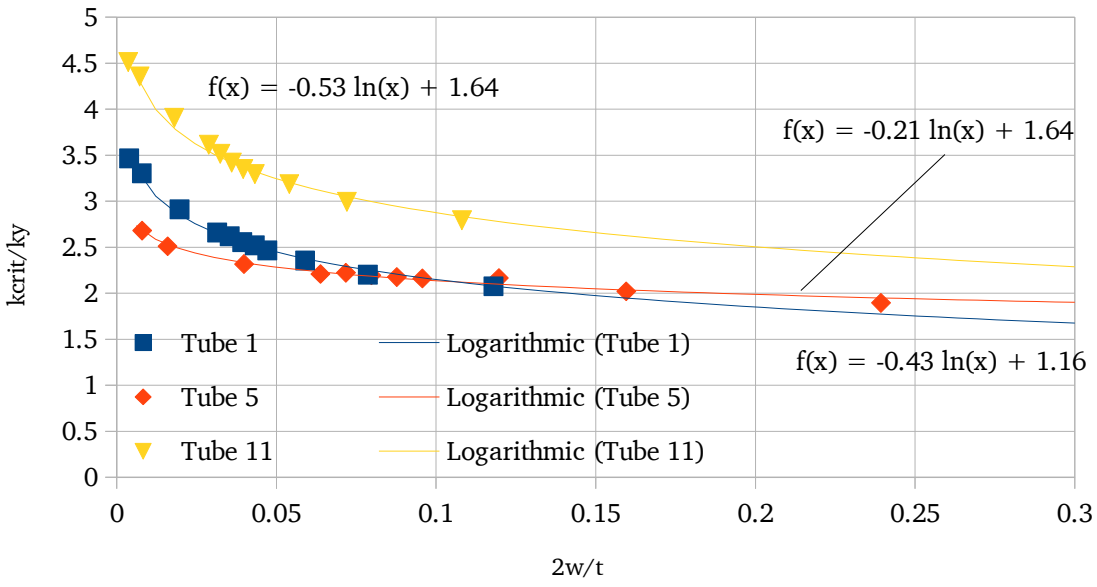

Figure 151: Effect of 2w on the critical curvature of real tubes

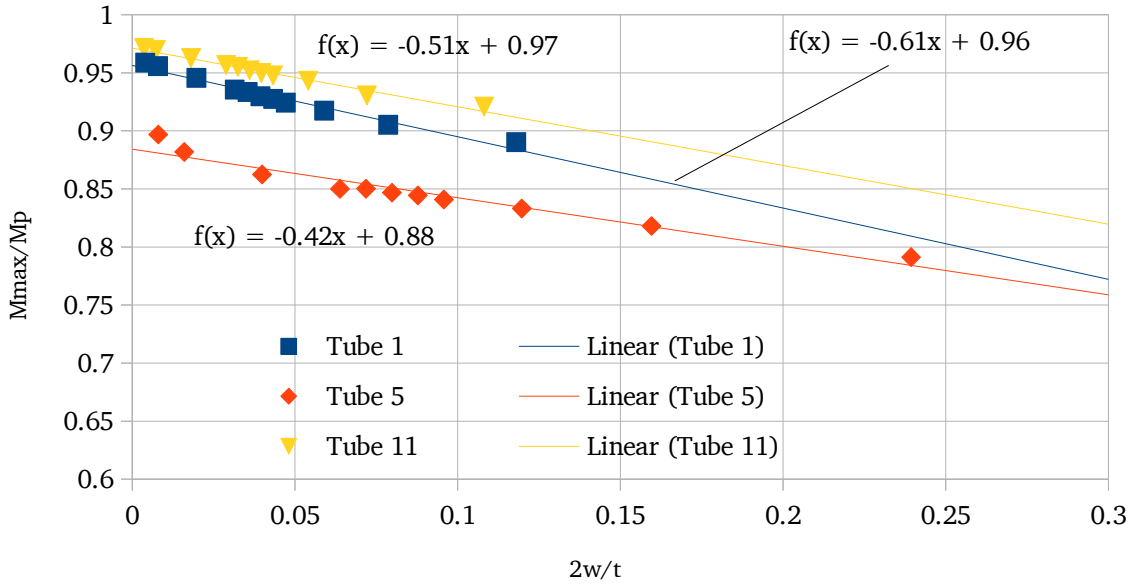

Figure 152: Effect of 2w on the maximum moment of real tubes

6.2.3 Discussion

Figures 145-150 clearly show that the imperfection amplitude 2w does not affect the pre-buckling response of the tubes. Increasing 2w simply causes the buckling point to "move back" along the equilibrium path.

The trends are shown in detail in Figures 151 and 152. In terms of k_{crit}, logarithimic trendlines were found to best fit the data, while for M_{max}, the trends were approximated linearly.

Due to the observation that a change in 2w simply moves the buckling point along the equilibrium path, the influence of 2w depends on the shape of the equilibrium path. The shape of this path depends on D/t, f_{resid}/f_y, the material model, and possibly other factors as well. These variables have not been excluded from each other in this study, so further research is needed to find out exactly how 2w influences k_{crit} and M_{max} for different types of tubes.

6.2.4 Conclusions and Recommendations

The results of this study show that imperfection amplitude does not change the pre-buckling equilibrium path, but does significantly affect k_{crit}. It is shown that k_{crit} decreases logarithmically as 2w is increased and that M_{max} decreases linearly as 2w is increased. This means that a very small increase in 2w could theoretically have a profound effect on deformation capacity. However, in the real tubes, 2w/t generally varied between 0.036 and 0.191, and in this range the influence is much less severe.

6.3 Influence of D/t Ratio

6.3.1 Approach and Methods

The effect of D/t ratio on capacity was investigated by varying the thickness of Tubes 1, 5, and 11. The results are presented through normalized moment-curvature and ovalization-curvature paths and by plotting the effect of D/t on k_{crit} and M_{max}.

6.3.2 Results

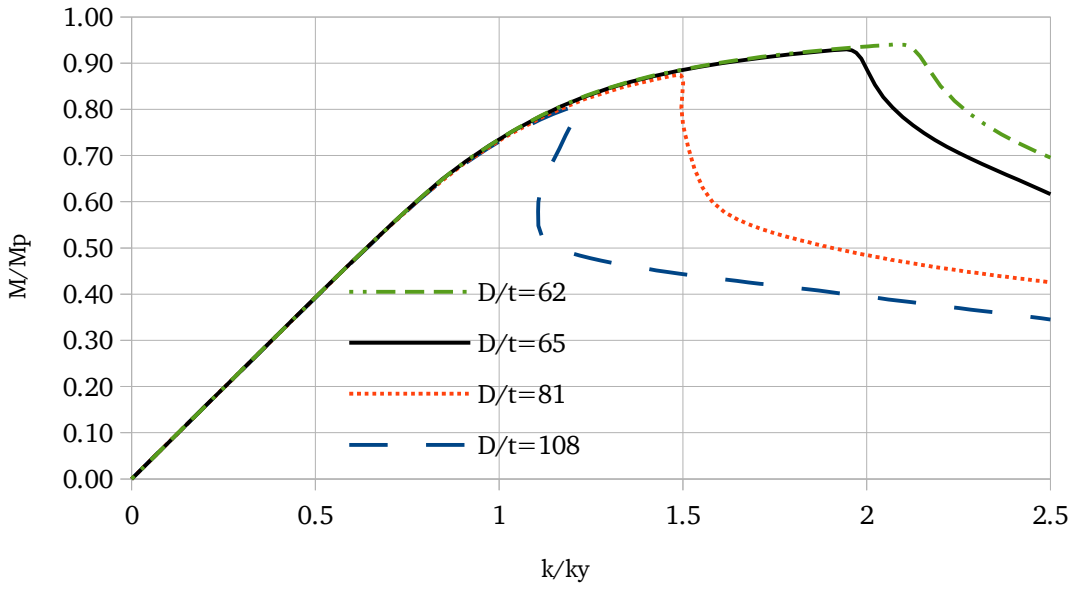

Figure 153: Effect of D/t on equilibrium path of Tube 1

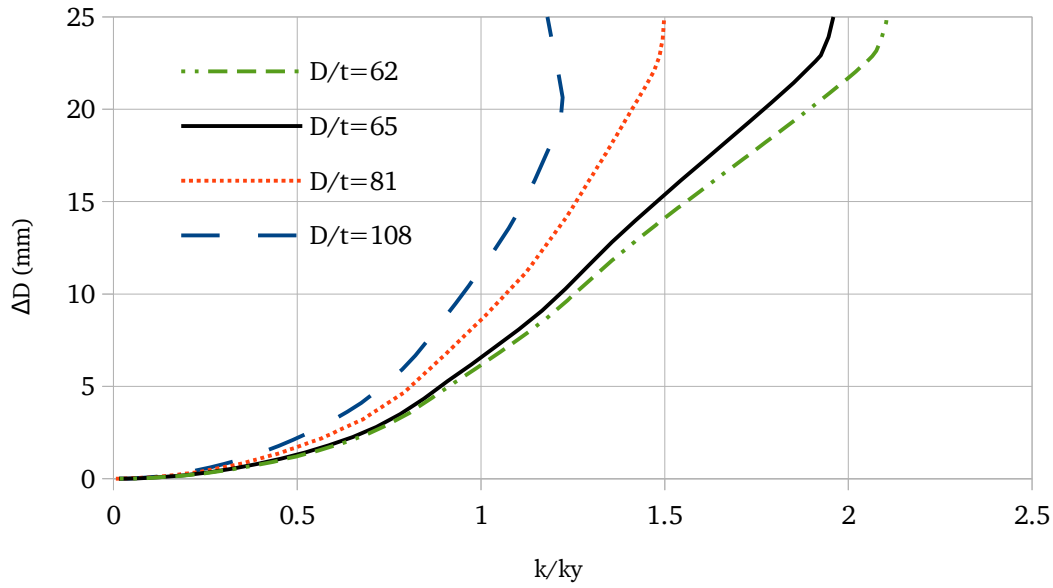

Figure 154: Effect of D/t on ovalization of Tube 1

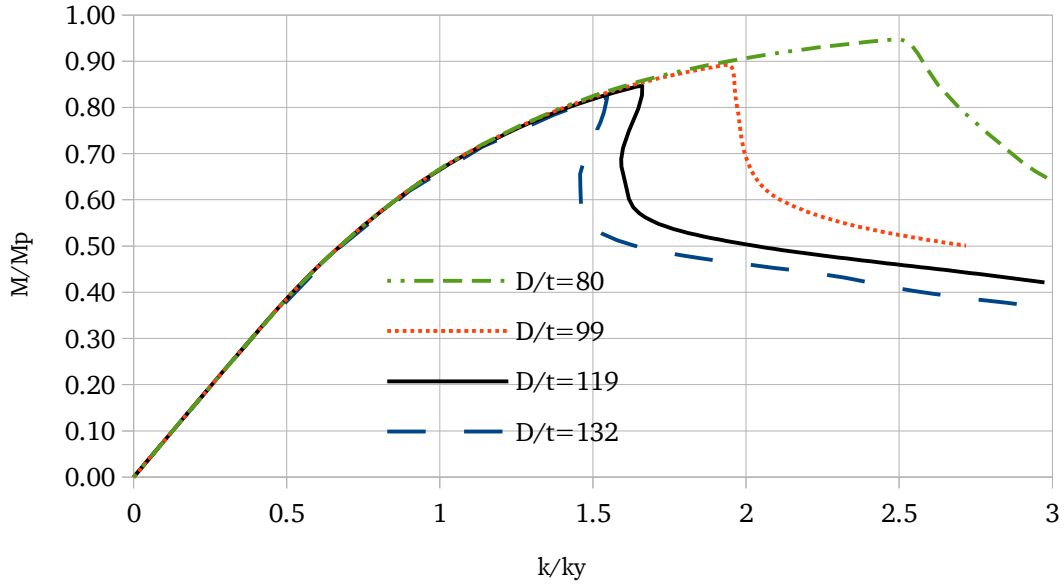

Figure 155: Effect of D/t on equilibrium path of Tube 5

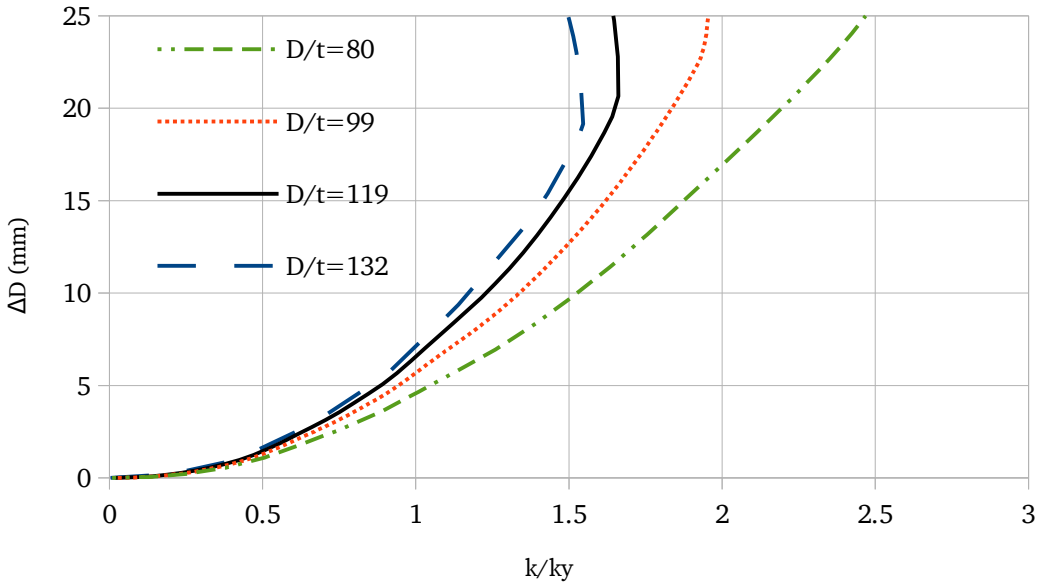

Figure 156: Effect of D/t on ovalization of Tube 5

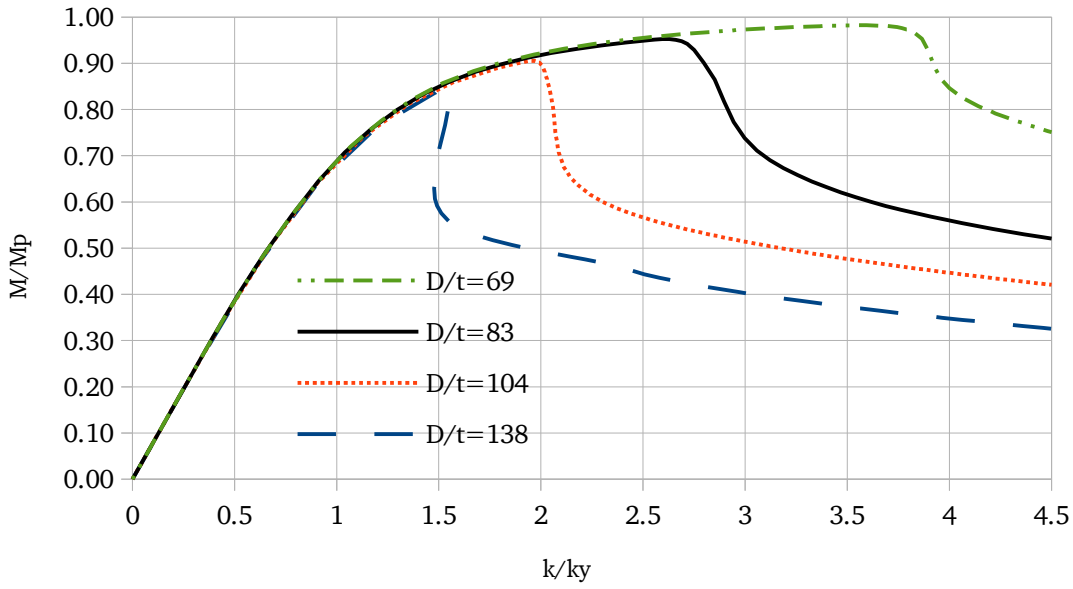

Figure 157: Effect of D/t on equilibrium path of Tube 11

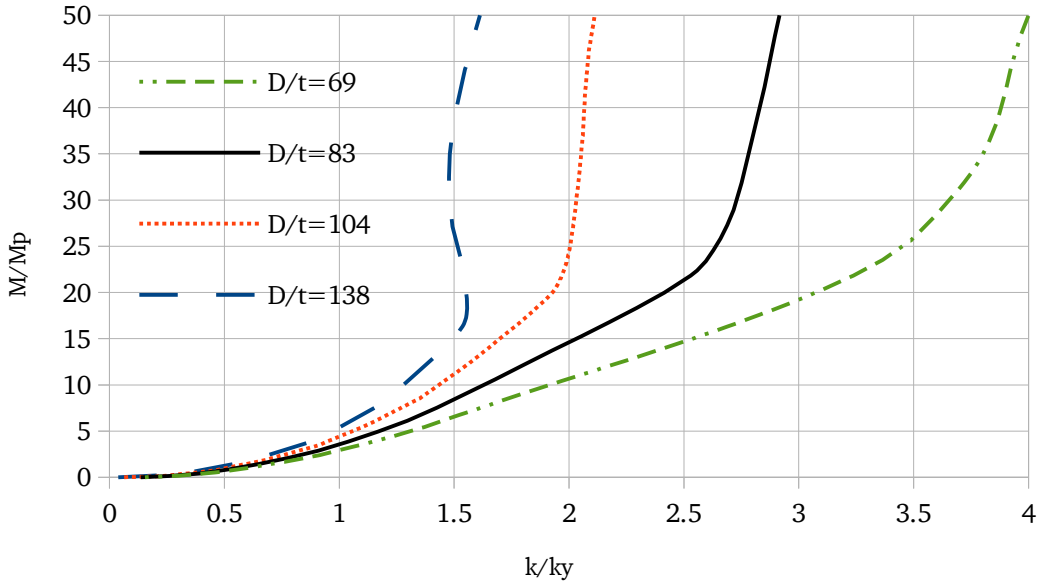

Figure 158: Effect of D/t on ovalization of Tube 11

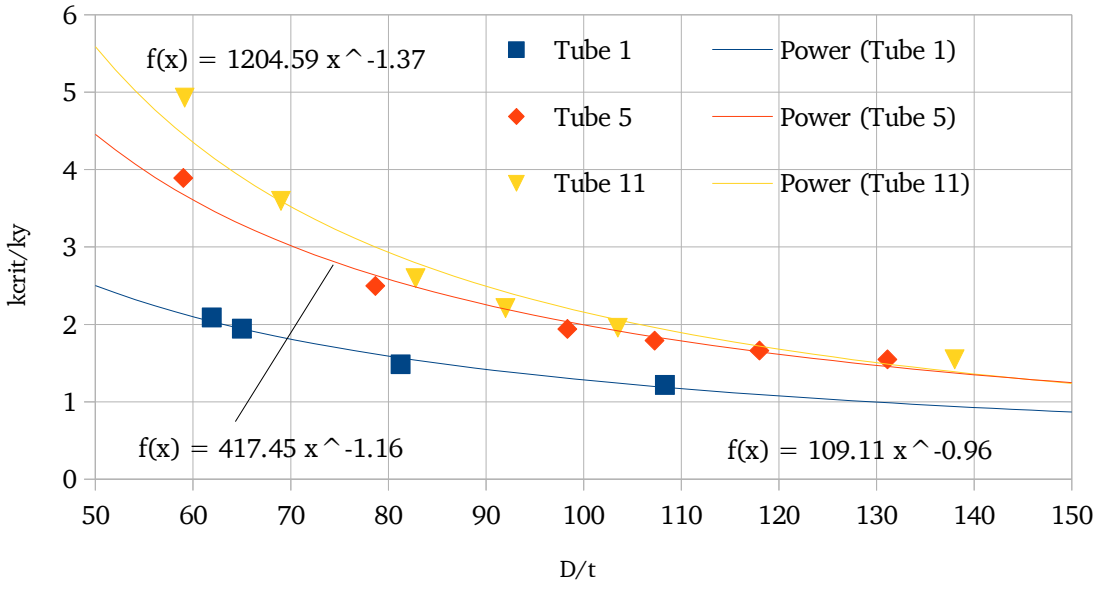

Figure 159: Effect of D/t on normalized critical curvature of real tubes

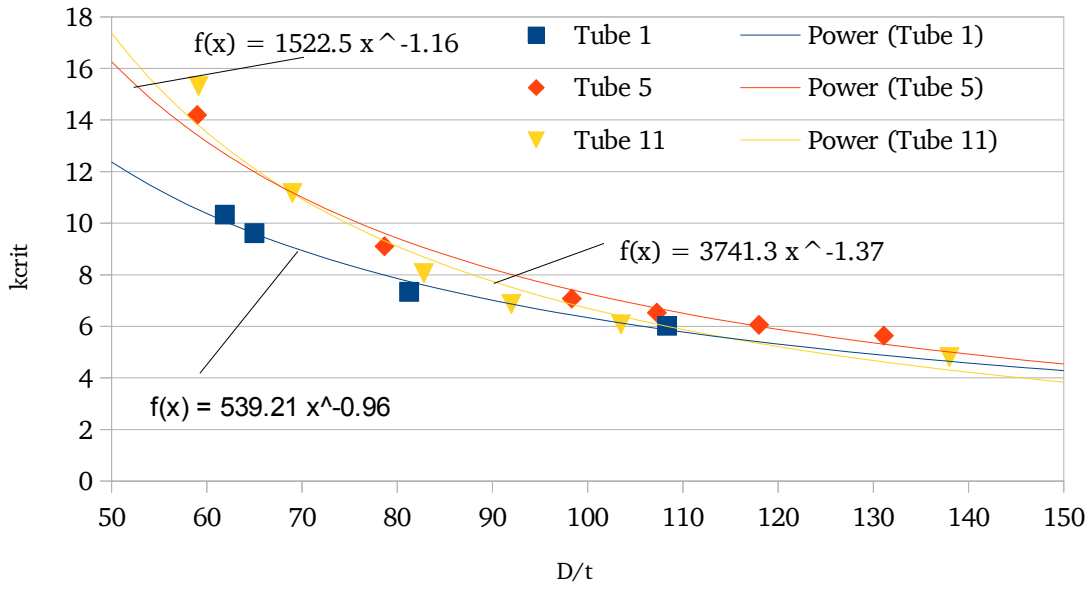

Figure 160: Effect of D/t on absolute critical curvature of real tubes

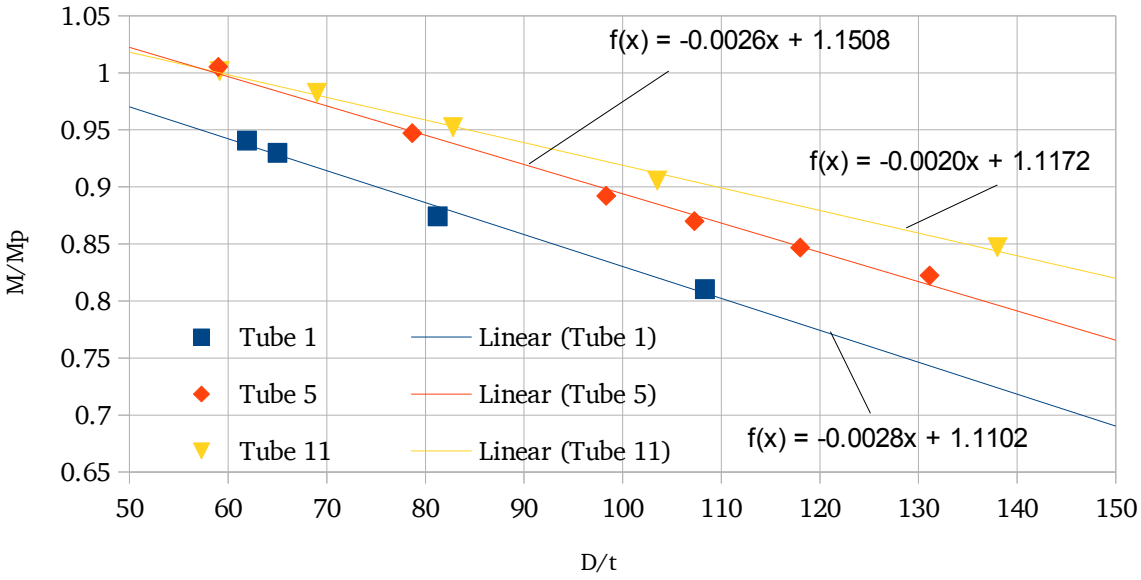

Figure 161: Effect of D/t on maximum moments of real tubes

6.3.3 Discussion

The results of this study show that D/t has a profound effect on the behavior of the tubes. Since D/t influences the stiffness of the tubes, it changes their ovalization, as shown in Figures 154, 156, and 158. Figures 153, 155, and 157 show that as D/t decreases, ductility increases and the tubes buckle at a higher critical curvature and closer to M_p.

Figures 159 and 160 show that the effect of D/t on k_{crit} is nonlinear. In fact, power curves have been used to describe the trends. This is significant because it means that a small increase in thickness (decrease in D/t) of the tubes potentially leads to a large increase in strain capacity. On the other hand, maximum moment increases linearly with decreasing D/t, as shown in Figure 161.

As with the previous studies, it is difficult to attribute the difference in behavior between the three tubes to any single factor. It is likely a combination of effects due to 2w, the material model, and the residual stresses.

6.3.4 Conclusions and Recommendations

In this section, it has been shown that decreasing D/t nonlinearly increases k_{crit}, which means that strain capacity can easily be increased by varying the thickness of the plates used to manufacture the tubes. It is also shown that the effect on M_{max} is linear. Finally, it is noted that there is a difference in the effect of D/t on k_{crit} and M_{max} between the three tubes, and that further studies are needed to find out what the significant parameters are.

6.4 3 Variable Parameter Study

6.4.1 Approach and Methods

In, this section, a three-variable parameter study is conducted, based on the parameters shown in Table 31. All combinations of the parameters shown here were investigated and relationships and trends were found based on the results. The results were also used to determine the most favorable combinations and the parameters which have the most significant influence on the capacity of the tubes.

Table 31: Parameters used in three variable parameter study

D/t	**2w/t**	**f_y (MPa)**
60	.01	320
80	.04	380
100	.07	420
120	.1	520
	.14	600
		700

The basic setup is a tube with L=8,100mm (Model 1), D=1,067mm, and a material model as shown in Figure 162. The elastic branch has E=205,000 MPa, while linear strain hardening is assumed in the plastic branch with H=E/30.

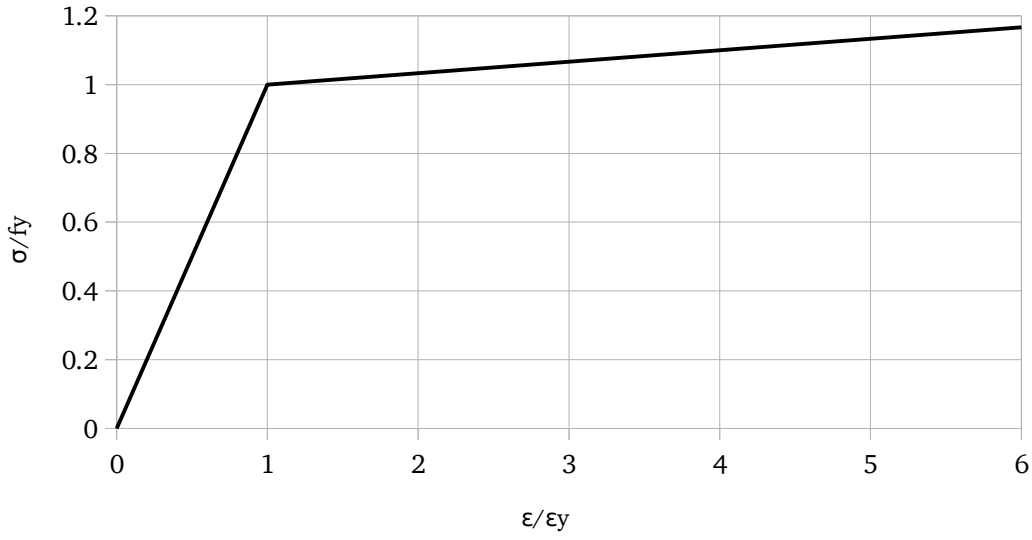

Figure 162: Material model for 3 variable parameter study

This setup was chosen to make it very easy to change the parameters independently of each other. D/t could be changed simply by changing the thickness of the shell elements, and the material model could be scaled by changing f_y without changing the shape of the stress-strain curve. Residual stresses were always included based on the chosen yield stress, and the imperfection was introduced based on the summation of the 5^{th} and 6^{th} buckling modes.

The results are described by first describing the effect of each parameter individually, and then a multiple regression analysis is used to derive a model capable of describing the behavior of a tube based on any combination of D/t, 2w/t and f_y.

6.4.2 Results: Constant f_y

First the results are presented for the influence of f_y on k_{crit}. Logarithmic regressions have been used of the following form:

$$y = a * \ln(x) + b \tag{55}$$

The regressions themselves are plotted in the figures for each f_y, and the regression coefficients are reported in the tables.

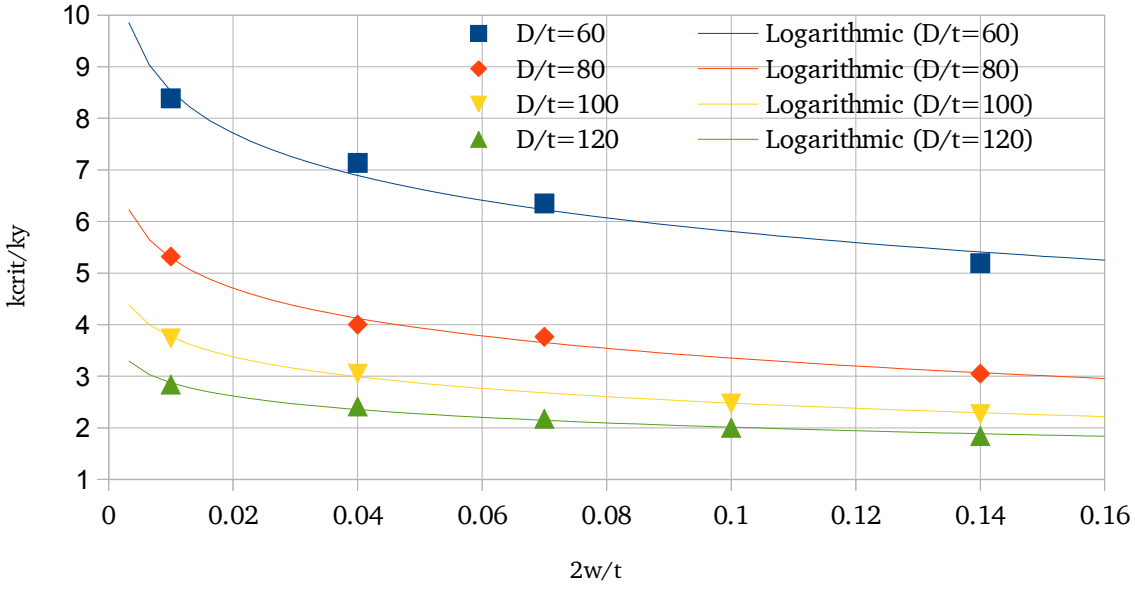

Figure 163: Effect of 2w on k_{crit} (f_y=320 MPa)

Table 32: Regression analysis for f_y=320 (k_{crit})

D/t	a	b	R^2
60	-1.183	3.083	0.974
80	-0.842	1.414	0.990
100	-0.557	1.199	0.996
120	-0.375	1.151	0.998

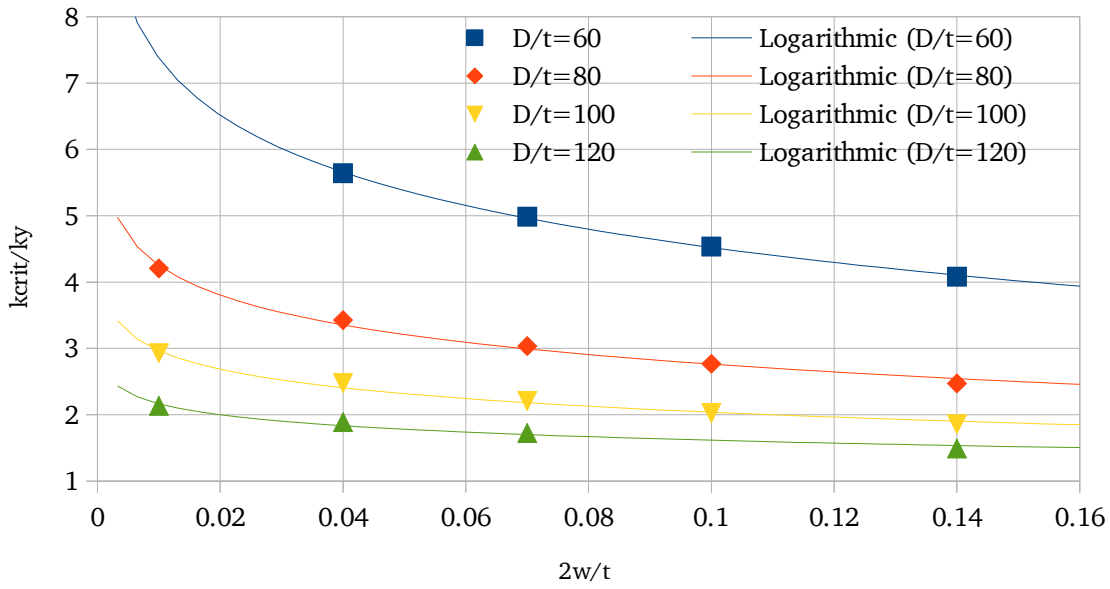

Figure 164: Effect of 2w on k_{crit} (f_y=380 MPa)

Table 33: Regression analysis for f_y=380 (k_{crit})

D/t	**a**	**b**	**R^2**
60	-1.239	1.668	0.999
80	-0.647	1.274	0.992
100	-0.403	1.111	0.987
120	-0.239	1.066	0.970

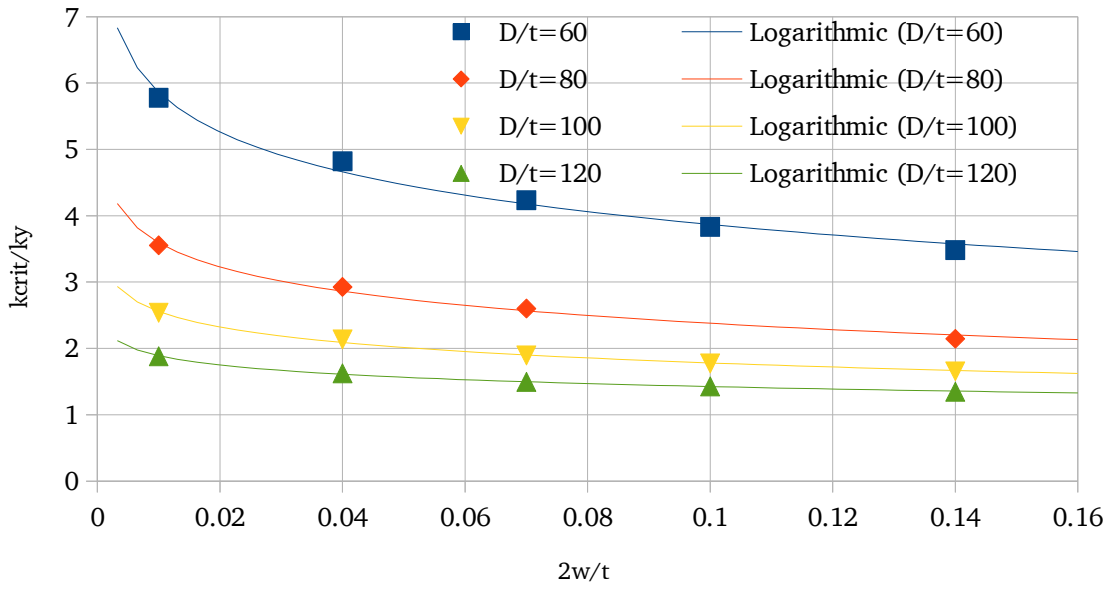

Figure 165: Effect of 2w on k_{crit} (f_y=420 MPa)

Table 34: Regression analysis for f_y=420 (k_{crit})

D/t	a	b	R^2
60	-0.866	1.873	0.986
80	-0.527	1.165	0.991
100	-0.337	1.005	0.995
120	-0.202	0.958	0.998

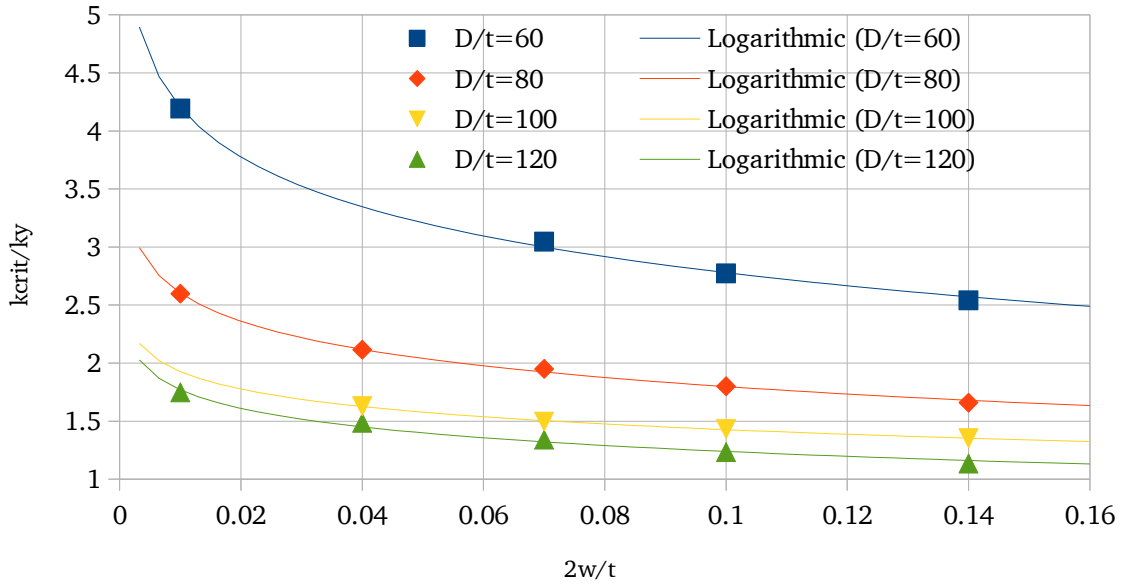

Figure 166: Effect of 2w on k_{crit} (f_y=520 MPa)

Table 35: Regression analysis for f_y=520 (k_{crit})

D/t	**a**	**b**	**R^2**
60	-0.619	1.355	0.998
80	-0.350	0.992	0.998
100	-0.218	0.926	0.998
120	-0.231	0.708	0.988

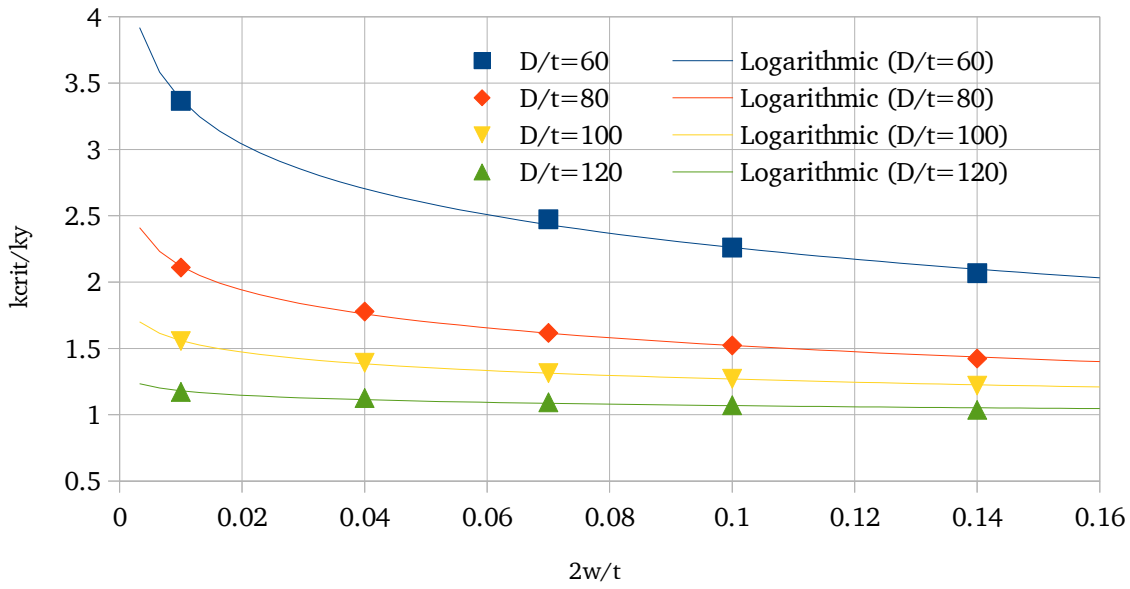

Figure 167: Effect of 2w on k_{crit} (f_y=600 MPa)

Table 36: Regression analysis for f_y=600 (k_{crit})

D/t	a	b	R^2
60	-0.485	1.144	0.997
80	-0.259	0.925	0.998
100	-0.126	0.978	0.998
120	-0.048	0.958	0.946

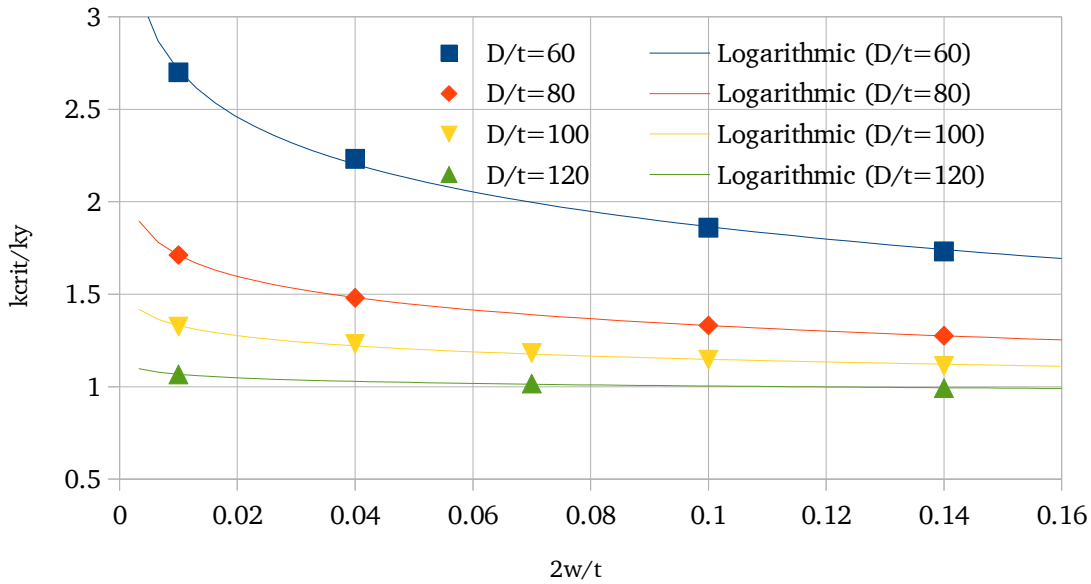

Figure 168: Effect of 2w on k_{crit} (f_y=700 MPa)

Table 37: Regression analysis for f_y=700 (k_{crit})

D/t	a	b	R^2
60	-0.368	1.019	0.998
80	-0.165	0.950	1.000
100	-0.079	0.966	0.991
120	-0.027	0.941	0.994

For M_{max}, linear trendlines have been used of the following form:

$$y = ax + b \tag{56}$$

Again, the results are reported for each f_y through the use of figures and tables.

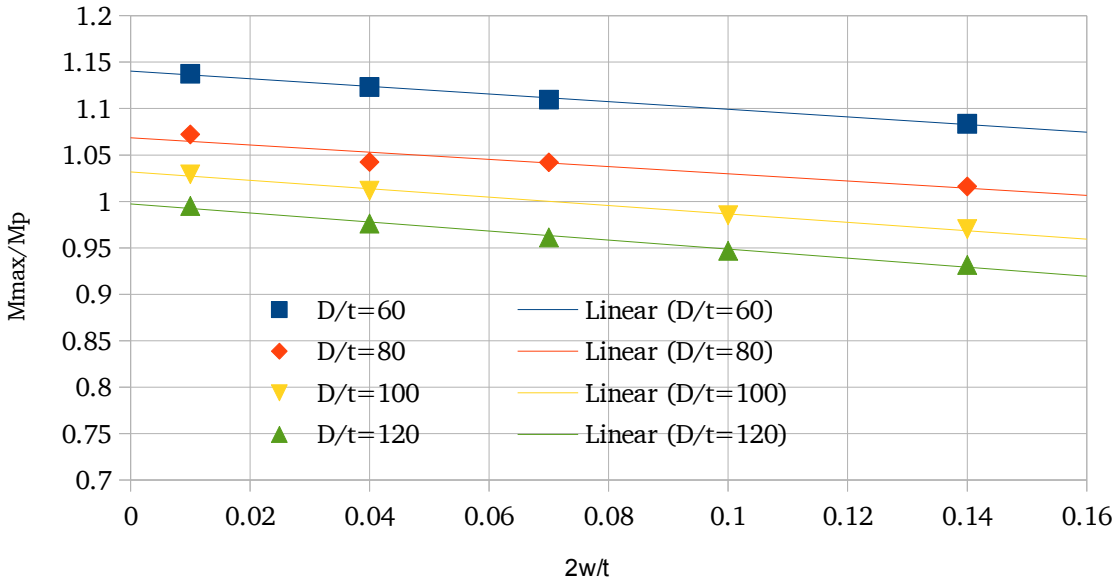

Figure 169: Effect of 2w on M_{max} (f_y=320 MPa)

Table 38: Regression analysis for f_y=320 (M_{max})

D/t	a	b	R^2
60	-0.411	1.140	0.996
80	-0.388	1.068	0.891
100	-0.451	1.032	0.994
120	-0.487	0.997	0.991

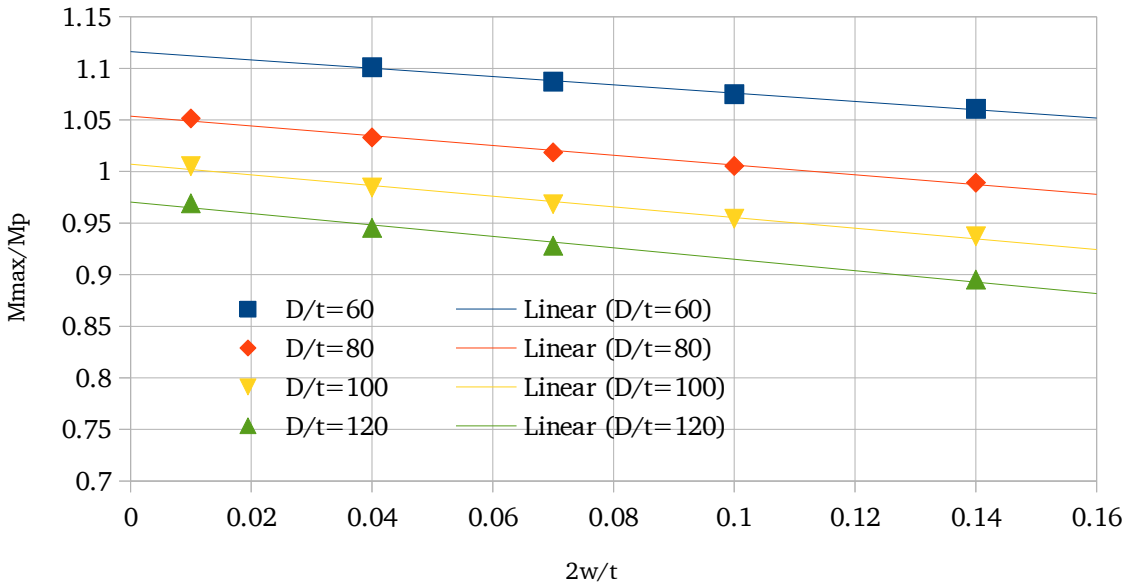

Figure 170: Effect of 2w on M_{max} (f_y=380 MPa)

Table 39: Regression analysis for f_y=380 (M_{max})

D/t	a	b	R^2
60	-0.401	1.116	0.996
80	-0.474	1.054	0.992
100	-0.517	1.007	0.990
120	-0.554	0.971	0.985

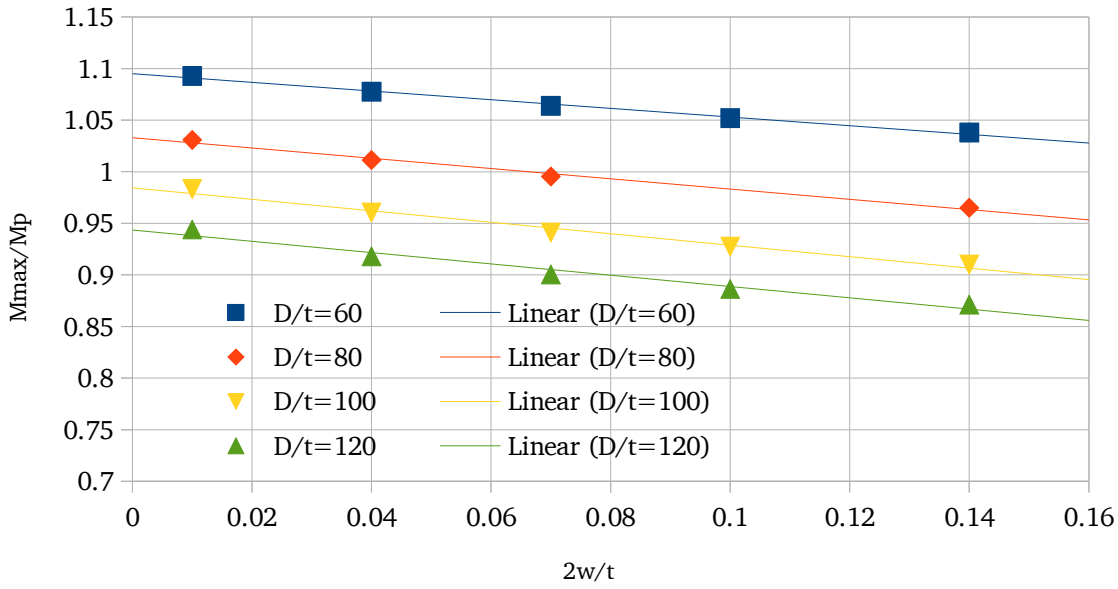

Figure 171: Effect of 2w on M_{max} (f_y=420 MPa)

Table 40: Regression analysis for f_y=420 (M_{max})

D/t	a	b	R^2
60	-0.421	1.095	0.994
80	-0.498	1.033	0.991
100	-0.556	0.984	0.983
120	-0.549	0.944	0.970

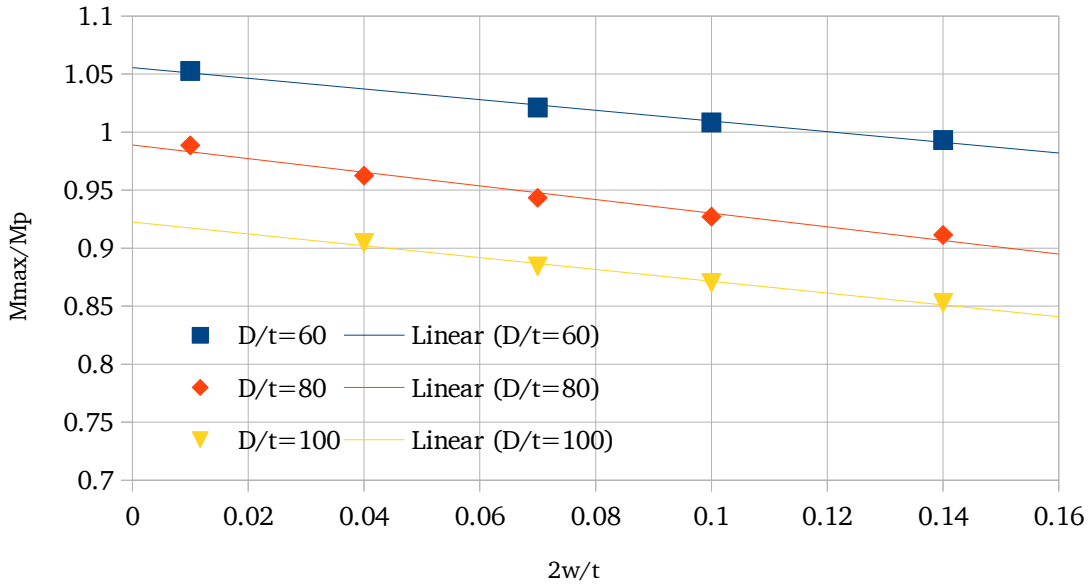

Figure 172: Effect of 2w on M_{max} (f_y=520 MPa)

Table 41: Regression analysis for f_y=520 (M_{max})

D/t	**a**	**b**	**R^2**
60	-0.460	1.056	0.993
80	-0.588	0.989	0.975
100	-0.510	0.922	0.988

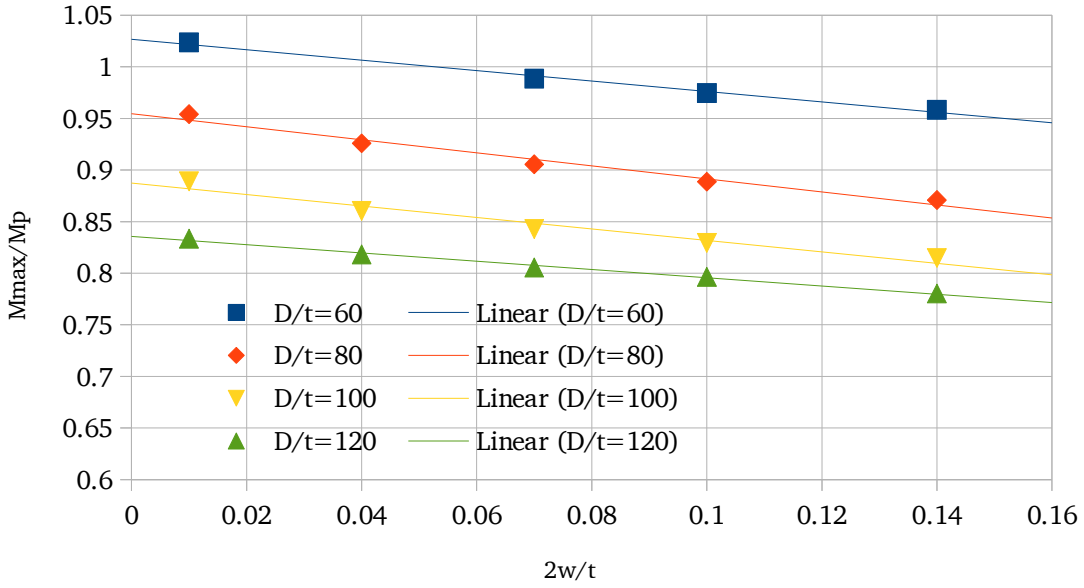

Figure 173: Effect of 2w on Mmax (fy=600 MPa)

Table 42: Regression analysis for f_y=600 (M_{max})

D/t	**a**	**b**	**R^2**
60	-0.507	1.027	0.991
80	-0.631	0.954	0.976
100	-0.556	0.887	0.959
120	-0.400	0.836	0.993

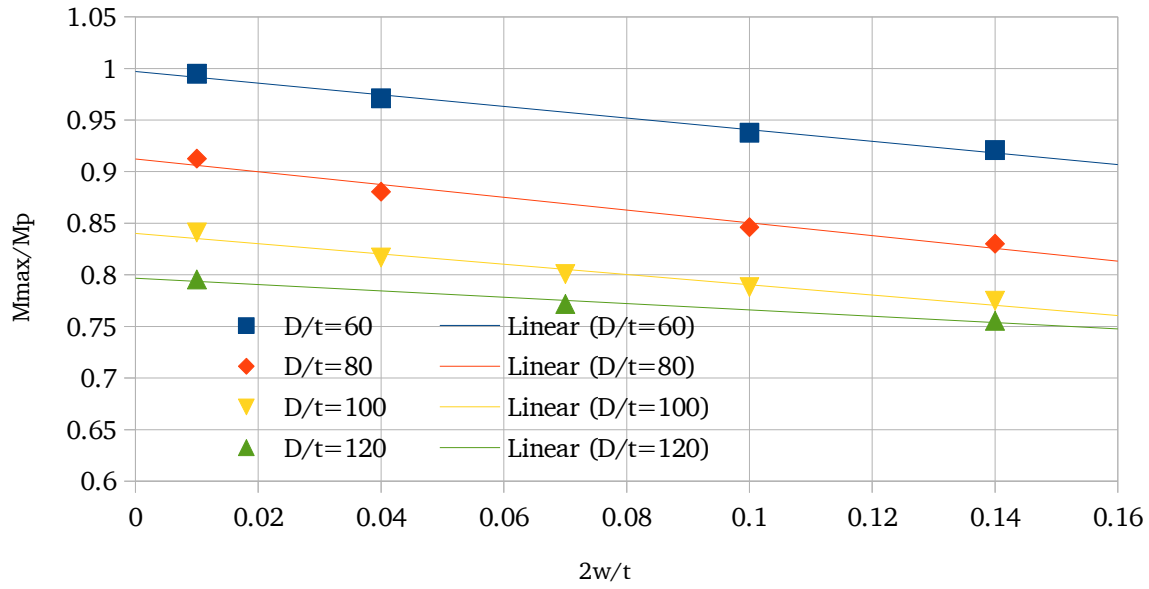

Figure 174: Effect of 2w on M_{max} (f_y=700 MPa)

Table 43: Regression analysis for f_y=700 (M_{max})

D/t	**a**	**b**	**R^2**
60	-0.563	0.997	0.988
80	-0.619	0.912	0.968
100	-0.498	0.840	0.965
120	-0.307	0.797	0.976

6.4.3 Results: Constant D/t

The effect of 2w on k_{crit} has been described using logarithmic trendlines.

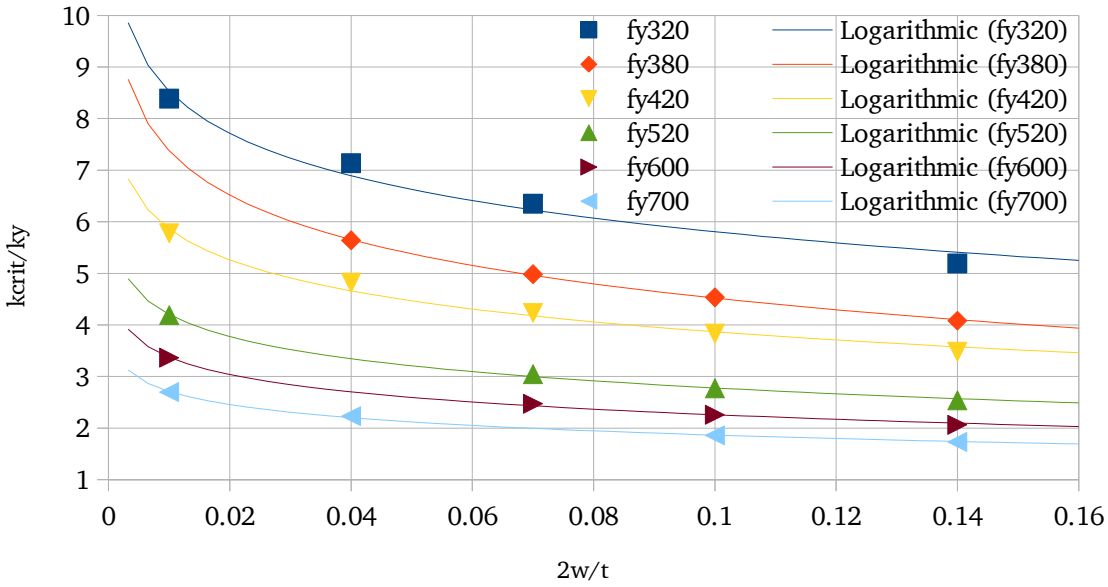

Figure 175: Effect of 2w on k_{kcrit} (D/t =60)

Table 44: Regression analysis for D/t=60 (k_{crit})

f_y (MPa)	**a**	**b**	**R^2**
320	-1.183	3.083	0.974
380	-1.239	1.668	0.999
420	-0.866	1.873	0.986
520	-0.619	1.355	0.998
600	-0.485	1.144	0.997
700	-0.368	1.019	0.998

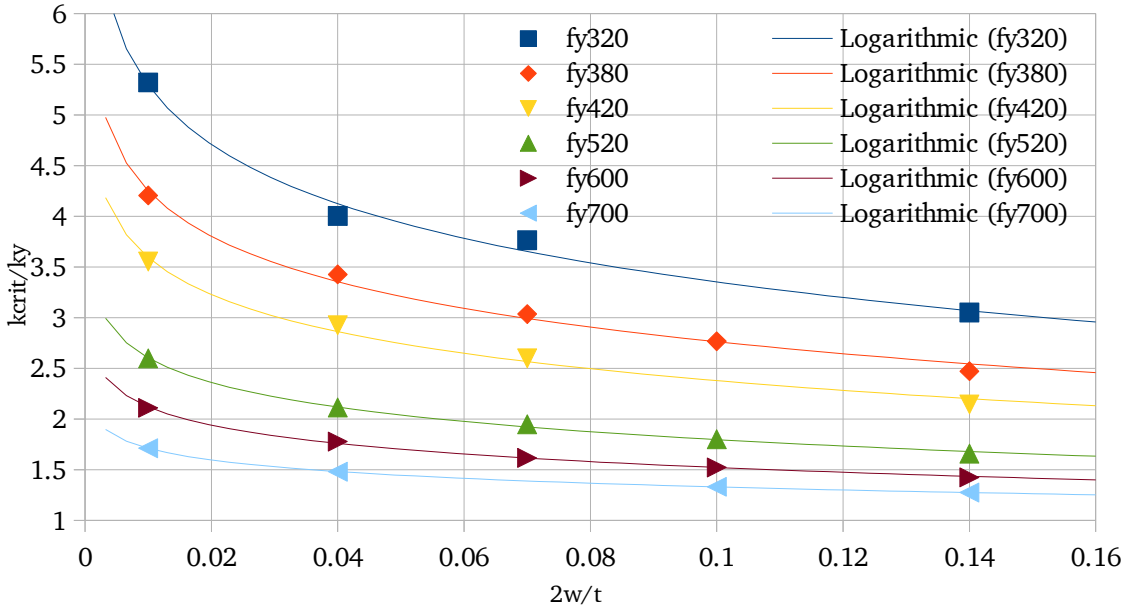

Figure 176: Effect of 2w on k_{kcrit} (D/t =80)

Table 45: Regression analysis for D/t=80 (k_{crit})

f_y (MPa)	**a**	**b**	**R^2**
320	-0.842	1.414	0.990
380	-0.647	1.274	0.992
420	-0.572	1.165	0.991
520	-0.350	0.992	0.998
600	-0.259	0.925	0.998
700	-0.165	0.950	1.000

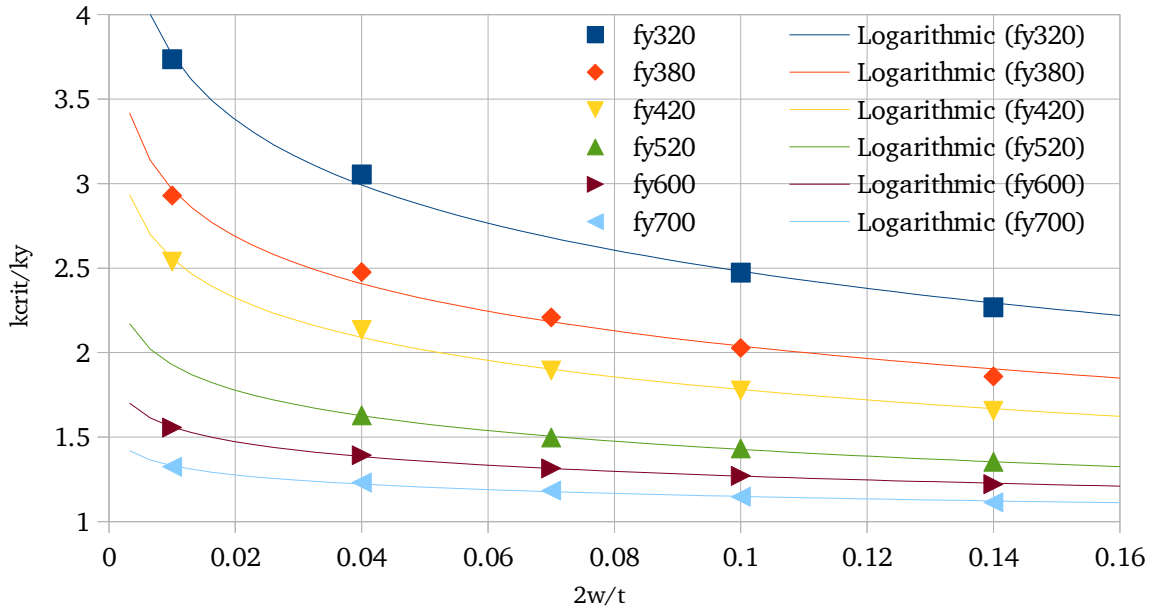

Figure 177: Effect of 2w on k_{kcrit} (D/t =100)

Table 46: Regression analysis for D/t=100 (k_{crit})

f_y (MPa)	**a**	**b**	**R^2**
320	-0.557	1.199	0.996
380	-0.403	1.111	0.987
420	-0.337	1.005	0.995
520	-0.218	0.926	0.998
600	-0.126	0.978	0.998
700	-0.079	0.966	0.991

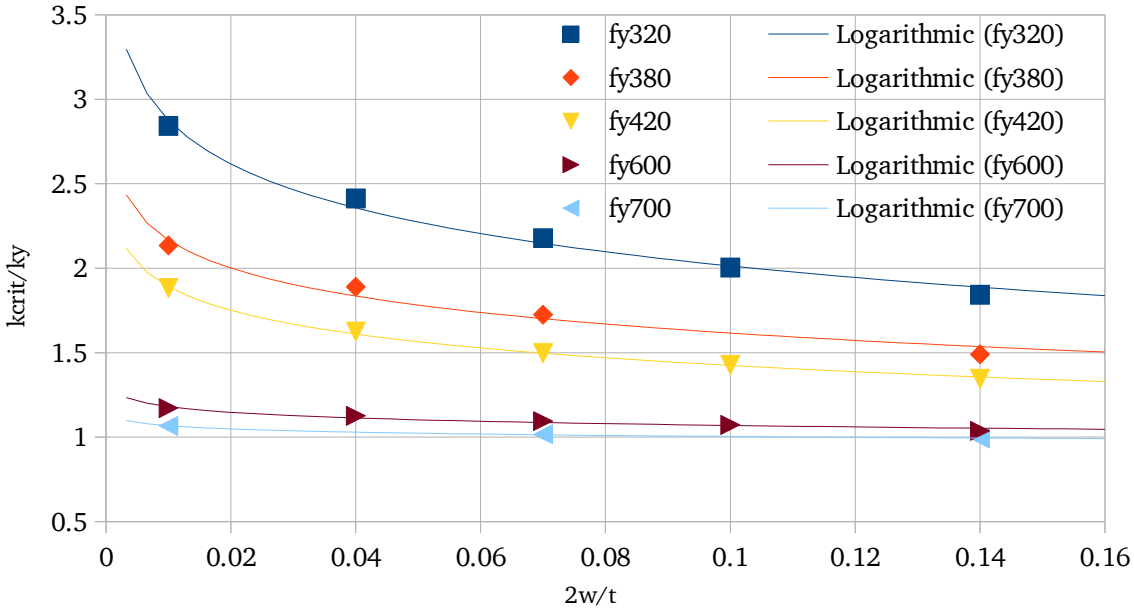

Figure 178: Effect of 2w on k_{kcrit} (D/t =120)

Table 47: Regression analysis for D/t=120 (k_{crit})

f_y (MPa)	**a**	**b**	**R^2**
320	-0.375	1.151	0.988
380	-0.239	1.066	0.970
420	-0.202	0.958	0.998
600	-0.048	0.958	0.946
700	-0.027	0.941	0.994

Linear trendlines have been used to describe the behavior of M_{max}:

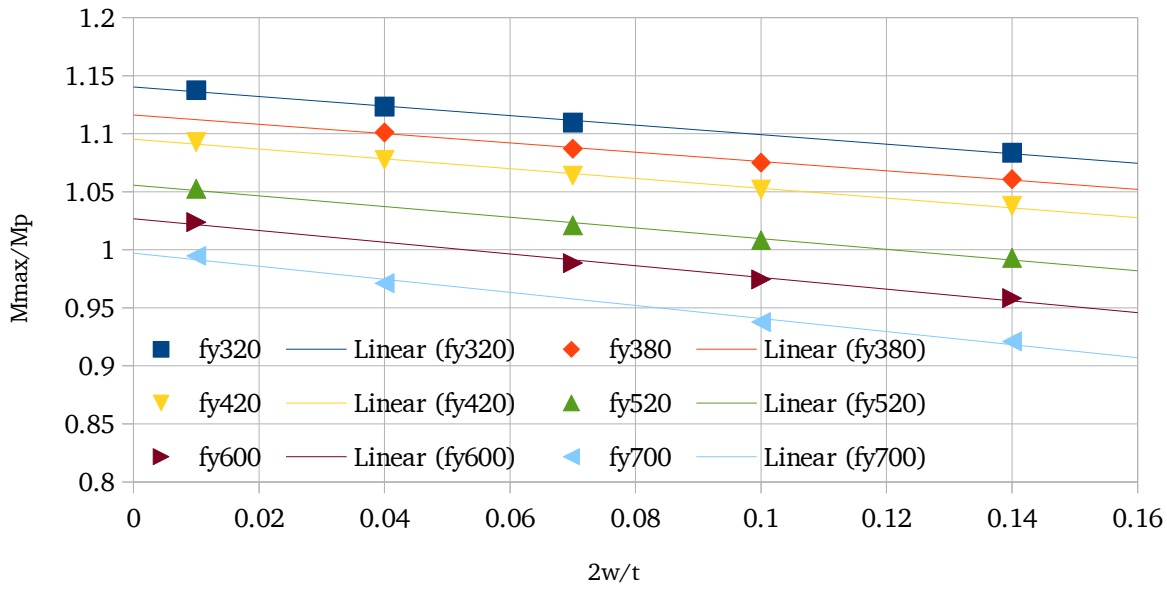

Figure 179: Effect of 2w on M_{max} (D/t =60)

Table 48: Regression analysis for D/t=60 (M_{max})

f_y (MPa)	**a**	**b**	**R^2**
320	-0.411	1.140	0.996
380	-0.401	1.116	0.996
420	-0.421	1.095	0.994
520	-0.460	1.056	0.993
600	-0.507	1.027	0.991
700	-0.563	0.997	0.988

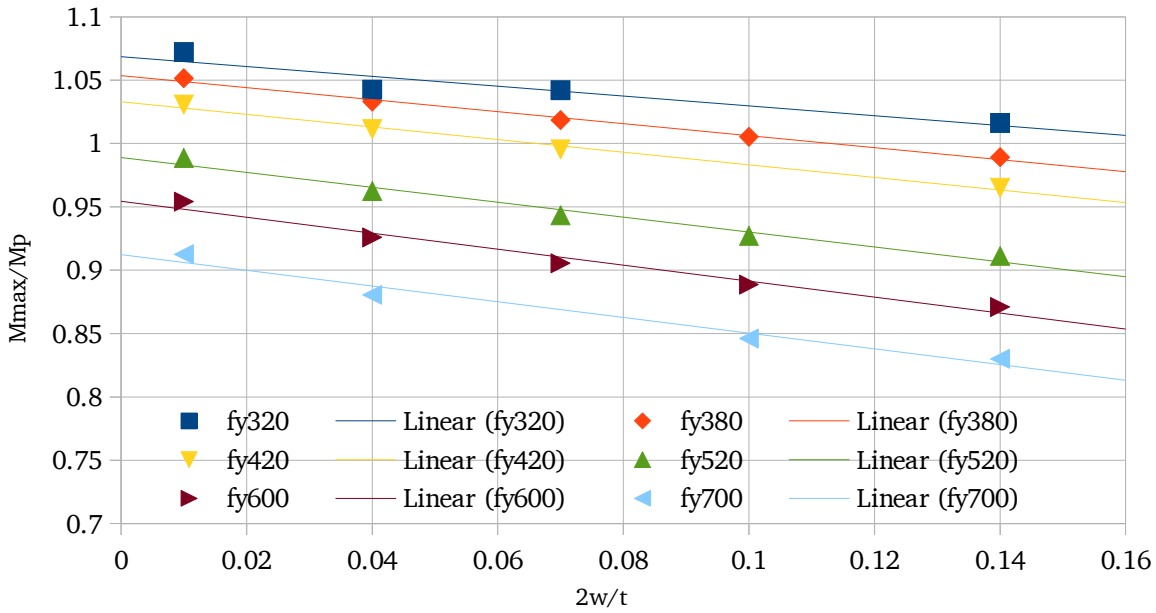

Figure 180: Effect of 2w on M_{max} (D/t =80)

Table 49: Regression analysis for D/t=80 (M_{max})

f_y (MPa)	**a**	**b**	**R^2**
320	-0.388	1.068	0.891
380	-0.474	1.054	0.992
420	-0.498	1.033	0.991
520	-0.588	0.989	0.975
600	-0.631	0.954	0.976
700	-0.619	0.912	0.968

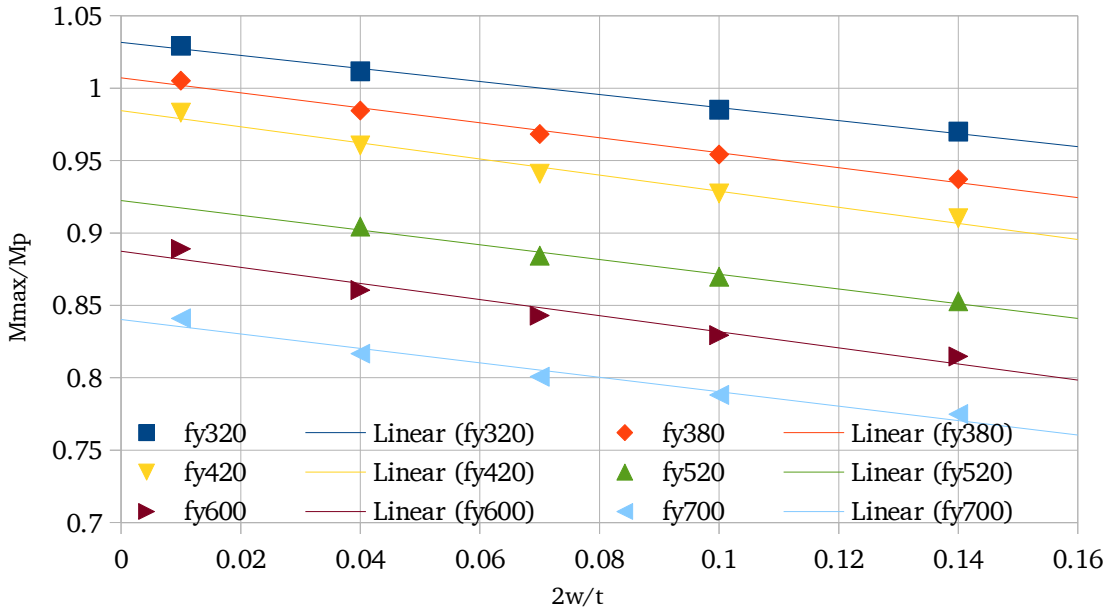

Figure 181: Effect of 2w on M_{max} (D/t =100)

Table 50: Regression analysis for D/t=100 (M_{max})

f_y (MPa)	**a**	**b**	**R^2**
320	-0.451	1.032	0.994
380	-0.517	1.007	0.990
420	-0.556	0.984	0.983
520	-0.510	0.922	0.988
600	-0.556	0.887	0.959
700	-0.498	0.840	0.965

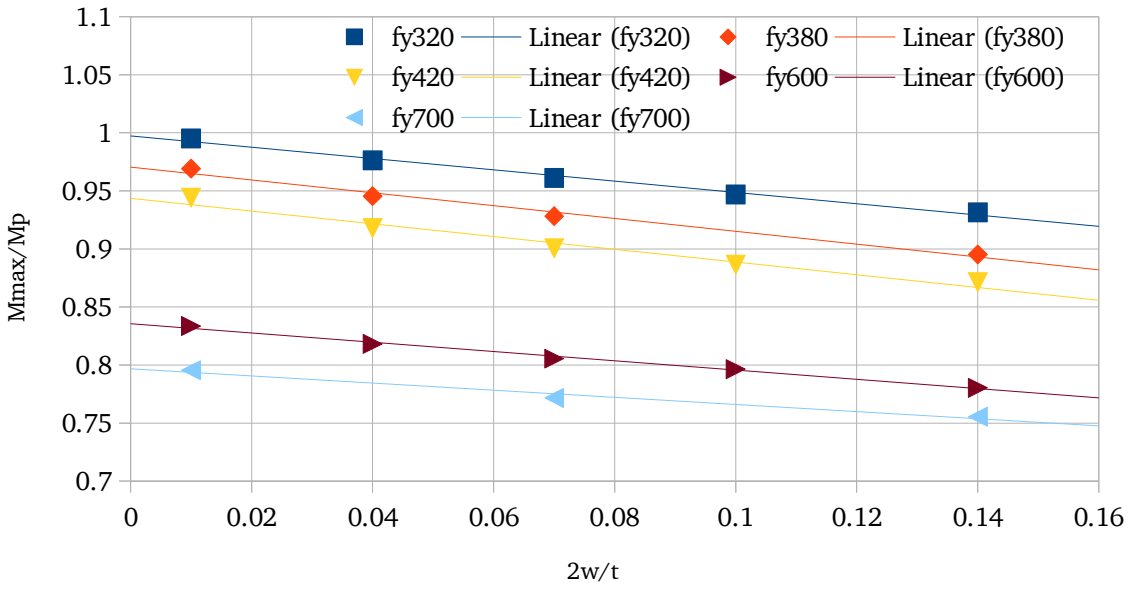

Figure 182: Effect of 2w on M_{max} (D/t =120)

Table 51: Regression analysis for D/t=120 (M_{max})

f_y (MPa)	**a**	**b**	**R^2**
320	-0.487	0.997	0.991
380	-0.554	0.971	0.985
420	-0.549	0.944	0.970
600	-0.400	0.836	0.976
700	-0.307	0.797	0.991

6.4.4 Results: Constant 2w/t

For k_{crit}, power trendlines were usedof the following form:

$$y = ax^{b} \tag{57}$$

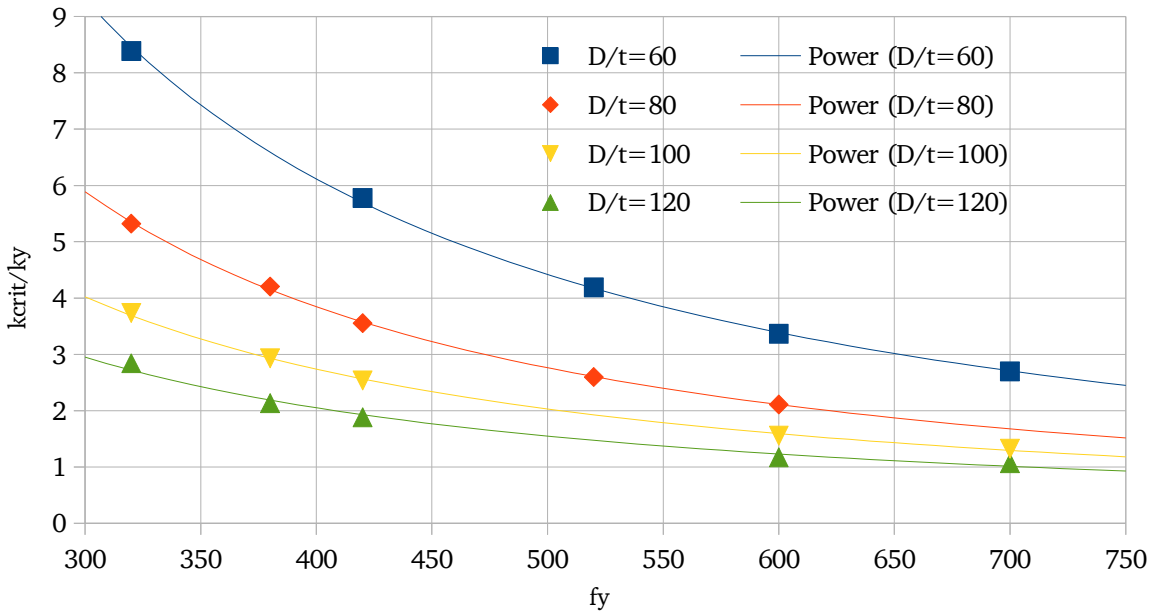

Figure 183: Effect of f_y on k_{crit} (2w/t=0.01)

Table 52: Regression analysis for 2w/t=0.01 (k_{crit})

D/t	a	b	R^2
60	37788.456	-1.457	1.000
80	27649.844	-1.482	1.000
100	8277.596	-1.338	0.998
120	3950.285	-1.262	0.988

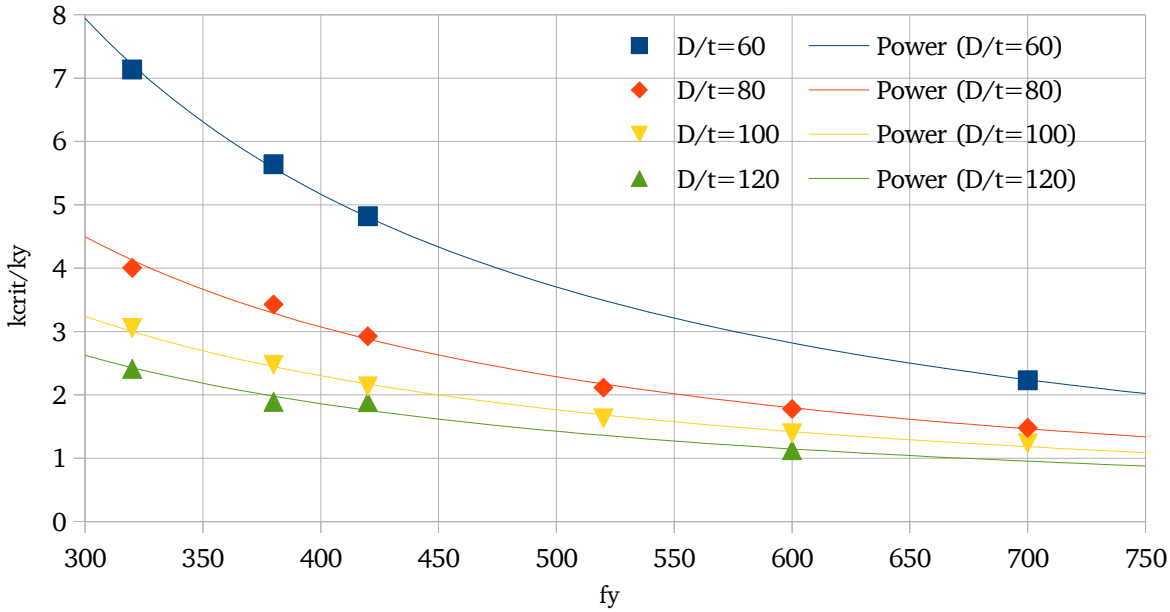

Figure 184: Effect of f_y on k_{crit} (2w/t=0.04)

Table 53: Regression analysis for 2w/t=0.04 (k_{crit})

D/t	a	b	R^2
60	39879.275	-1.494	1.000
80	8498.904	-1.323	0.995
100	2854.452	-1.189	0.994
120	2392.445	-1.195	0.976

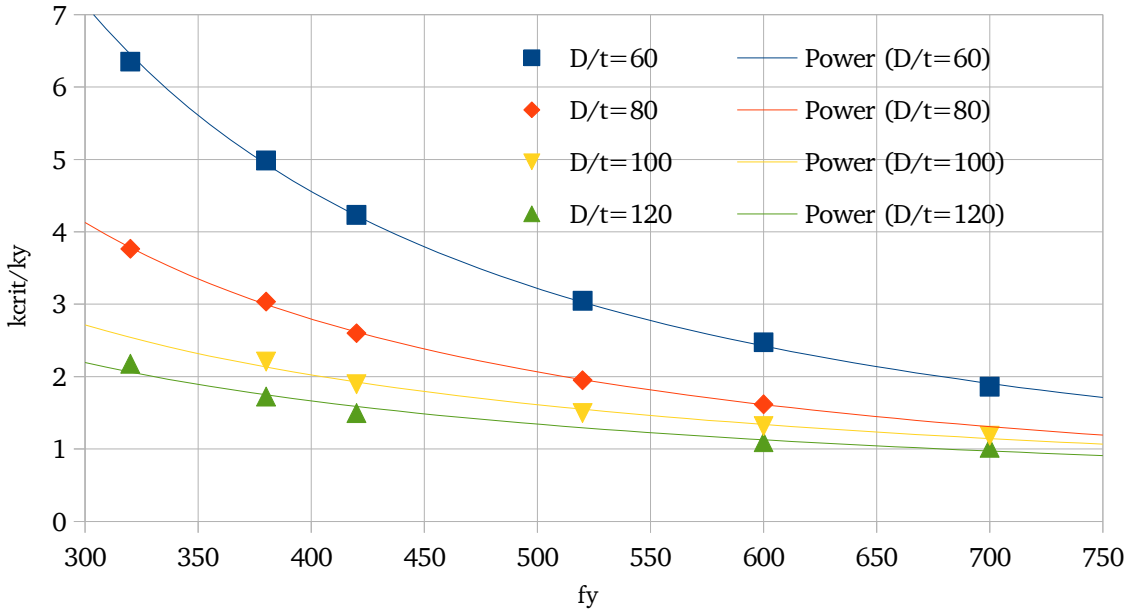

Figure 185: Effect of f_y on k_{crit} (2w/t=0.07)

Table 54: Regression analysis for 2w/t=0.07 (k_{crit})

D/t	a	b	R^2
60	51791.815	-1.559	0.999
80	9444.300	-1.356	0.999
100	910.209	-1.020	0.984
120	530.645	-0.962	0.976

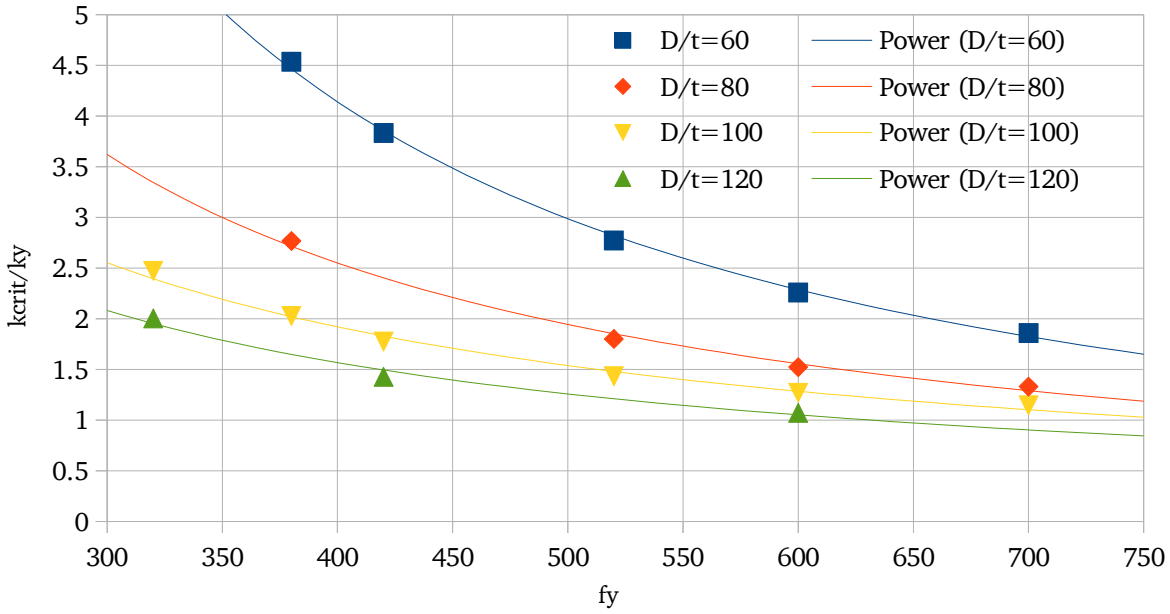

Figure 186: Effect of f_y on k_{crit} (2w/t=0.1)

Table 55: Regression analysis for 2w/t=0.1 (k_{crit})

D/t	a	b	R^2
60	26622.600	-1.464	0.998
80	3749.952	-1.217	0.991
100	729.592	-0.991	0.989
120	571.837	-0.985	0.984

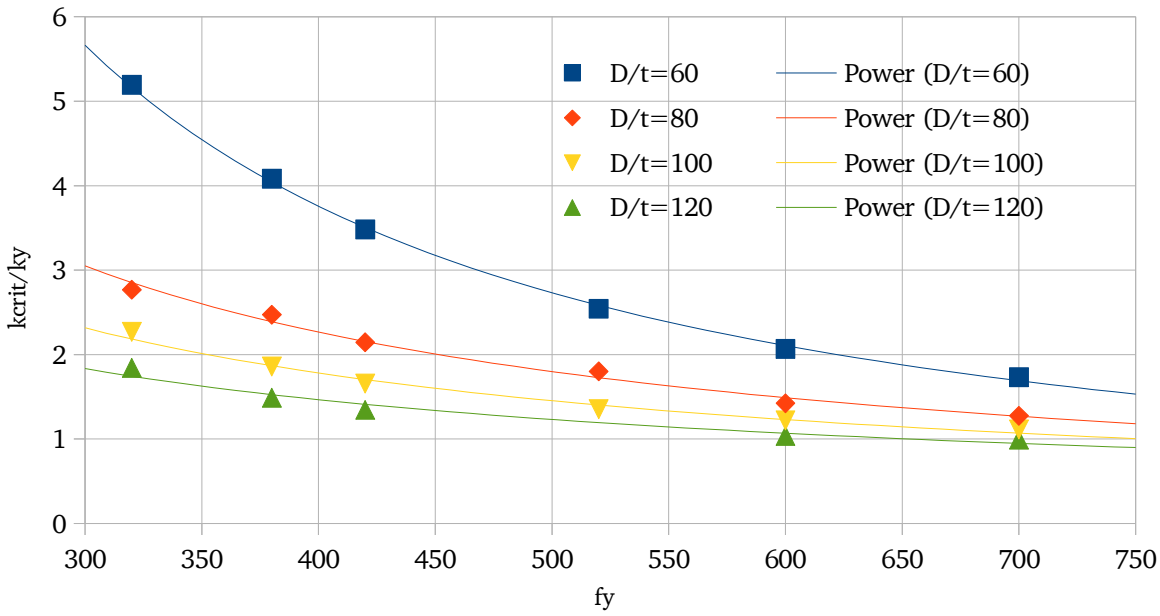

Figure 187: Effect of f_y on k_{crit} (2w/t=0.14)

Table 56: Regression analysis for 2w/t=0.14 (k_{crit})

D/t	a	b	R^2
60	19401.609	-1.427	0.998
80	1114.122	-1.03	0.987
100	420.737	-0.912	0.985
120	155.976	-0.779	0.967

For M_{max}, linear trendlines were used.

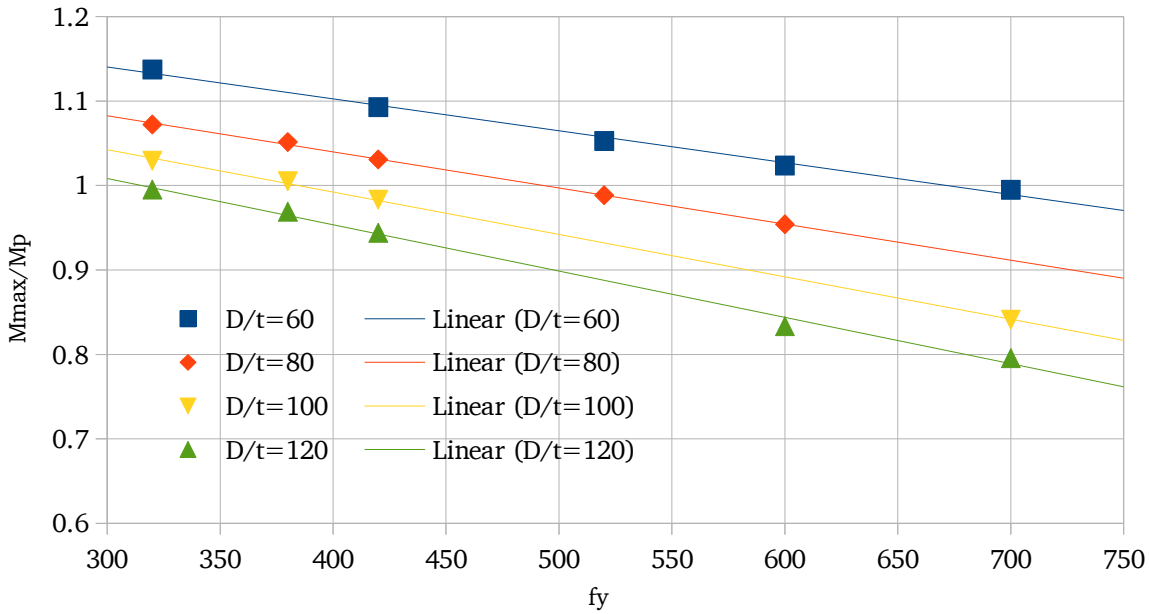

Figure 188: Effect of f_y on M_{max} (2w/t=0.01)

Table 57: Regression analysis for 2w/t=0.01 (M_{max})

D/t	a	b	R^2
60	-0.000377	1.254	0.993
80	-0.000427	1.211	0.999
100	-0.000502	1.193	0.999
120	-0.000548	1.173	0.994

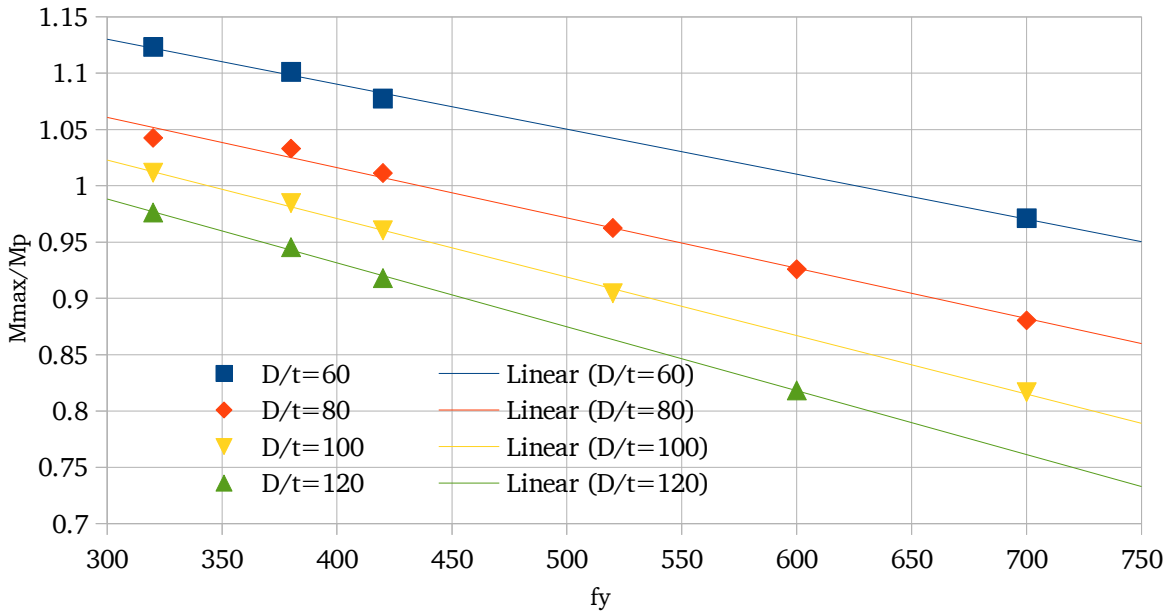

Figure 189: Effect of f_y on M_{max} (2w/t=0.04)

Table 58: Regression analysis for 2w/t=0.04 (M_{max})

D/t	a	b	R^2
60	-0.000399	1.250	0.998
80	-0.000447	1.195	0.992
100	-0.000519	1.179	0.999
120	-0.000568	1.159	0.999

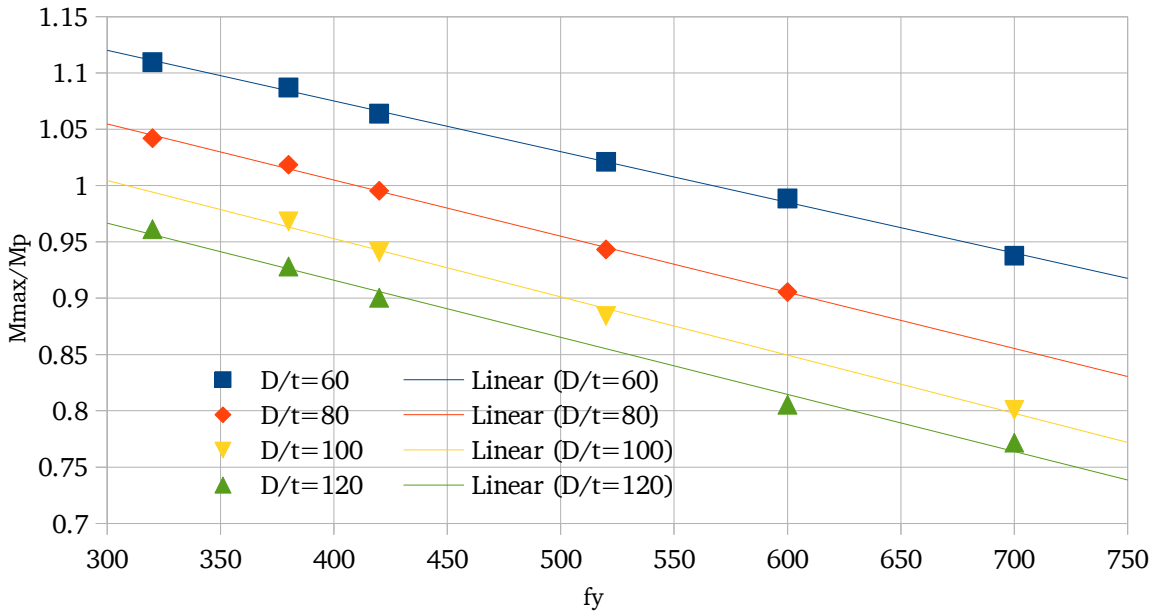

Figure 190: Effect of f_y on M_{max} (2w/t=0.07)

Table 59: Regression analysis for 2w/t=0.07 (M_{max})

D/t	a	b	R^2
60	-0.000450	1.255	0.998
80	-0.000498	1.204	0.998
100	-0.000517	1.160	0.995
120	-0.000507	1.119	0.993

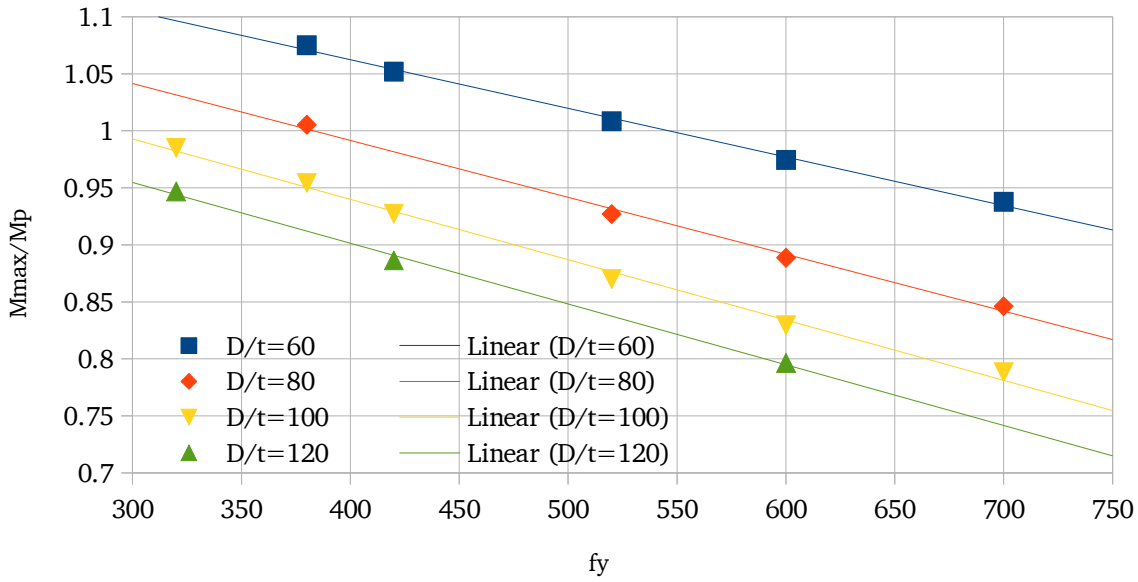

Figure 191: Effect of f_y on M_{max} (2w/t=0.1)

Table 60: Regression analysis for 2w/t=0.1 (M_{max})

D/t	a	b	R^2
60	-0.000426	1.232	0.996
80	-0.000499	1.191	0.995
100	-0.000529	1.152	0.995
120	-0.000533	1.114	0.997

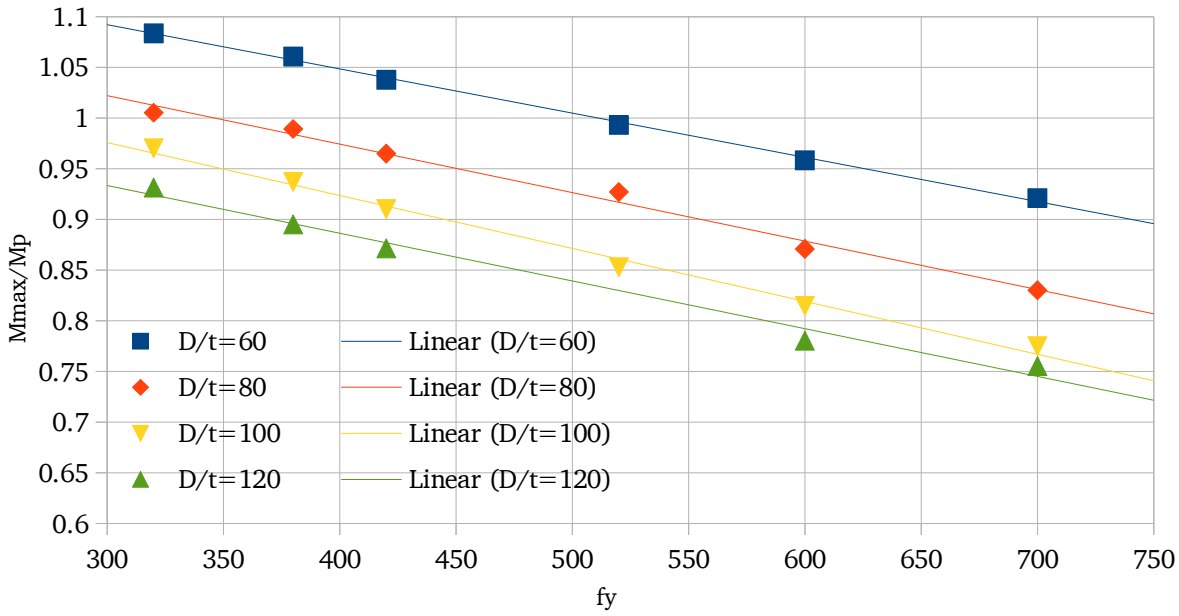

Figure 192: Effect of f_y on M_{max} (2w/t=0.14)

Table 61: Regression analysis for 2w/t=0.14 (M_{max})

D/t	a	b	R^2
60	-0.000436	1.223	0.998
80	-0.000479	1.166	0.990
100	-0.000522	1.132	0.993
120	-0.000471	1.075	0.985

6.4.5 Statistical Analysis of 3 Variable Parameter Study

In this section, a regression analysis is performed on the results of the parameter study. A full table of results can be found in Appendix F.

First, some definitions are given:

SE = standard error

t_{crit} = critical t-value for 95% confidence

$t_{observed}$ = observed t-value

p = p-value corresponding to t-distribution

R^2 = coefficient of determination

F = observed F-value

F_{crit} = critical F-value for 95% confidence

SS = sum of squares

d.f. = degrees of freedom

n = sample size

The following linear model is suggested to predict M_{max}:

$$M_{max} = a_1(2w/t) + a_2(fy) + a_3(D/t) + a_0 \quad (58)$$

The results of the multiple regression analysis using this model are shown in Table 62.

Table 62: Multiple regression analysis for M_{max}

	a_1	a_2	a_3	a_0
Estimate	-3111.180	10.006	-93.651	10238.944
SE	1597.715	0.559	3.337	430.242
$t_{observed}$	1.947	17.891	28.067	23.798
p	0.054	0.000	0.000	
R^2	0.923	717.779	SE_{Mmax} **(kNm)**	
F	378.187	94	**d.f.**	
$SS_{regression}$	584532335.671	48429394.006	$SS_{residual}$	
t_{crit}	1.986	98	**n**	
F_{crit}	2.701			

Based on this regression, it is possible to calculate the expected values of M_{max} for every combination of 2w/t, f_y, and D/t. The results are shown in Figure 194. The x-axis shows the result predicted by the regression model, while the y-axis shows the value calculated using ABAQUS®. The dashed red line shows the regression model itself.

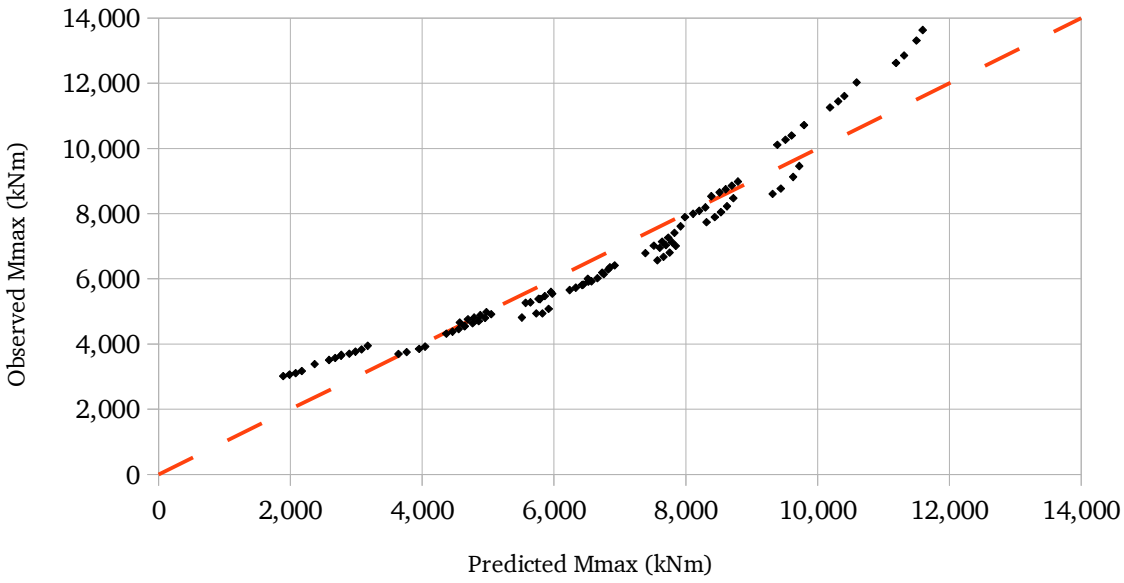

Figure 193: Accuracy of regression model for predicting M_{max} of parameter study

Finally, the total possible influence of each parameter was calculated. The results are shown in Table 63.

Table 63: Influence of parameters on M_{max}

	Minimum	**Maximum**	**Influence (kNm)**
2w/t	0.01	0.14	404.5
f_y	320	700	3,802.3
D/t	60	120	5,619.1

A similar analysis has been performed for k_{crit}, but in this case a power model is used:

$$\ln(k_{crit}) = a_1 \ln(2w/t) + a_2 \ln(f_y) + a_3 \ln(D/t) + a_0 \quad (59)$$

The results of the regression analysis are presented in Table 64.

Table 64: Multiple regression analysis for k_{crit}

	a_1	a_2	a_3	a_0
Estimate	-0.145	-0.246	-1.360	9.387
SE	0.008	0.030	0.031	0.234
$t_{observed}$	17.209	8.284	43.485	40.100
p	0.000	0.000	0.000	
R2	0.959	1.081	**SE_{Mmax} (10^6 /mm)**	
F	728.274	94	**d.f.**	
$SS_{regression}$	13.413	0.577	$SS_{residual}$	
t_{crit}	1.986	98	**n**	
F_{crit}	2.701			

As with M_{max}, the accuracy of the regression model in predicting the results of the parameter study are investigated.

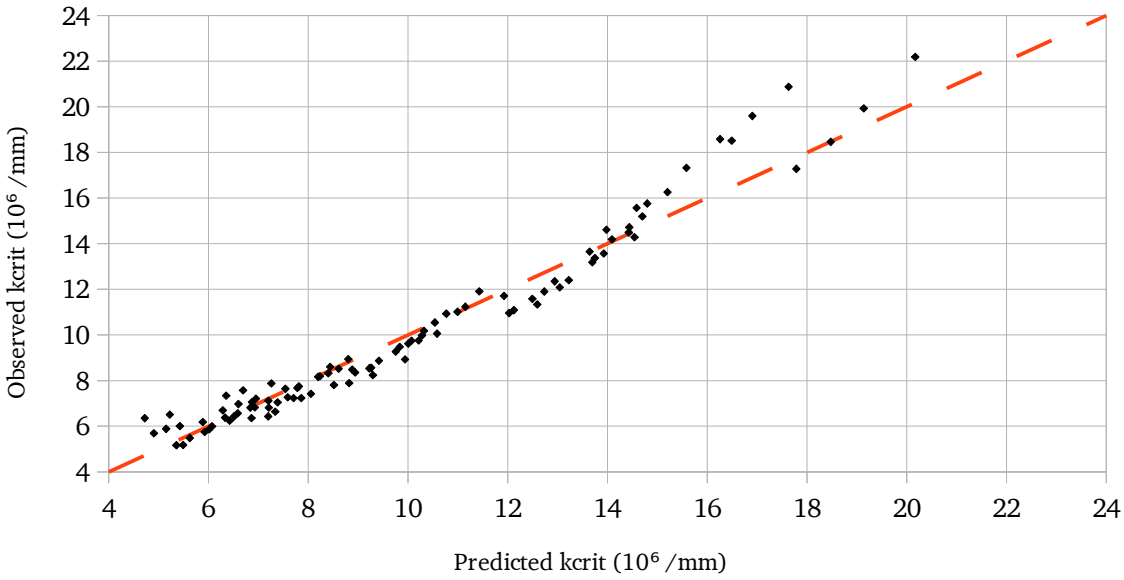

Figure 194: Accuracy of regression model for predicting k_{crit} of parameter study

Table 65: Influence of parameters on k_{crit}

	Minimum	Maximum	Influence (10^6 /mm)
2w/t	0.01	0.14	6.83
f_y	320	700	2.57
D/t	60	120	7.38

Finally, it was attempted to find optimal combinations of parameters to find the best balance between k_{crit} and M_{max}. This was done by plotting k_{crit} against M_{max}. The values plotted here are the values from the FEM analyses, not from the regression analyses.

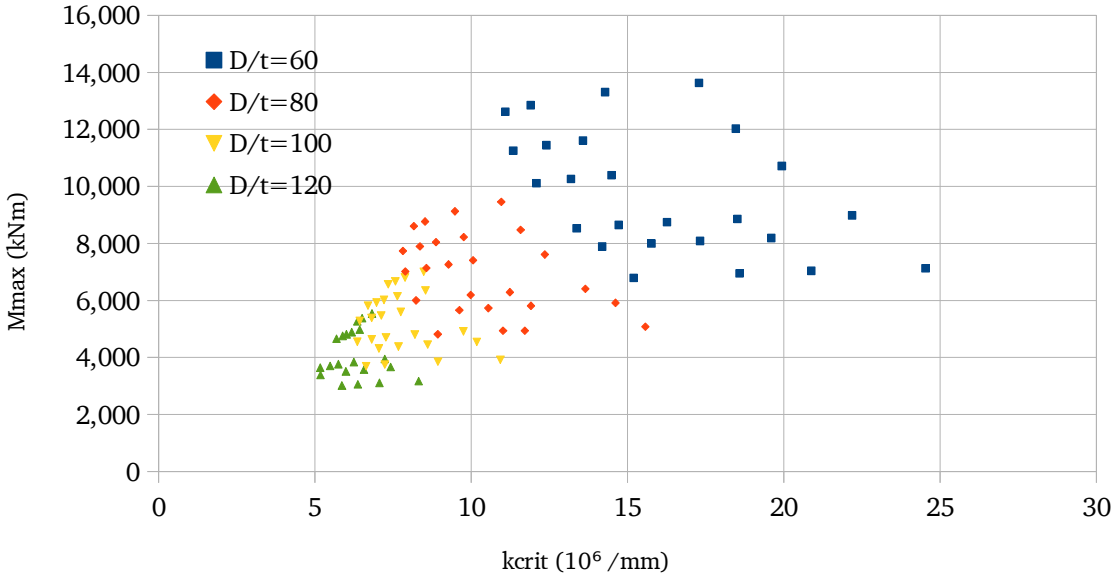

Figure 195: Combinations of k_{crit} and M_{max}

6.4.6 Discussion

First, the case is investigated where f_y is held constant. In this case, it is found that k_{crit}/k_y decreases logarithmically as 2w/t increases. For any given yield strength, it is shown that k_{crit}/k_y decreases more rapidy for tubes with lower D/t. Finally, it is found that for any D/t, k_{crit}/k_y also decreases more rapidly for tubes with lower yield strength.

These observations make sense because it is already known that imperfections do not change the shape of the pre-buckling equilibrium path. This means that the effect of 2w depends completely on the equilibrium path's shape due to other factors. In fact, an increase in D/t tends to increase ductility by increasing the critical curvature k_{crit}, without changing k_y. On the other hand, an increase in f_y tends to decrease ductility by increasing M_{max} at the expense of k_{crit}. This effect also increases the slope of the equilibrium path between k_y and k_{crit}. This means that for tubes with a low D/t ratio or low yield strength, 2w/t should influence k_{crit} more than M_{max}.

This is partially confirmed in the figures showing the effect of 2w/t on M_{max}. In this case, the trend was always linear, and as expected, the slope of the trendline generally increased upon increasing f_y and D/t, but only up to a point. For tubes with both high D/t and high f_y, it was found that 2w/t did not affect M_{max} as significantly. It is thought that this is due to the fact that it is the combined effect of D/t and f_y that influences the shape of the equilibrium path, and for some combinations it simply results in a less sensitive tube. In any case, the effect of 2w/t on M_{max} is relatively small for any of the investigated tubes.

In the next section, D/t is held constant and the effect of 2w/t is investigated on tubes with various yield strengths. The graphs in this section are simply another way of visualizing the effect of 2w/t, and the results are similar. Once again, k_{crit}/k_y decreases logarithmically upon increasing 2w/t, and the effect is most pronounced for tubes with low D/t ratio and low f_y. M_{max}/M_p decreases linearly upon an increase in 2w/t, and the slope of the trendline increases upon an increase in f_y for tubes with both low D/t and low f_y. This trend becomes much less pronounced for tubes with high D/t and high f_y.

When 2w/t is held constant and f_y is varied, the results are very interesting. In this case, it can be seen that the influence of f_y on k_{crit}/k_y is nonlinear. In fact, the relationships can be described with power trendlines. k_y linearly depends on f_y, so this means that the nonlinearity is in k_{crit}, and that the reduction in k_{crit} caused by an increasing f_y diminishes at higher yield strengths. k_{crit} is more significantly affected at lower D/t ratios, for reasons explained above. The effect on M_{max} is linear.

In the final section, a multiple regression analysis has been performed to derive equations to predict k_{crit} and M_{max} based on 2w/t, f_y, and D/t. First, the model for M_{max} is investigated. The results show that the regression is significant, because the observed F value is several orders of magnitude higher than the critical F value, which means that the probability that all of the regression constants are zero is very small. It can also be seen that the coefficient of determination is 0.923, and that the standard of error is 717.8 kNm. This is an error of about 10% of the average tube capacity, which is acceptable.

It can also be seen that the observed t value for 2w is smaller than the critical t value, and that the p-value for 2w is 0.054. *This means that 2w is less significant than the other parameters.* A p-value of 0.054 means that there is a 5.4% chance of obtaining the same prediction if the coefficient a_1 were taken as zero. 2w is therefore still an important parameter, just less significant than the other two parameters. In addition, Table 63 shows that 2w has less potential to influence M_{max} in the considered ranges of the parameters. Finally, in Figure it can be seen that the accuracy of the regression decreases at the extremes; that is, it decreases at high or low combinations of f_y and D/t.

The regression analysis for k_{crit} is similar. The regression is shown to be significant because the observed F value is significantly greater than the critical F value. The correlation was found to be 0.959 and the standard error was 1.081, which is also about 10% of the average tube capacity. However, in this case, it was found that all of the parameters are significant in predicting k_{crit}, although Table 65 shows that f_y has less potential to influence k_{crit} than the other parameters. As with M_{max}, it is found that the regression becomes less accurate for higher strength tubes.

Finally, it was decided use the regression equations to find the most favorable conditions. Since the equation for M_{max} is linear, capacity can be maximized by setting f_y=700 and D/t=60 while minimizing 2w/t. The equation for k_{crit} is also linear if a log transform is taken, and in this case, k_{crit} can be maximized if f_y=320 and D/t=120 while 2w/t is minimized. Since these results indicate that there is no single ideal tube, M_{max} and k_{crit} were plotted against each other in Figure 195. This figure shows that many values of M_{max} can be achieved with a wide range of tubes. However, the tubes with lower D/t ratios tended to give the highest critical curvatures, indicating that in general it may be more desirable to use a thicker tube with a lower yield strength for design rather than a thinner tube with a higher strength.

6.4.7 Conclusions and Recommendations

In this section, four parameters were investigated: D/t, imperfection height, yield strength, and residual stress ratio. The studies on the real tubes show that all of these parameters are significant. The most significant parameter for k_{crit} is the imperfection height 2w, because the logarithmic trend means that a very small change in 2w causes a significant drop in k_{crit}. 2w is also thought to be significant because the results of Section 5 show that it is very difficult to relate the measured imperfections to a buckling mode amplitude. Questions remain about how to do this most appropriately and whether or not this is the best way of introducing imperfections.

Residual stresses were also found to influence k_{crit} significantly, especially at low D/t ratios. This is also a significant parameter because it is very difficult to estimate the magnitude of these stresses, since they come from several sources and can vary depending on which part of a coil the plate came from to produce a tube, etc.

D/t was found to have a nonlinear effect on k_{crit}. This is a significant result because it means that a small increase in D/t can cause a significant decrease in k_{crit}. The effect of f_y on k_{crit} was similarly nonlinear, although it is shown that f_y has less potential to influence k_{crit} than D/t. Together, these results suggest that, from a purely mechanical point of view, it may be more efficient to use low strength steels and thick tubes rather than high strength steels and thin tubes. However, data is missing because it is not known if it is more cost effective to use more low strength steel or less high strength steel.

In terms of M_{max}, all parameters were found to influence capacity linearly. Residual stresses do not influence M_{max} significantly. The effect of 2w on M_{max} is less significant than the effects of f_y or D/t, but it is still a factor, especially in the case of the real tubes.

In summary, D/t is found to be the most influential parameter for both k_{crit} and M_{max}, but D/t is also one of the most certain parameters because it is directly controlled in the manufacturing process. The most uncertain parameter by far is 2w/t, which is found to have a significant influence on k_{crit}, and it was also found to be difficult to relate the measured imperfections to the imposed imperfections. Residual stresses are also quite uncertain and are thought to influence k_{crit} significantly, but they were not analyzed as rigorously in this study. Neither of these parameters influenced M_{max} significantly, but M_{max} is very highly influenced by f_y. Overall, there is much less uncertainty in M_{max} because the most uncertain parameters do not influence M_{max} as strongly.

Recommendations for further research in this area are to relate the material data that was used to the actual measured material models, but in a way where it can be scaled based on f_y. This introduces an added level of complexity because it likely requires the introduction of a yield plateau, and then it must be determined if the yield plateau should be scaled based on f_y or not, and what the general effect of this parameter is. It is also possible that several material models may be required. If this is done successfully, a multiple regression analysis could be performed on the results and used to predict the experimental results. If this were done, it is also thought that M_{max} could be predicted with a very high level of accuracy.

It is also recommended to further study the imperfections, and in particular, to investigate new ways of introducing imperfections into the FEM models and to investigate different ways of relating the size of the imposed imperfections to the height of the actual imperfections in the tubes. Finally, it is recommended to include cost as a parameter in order to find optimal combinations of D/t and f_y for various design situations.

7 Analysis of Analytical Model

7.1 Approach and Methods

In order to verify the analytical model, FEM models were created with elastic-perfectly-plastic material models. Five different types of tubes were used for this study: Tubes 5 and 9 from the experimental program, a 30mm tube, a 40mm tube, and an 80mm tube. The 30mm and 40mm tubes were included to verify the ovalization model of Gresnigt at higher D/t ratios, and the impractical 80mm tube was included because it was desirable to compare with the behavior of a tube not subject to buckling. These thicknesses were chosen so that a tube from each cross sectional class would be represented. The parameters of the considered tubes are shown in Table 66.

Table 66: Geometry of tubes used for initial verification of FEM models

Tube	**5**	**9**	**30mm**	**40mm**	**80mm**
d (mm)	1067	1067	1067	1067	1067
t (mm)	9	16.4	30	40	80
f_y (MPa	400	570	540	540	540
D/t	118.6	65.1	35.6	26.7	13.4
λ_s	201.9	157.7	81.8	61.4	24.5
Section Class	4	4	3	2	1

For the 30mm, 40mm, and 80mm tubes, it was decided to use a yield strength of 540 MPa. For the other tubes, it was decided to use the stress at 0.2% plastic strain from the average curves given in Appendix A as a representative yield stress. The final chosen material properties are summarized in Table 67.

Table 67: Material properties used for initial verification

	Tube 5	**Tube 9**	**30mm**	**40mm**	**80mm**
E	205,000 MPa	205,000 MPa	205,000 MPa	205,000 MPa	205,000 MPa
ν	0.3	0.3	0.3	0.3	0.3
f_y	400 MPa	570 MPa	540 MPa	540 MPa	540 MPa

7.2 Results

The results are presented below in the form of moment-curvature and ovalization-curvature relations.

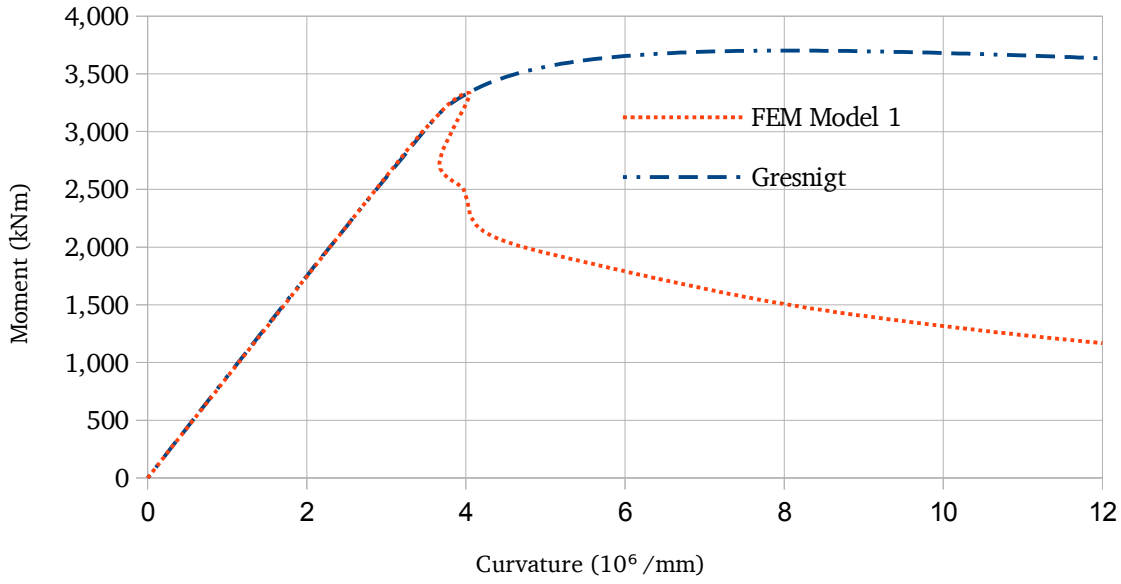

Figure 196: Elastic-perfectly-plastic moment-curvature relations for Tube 5

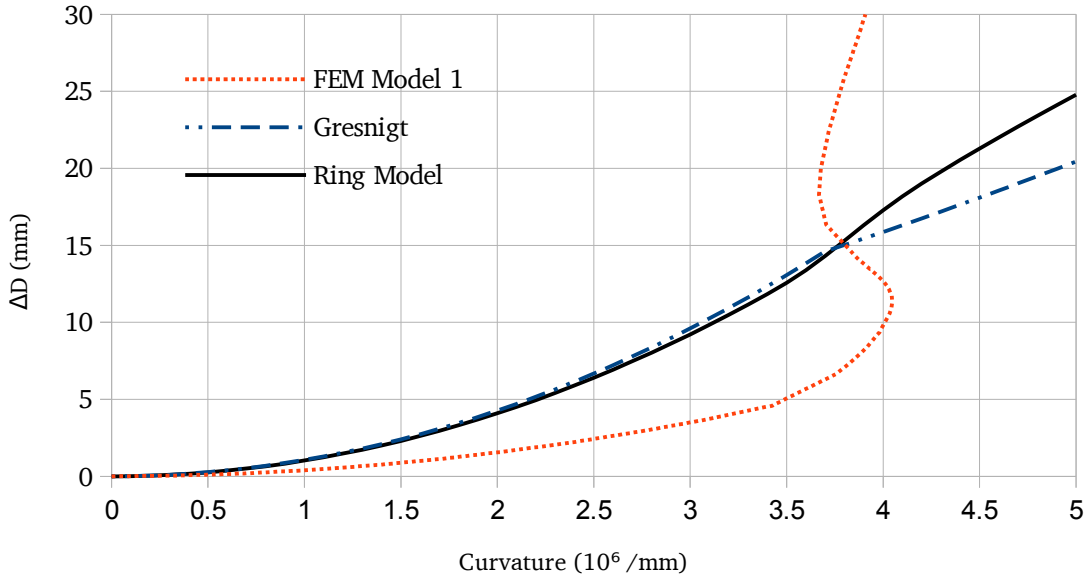

Figure 197: Elastic-perfectly-plastic ovalization-curvature relations for Tube 5

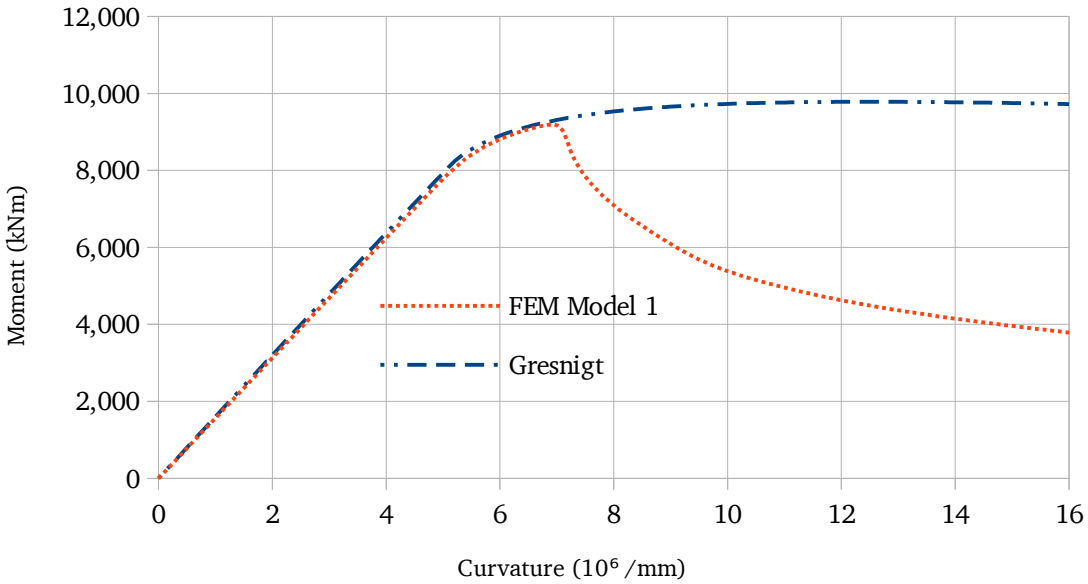

Figure 198: Elastic-perfectly-plastic moment-curvature relations for Tube 9

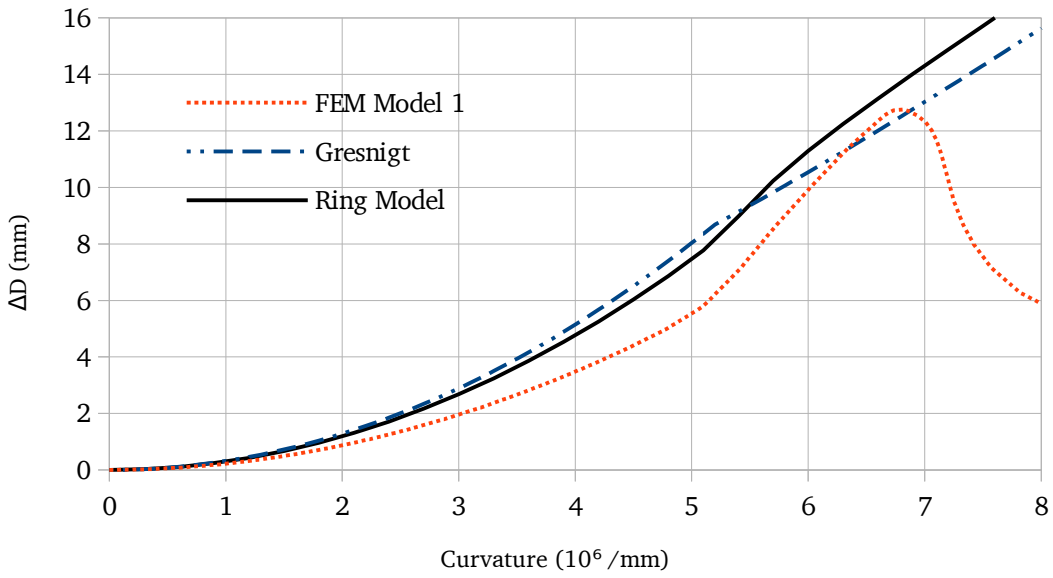

Figure 199: Elastic-perfectly-plastic ovalization-curvature relations for Tube 9

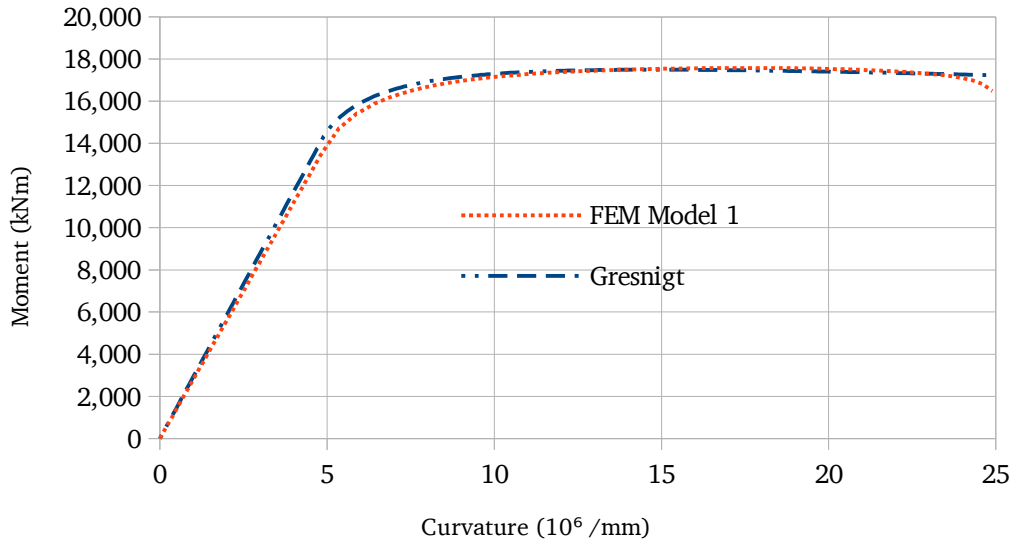

Figure 200: Elastic-perfectly-plastic moment-curvature relations for 30mm tube

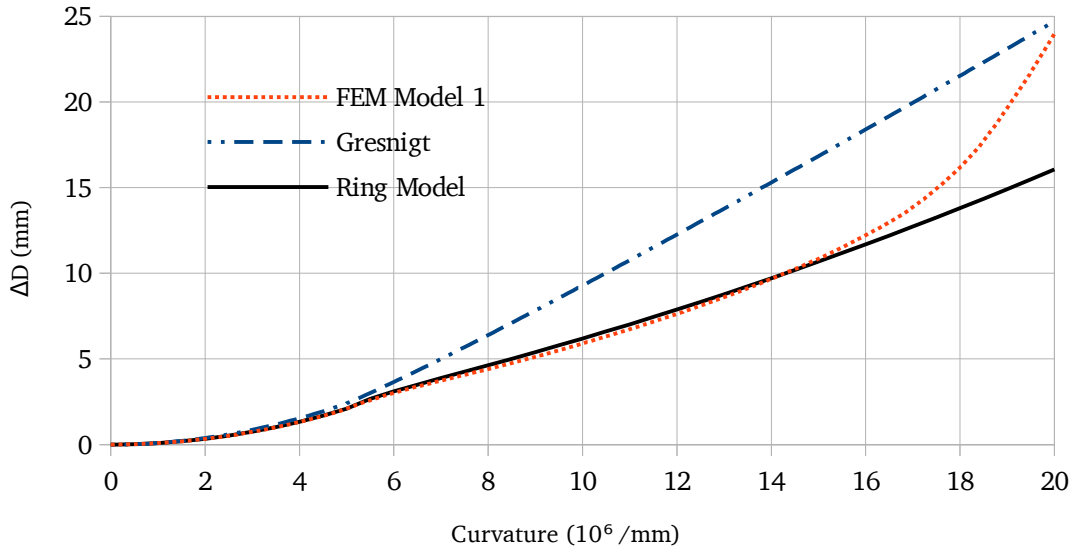

Figure 201: Elastic-perfectly-plastic ovalization-curvature relations for 30mm tube

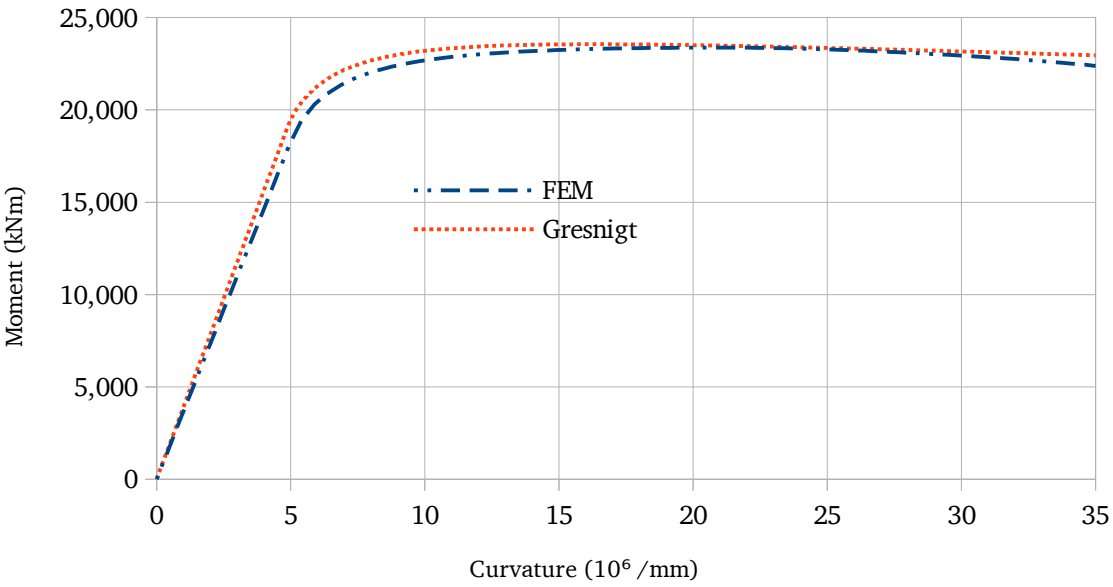

Figure 202: Elastic-perfectly-plastic moment-curvature relations for 40mm tube

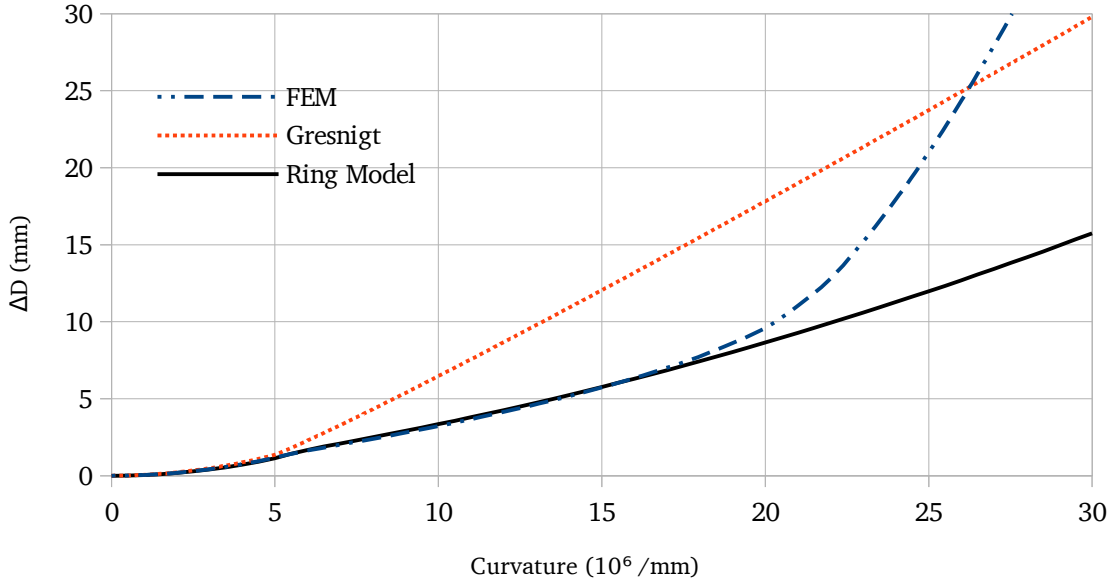

Figure 203: Elastic-perfectly-plastic ovalization-curvature relations for 40mm tube

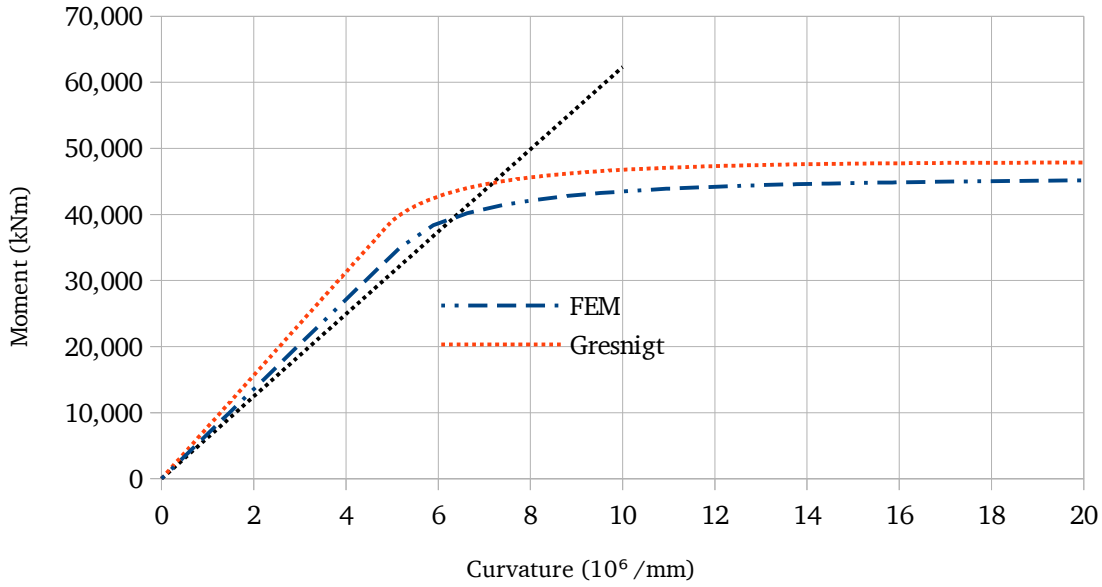

Figure 204: Elastic-perfectly-plastic moment-curvature relations for 80mm tube

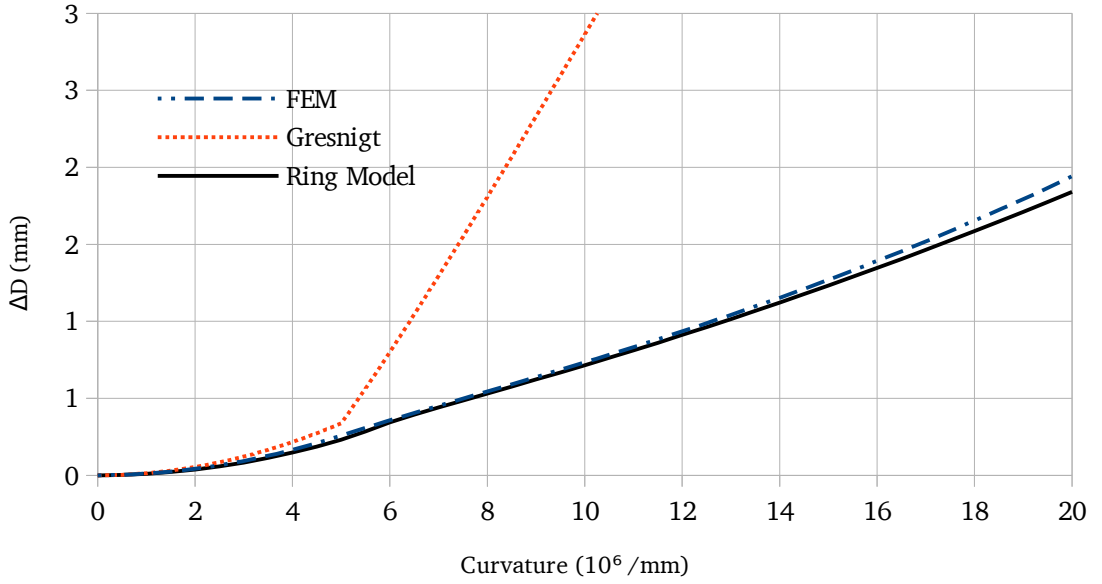

Figure 205: Elastic-perfectly-plastic ovalization-curvature relations for 80mm tube

7.3 Discussion

Figures 196-199 show good agreement in the pre-buckling equilibrium path for Tubes 5 and 9. In terms of ovalization, there is good agreement between the analytical model and the ring models. Model 1 underestimates these models, especially for Tube 5, suggesting that ovalization is being restrained due to the support conditions.

Figures 200-205 show an increasing deviation from the FEM solution as D/t decreases. This is due to the fact that the Gresnigt solution uses a single equation to describe the entire equilibrium path. In particular, it is due to the fact that Eqn. 33 poorly approximates the true elastic solution at low D/t ratios. There is also a strong deviation between the analytical model and the other models in terms of ovalization.

7.4 Conclusions and Recommendations

In this section, it is shown that there is good moment-curvature agreement between the analytical solution and Model 1 for tubes in the range of D/t ratios used in tubular piles ($60<D/t<120$). In terms of ovalization, it is shown that there is good agreement between the analytical model and the ring model in the elastic phase, while the FEM model underestimates the true ovalization. The analytical ovalization model is found to deviate from the ring model after yielding, but it is thought that ovalization has little effect on the pre-buckling behavior of the tubes, and it is also noted that for tubes in this D/t range, little plasticity is expected prior to buckling.

Finally, as D/t decreases, it is shown that there is an increasingly serious deviation from the FEM solution.

8 Overall Conclusions and Recommendations for Further Research

This research project has shown that there are still many unanswered questions about steel tubes, a deceivingly simple type of structural element. One of the major topics of this work was to analyze and characterize the imperfections measured during experimental testing. It was found that imperfections most significantly influence k_{crit}, especially at low D/t ratios and low yield strengths. It was found that FEM Model 1 could estimate k_{crit} much better than the analytical solution, but that there was still a significant error in this estimation. Therefore, it is concluded that one of the major focus areas for further research should be to improve the techniques used to account for imperfections. This work should focus not only on how to incorporate imperfections into FEM models, but also on answering the question of which imperfection height/shape is truly relevant, especially in the case of girth and coil connection welded tubes.

D/t, f_y, and residual stresses were also all significant in estimating k_{crit}. It is thought that the most important of these parameter is the residual stresses, because there is the largest uncertainty in this parameter. D/t has the largest influence, but it can be controlled very well. f_y has the smallest influence, and it is believed that simplified material models can be developed based on f_y to increase certainty in this parameter, but residual stresses have many sources and their influence is not yet well understood.

It was much easier to predict M_{max} than k_{crit}, mainly due to the fact that there is more certainty in the parameters which influence M_{max}. Therefore, it is concluded that perhaps stress-based design should not be thrown away completely as an alternative to strain-based design, at least until k_{crit} can be predicted with sufficient accuracy. Very preliminary evidence is also found suggesting that it is not a critical strain but a critical stress that is relevant for buckling, because it was found that the strain at buckling was lower in Model 2 compared to Model 1. The exact differences between the two FEM models are still unknown, however, althought it is thought to be a geometric effect. It is concluded that the only way to truly understand is to create a FEM model which allows free ovalization at the supports. Nevertheless, it is thought that ovalization has only a small influence on the capacity of the tubes. It is also shown that the FEM models are no more accurate in predicting M_{max} than the analytical solution is.

Finally, it is concluded that the material model has a profound effect, especially on M_{max} and on the shape of the equilibrium path itself. It is thought that a material model can be created which approximates the true material properties, and which can be scaled based on f_y. It is thought that thought that this type of model should be used to perform a parameter study like the one described in this report, and that the results of this type of study should be used to estimate the experimental results. The results of the current study have shown that it is possible to predict the behavior of the tubes used in the parameter study, and it is thought that the final key to the puzzle is to create a regression model based on 2w/t, D/t, and f_y which can accurately predict the behavior of real tubes. Given the high correlation between these parameters and the resulting effect on k_{crit} and M_{max}, it is thought that this is entirely possible if imperfections could be measured and incorporated more appropriately and if a representative material model could be found.

References

Ades, C. S. (1957). “Bending Strength of Tubing in the Plastic Range.” *Journal of the Aeronautical Sciences (Institute of the Aeronautical Sciences)*, 24(8).

Brazier, L. G. (1927). “On the Flexure of Thin Cylindrical Shells and Other ‘Thin’ Sections.” *Proceedings of the Royal Society A: Mathematical, Physical and Engineering Sciences*, 116(773), 104–114.

Elchalakani, M., Zhao, X. L., and Grzebieta, R. (2002a). “Bending Tests to Determine Slenderness Limits for Cold-Formed Circular Hollow Sections.” *Journal of Constructional Steel Research*, 58(11), 1407–1430.

Elchalakani, M., Zhao, X. L., and Grzebieta, R. H. (2002b). “Plastic Mechanism Analysis of Circular Tubes under Pure Bending.” *International Journal of Mechanical Sciences*, 44(6), 1117–1143.

Van Es, S. H. J., Gresnigt, A. M., Kolstein, M. H., and Bijlaard, F. S. K. (2013). “Local Buckling of Spirally Welded Tubes – Analysis of Imperfections and Physical Testing.” *The proceedings of the Twenty-third (2013) International Offshore and Polar Engineering Conference Anchorage, Alaska, June 30-July 5, 2013*.

Eurocode 3 - Design of Steel Structures - Part 1-1: General Rules and Rules for Buildings. (2005). European Committee for Standardization.

Eurocode 3 - Design of Steel Structures - Part 1-5: Plated Structural Elements. (2006). European Committee for Standardization.

Eurocode 3 - Design of Steel Structures - Part 1-6: Strength and Stability of Shell Structures. (2007). European Committee for Standardization.

Eurocode 3 - Design of Steel Structures - Part 4-3: Pipelines. (2007). European Committee for Standardization.

Fabian, O. (1977). “Collapse of Cylindrical, Elastic Tubes under Combined Bending, Pressure and Axial Loads.” *International Journal of Solids and Structures*, 13(12), 1257–1270.

Gellin, S. (1980). “The Plastic Buckling of Long Cylindrical Shells under Pure Bending.” *International Journal of Solids and Structures*, 16(5), 397–407.

Giordano, A., Walker, A. C., and Guarracino, F. (2008). “Finite Element Modelling Techniques and Testing Methods of Submerged Pipes.”

Gresnigt, A. M. (1986). “Plastic Design of Buried Pipelines in Settlement Areas.” *HERON*, 31(4), 1–113.

Gresnigt, A. M., Williams, C. A., and Karamanos, S. A. (2010). “Local Buckling Limits of Tubular Sections in Bending and Compression.” *Tubular Structures XII: Proceedings of the 13th International Symposium on Tubular Structures*, University of Hong Kong, Hong Kong.

Guarracino, F., Walker, A. C., and Giordano, A. (2008). “Effects of Boundary Conditions on Testing of Pipes and Finite Element Modeling.” *International Journal of Pressure Vessels and Piping*, 86, 196–206.

Houliara, S., and Karamanos, S. A. (2006). “Buckling and Post-Buckling of Long Pressurized Elastic Thin-Walled Tubes under In-Plane Bending.” *International Journal of Non-Linear Mechanics*, 41, 491–511.

Houliara, S., and Karamanos, S. A. (2011). “Buckling of Thin-Walled Long Steel Cylinders Subjected to Bending.” *Journal of Pressure Vessel Technology*, 133(1), 011201.

Hutchinson, J. W. (1968). “Buckling and Initial Postbuckling Behavior of Oval Cylindrical

Shells under Axial Compression." *Journal of Applied Mechanics*, 35(1), 66–72.
Jirsa, J. O., Fook-Hoy, L., Wilhoit, Jr., J. C., and Merwin, J. E. (1972). "Ovaling of Pipelines under Pure Bending." *Proceedings of the Fourth Annual Offshore Technology Conference*, Houston, Tx.
Ju, G. T., and Kyriakides, S. (1992). "Bifurcation and localization instabilities in cylindrical shells under bending Part II: Predictions." *International Journal of Solids and Structures*, 29(9), 1143–1171.
Karamanos, S. A. (2002). "Bending Instabilities of Elastic Tubes." *International Journal of Solids and Structures*, 39(8), 2059–2085.
Kyriakides, S., and Ju, G. T. (1992). "Bifurcation and Localization Instabilities in Cylindrical Shells under Bending Part I: Experiments." *International Journal of Solids and Structures*, 29(9), 1117–1142.
Lee, C.-H., Baek, J.-H., and Chang, K.-H. (2012). "Bending Capacity of Girth-Welded Circular Steel Tubes." *Journal of Constructional Steel Research*, 75, 142–151.
Mamalis, A. G., Manolakos, D. E., Baldoukas, A. K., and Viegelahn, G. L. (1989). "Deformation Characteristics of Crashworthy Thin-Walled Steel Tubes Subjected to Bending." *Journal of Mechanical Engineering Science*, 203, 411–417.
Poonaya, S., Teeboonma, U., and Thinvongpituk, C. (2009). "Plastic Collapse Analysis of Thin-Walled Circular Tubes Subjected to Bending." *Thin-Walled Structures*, 47(6-7), 637–645.
Reddy, B. D. (1979). "An Experimental Study of the Plastic Buckling of Circular Cylinders in Pure Bending." *International Journal of Solids and Structures*, 15(9), 669–683.
Reissner, E., and Weinitschke, H. J. (1963). "Finite Pure Bending of Circular Cylindrical Tubes." *Quarterly of Applied Mathematics*, XX(4), 305–319.
Spence, J., and Toh, S. L. (1979). "Collapse of Thin Orthotropic Elliptical Cylindrical Shells under Combined Bending and Pressure Loads." *Journal of Applied Mechanics*, 46.
Spinelli, C. M., Demofonti, G., Fonzo, A., Lucci, A., Ferino, J., Di Biagio, M., Flaxa, V., Zimmermann, S., Kalwa, C., and Knoop, F. M. (2011). *Full Scale Investigation on Strain Capacity of High Grade Large Diameter Pipes*. Europipe Technical Publications.
Spirally Welded Steel Pipes. (2010). ArcellorMittal.
Tatting, B. F., Gürdal, Z., and Vasiliev, V. V. (1997). "The Brazier effect for Finite Length Composite Cylinders under Bending." *International Journal of Solids and Structures*, 34(12), 1419–1440.
Ueda, S. (1985). "Moment-Rotation Relationship Considering Flattening of Pipe Due To Pipe Whip Loading." *Nuclear Engineering and Design*, 85, 251–259.
Vasilikis, D., and Karamanos, S. A. (2014). *Bending Resistance of Steel Tubes in CombiWalls Task 4.2: Modeling of the Spiral-Welded Pipe*. Research Report, University of Thessaly.
Wadee, M. K., Wadee, M. A., Bassom, A. P., and Aigner, A. A. (2006). "Longitudinally Inhomogeneous Deformation Patterns in Isotropic Tubes under Pure Bending." *Proceedings of the Royal Society*, 462(2067), 817–838.
Wierzbicki, T., and Sinmao, M. V. (1997). "A Simplified Model of Brazier Effect in Plastic Bending of Cylindrical Tubes." *International Journal of Pressure Vessels and Piping*, 71(1), 19–28.

Appendix A: Material Test Data

Nominal stress-strain curves for all modeled tubes are given below.

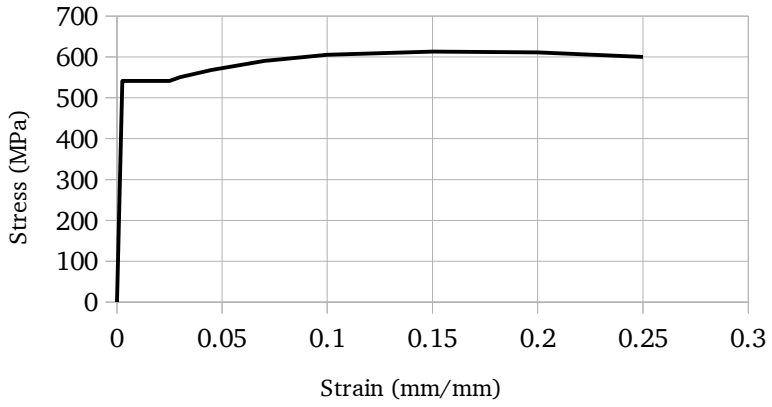

Figure 206: Nominal stress-strain curve for Tube 1

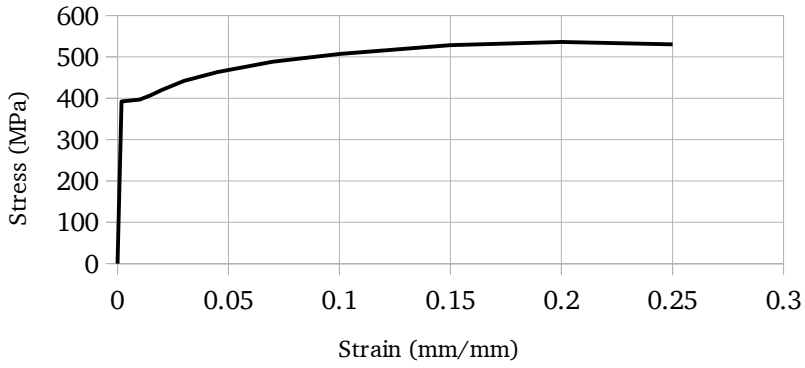

Figure 207: Nominal stress-strain curve for Tube 2

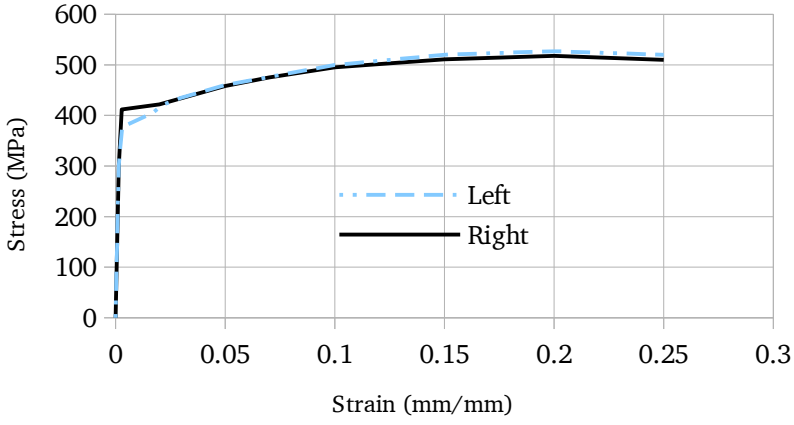

Figure 208: Nominal stress-strain curves for Tube 3

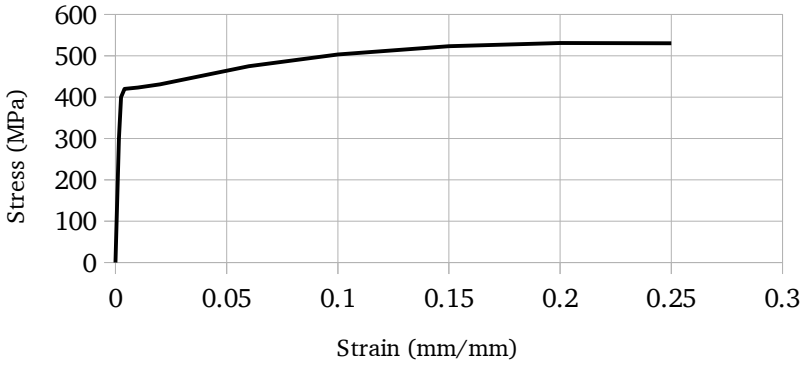

Figure 209: Nominal stress-strain curve for Tube 4

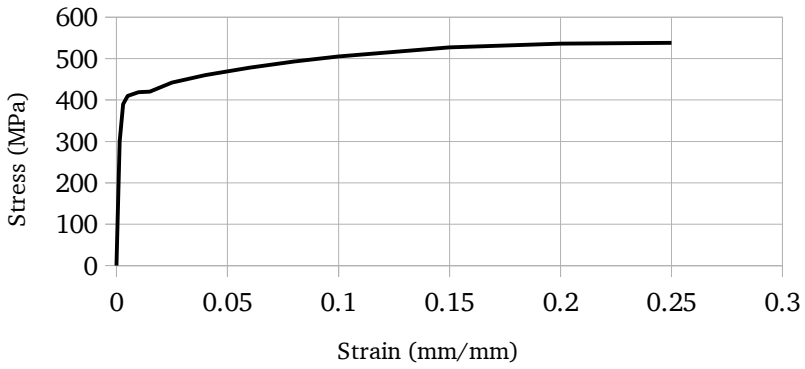

Figure 210: Nominal stress-strain curve for Tube 5

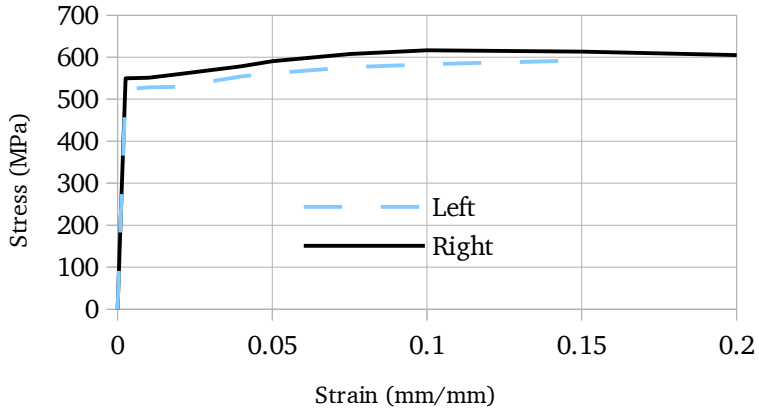

Figure 211: Nominal stress-strain curves for Tube 6

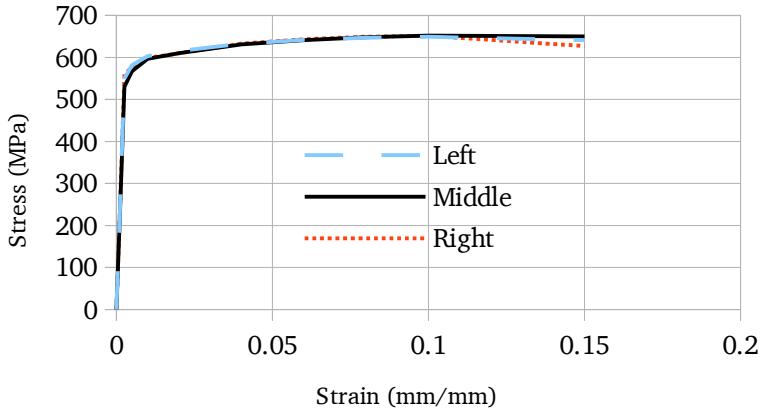

Figure 212: Nominal stress-strain curves for Tube 7

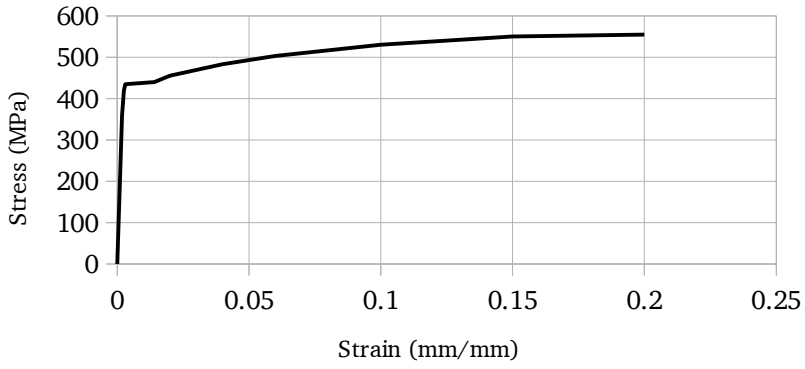

Figure 213: Nominal stress-strain curve for Tube 8

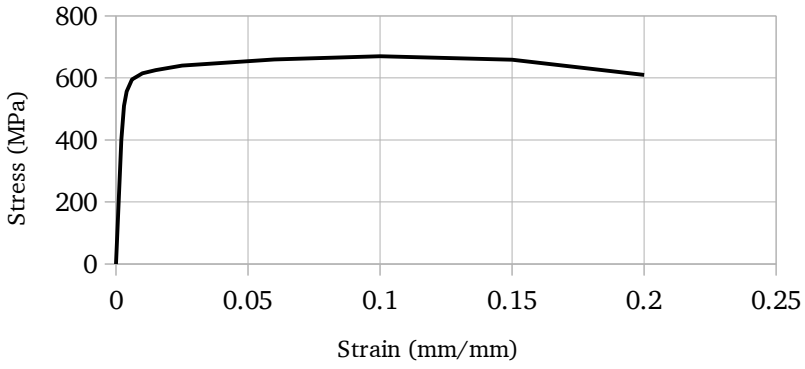

Figure 214: Nominal stress-strain curve for Tube 9

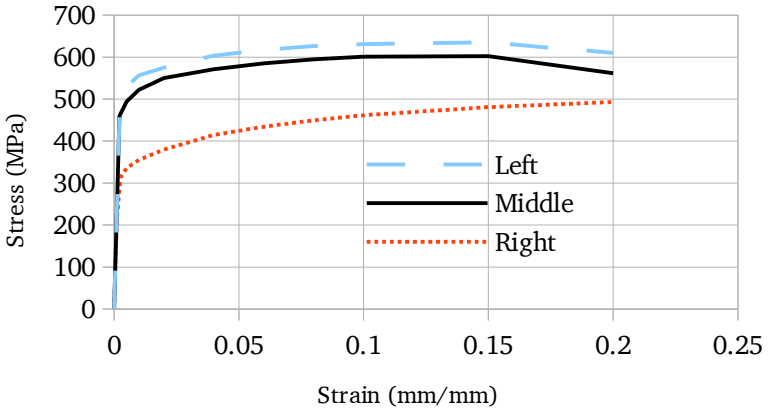

Figure 215: Nominal stress-strain curves for Tube 10

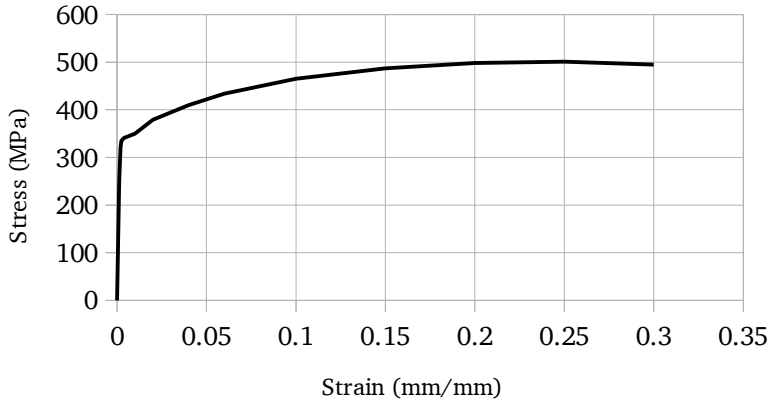

Figure 216: Nominal stress-strain curve for Tube 11

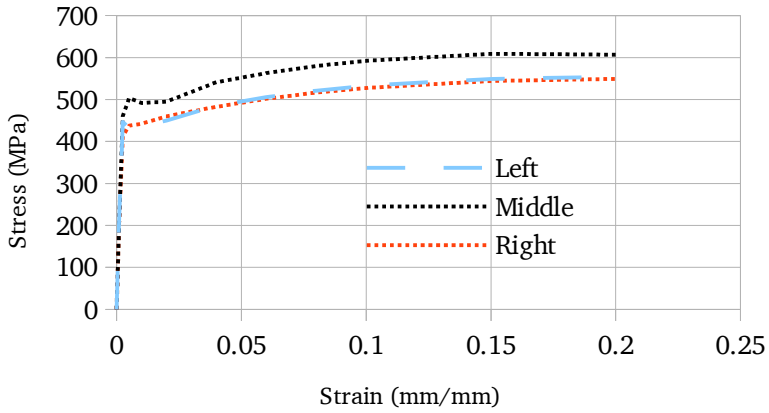

Figure 217: Nominal stress-strain curves for Tube 12

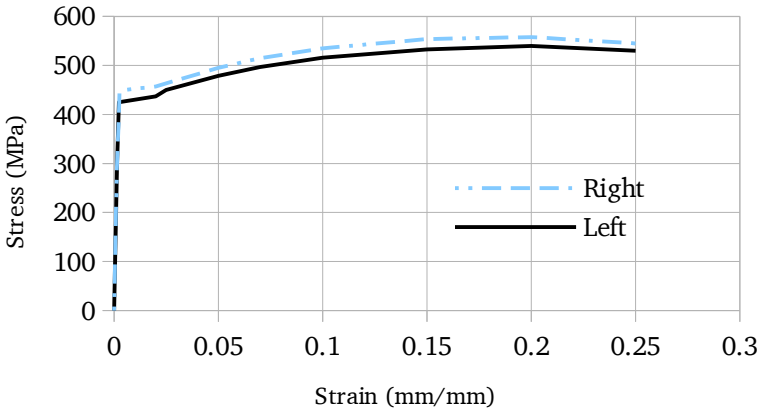

Figure 218: Nominal stress-strain curves for Tube 13

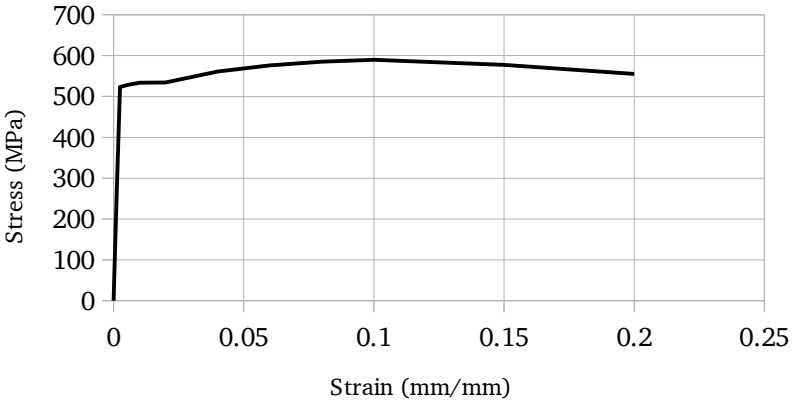

Figure 219: Nominal stress-strain curve for Tube 14

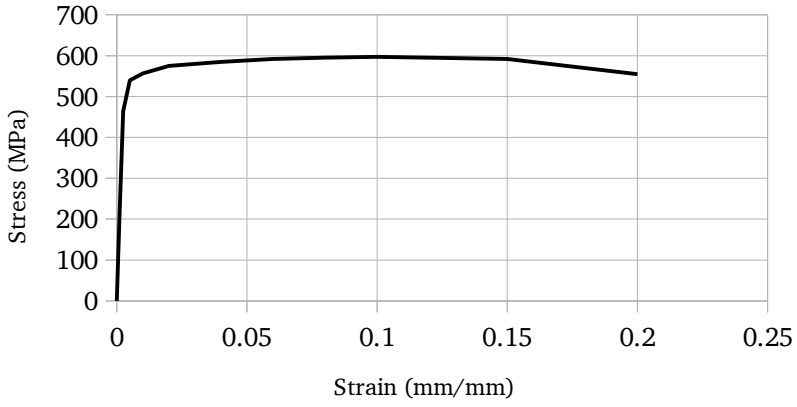

Figure 220: Nominal stress-strain curve for Tube 15

Appendix B: Detailed Initial Imperfection Profiles

The following figures shown the initial profiles of the compression side of the tubes used in the experimental program.

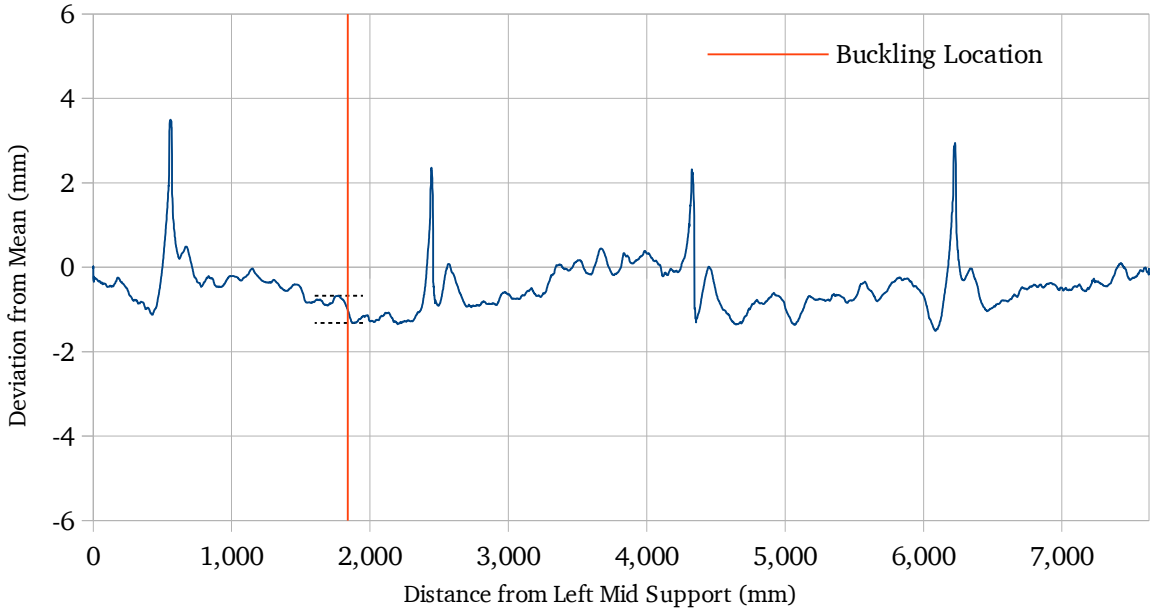

Figure 221: Initial profile of Tube 1

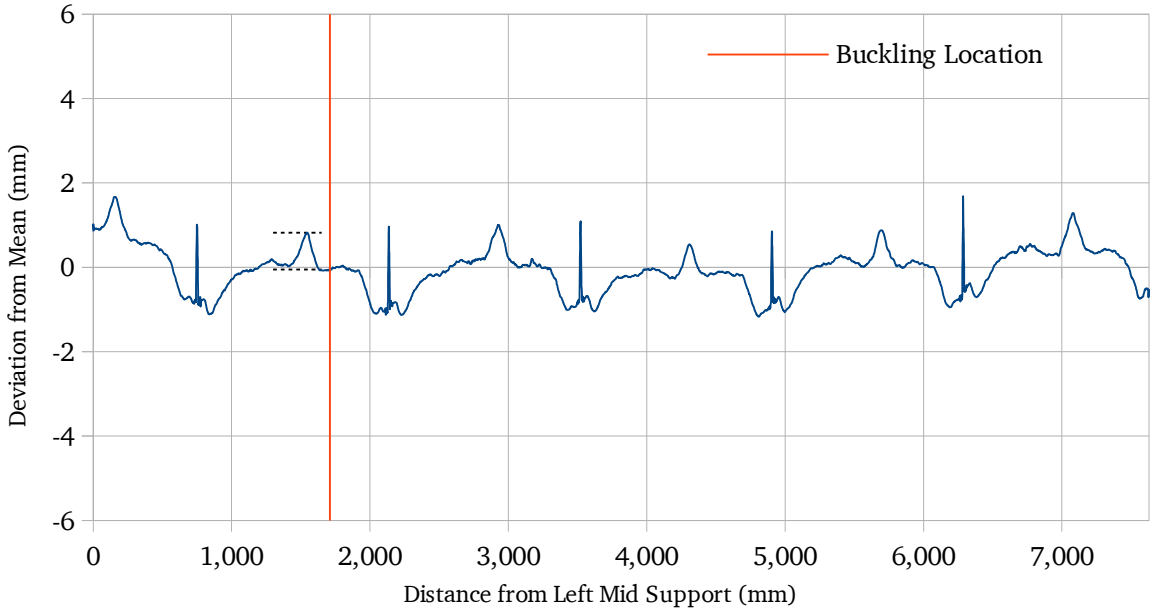

Figure 222: Initial profile of Tube 2

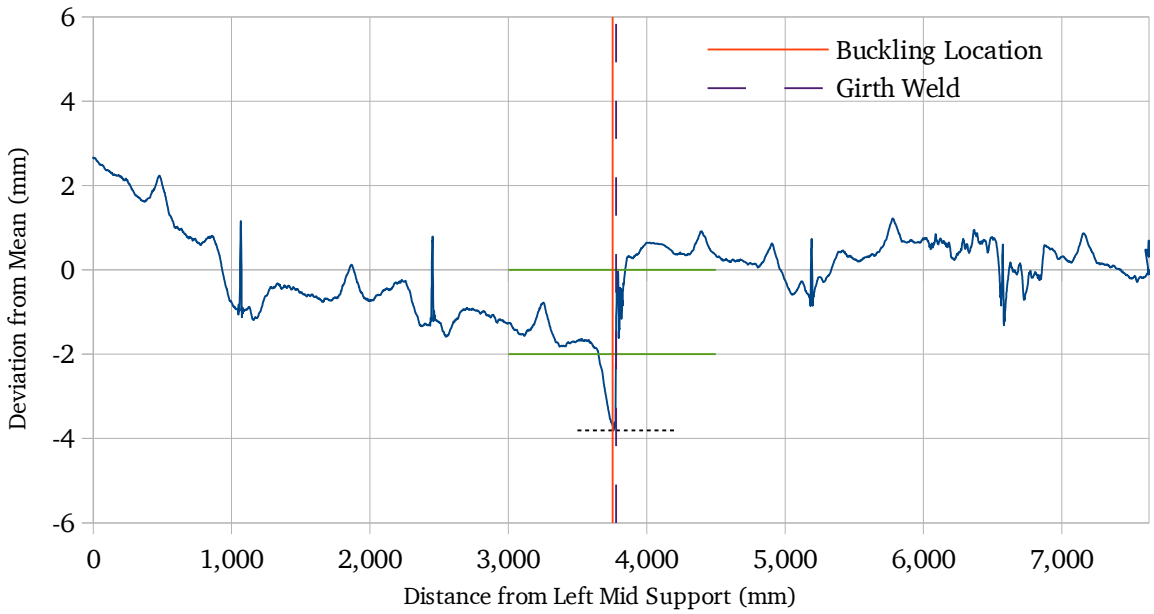

Figure 223: Initial profile of Tube 3

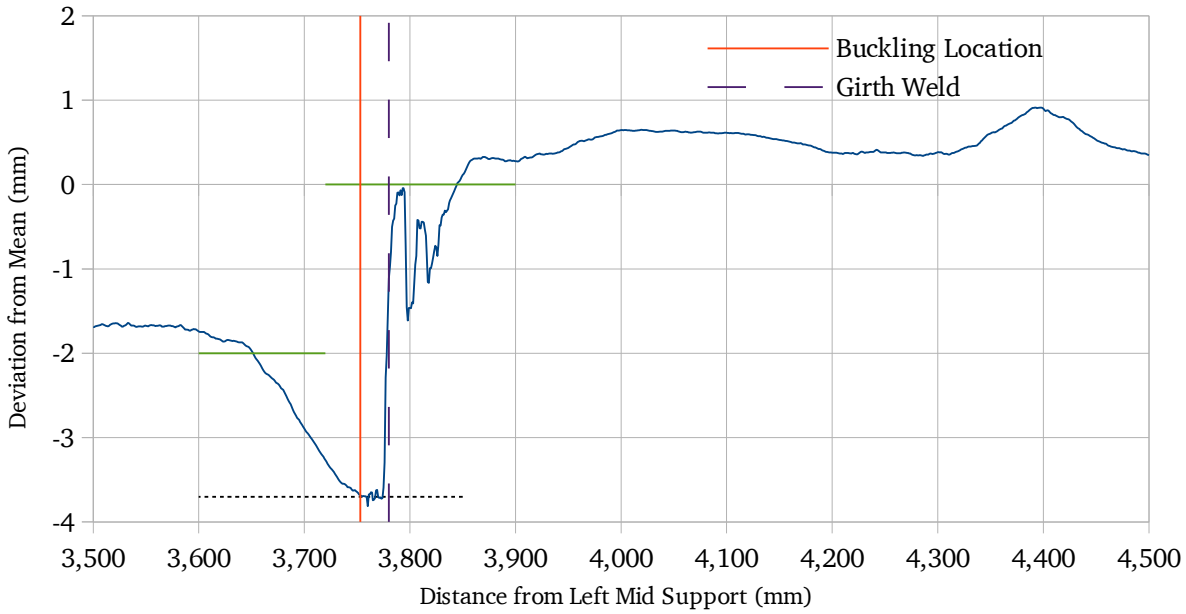

Figure 224: Girth weld profile of Tube 3

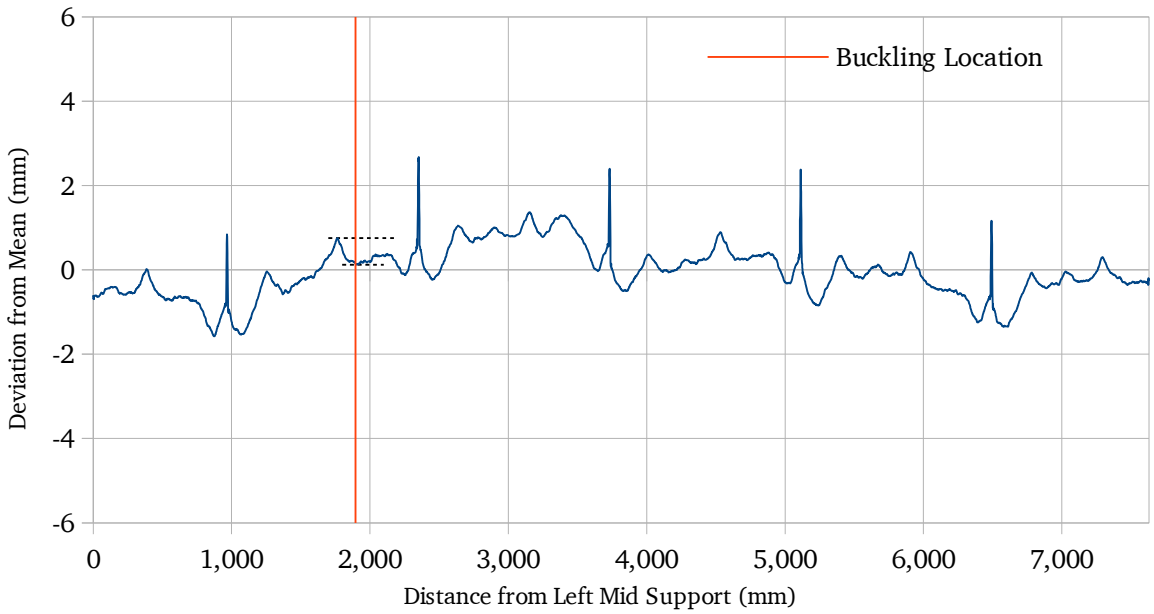

Figure 225: Initial profile of Tube 4

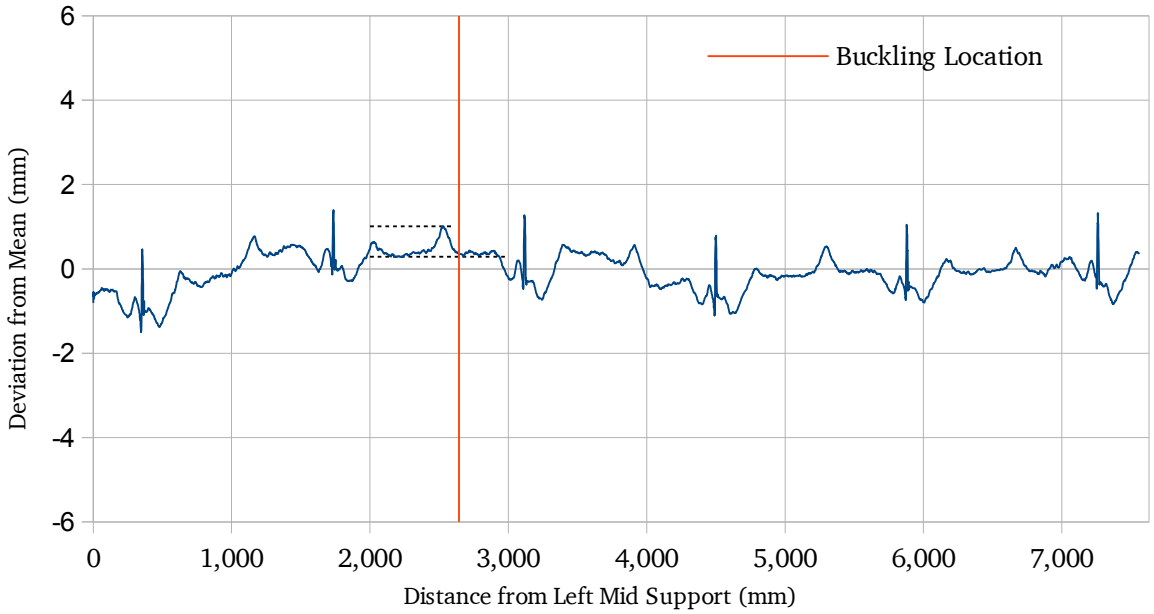

Figure 226: Initial profile of Tube 5

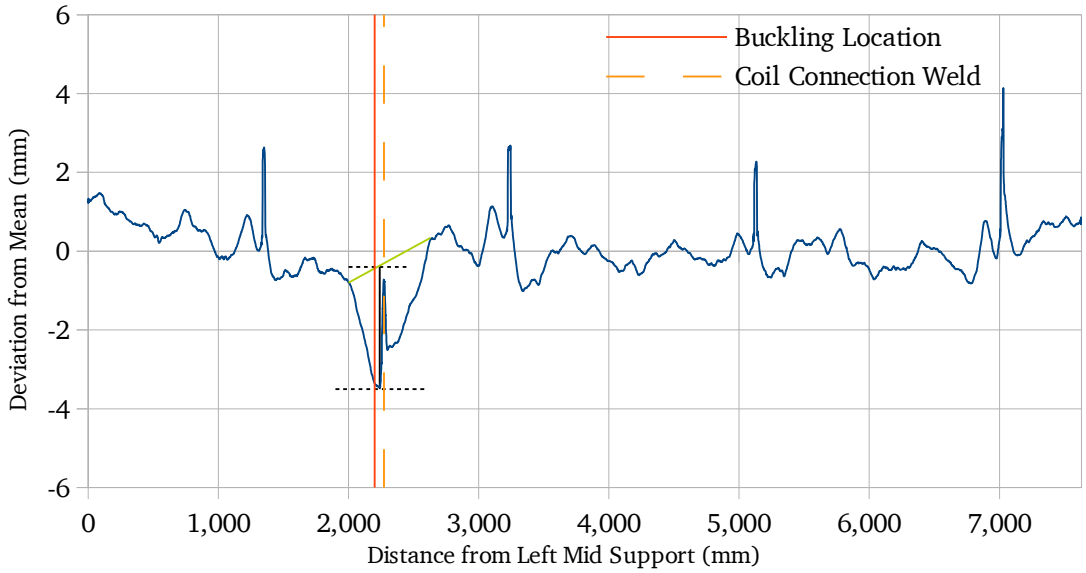

Figure 227: Initial profile of Tube 6

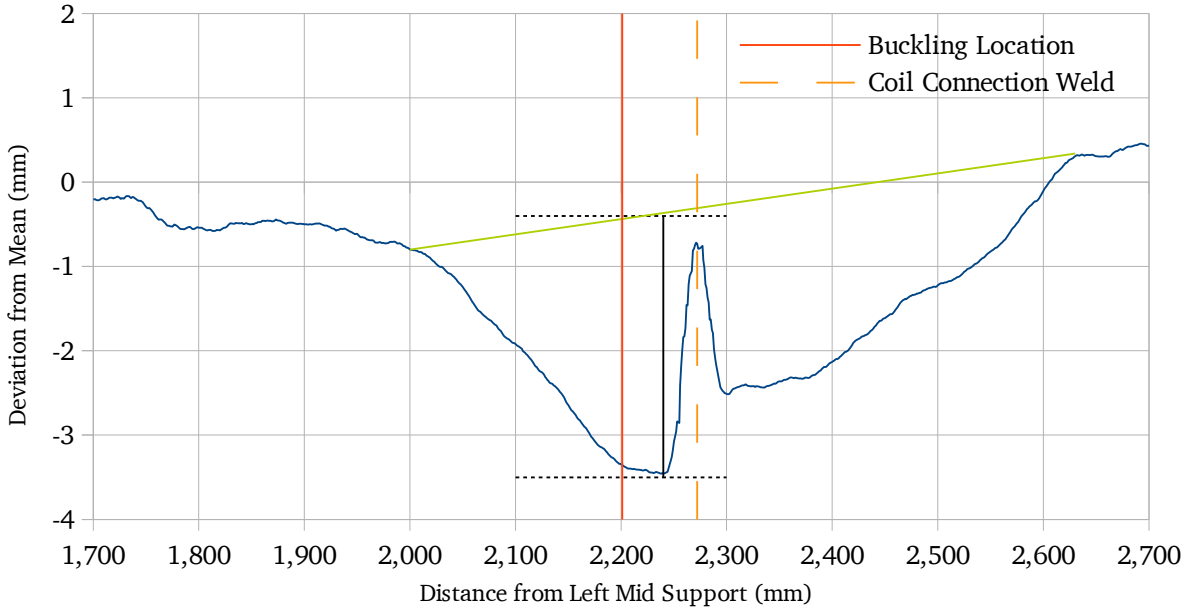

Figure 228: Coil connection weld profile of Tube 6

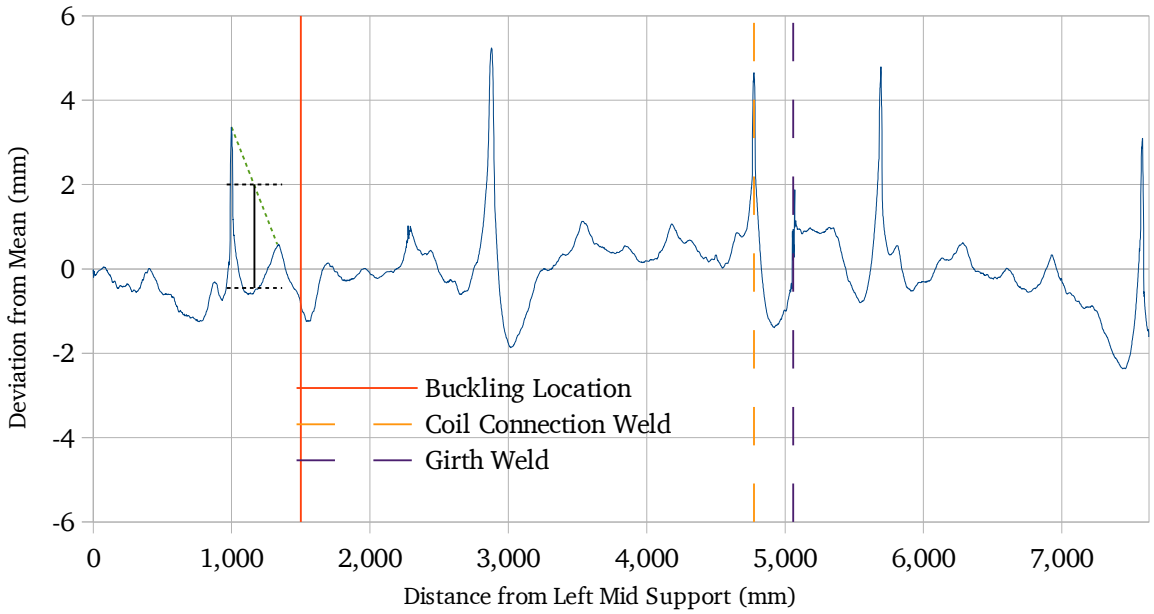

Figure 229: Initial Profile of Tube 7

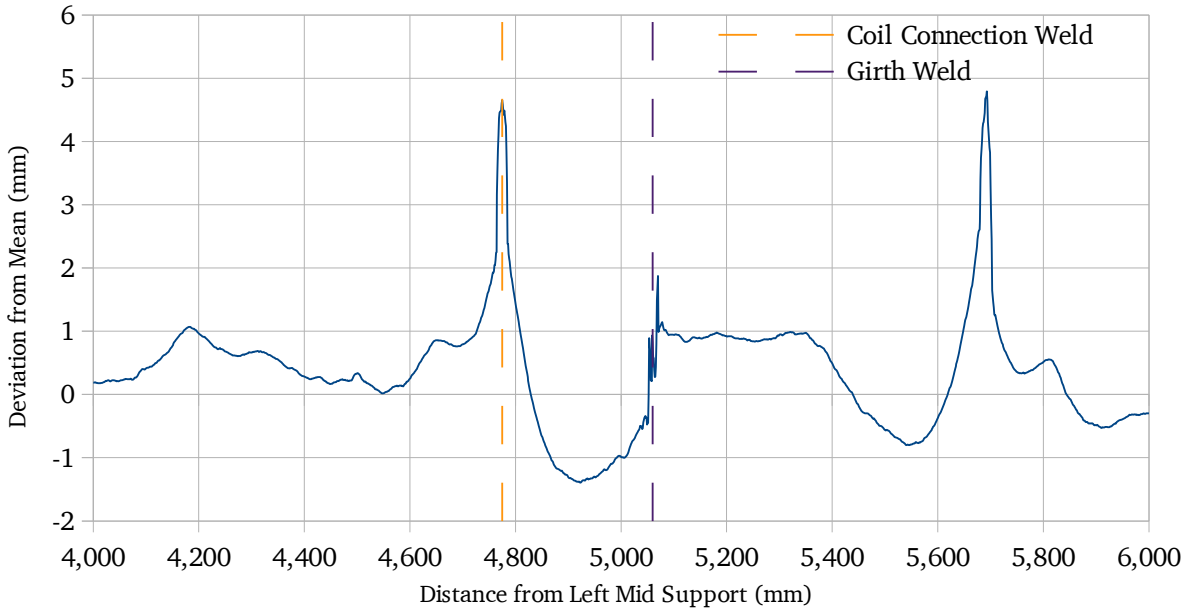

Figure 230: Girth and coil connection weld profiles of Tube 7

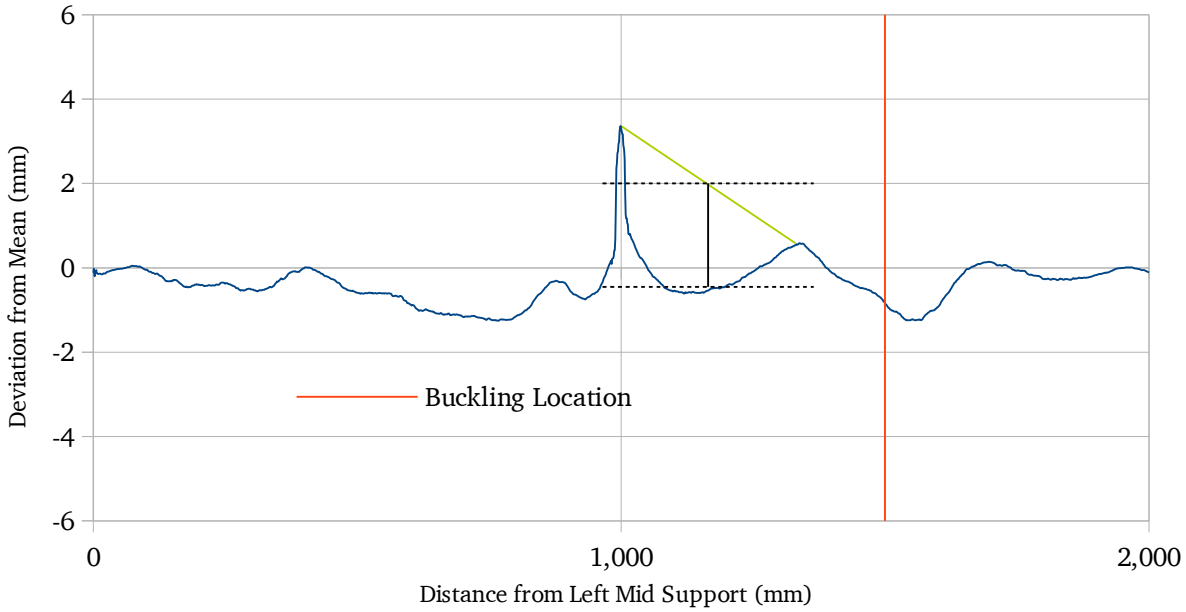

Figure 231: Spiral weld profile of Tube 7

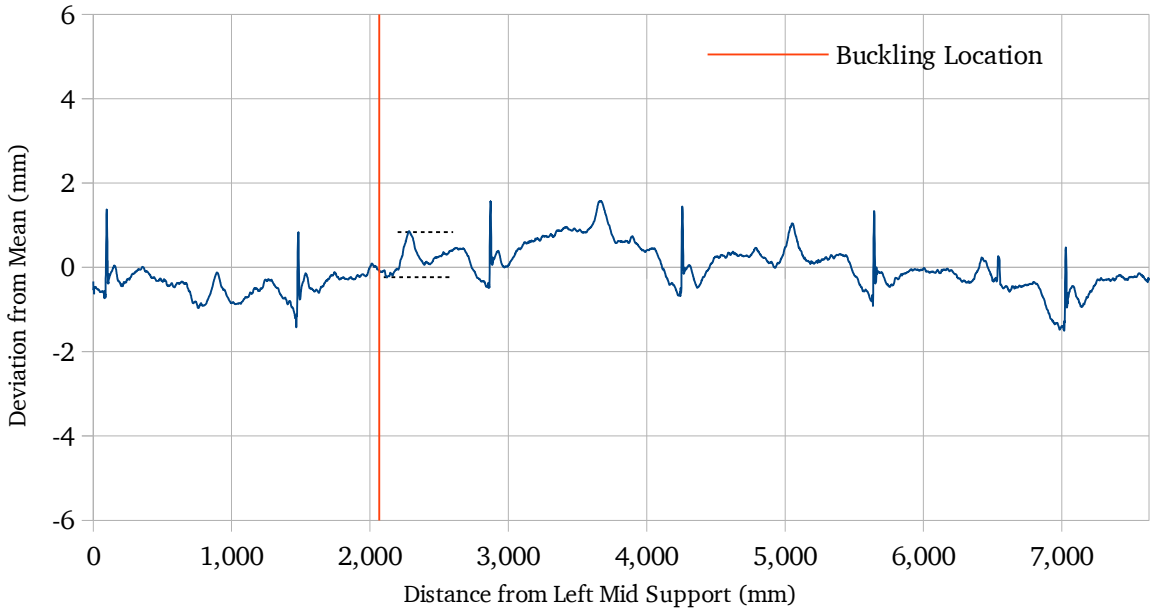

Figure 232: Initial profile of Tube 8

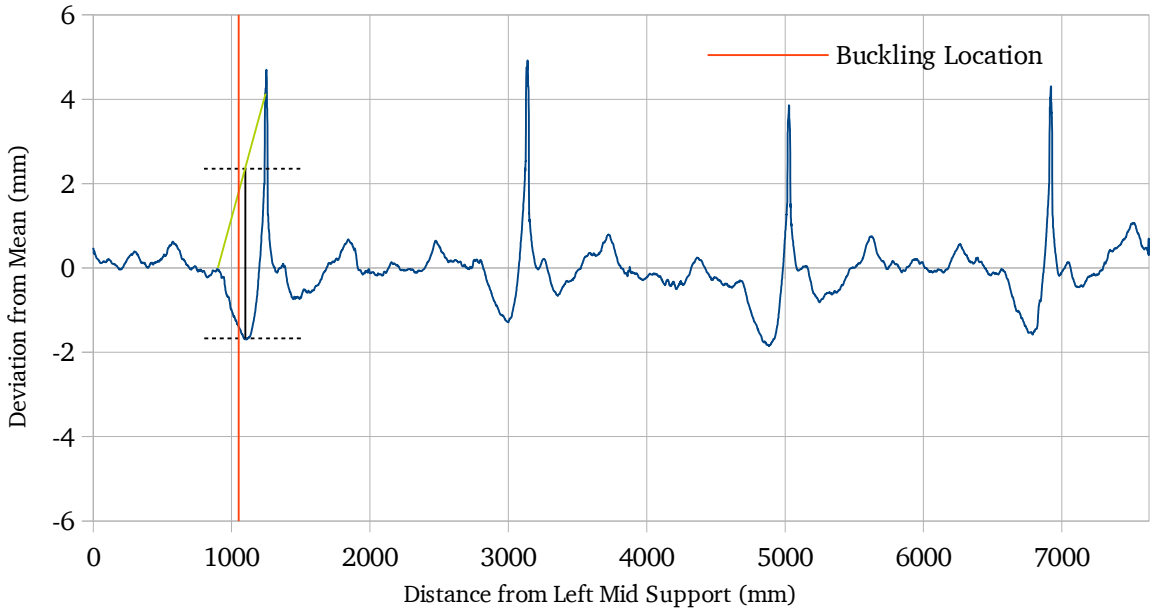

Figure 233: Initial profile of Tube 9

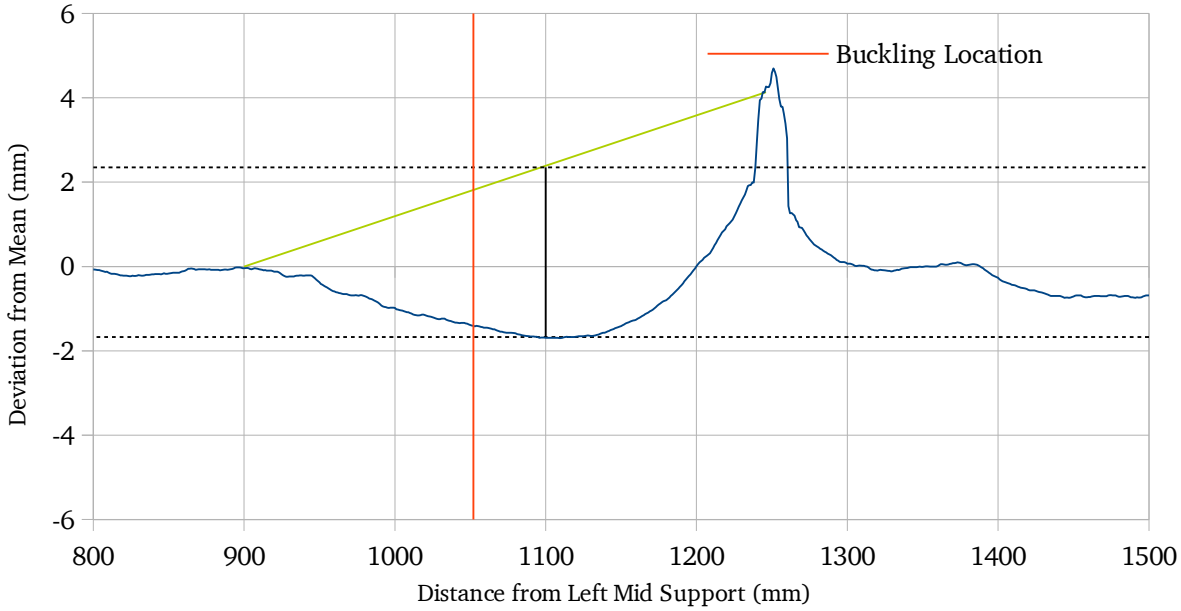

Figure 234: Spiral weld profile of Tube 9

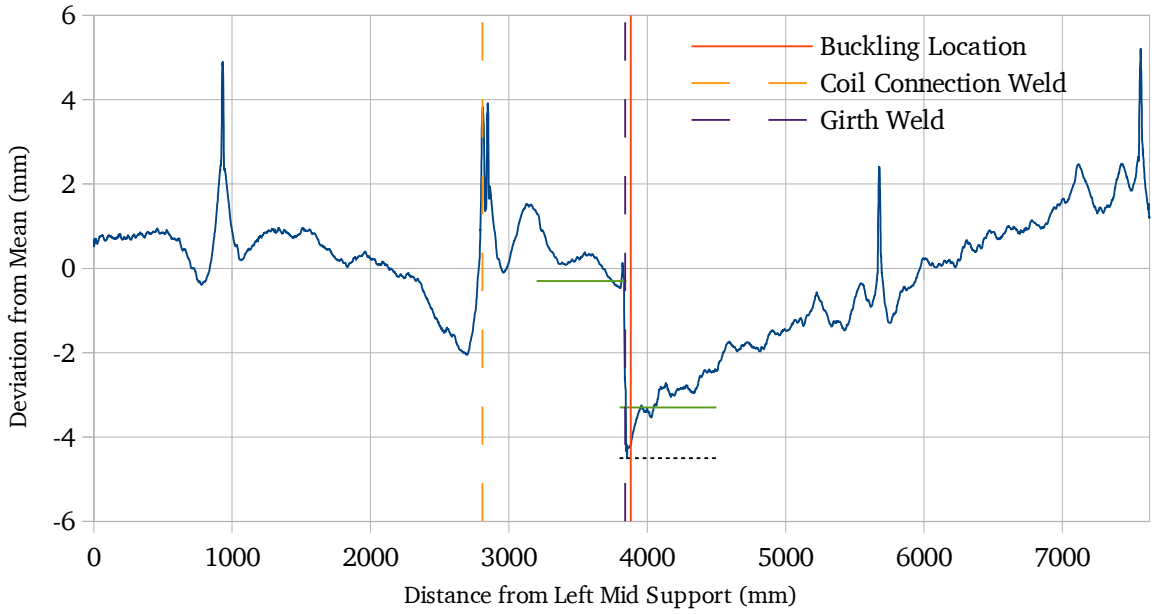

Figure 235: Initial profile of Tube 10

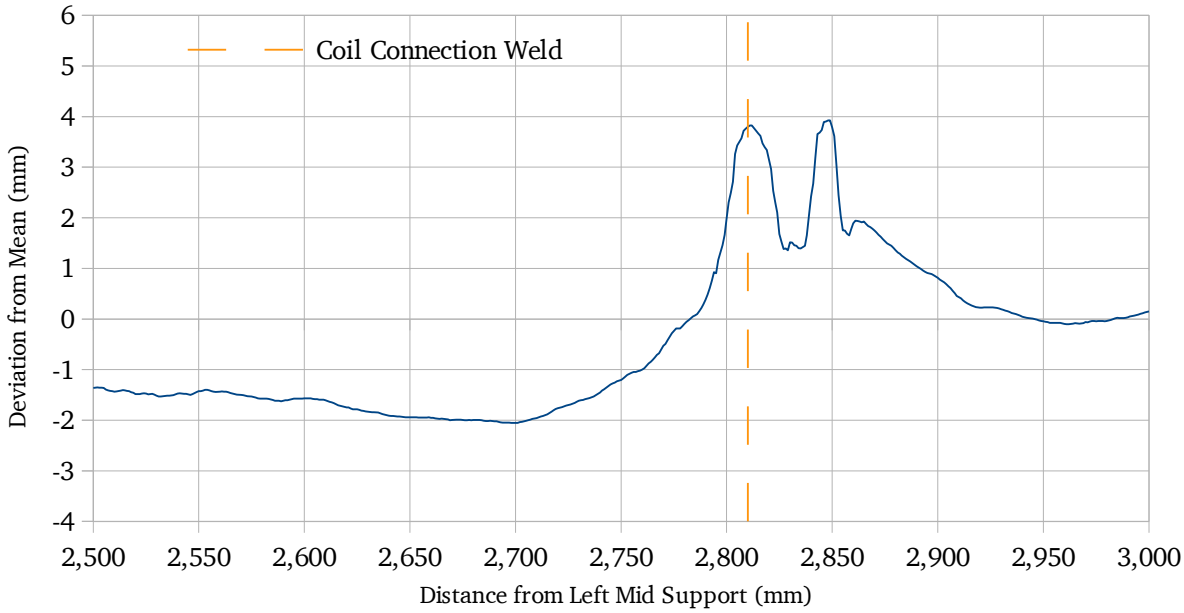

Figure 236: Coil connection weld profile of Tube 10

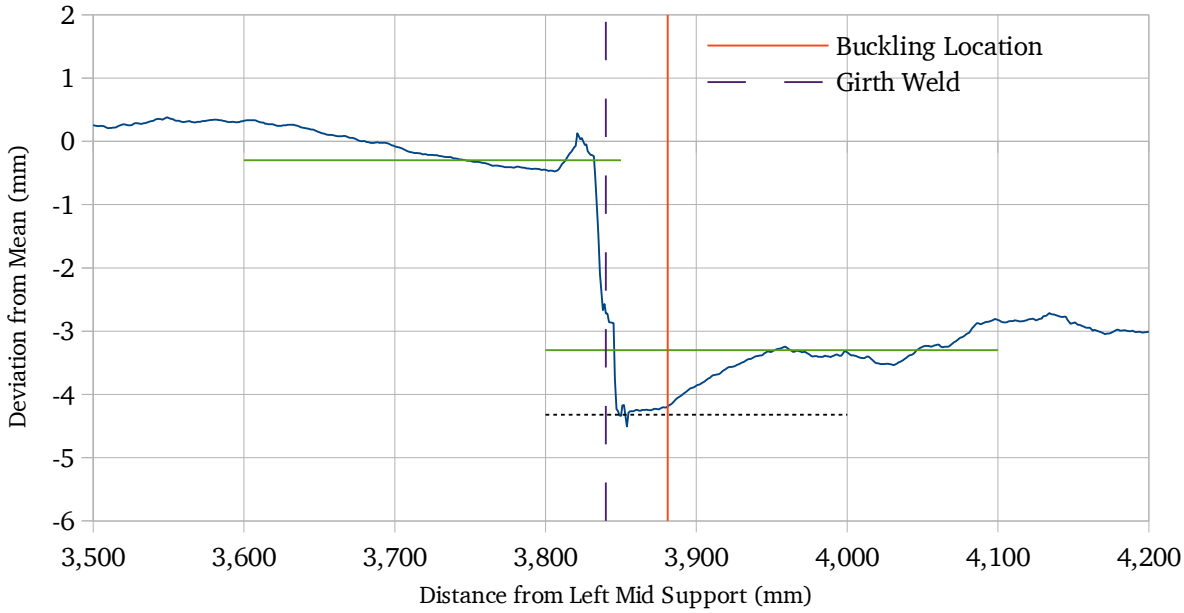

Figure 237: Girth weld profile of Tube 10

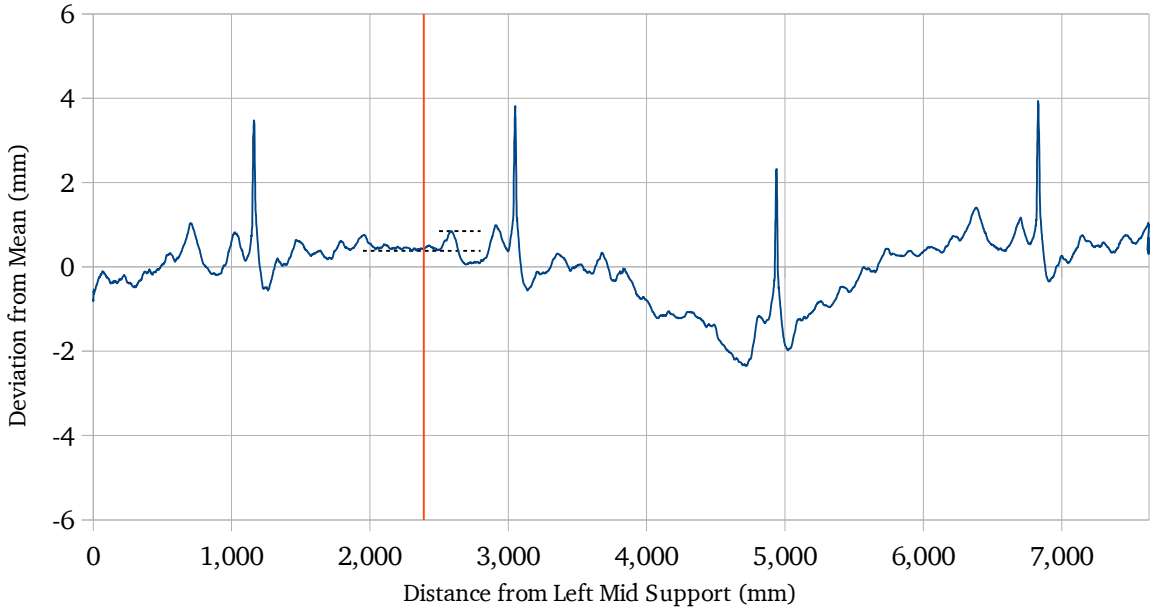

Figure 238: Initial profile of Tube 11

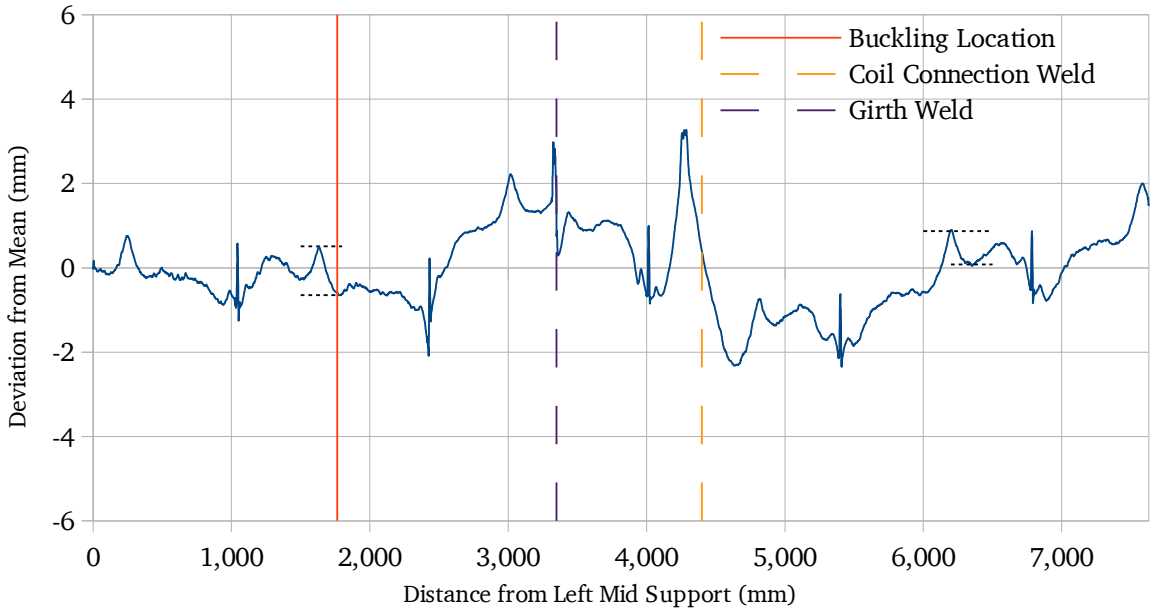

Figure 239: Initial profile of Tube 12

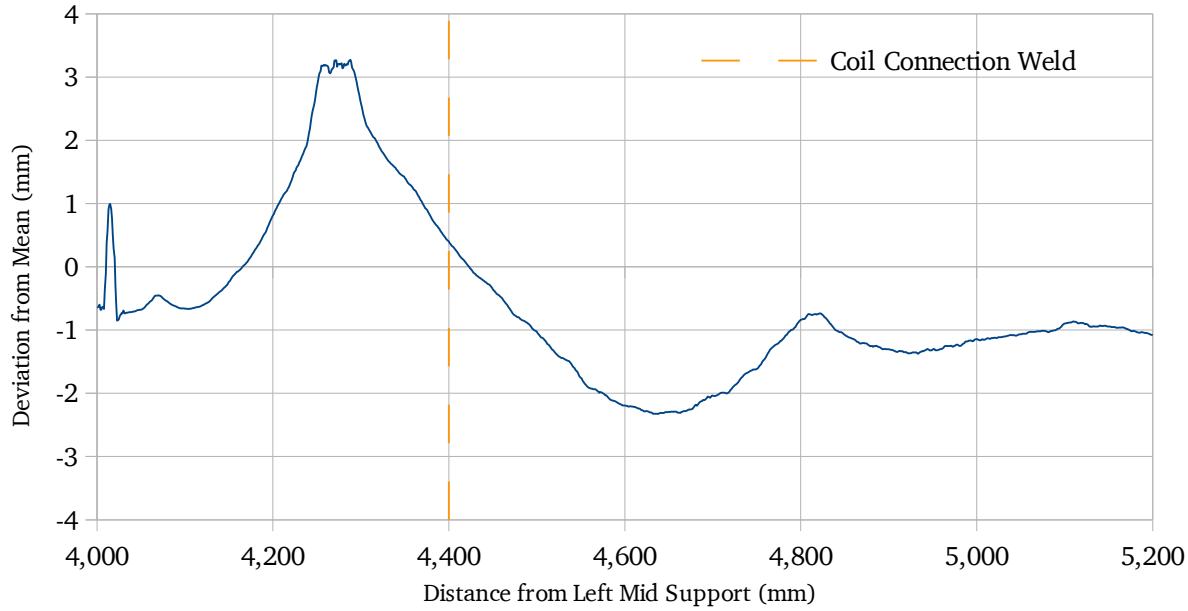

Figure 240: Coil connection weld profile of Tube 12

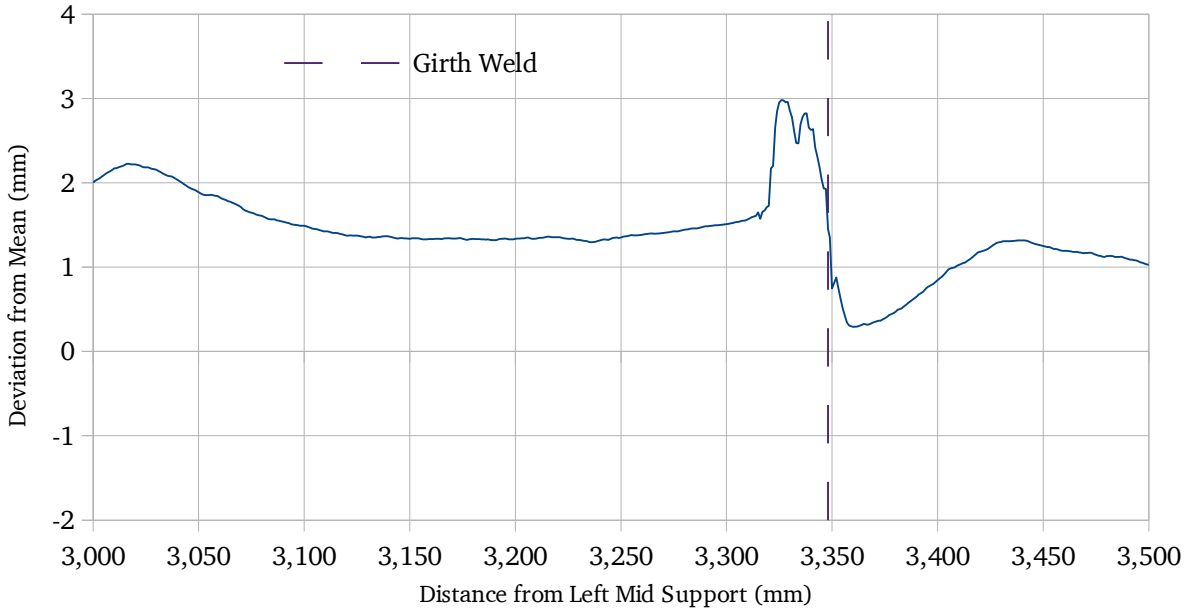

Figure 241: Girth weld profile of Tube 12

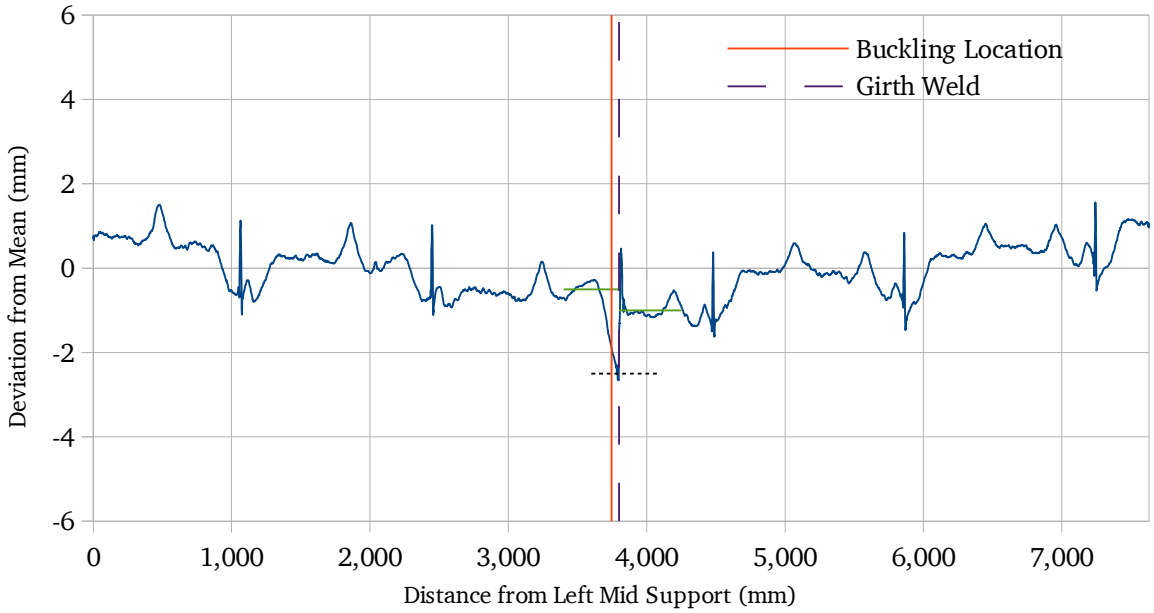

Figure 242: Initial profile of Tube 13

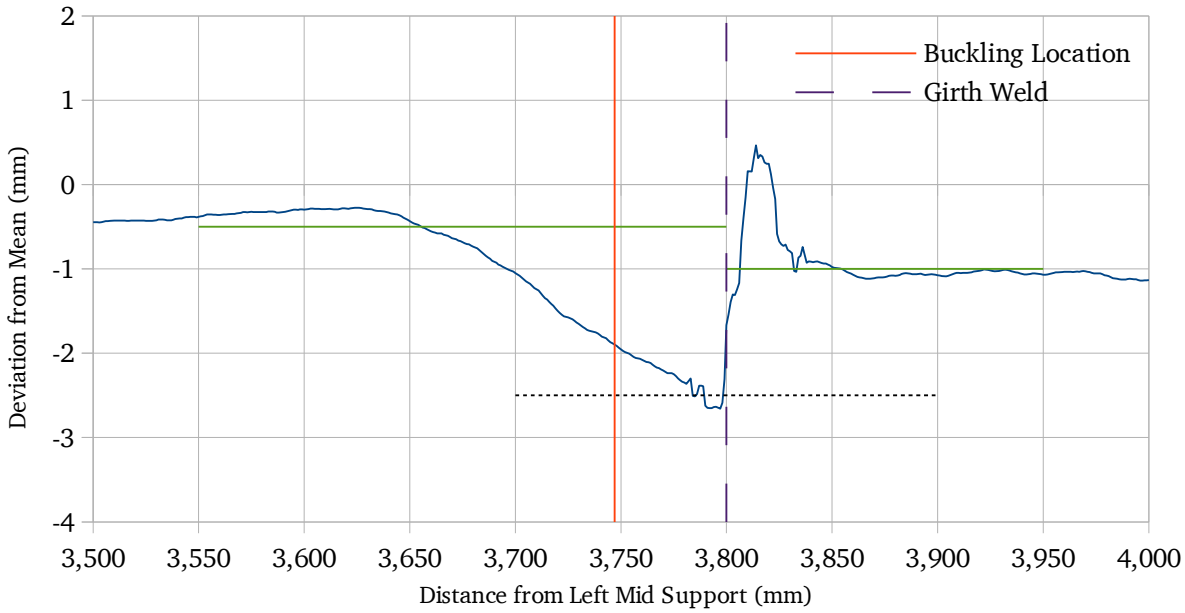

Figure 243: Girth weld profile of Tube 13

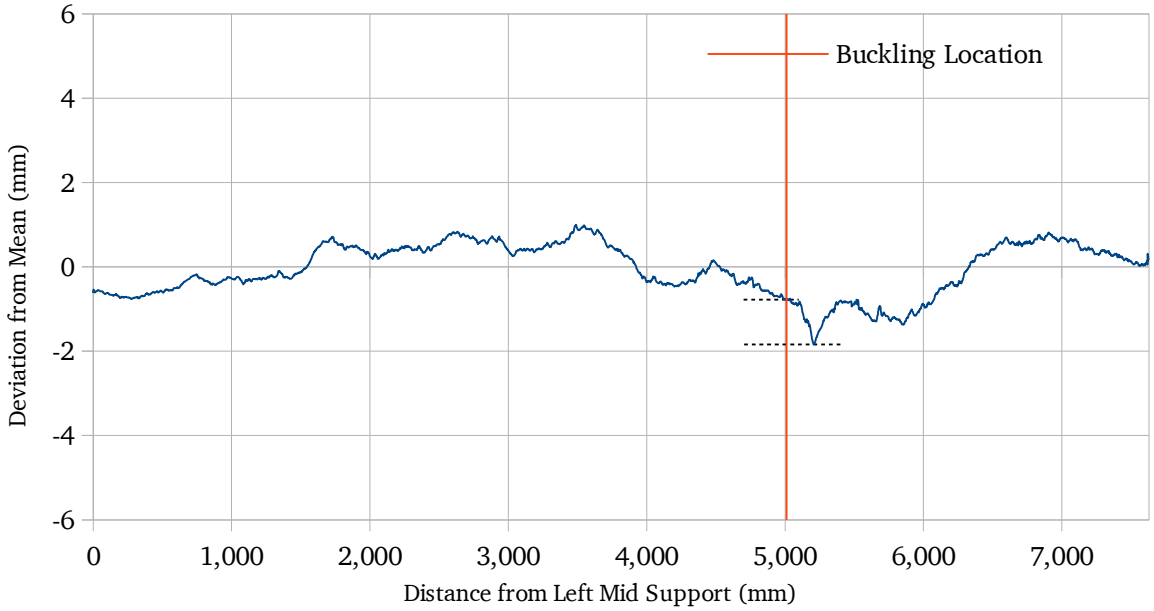

Figure 244: Initial profile of Tube 14

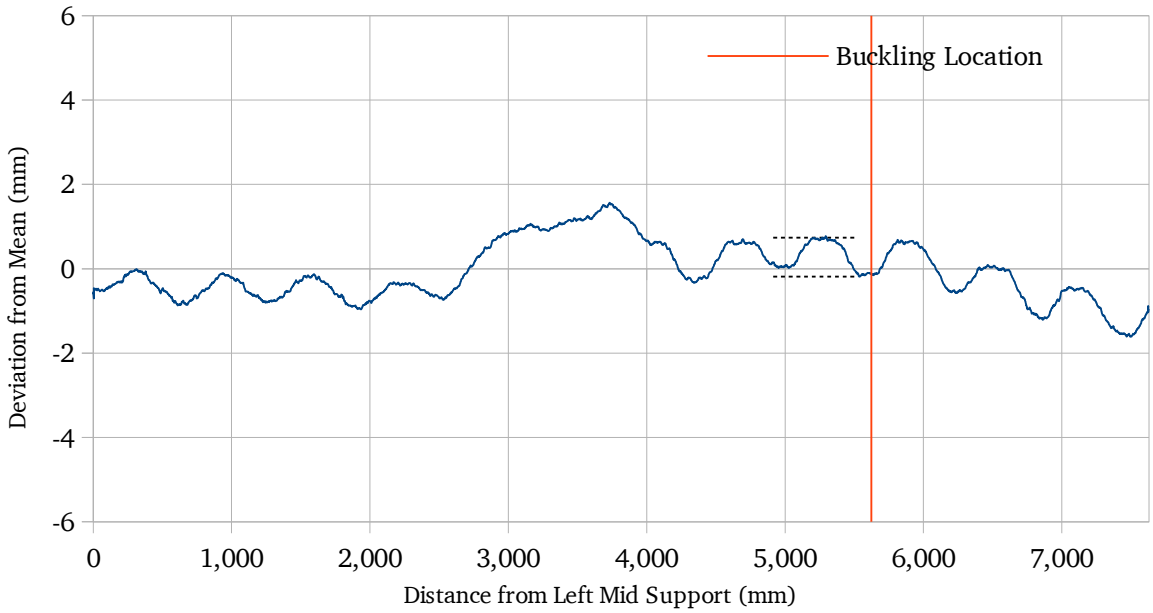

Figure 245: Initial profile of Tube 15

Appendix C: MATLAB Implementation of Analytical Solution

```
clear
clc
format long

%Tube parameters
t=9;
d=1067;
r=d/2;
E=205000;
fy=400;

%Section 6.1.5
Mp=4*r^2*t*fy;
Me=pi*r^2*t*fy;
mp=.25*t^2*fy;

%Initialization of Variables
i=1;
k=0;
dk=1*10^-7;
M=0;
Mm=Mp;
a=0;
phi=pi/2;
M_Plastic=Mp;
mom_inertia=(pi/4)*(r^4-(r-t)^4);
k_elastic=Me*10^6/(E*mom_inertia);

curvature(i)=k*10^6;
moment(i)=M*10^-6;
max_moment(i)=Mm*10^-6;
elastic_moment(i)=Me*10^-6;
plastic_moment(i)=Mp*10^-6;
ovalization(i)=a;
MMp(i)=1;
mymp(i)=0;

%Iterate until maximum desired curvature is reached
while k<8*10^-6
    i=i+1;
    k=k+dk;

    %Calculation of Elastic Ovalization
    %Eqn. 6.1-19
    alpha=(k*r^2)*sqrt(12)/t;

    %Eqn 6.1-18
    a_elastic=r*(alpha^2/12);
```

```
%Calculation of Plastic Ovalization
    %Apply plastic ovalization once section starts to yield
    if phi>=pi/2
        a=a_elastic;
    else
        a_old=a;
        da=-(r^3/t)*(2*psi*dk);
        a_plastic=a+da*M/Mm;
        a=a_plastic;
    end


    %Calculation of Max Moment
    %Section 6.1.5
    f0=1+a/r;
    my=.071*Mm*k*f0;
    ny=.2*Mm*k/r;
    np=t*fy;
    c1=sqrt(4-3*(ny/np)^2-2*sqrt(3)*abs(my/mp));
    c2=sqrt(4-3*(ny/np)^2);
    g=c1/6+c2/3;

    %Eqn. 6.1-66
    h=1-(2/3)*(a/r);

    %Eqn. 6.1-67
    Mm=h*Mp*g;

    %Calculation of Moment

    %Eqn 6.3-5
    EI=E*pi*r^3*t*(1-1.5*(a/r));

    %Eqn 6.3-3
    Mep=(Me/Mp)*Mm;

    %Eqn 6.3.4
    Kep=Mep/EI;

    %Eqn 6.3-6
    phi=asin(Kep/k);

    M=Mm*.5*(phi/sin(phi)+cos(phi));

    %Calculation of Elastic Perfectly Plastic Moment
    %Used for Plastic Ovalization Calculation
    f=1;
    M_plastic = g*f*Mp;
    Mm_plastic = h*M_plastic;

    %Calculation of Angle of Yield Contour Psi for Next Iteration
    MMp(i)=M_plastic/Mp;
    mymp(i)=my/mp;
    psi = (MMp(i)-MMp(i-1))/(mymp(i)-mymp(i-1));
```

```
%Update of Variables
    curvature(i)=k*10^6;
    moment(i)=M*10^-6;
    max_moment(i)=Mm*10^-6;
    elastic_moment(i)=Me*10^-6;
    plastic_moment(i)=Mp*10^-6;
    ovalization(i)=a;
    elastic_ovalization(i)=a_elastic;

end
moment = real(moment);

capacity=max(moment);
loc=find(moment==capacity);
cap_curv=curvature(loc);
cap_ov=ovalization(loc);

%Export output to file results.txt
output = [moment' ovalization' elastic_ovalization' curvature'];
dlmwrite('results.txt',output);

%Output results
fprintf('The section slenderness of this tube is %d \n', (fy/235)*(D/t))
fprintf('The capacity of this tube is %d kN*m \n',capacity)
fprintf('The curvature at this point is %d /mm \n',cap_curv)
fprintf('The ovalization at this point is %d mm \n',cap_ov)
fprintf('The plastic moment is %d kN*m \n', Mp/1000/1000)
fprintf('The results have been output to results.txt \n')

%Plot results
subplot(1,2,1)
plot(curvature, moment, 'linewidth', 2)
hold on
plot(curvature, max_moment, '--k')
plot(curvature, plastic_moment, 'r')
plot(curvature, elastic_moment, '--g')
xlabel('Curvature (10^6 /mm)')
ylabel('Moment (kNm)')
legend('M', 'Mm', 'Mp', 'Me', 'Location', 'SouthEast')
hold off
subplot(1,2,2)
plot(curvature, 2*ovalization, 'r', 'linewidth', 2)
hold on
plot(curvature, 2*elastic_ovalization, 'linewidth', 2)
xlabel('Curvature (10^6 /mm')
ylabel('Total Ovalization (mm)')
legend('Plastic Ovalization','Elastic Ovalization','Location','SouthEast')
```

Appendix D: Creation of Models in ABAQUS

The first step increating a tube model is to create the geometry. The geometry can be created by sketching the cross section and extruding it to the required length. The geometry should be created based on the outside diameter of the tube. The part parameters should be selected as shown in the figures.

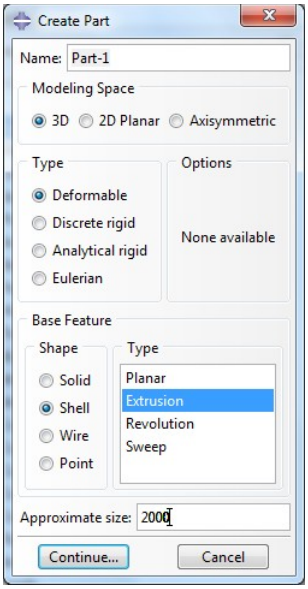

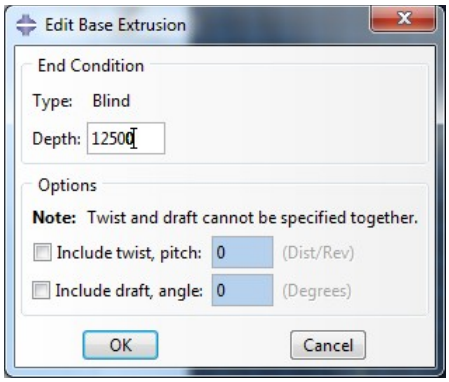

Next the material model can be defined. For an elastic analysis, only the elastic modulus needs to be defined. For a nonlinear analysis, the full stress-strain curve should be defined, in terms of true stress-true plastic strain:

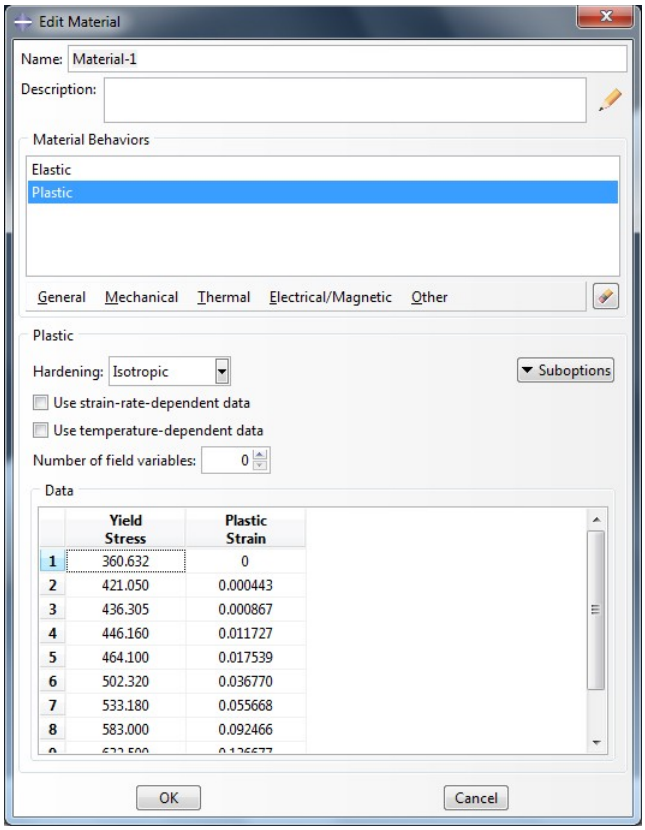

The section can also be defined. The section type 'homogeneous shell' should be used, and the shell thickness, number of integration points, and material model should be assigned appropriately:

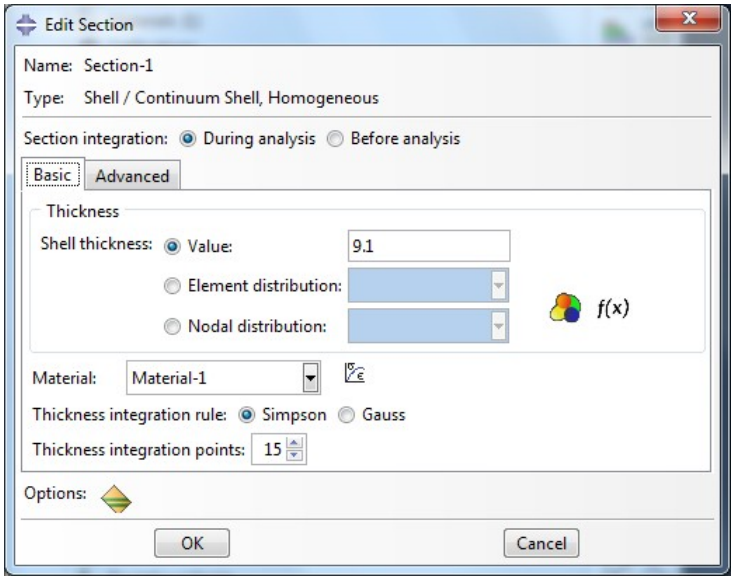

Now the section can be assigned to the geometry, by selecting "Section Assignments" from within the parts manager. The top surface should be selected for the shell offset definition:

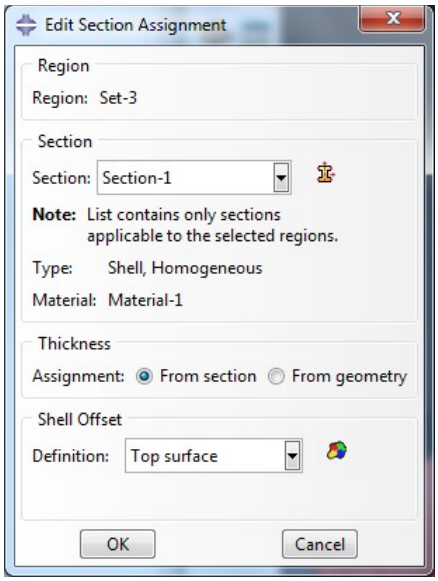

In order to assign the section correctly, the material orientation and element normals must be defined. The element normals can be defined by going to Assign->Element Normal. If the outside surface of the tube is brown, then the shell orientation has been assigned correctly and the thickness of the tube will be offset from the outside surface.

In order to define the material orientation, a local cylindrical oordinate system has to be defined, because the residual stresses are given in terms of hoop stress and axial stress.

The local system can be defined by going to the "Create Datum CSYS: 3 Points" function while in the parts manager. A cylindrical coordinate system should be created with the origin at the origin of the tube.

Next, the material orientation is defined by going to Assign->Material Orientation. The new coordinate system should be selected, and then the correct axis should be selected as the normal direction. Direction 1 should correspond to the axial direction of the tube and direction 2 should correspond with the hoop direction. This is important for defining the residual stresses correctly:

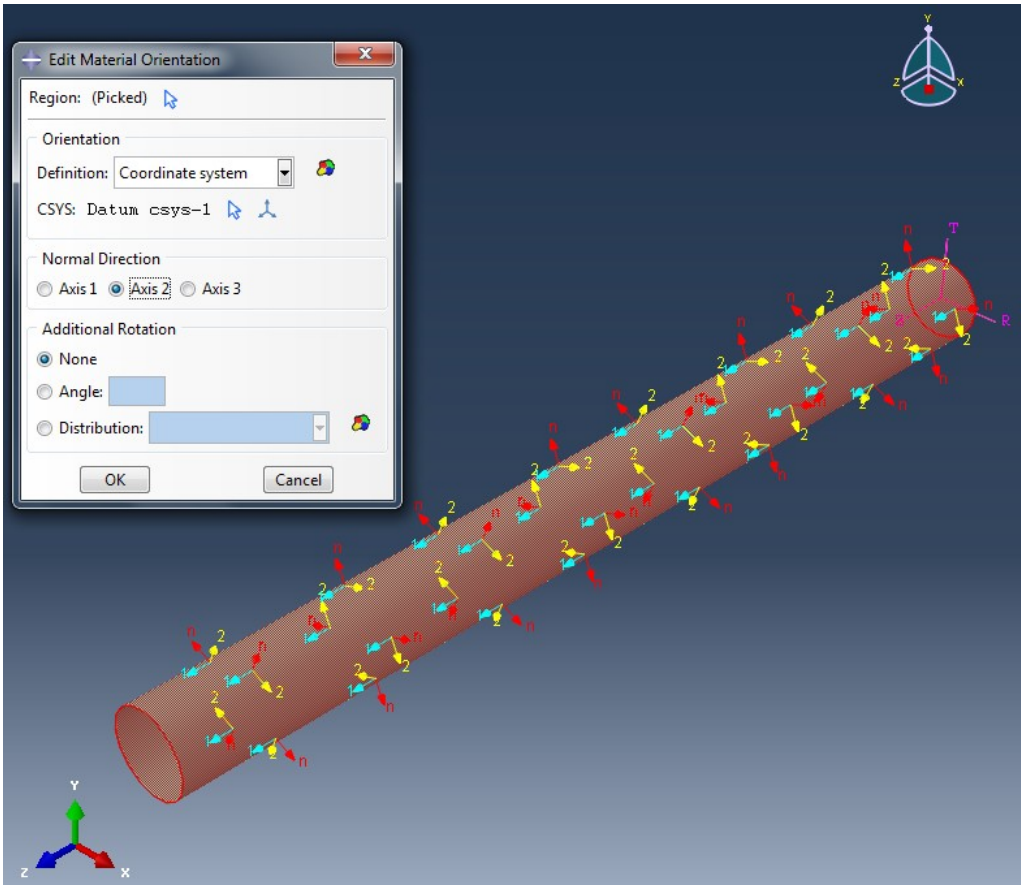

These orientations can be verified using the "Query" tool.

At this point the part definition is complete. An assembly can be created by going to the assembly manager and double clicking "Instances". The instance should be set as independent.

The assembly can now be meshed. First, global seeds are created by selecting "Seed Part Instance" from the mesh toolbar. In this case, a 25mm mesh will be created:

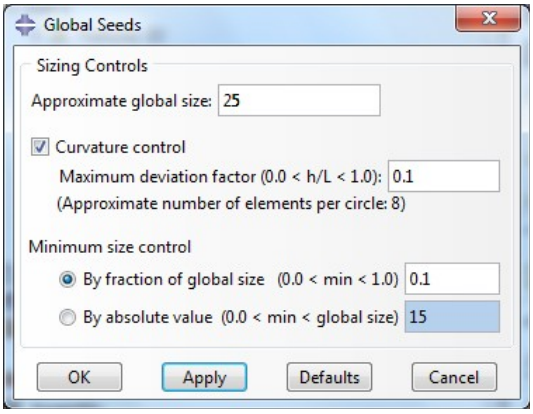

The element type can be chosen by clicking on "Select Element Type". Linear finite-strain elements should be selected. Reduced integration can be used to control the possibility of shear locking, but the stiffness of the element will also be reduced slightly:

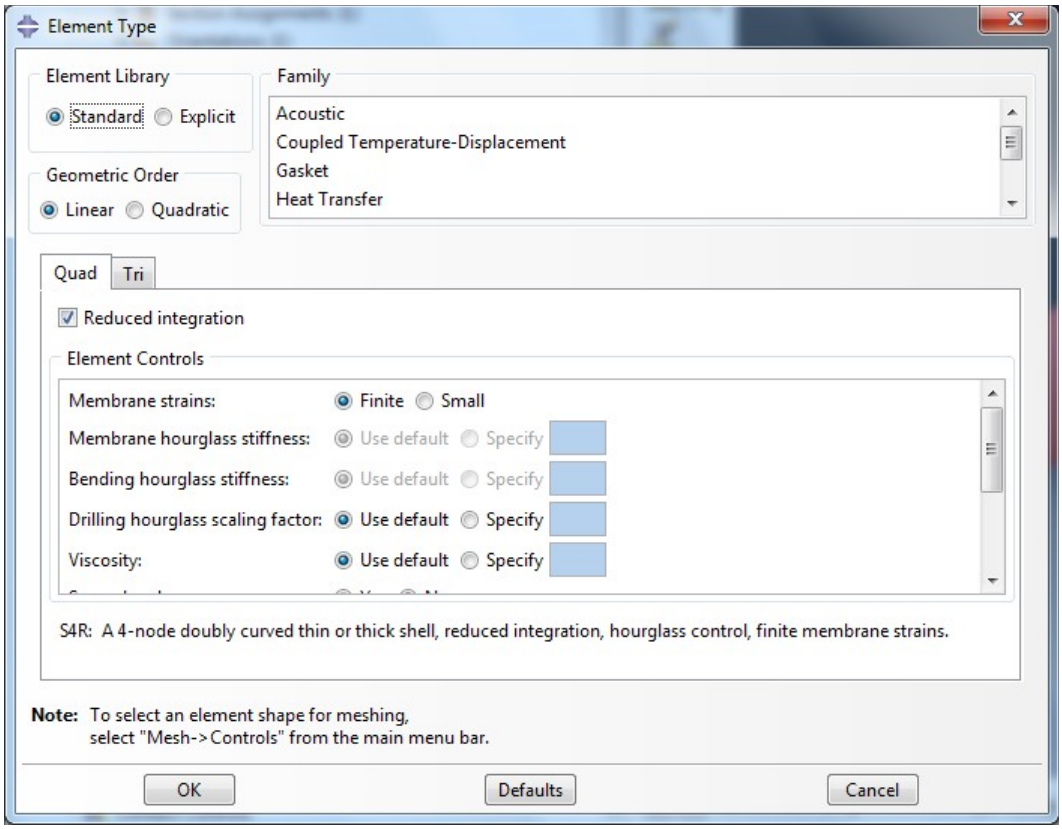

In order to ensure that the mesh is assigned correctly, the mesh controls should be checked. If quadrilateral elements were selected, a quad element shape is appropriate:

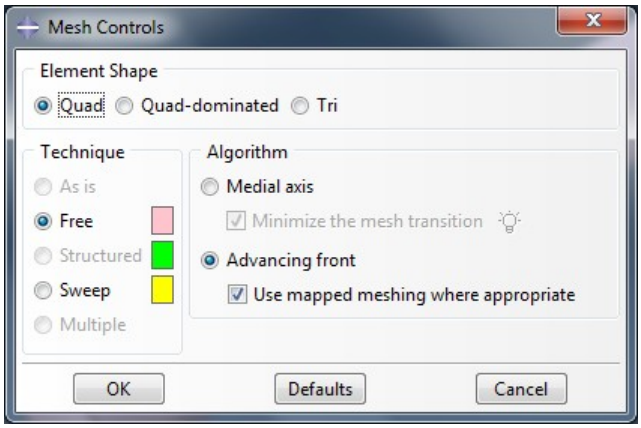

Now the part can be meshed by selecting "Mesh Part Instance".

In order to apply the boundary conditions, two reference points should be created now, one at each end of the tube. In this case, one is assigned at 0,0,0 and one is assigned at 0,0,12500. In addition, datum planes are created to make it clear where the center of the tube is:

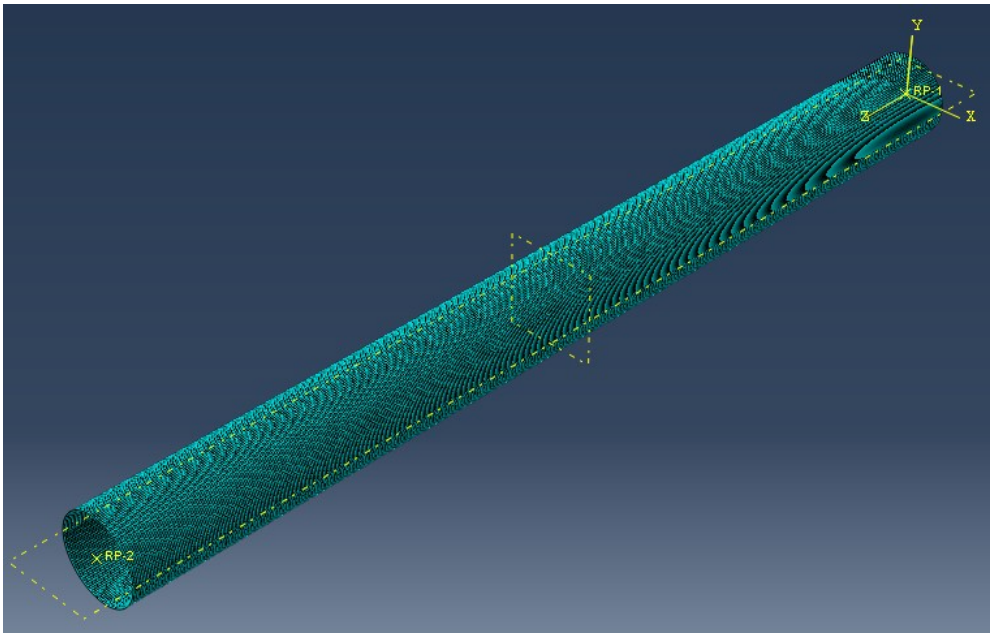

Some sets have to be assigned now in order to make it easier to export the output and in order to assign residual stresses. An element set of all elements is created to which the residual stresses are assigned, and two sets are created at the points where the output is required. One of these sets is a geometry set of the reference points, because the moment and rotation are measured here, and one is a node set located at the center of the tube on one of the sides, to measure horizontal ovalization. The datum planes that were defined can be used to locate the node nearest to the center:

The next step is to define the analysis steps. If residual stresses are applied, an empty static general step has to be applied in order to check for equilibrium before analysis. Next, a static riks step has to be defined. A stopping criteria can be specified by specifying the maximum rotation at the end supports:

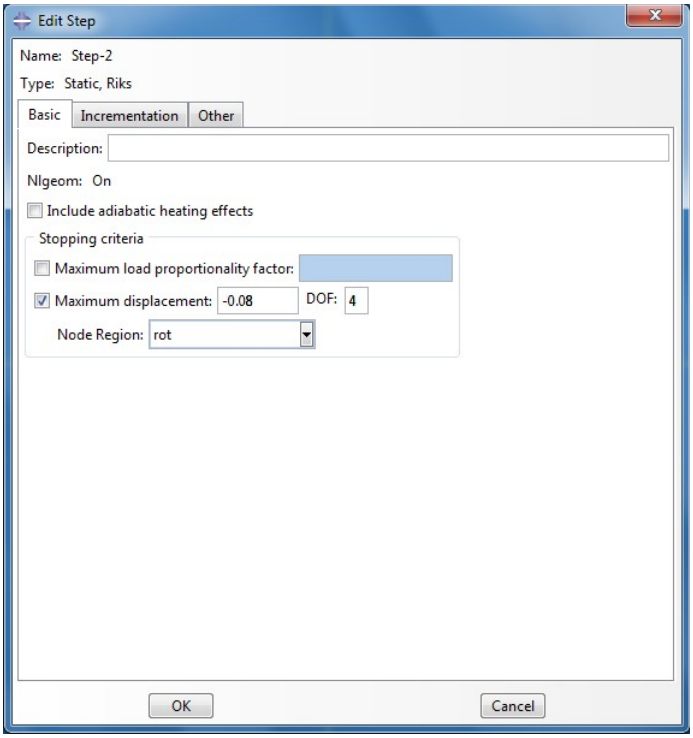

The incrementation is important because it controls the smoothness of the resulting solution, and can influence whether or not the solution converges close to buckling. A maximun and initial step size of 0.5 is a good initial guess, and the minimum step size can also be decrased if the solution does not converge (1E-8 is a good guess):

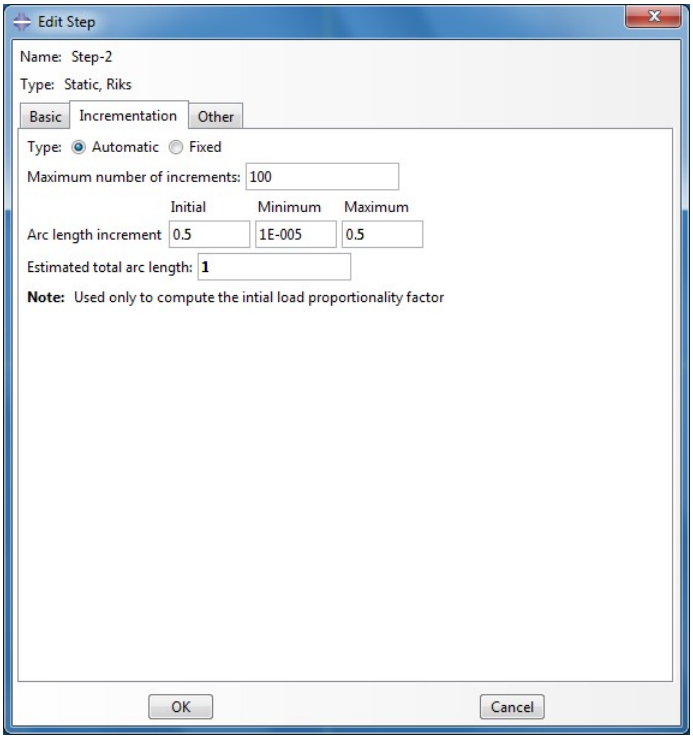

The nonlinear geometry flag should be activated for both steps.

It should also be verified that the correct output is being requested under "Field Output Requests" and "History Output Requests". It should be verified that output is being requested for all steps, and that the values of interest are selected (the preselected defaults are usually sufficient). It should also be verified that output is being requested after every increment.

Next some constraints have to be defined. Kinematic couplings should be used to tie the reference points at each tube end to the corresponding tube opening:

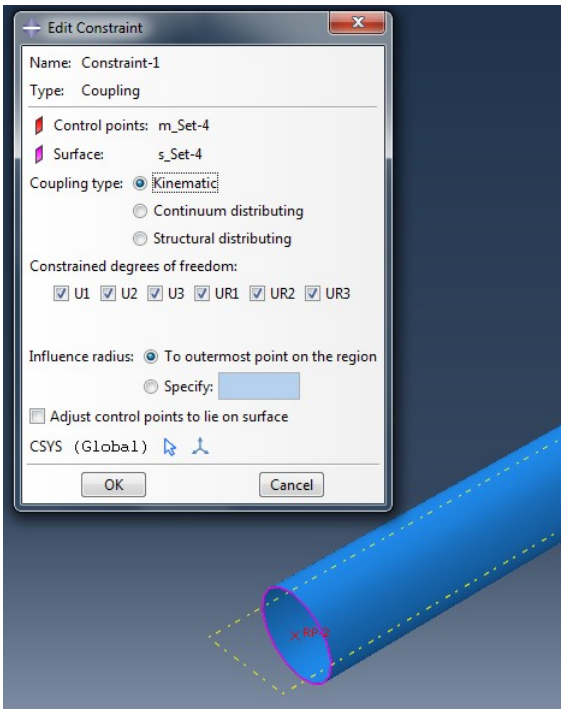

Now the boundary conditions can be defined. One end should be constrained in the directions U1, U2, UR2, and UR3, and the other end should be constrained in U1, U2, U3, UR2, and UR3. These conditions prevent the tube from rotating or moving, but allow one end of the tube to slide along the tube axis.

The loads can also be applied to the same points. The loads should be symmetric. In the static riks analysis, these loads will be increased during the analysis proportional to the load step increments defined earlier. Applying a moment equal to 10-20% of the yield moment is a good starting point.

Finally, the initial imperfections and initial conditions are applied. They are both applied by editing the input file. Within the graphical user interface, this can be done by right-clicking the name of the model and clicking "Edit Keywords". The keywords are then entered as shown below:

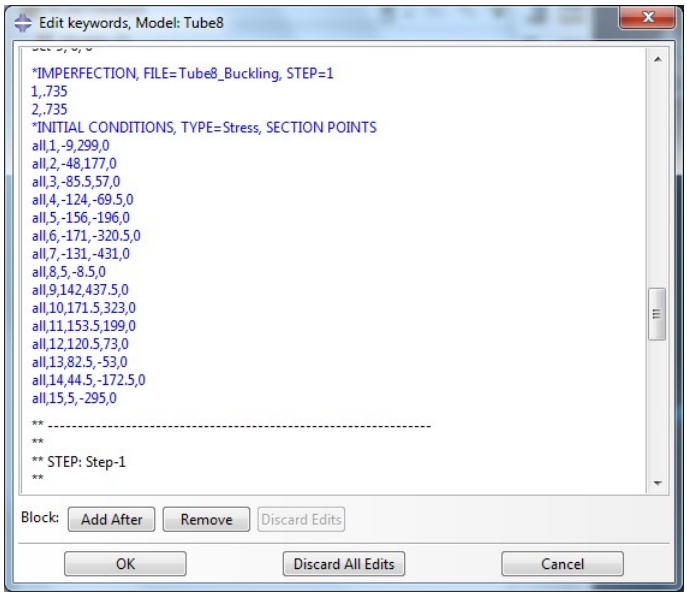

It is important that the imperfection is entered first and that both conditions are entered before the step. The syntax is as follows.

For the initial imperfection:

*IMPERFECTION, FILE=*name of buckling analysis*, STEP=1
mode number, scale factor

For the residual stresses:

*INITIAL CONDITIONS, TYPE=Stress, SECTION POINTS
element set name, thickness integration point, s11, s22, s12

Before this analysis will work, a buckling analysis has to be performed. The tube model is simply copied and the following changes are made:

1. The static steps are suppressed and a Linear perturbation->Buckle step is added. The Lanczos solver can be used and a minimum eigenvalue of 0 can be specified.

2. A load should be applied. The calculated eigenvalues will be proportional to this load, so a load such as 1,000 N*mm is a good choice.

3. The following keyword should be added to the input file right before the keyword *End Step:

*NODE FILE
u

Now the buckling analysis can be submitted. First a job is created. The name of the job must match the name of the job from which the initial imperfections will be taken. In order to speed up the analysis, CPU parallelization can be selected by going to the "Parallelization" tab.

After the buckling analysis is complete, the static analysis can be submitted in the same way.

The jobs can be monitored by right clicking on the job and clicking on "Monitor", and the results can be viewed by clicking on "Results".

One way to export the output is to go to Tools->XY Data->Manager, in the results viewer. XY data can be created based on the ODB field output.

In the dialog box, the position "Unique Nodal" should be selected. Then the required output variables can be selected. To generate a moment-curvature diagram, the output variables CM1 and UR1 should be selected. The initial empty static step should also be deselected, so that only output from the Riks analysis is requested:

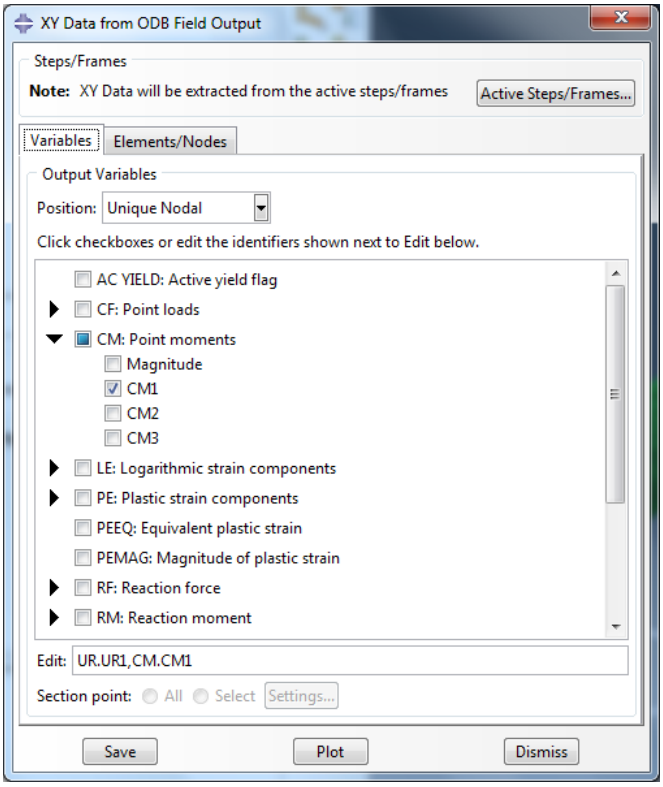

The node set corresponding to the reference point at the support can be selected under the "Elements/Nodes" tab. The output can now be viewed by clicking "Plot", and prepared to be exported by clicking "Save".

Finally, a text file can be generated from this output by going to the Report->XY. The data can now be further manipulated in another program.

One way of running multiple analyses is to use batch files. An input file can be created from within the graphical interface by right clicking on the job and selecting "Write Input". Next a batch file has to be created to call this input file. The syntax is as follows:

abaqus job=*name of input file* interactive

Multiple batch files can be created which correspond to different input files. In order to call them, a master batch file is also created, which has the following syntax to call the batch files defined above. Multiple jobs can be called this way:

call *name of batch file*.bat

Appendix E: Evolution of Deformed Shape

In this section, images are presented which show how the initial imperfections localize and how the buckled shape forms.

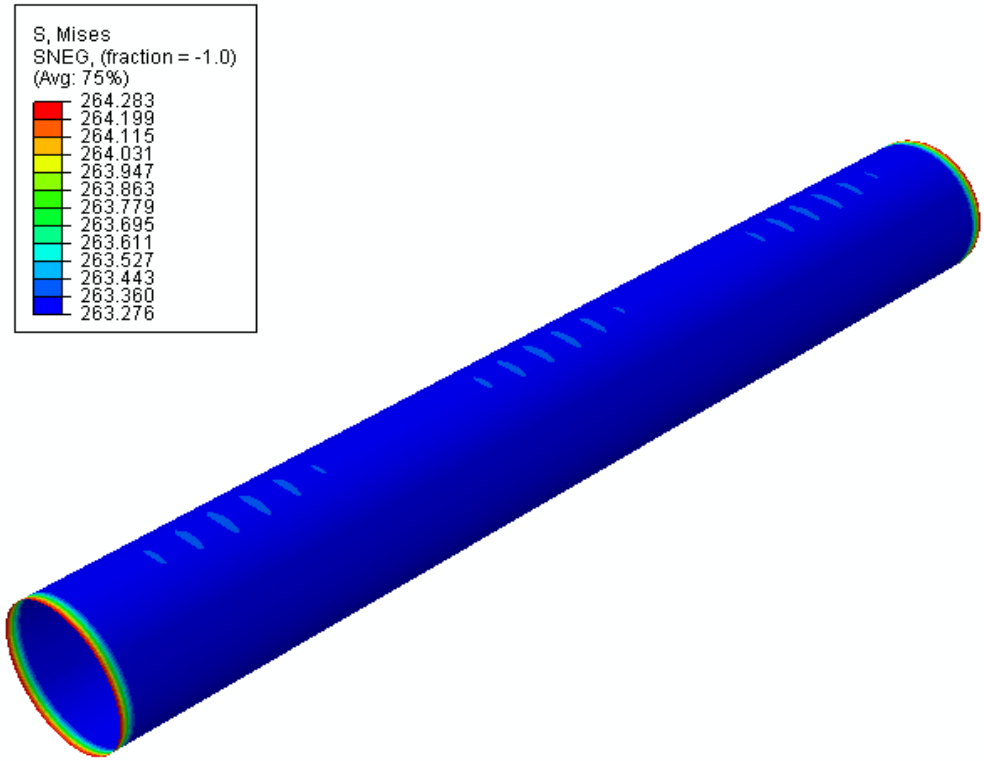

Figure 246: Deformed shape after application of residual stresses and imperfections

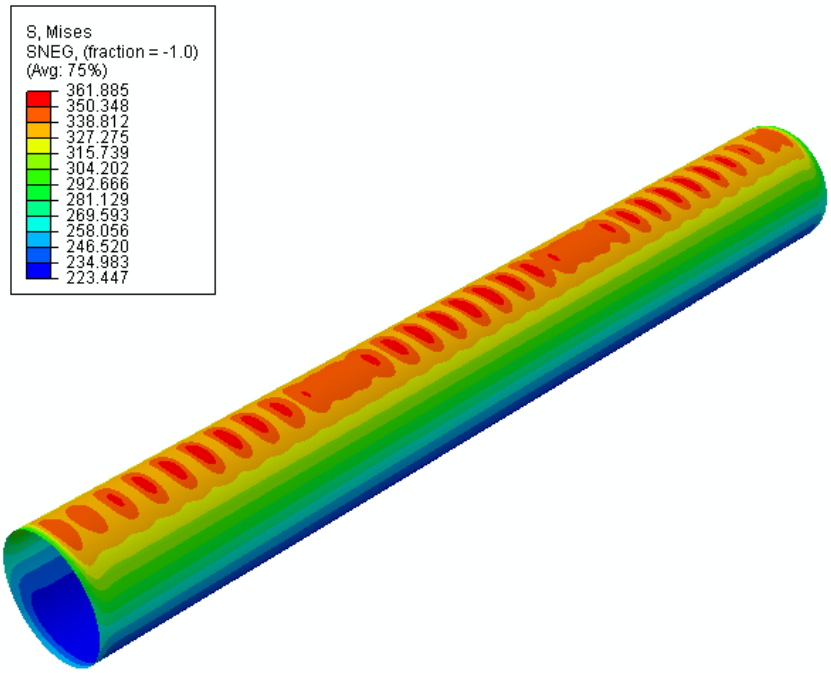

Figure 247: von Mises stresses in elastic region

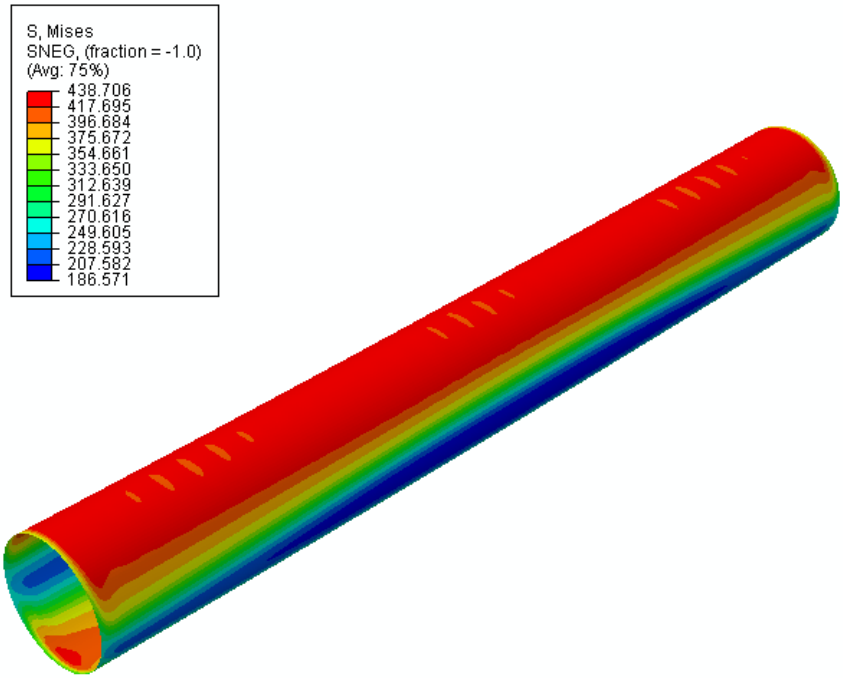

Figure 248: von Mises stresses after start of yielding

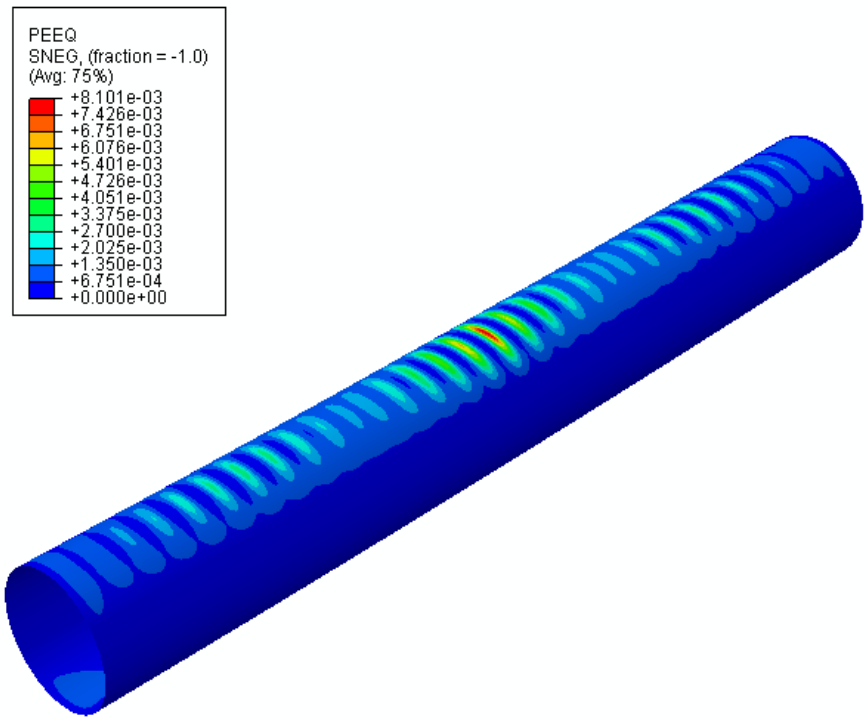

Figure 249: Equivalent plastic strains after yielding

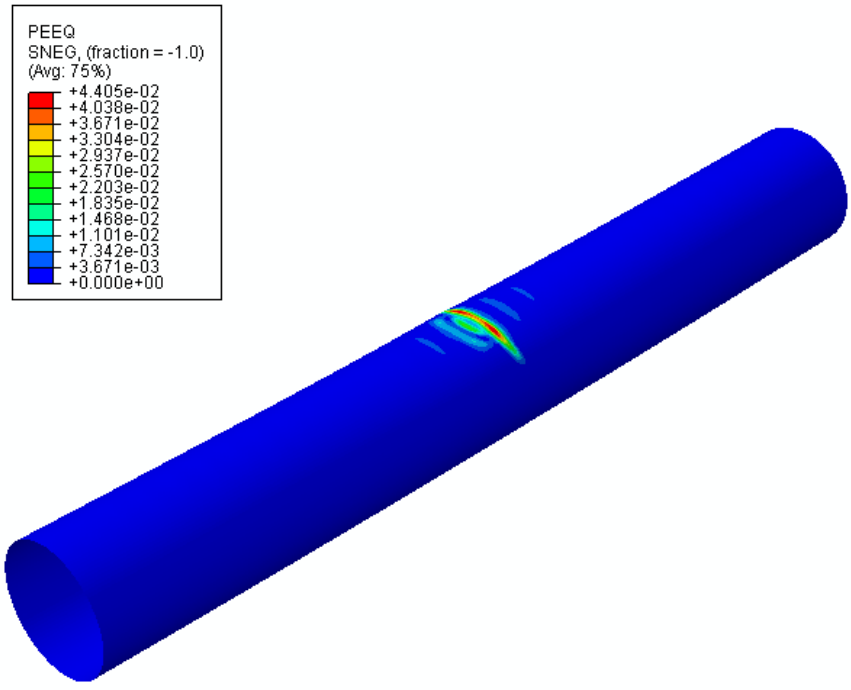

Figure 250: Equivalent plastic strains at start of buckling

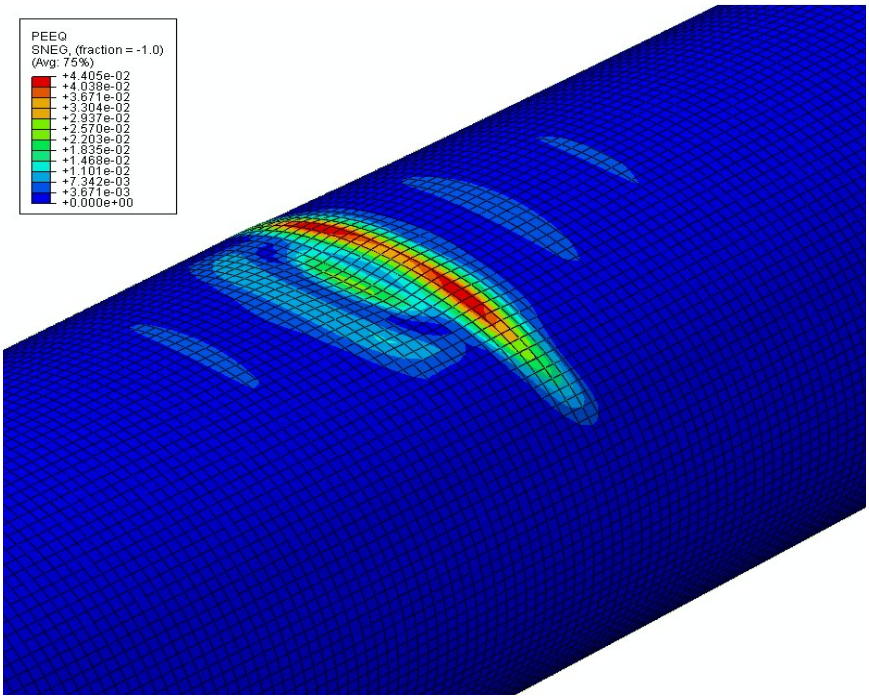

Figure 251: Detail of equivalent plastic strains at start of buckling

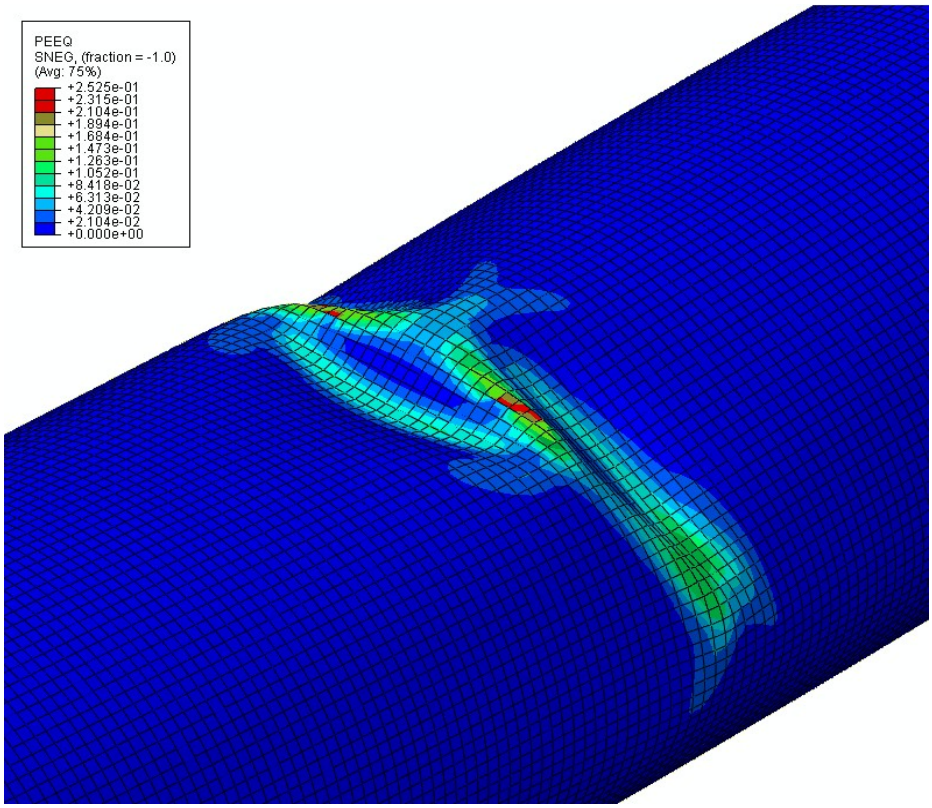

Figure 252: Equivalent plastic strains after buckling

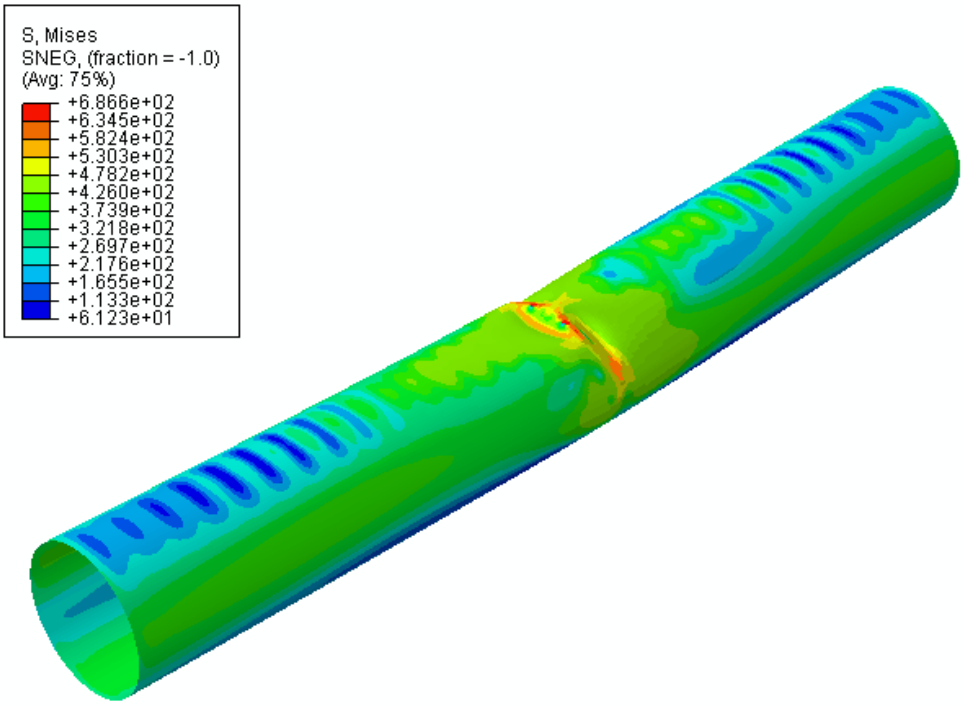

Figure 253: von Mises stresses after buckling

Appendix F: Raw Data of 3 Variable Parameter Study

Table 68: Results of 3 variable parameter study

D/t	fy	2w/t	k_{crit}/k_y	M_{max}/M_p	k_{crit} (10^6 /mm)	M_p (kNm)
60	320	0.01	8.39	1.14	24.53	7126.55
60	320	0.04	7.13	1.12	20.88	7037.81
60	320	0.07	6.35	1.11	18.58	6952.05
60	320	0.14	5.19	1.08	15.20	6789.42
60	380	0.04	5.64	1.10	19.60	8191.86
60	380	0.07	4.99	1.09	17.32	8087.86
60	380	0.1	4.54	1.08	15.76	7998.05
60	380	0.14	4.08	1.06	14.19	7892.18
60	420	0.01	5.78	1.09	22.18	8985.89
60	420	0.04	4.82	1.08	18.51	8860.12
60	420	0.07	4.23	1.06	16.26	8748.65
60	420	0.1	3.83	1.05	14.72	8650.55
60	420	0.14	3.48	1.04	13.37	8534.73
60	520	0.01	4.19	1.05	19.93	10716.70
60	520	0.07	3.05	1.02	14.49	10396.40
60	520	0.1	2.77	1.01	13.19	10265.70
60	520	0.14	2.54	0.99	12.09	10111.50
60	600	0.01	3.37	1.02	18.46	12026.60
60	600	0.07	2.47	0.99	13.57	11612.90
60	600	0.1	2.26	0.97	12.40	11448.20
60	600	0.14	2.07	0.96	11.34	11257.80

D/t	fy	2w/t	k_{crit}/k_y	M_{max}/M_p	k_{crit} (10^6 /mm)	M_p (kNm)
60	700	0.01	2.70	0.99	17.28	13634.10
60	700	0.04	2.23	0.97	14.28	13310.60
60	700	0.1	1.86	0.94	11.90	12852.10
60	700	0.14	1.73	0.92	11.09	12623.00
80	320	0.01	5.32	1.07	15.57	5080.55
80	320	0.04	4.00	1.04	11.71	4940.14
80	320	0.07	3.76	1.04	11.01	4938.24
80	320	0.14	3.05	1.02	8.93	4815.26
80	380	0.01	4.21	1.05	14.61	5916.81
80	380	0.04	3.43	1.03	11.91	5813.02
80	380	0.07	3.04	1.02	10.55	5731.27
80	380	0.1	2.77	1.01	9.62	5656.80
80	420	0.01	3.55	1.03	13.65	6411.12
80	420	0.04	2.93	1.01	11.24	6289.84
80	420	0.07	2.60	1.00	9.98	6190.92
80	420	0.14	2.14	0.96	8.24	6001.61
80	520	0.01	2.60	0.99	12.35	7612.05
80	520	0.04	2.11	0.96	10.06	7411.04
80	520	0.07	1.95	0.94	9.27	7264.08
80	520	0.1	1.80	0.93	8.56	7138.69
80	520	0.14	1.66	0.91	7.89	7017.07

D/t	fy	2w/t	k_{crit}/k_y	M_{max}/M_p	k_{crit} (10^6 /mm)	M_p (kNm)
80	600	0.01	2.11	0.95	11.58	8476.93
80	600	0.04	1.78	0.93	9.76	8226.61
80	600	0.07	1.62	0.91	8.87	8045.58
80	600	0.1	1.52	0.89	8.36	7895.91
80	600	0.14	1.42	0.87	7.81	7738.28
80	700	0.01	1.71	0.91	10.96	9460.26
80	700	0.04	1.48	0.88	9.48	9127.04
80	700	0.1	1.33	0.85	8.52	8770.91
80	700	0.14	1.28	0.83	8.16	8604.60
100	320	0.01	3.74	1.03	10.93	3921.37
100	320	0.04	3.05	1.01	8.94	3854.10
100	320	0.1	2.47	0.99	7.24	3753.23
100	320	0.14	2.27	0.97	6.64	3695.91
100	380	0.01	2.93	1.01	10.18	4547.67
100	380	0.04	2.48	0.98	8.60	4454.51
100	380	0.07	2.21	0.97	7.67	4381.06
100	380	0.1	2.03	0.95	7.04	4317.49
100	420	0.01	2.54	0.98	9.75	4916.02
100	420	0.04	2.13	0.96	8.19	4802.90
100	420	0.07	1.89	0.94	7.27	4705.63
100	420	0.1	1.78	0.93	6.82	4637.06
100	420	0.14	1.66	0.91	6.36	4551.08

D/t	fy	2w/t	k_{crit}/k_y	M_{max}/M_p	k_{crit} (10^6 /mm)	M_p (kNm)
100	520	0.04	1.63	0.90	7.74	5599.56
100	520	0.07	1.50	0.88	7.12	5474.68
100	520	0.1	1.43	0.87	6.81	5385.58
100	520	0.14	1.35	0.85	6.43	5279.70
100	600	0.01	1.56	0.89	8.53	6350.88
100	600	0.04	1.39	0.86	7.64	6147.15
100	600	0.07	1.31	0.84	7.21	6021.41
100	600	0.1	1.27	0.83	6.97	5924.94
100	600	0.14	1.22	0.81	6.69	5820.51
100	700	0.01	1.32	0.84	8.48	7009.53
100	700	0.04	1.23	0.82	7.88	6806.29
100	700	0.07	1.18	0.80	7.57	6673.97
100	700	0.1	1.15	0.79	7.34	6569.18
120	320	0.01	2.84	1.00	8.32	2131.32
120	320	0.04	2.41	0.98	7.06	2090.90
120	320	0.07	2.18	0.96	6.37	2058.70
120	320	0.1	2.00	0.95	5.86	2027.90
120	380	0.01	2.13	0.97	7.42	2464.77
120	380	0.04	1.89	0.95	6.57	2404.58
120	380	0.07	1.72	0.93	5.99	2360.59
120	380	0.14	1.49	0.90	5.18	2276.89

D/t	**fy**	**2w/t**	**k_{crit}/k_y**	**M_{max}/M_p**	**k_{crit} (10^6 /mm)**	**M_p (kNm)**
120	420	0.01	1.88	0.94	7.23	2653.78
120	420	0.04	1.63	0.92	6.24	2580.58
120	420	0.07	1.50	0.90	5.75	2531.34
120	420	0.1	1.43	0.89	5.48	2491.65
120	420	0.14	1.35	0.87	5.17	2449.39
120	600	0.01	1.17	0.83	6.43	3347.39
120	600	0.04	1.13	0.82	6.18	3285.66
120	600	0.07	1.10	0.81	6.01	3234.65
120	600	0.1	1.07	0.80	5.88	3198.48
120	600	0.14	1.04	0.78	5.69	3133.62
120	700	0.01	1.07	0.80	6.83	3727.35
120	700	0.07	1.02	0.77	6.51	3615.25
120	700	0.14	0.99	0.76	6.35	3539.19